Etude par neuroimagerie IRM de la représentation centrale des mouvements de la main chez les sujets sains et chez les patients après chirurgie de la main

Fabrizio Pizzagalli

UNIVERSITÉ DE GRENOBLE

THÈSE

Pour obtenir le grade de

DOCTEUR DE L'UNIVERSITÉ DE GRENOBLE

Spécialité : **BIS - Biotechnologie, instrumentation, signal et imagerie pour la biologie, la medecine et l'environnement**

Arrêté ministériel : 7 août 2006

Présentée par

Fabrizio Pizzagalli

Thèse dirigée par **Chantal Delon-Martin**
et codirigée par **Michel Dojat**

préparée au sein du **Grenoble Institut des Neurosciences**
et de **l'Ecole doctorale ingénierie pour la santé, la cognition et l'environnement**

Multimodal MR imaging to investigate hand movement cortical representation in healthy subjects and in patients following hand surgery

Thèse soutenue publiquement le **8 Novembre 2012**,
devant le jury composé de :

Jean-François Mangin
PhD CEA NeuroSpin, Rapporteur

Jean-Philippe Ranjeva
PhD CRMBM UMR CNRS 6612, Rapporteur

François Moutet
Prof. Hopital Albert Michallon CHU de Grenoble, Examinateur

Habib Benali
PhD INSERM-Paris VI , Examinateur

Chantal Delon-Martin
PhD - INSERM, Directeur de thèse

Michel Dojat
PhD - INSERM, Co-Directeur de thèse

Contents

Part I

Motivations and context

CHAPTER 1

Motivations

1.1 Medical motivation

The main motivation of this work is based on an important question raised from Professor François MOUTET, Professor of *Chirurgie Plastique Réparatrice de la Main et des Brules* at the Albert Michallon Hospital, CHU - Grenoble: **which structural and/or functional plasticity occurs in the brain cortex after a hand tendinous transfer surgery?**

Paralysis of the hands produces major functional impairments. The ability to perform activities of daily life can be severely compromised, especially in bilateral paralysis. When some muscle-tendon units remain functional in an extremity, it is possible to take advantage of a redundant function to restore another one by transferring the working unit to a new location. Restoring something as simple as a pinch grip can create major improvement for the patient in the functionality of his/her extremity. The use of a normal tendon to replace another one that has been damaged is called **tendinous transfer** [Tsuge 1969] (see Chapter 7.1). Tendinous transfer is a surgery that uses a normal flexor tendon to replace an extensor one that has been damaged. In other words a **flexion/exenstion function inversion** occurs.

The investigation of the correlation between reacquired motor skills and the consequent functional brain reorganization, after hand tendon transfer surgery, is the main goal of this research project.

We know that the primary motor cortex (**M1**) is a part of a neuronal network devoted to voluntary movement. The general aspects of this network are described in Chapter 3. Knowing that one single muscle can be driven by multiple neuronal units, that a single neuronal unit can drive multiple muscles and that M1 contains a dense network of horizontal connections, one can understand that the relationship between neuronal units of M1 and muscle activation is not straightforward. Many teams have been working on this relationship in normal context (for example,

[Georgopoulos 1982, Caminiti 1991, Sanes 2000, Schieber 2001]) and in the context of brain reorganization following a perturbation. Here, we address the functional reorganization of the motor network at a macroscopic level, accessible via neuro-imaging tools, and not at a microscopic level.

1.2 Cerebral plasticity in the motor network

Ernesto Lugaro (Italian psychiatrist) first introduced the term **plasticity** in neuroscience in 1906 [Lugaro 1906, Berlucchi 2002]. Donald Hebb in 1949 [Hebb 1949], postulates that cortical neuronal connections are modulated according to the life experiences of the subject. Brain plasticity is defined as a functional reorganization following a brain injury or a specific learning, including motor (Hebb et al. 1958). Recent studies demonstrate that plasticity includes structural changes at a microscopic level (synaptogenesis, glial proliferation and angiogenesis) but also at a macroscopic level [Draganski 2008]. Researchers are also studying the dynamic of functional changes related to motor tasks learning and motor adaptation after perturbation in the environment [Ungerleider 2002].

Brain plasticity is also involved in recovery from stroke. In particular, after a focal lesion in the primary motor cortex, the recovery was co-occurent with cortical reorganization [Nudo 2001], coherent with a vicarious process (reorganization within cortical M1 mediated by horizontal connections) [Jaillard 2005]. Other cortical areas such as the supplementary motor area (**SMA**) [Picard 2001] and the contralesional M1 are also involved during the recovery process [Marshall 2000]. Recent fMRI pilot investigations shown how, without overt behavior, the sensory motor system is activated more by motor imagery rather than passive movement or movement observation, in stroke patients [Szameitat 2012].

But what about for peripheral nerve damage or restoration?
Few studies address the brain plasticity on patients who experienced a peripheral injury or surgery, such as limb-amputation or grafts. In case of peripheral nerve injury, one observes a reorganization of the functional connections between cortical areas adjacent to the fingers areas [Sanes 2000]. Other studies on limb-amputed subjects have shown an expansion of cortical representations of adjacent body parts, probably induced by the "deafferentation" of the limb area during the amputation, associated with the phantom limb syndrome occurrence [Weiss 2000, Lotze 2001]. For the congenital absence of a limb, the cortical organization was modified in comparison with normal

subjects. A shift in adjacent areas exists, especially from the face and tongue areas to the hand area, but without onset of phantom limb sensation [Funk 2008a, Funk 2008b]. In the first patient who had a double hand graft, the representation of the hands in the cortex shifted more medially, in a more typical location, after 6 months of rehabilitation [Giraux 2001] (Fig. 1.1).

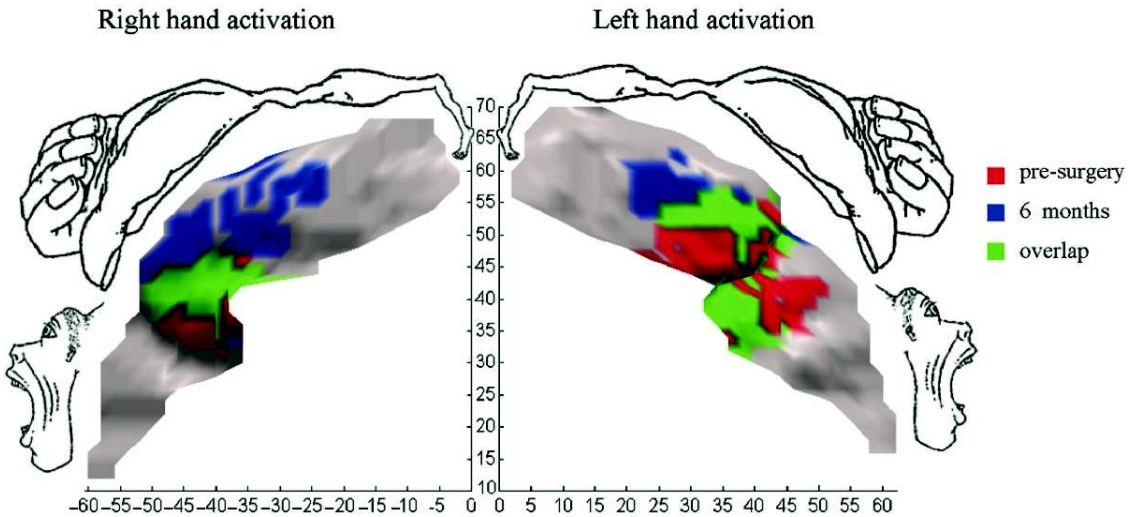

Figure 1.1: *Hand movement activation maps overlapped on the M1 surface, for both hemispheres. The Penfield's motor homunculus matches the "hand-knob" region. Activations were obtained in the exams before surgery (red) and six months afterward (blue), and their overlap (green) [Giraux 2001].*

It has been shown that, after a *toe-to-finger transplantation*, M1 and the the primary somatosensory cortex (**S1**) recovered their functionality, as in "normal" subjects [Chen 2006]. In the only study on tendinous transfer, an 84 y.o. patient was examined fifteen years after surgery (thumb movement restoration from finger IV). The voluntary thumb movement evidenced a cortical activation in M1 corresponding to the location of thumb in normal subjects [Viswanathan 2006]. A theory of "*maladaptive*" plasticity has also been proposed. The high capability of the brain to change may lead to harmful configurations. The focal hand dystonia (FHD) ("writer's cramp") is an example of maladaptive plasticity. By using fMRI Pujol and collaborators examined five guitarists during dystonic symptoms provocation [Pujol 2000]. They found an abnormal recruitment of cortical areas for dystonic musicians. Resent studies have shown that in FHD patients there is less activation in the contro-lateral sensorymotor *Putamen* and in the ipsilateral *Cerebellum* comparing to a group of healthy subjects. And a compensative process could be exist, highlighted by the increased con-

nectivity between the sensory motor and associative striato-cortical circuits in FHD [Moore 2012]. This maladaptive plasticity is also related to structural changes such as the grey matter volume increase for FHD [Garraux 2004] and loss of thalamic gray matter contralateral to the amputated limb, causing a "negative" structural reorganization [Draganski 2006]. Both of this studies used the voxel-based morphometry (VBM) method [Ashburner 2000]. VBM has been used also to show gray matter change induced by **training** [Draganski 2004] (Fig. 1.2).

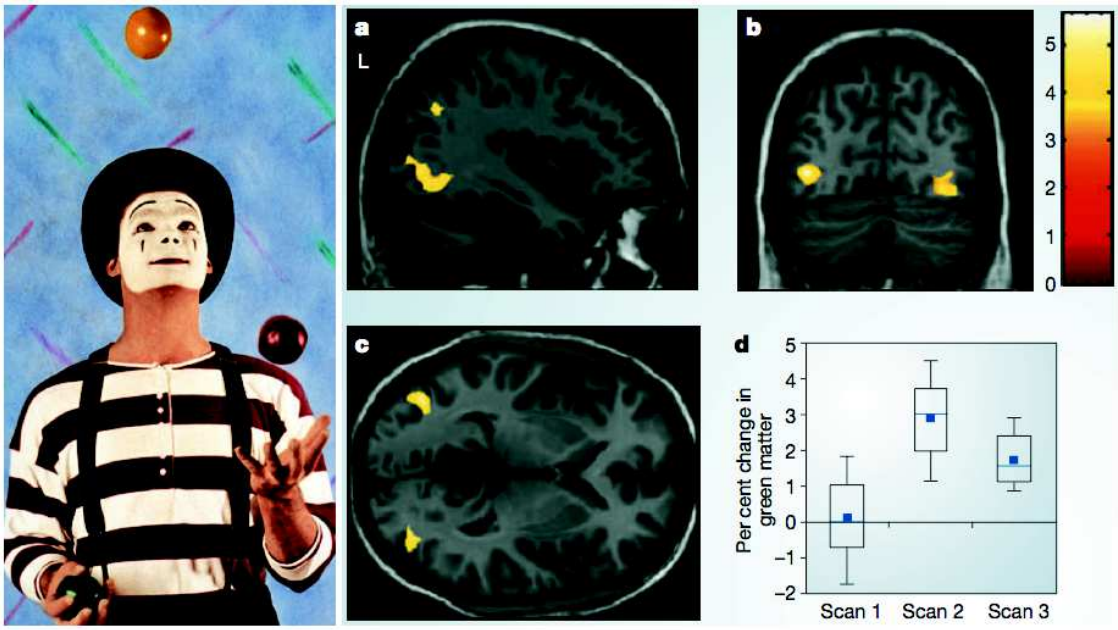

Figure 1.2: *Transient changes in brain structure induced while learning to juggle. Statistical parametric maps showing the areas with transient structural changes in grey matter for the jugglers group compared with non-juggler controls. A significant expansion in grey matter was found between the first and second scans in the mid temporal area bilaterally and in the left posterior intraparietal sulcus. Color scale indicates Z-scores,which correlate with the significance of the change. The box plot shows the standard deviation,range and the mean for each time point. Adapted from [Draganski 2004].*

Doyon and Ungerleider [Doyon 2005] proposed a model of cerebral plasticity within the cortico-striatal system during the course of learning a new sequence of movements (motor sequence learning) or a cortico-cerebellar system during adaptation to environmental perturbations (motor adaptation) (Fig. 1.3). Their model, which relies on an extended review of the literature, proposes that, depending on the nature of the cognitive processes required during learning, both

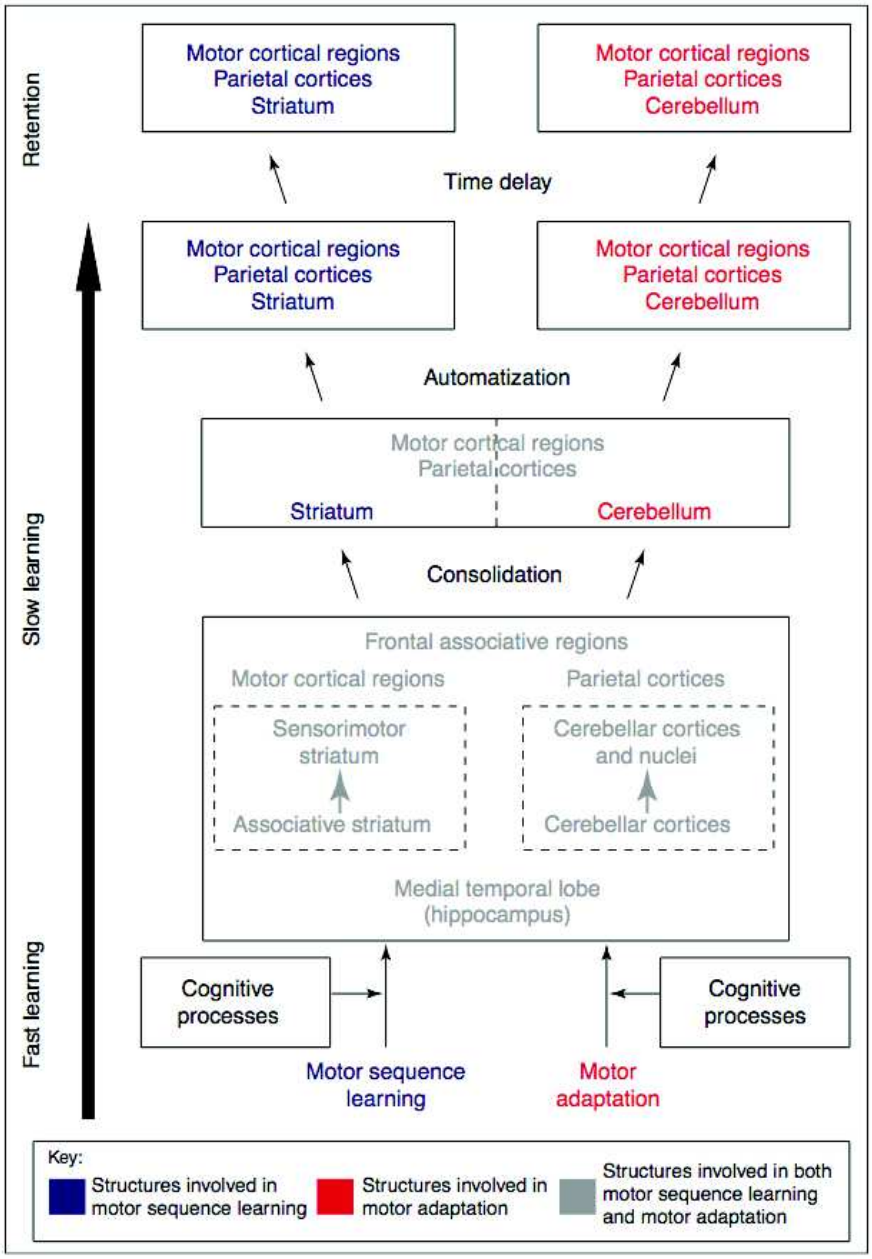

Figure 1.3: *Doyon and Ungerleider model for the plasticity of the brain regarding motor skills learning. The model suggests that for motor adaptation, the striatum is no longer necessary for the retention and execution of the acquired skill; regions representing the skill now include the cerebellum and related cortical regions. By contrast, a reverse pattern of plasticity is thought to occur in motor sequence learning, such that with extended practice the cerebellum is no longer essential, and the long-lasting retention of the skill is now believed to involve representational changes in the striatum and associated motor cortical regions [Doyon 2005].*

motor sequence and motor adaptation tasks recruit similar cerebral structures early in the learning phase: the striatum, cerebellum, motor cortical regions, in addition to prefrontal and parietal areas. Dynamic interactions between these structures are likely to be crucial for establishing the motor routines necessary to learn the skilled motor behavior. Furthermore, new evidence indicates that cerebral functional plasticity within the striatum and the cerebellum can also be observed. A shift of motor representation from the associative to the sensorimotor striatal territory can be seen during sequence learning, whereas additional representation of the skill can be observed in the cerebellar nuclei after practice on a motor adaptation task. The neural representation of a new motor skill is believed to be distributed in a network of structures that involves the CS (cortico-striatal) or CC (cortico-cerebellar) circuit depending on the type of motor learning acquired. When consolidation has occurred, the subject has achieved asymptotic performance which becomes automatic. The neural representation of this motor behavior is then thought to be distributed in a network of structures involving mainly one of these two circuits.

1.3 Aims of the thesis

The aim of this study is to investigate the dynamic of the functional reorganization of the motor circuit in patients who underwent a tendinous transfer rehabilitative surgery. Within this framework, high spatial resolution fMRI was used focusing on cortical and cerebellar structures. In order to compare the patients functional patterns to reference patterns, a group of healthy subjects was evaluated with the same protocol than the patients. In order to get rid of inter-subjects variability, we introduced and evaluated different accurate registration methods in the analysis.

CHAPTER 2

Scientific hard points and our approach

Studying the functional and structural reorganization of the primary motor cortex after hand tendons transfer surgery is highly challenging. The poor knowledge of the motor cortex functional organization hampers a clear understanding of what exactly happens in the brain of operated patients. This is a neuroscientific challenge that is accompanied by a methodological challenge: **which is the best acquisition and data analysis method to achieve robust results and a clear separation of activated clusters following hand movements?** The interpretation of results would strongly depends on the method used.

2.1 Hand functional organization is poorly known

Functional arrangement of body parts, that is the correspondence of an area of the body to a region on the central nervous system (CNS), is poorly known. As we will see in section 3.2, several studies, across the last century, deal with the somatotopy investigation. J. Hughlings Jackson (1873) [Hughlings-Jackson 1873] was the first to postulate the existence of distinct cortical representations of different movements based on epilepsy patients observations. Penfield, by using electric stimulation, mapped the sensory and motor cortex and his findings are summarized by the famous homunculus [Penfield 1950]. He founded several "point" corresponding to a given movement. Schieber collected and reviewed different studies, from Penfield and others, showing different activated regions for a single movement and an important degree of overlap between them (Fig. 2.1) [Schieber 2001]. Recent studies confirm the idea that a single cortex region mapping a single movement should be abandoned for a " **synergetic interconnected area**" model. By using fMRI (functional Magnetic Resonance Imaging) a large overlap representation covering large portions of the M1 hand area performing individual movements of all fingers has been detected [Hlustík 2001, Dechent 2003], highlighting the complex hand movement arrangement in the brain

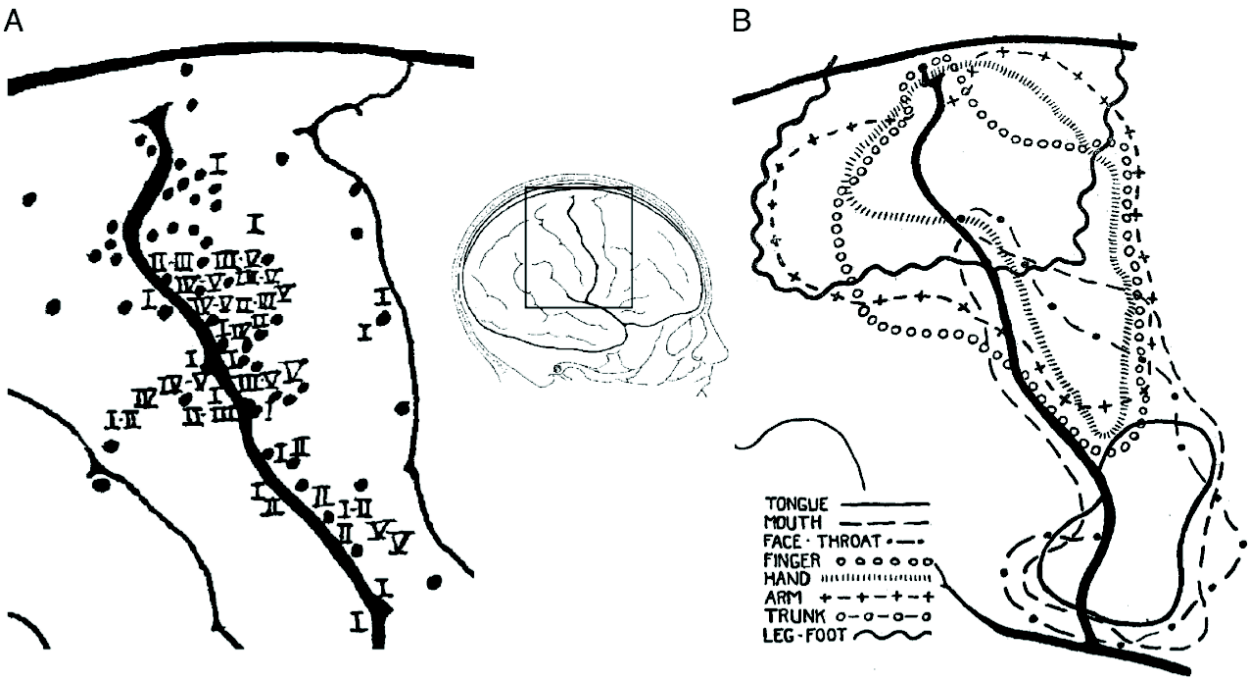

Figure 2.1: *Convergence and overlap in Penfield's data. Enlargements are shown from Figs. 12A and 25B of Penfield and Boldrey [Peinfield 1937]. The region enlarged is indicated by the rectangle drawn on the inset taken from their standardized map of the hemisphere, but note that whereas the region shown in B extends laterally to the Sylvian fissure and therefore includes the face representation, the region shown in A does not. A: locations from which finger movements were elicited in data compiled from 126 patients. If only certain digits moved, they are indicated with Roman numerals: I=thumb through V=little finger. Black dots indicate locations where stimulation elicited movement of all the digits. Note that, contrary to the discrete order implied by the homunculus, thumb movements were elicited medially as well as laterally, and little finger movements were elicited laterally as well as medially. B: outlines encompass the total territory from which movements of the fingers (○ ○ ○), entire hand (¦¦¦), or more proximal arm (+ − + − +) were evoked. Note the overlap of distal and proximal representations. Extracted from [Schieber 2001].*

cortex (Fig. 3.8) [Meier 2008] .

2.2 Standard fMRI spatial resolution too low for a precise investigation

Among the existing techniques used to investigate functional organization and metabolic processes fMRI has the potential to link high spatial and temporal resolution studies to an understanding of systems organization across the brain (Fig. 2.2). In order to finely investigate the functional

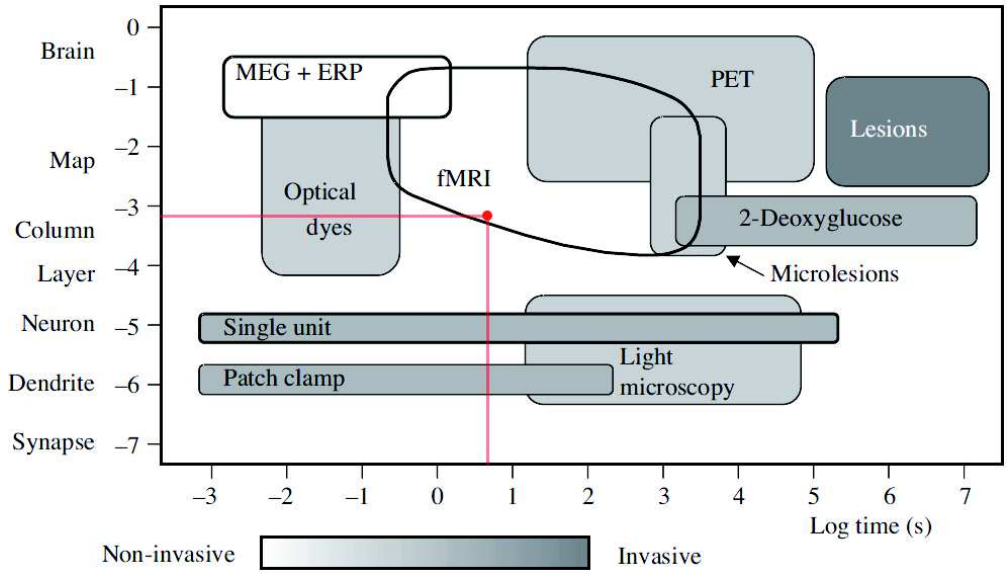

Figure 2.2: *This is an illustration of the relative spatial and temporal sensitivities of different functional brain mapping methods that can be used in animals, man, or isolated tissue preparations. The red spot indicates our experimental conditions (voxel size:1.5×1.5×1.5mm^3, TR=6sec)) and it shows how we have worked and the boundary of the fMRI conditions. Adapted from [Jezzard 2001].*

organization of the brain motor cortex, high spatial resolution fMRI is desirable. Since brain cortex thickness is 2-4 mm [Kandel 2000], it is difficult, with a low spatial resolution (*e.g.* 3×3×3 mm^3) to discriminate contiguous activated areas. As we can see in Fig. 2.3, for example, the spots of motor-related activations covered M1 and S1 regions for a IInd and Vth fingers extension/flexion. In that case the images were acquired with a voxel size of 2×2×3 mm^3 [Beisteiner 2001] (Fig. 2.3a).

On other hand, we recently know that exists a subdivision of Brodman area 4 into an anterior

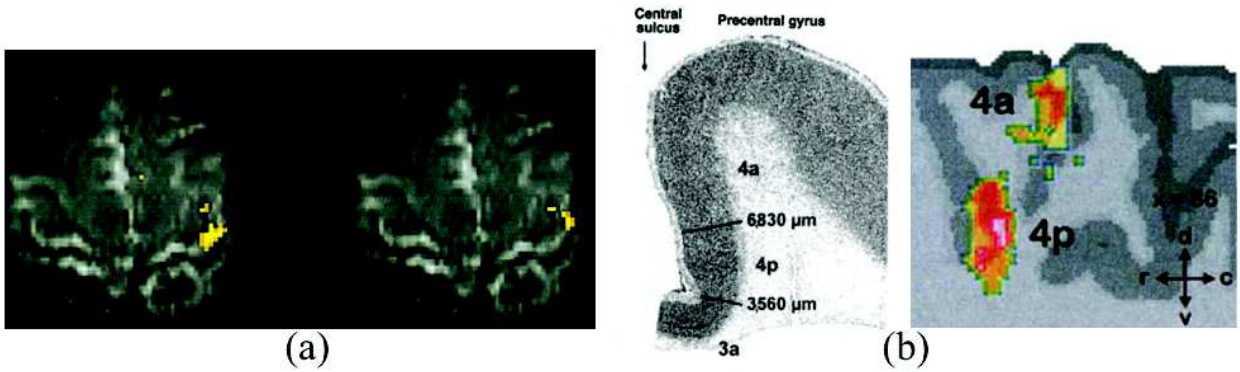

Figure 2.3: *(a) Left: IInd finger activity; Right: Vth finger activity. fMRI voxel size = 2×2×3 mm^3. Adabted from [Beisteiner 2001]. (b) Geyer's results: sagittal section representing the M1 subdivision into an anterior part (4a) and a posterior one (4p) by cytoarchitectonic study (left) and the regions where 4a and 4p were located in 3 of 5 brains (yellow), 4 of 5 (red) and 5 of 5 (white) on the right side of the figure [Geyer 1996].*

part (4a) and a posterior one (4p) [Geyer 1996]. Additionally, using PET and manual tasks, Geyer et al. found a double representation of thumb and index flexion in M1a and M1p whose functional roles remain to be clearly precised (Fig. 2.3b). Higher fMRI spatial resolution studies allow to identify a somatotopy only if centers of gravity are considered. Otherwise a large overlap is represented and an activated pattern following a somatotopic arrangement appear not identifiable [Kleinschmidt 1997, Lotze 2000, Dechent 2003, Pimentel 2011] (Fig. 2.4).

If we want to investigate finely the reorganization in motor circuit, we need high spatial resolution fMRI. A clear improvement in activation localization when increasing to 1.5×1.5×1.5mm^3 is seen in Fig. 2.5. Hyde *et al.* shown that such spatial resolution is the optimal for fMRI studies [Hyde 2001].

2.3 Anatomical variability, functional variability and inter-subject registration

The primary motor **M1** and somatosensory **S1** cortices are close to each other. M1 lies on the anterior bank of the central sulcus (**CS**) and extends across the precentral gyrus. The postcentral

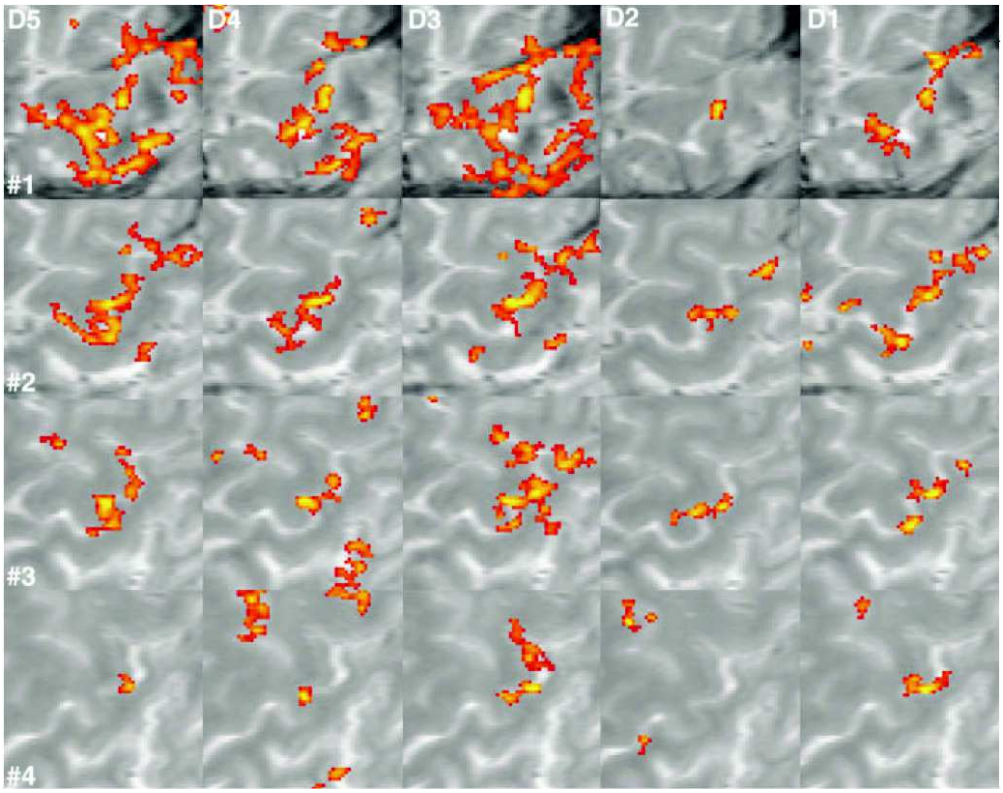

Figure 2.4: *Functional mapping of individual finger movements of the dominant right hand (i.e., D1 to D5 each vs. motor rest) in four consecutive sections covering the left-hemispheric M1 (single subject). The overlap of activated areas within the M1 hand area reveals no clear somatotopy. fMRI voxel size:* $1.56 \times 0.78 \times 4$ mm^3 *[Dechent 2003].*

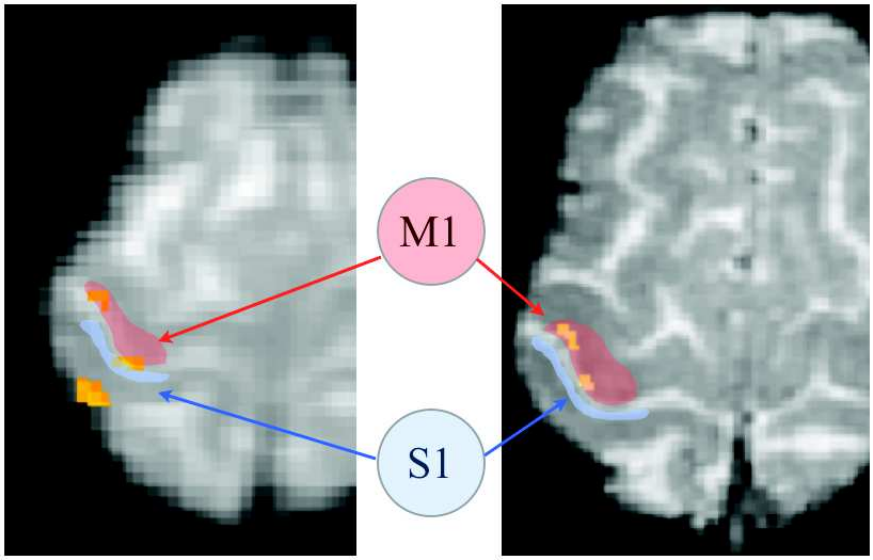

Figure 2.5: *Controlateral activation* ***we obtained****, following a right thumb flexion with a low fMRI spatial resolution* $3\times3\times3$ mm^3 *(left) and a high resolution* $1.5\times1.5\times1.5$ *mm*^{3}*.* $p<0.001$*,* $k>10$*. A clear localization of activated cluster in M1 is obtained with the latter.*

gyrus or somatosensory cortex S1 lies on the posterior bank of CS (Fig. 2.5). Folding is a good predictor of cytoarchitectonics especially for primary cortex areas [Fischl 2008] and could thus be a good predictor of functional specialization in the primary motor cortex. The segment of the precentral gyrus, which is shaped like an inverted omega or epsilon in the axial plane and like a hook in the sagittal plane, is a reliable landmark for identifying the precentral gyrus under normal and pathological conditions that most often contained M1 [Yousry 1997]. It is generally referred as the *omega* like structure and is highly variable between subjects (see Figure 2.6 and [Sun 2011]).

For group studies, the high **inter-subject variability** of the human cortices hampers their precise registration. In Figure 2.7 a series of photos representing left and right central sulcus is shown, pointing out the high level of variability between and within subjects [White 1997].

Because *hand-knob* is a good predictor of M1, **we hypothesized that the combination of a perfect alignment of all *hand-knobs* of all subjects with high resolution fMRI, insuring each functional voxel to be attributed to a single gyrus, could improve the functional areas overlap and increase the significance of statistical parametric maps.**

The fundamental challenge in the analysis of functional MRI experiments is to identify voxels

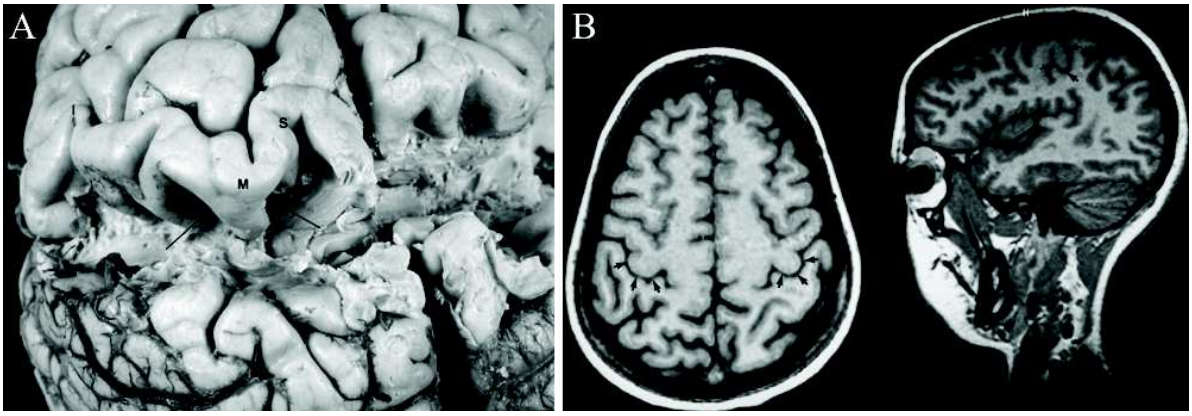

Figure 2.6: *A: Brain specimens after removal of the postcentral gyrus: the anteriorly directed superior genu (S), the posteriorly directed middle genu (M) and the anteriorly directed inferior genu (I) of the central sulcus (CS). B: Axially (left) the precentral knob is omega-shaped in the left and epsilon-shaped in the right hemisphere. The knobs are posterior to the intersection of the superior frontal sulcus with the precentral sulcus. Sagittally (right) the posteriorly directed hook is identified at the level of the posterior part of the insula. Adapted from [Yousry 1997].*

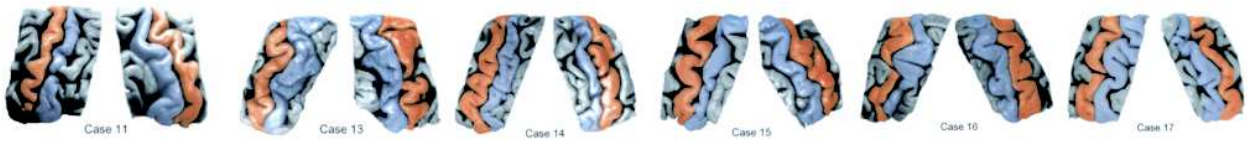

Figure 2.7: *The superficial appearance of the left and right central sulci in eight specimens. Photographs were taken of the hemispheric blocks at an angle orthogonal to the dorsolateral convexity oft he cerebral surface (red, pre-central gyrus;blue, post-central gyrus). Note the wide variation in the configuration of the central sulcus among specimens and between the two hemispheres of individual brains. Adapted from [White 1997]*

that show signal changes varying with changing brain states. This is a difficult problem: firstly because the signal to noise ratio is generally poor, with the activation signal being often no larger than the noise level; secondly, the neurophysiology which couples the underlying brain activity to the measured response in fMRI is complex and generally poorly understood; thirdly, the noise consists of a complex blend of spatio-temporal deterministic and stochastic components due to physiological and scanner-based artefacts; and fourthly, for the group studies, the **inter-subject functional variability**. For group analysis of fMRI, the poor cross-participant alignment leads to the underestimation or the missing of activation in M1. Moreover, spatial alignment and spatial filtering, performed prior to statistical analysis to reinforce the overlap between individual active areas, introduce *per se* a functional blurring and a loss of a precise localization of fMRI signals. This clearly impedes the separation of activated clusters found in M1. For all these reasons each part of fMRI experiment, from the choose of subjects, through the paradigm design until image processing has to take into account carefully. The preprocessing steps might interact with virtually every choice made in designing and performing an fMRI experiment.

The magnetic field strength also plays an important role in processing pipeline decisions. Many groups are upgrading from 1.5 T to 3.0 T, and even 7.0 T fields or higher for research scanners. It is well established that 3.0 T fields have a significantly higher contrast-to-noise for the BOLD effect than 1.5 T fields in homogeneous brain tissue [Gati 1997, Triantafyllou 2005]. However, this advantage is somewhat reduced by a higher physiological noise fraction, greater artifacts at air-tissue boundaries, and reduced decay times [Krüger 2001], *i.e.*, preprocessing becomes more important with increasing field strength.

In addition to fMRI images, structural magnetic resonance images were processed. These provide an anatomical reference (*i.e.* **Template**) for the statistical parametric images output from the data analysis stage and allow multiple subjects to be registered within a common coordinate system.One of the most important is the Talairach referential based on a single older brain [Talairach 1988]. Recent studies are based on population standard template defined by many MRIs. There are a number of such standard templates developed by the Montreal Neurological Institute (**MNI**) and the International Consortium for Brain Mapping (**ICBM**). These templates are introduced and their relationship to Talairach coordinates is described by Brett et al. [Brett 2002], with additional details and web links at `http://imaging.mrc-cbu.cam.ac.uk/imaging/MniTalairach`.

Another strategy is to develop a group-specific template that minimizes the differences between

itself and all scans for the group of subjects being analyzed, a strategy that we explored in this work.

Hellier et al. [Hellier 2003] have shown that global metrics assessing the registration of structural MRIs improve with increasing degrees of freedom (**DOF**) and Klein *et al.* [Klein 2009], comparing nonlinear brain image registration algorithm working on the whole brain, corroborates Hellier's evaluation. Yassa and Stark [Yassa 2009] compared nonlinear registration methods on specific brain regions founding that the ROI-AL ("Region of Interest based ALignment") approaches can substantially improve the alignment. Other studies compare volume-based registration methods with surface-base registration methods [Klein 2010]. In this work, we have also investigated some of these approaches.

In all these studies a set of quantitative measures was used to compare deformed structural MR source image and one target. The effect of registration on brain activation detection was not reported. In this thesis we take a different perspective: we are mainly interested in exploring the effects on nonlinear registration methods on the robustness of activation detection applied here to fine motor cortex investigation.

2.4 Proposed approach

2.4.1 Investigation of hand functions cortical representation

To better understand the representation of the hand's movements of flexion and extension in the primary motor cortex, we carried out a functional MRI study (using a static magnetic field of 3 Tesla), on a group of 13 healthy subjects (**group study**). The investigated tasks were the voluntary movements of the thumb, wrist and fingers, for both hands and for different movement direction (extension/flexion).

In order to study the functional plasticity, two patients who underwent a hand tendons surgery have been examined. They were followed up in a **fMRI longitudinal study** framework: before surgery (M0) and 1 month (M1), 3 (M3), 6 (M6) and 12 months (M12) after surgery.

2.4.2 High resolution fMRI

The improvement of fMRI spatial resolution can be achieved by decreasing plane thickness, increasing the in-plane acquisition matrix using multi-shot multi-slice Echo Planar Imaging (EPI) sequences and restricting the acquired volume to encompass the primary motor area and the cerebellum.

2.4.3 Inter-subject registration

We have explored the effects of nonlinear registration methods on the robustness of activation detection applied here to fine motor cortex investigation. For this purpose we selected four different recent methods as representative of the state of the art in this active research field. The performances of the methods were quantitatively evaluated using both anatomical and high resolution fMRI data coming from our group of healthy control subjects.

First, we considered DARTEL [Ashburner 2007] as representative of standard diffeomorphic methods where the deformation constraints, estimated globally on the whole brain scans, align the cortical valleys and crests but without guarantee that sulci of identical anatomical denomination would be properly aligned altogether. Then, we considered DISCO+DARTEL [Auzias 2011] as representative of a class of methods where explicit sulcal landmarks are used to constraint the 3D deformation. Finally, we considered Diffeomorphic Demons [Vercauteren 2009] as representative of diffeomorphic methods where deformations can be estimated locally to align segmentations of specific three-dimensional region of interests (ROIs), here the *hand-knob* region. Data were also processed using the SPM8 normalization procedure [Ashburner 2005] widely used in the neuroscience community.

CHAPTER 3

Human motor cortex

Knowledge of structure and function of the motor system has advanced considerably. The emerging picture is a complex network, with ever-finer fractionation of functionally and microanatomically distinct subunits, operating as specialised components. Advances have been made in our understanding of the histology, physiology and anatomy of these different subunits, and the way in which they interact to carry out motor behaviour.

The sensory-motor system involves different cortical and subcortical regions of the brain (Fig. 3.1). In the following section 3.1 a general description of these regions are described, as the primary motor cortex, the premotor cortex, the supplementary motor area, the cerebellum, the basal ganglia and the thalamus. Since we focused on primary motor cortex and cerebellum hand movements representation, sections 3.2 and 3.3 are dedicated to their functional organization.

3.1 Anatomical organization

The original cytoarchitectonic maps of the human motor cortex differentiated between precentral and intermediate precentral cortex (Brodmann's areas 4 and 6 respectively). Fulton in 1935 [Fulton 1935] proposed a functional distinction between "primary" motor cortex (area 4, or **M1**) and "premotor" cortex (lateral area 6, or **PMC**) based on lesion studies. Area 6 on the medial wall was also designated as a functionally distinct unit, the "supplementary" motor area (**SMA**) [Woolsey 1952a]. Subsequently however, the anatomical description of the motor area has become significantly more complex [Rizzolatti 1998, Roland 1996, Geyer 1996]. Motor area cortex includes subregions whose functional roles are not yet well understood and difficult to investigate in humans. In monkeys, direct techniques can be used but not in humans where it is necessary to combine indirect methods for in vivo functional studies with knowledge derived from post-mortem or lesion study. One candidate scheme for the human motor cortex organization is proposed by

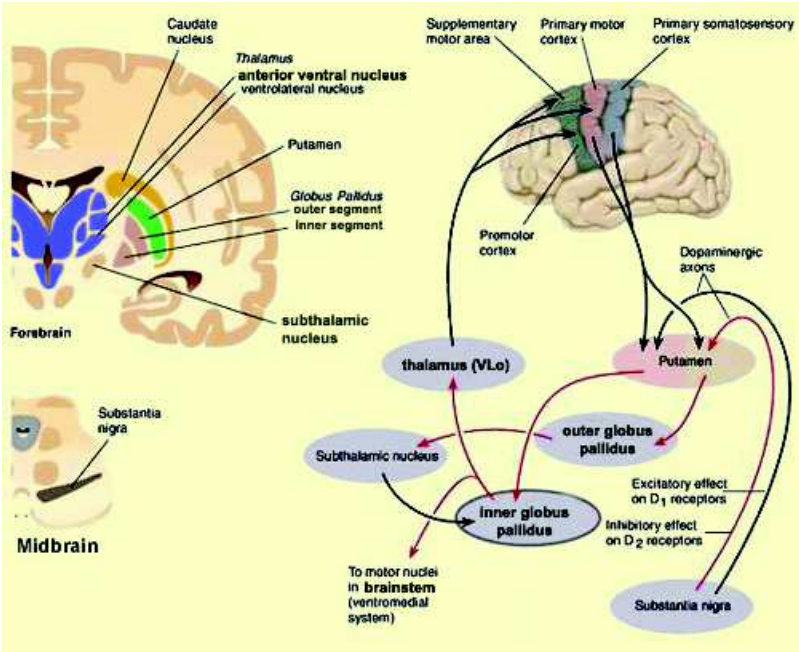

Figure 3.1: *The different subunits of the motor cortex. Source:* `http://thebrain.mcgill.ca/flash/index_a.html`

Heidi Johansen-Berg 2001 [Johansen-Berg 2001] as illustrated in Fig. 3.2. Many studies have investigated the motor cortex, in monkeys and humans, using various imaging techniques (see [Rowe 2011] for a review) and more precisely the cortical representation of hand movements.

3.1.1 Primary motor cortex (M1)

The primay motor cortex (**M1**) lies in the frontal part of the **central sulcus** (CS) (Figs. 3.2, 3.3), corresponding to the Brodmann's area 4. The central sulcus has a typical "*omega*" shape in axial view and a hook shape in sagittal plane [Yousry 1997] (Fig. 2.6, 3.3). It separates M1 from **S1**, the primary somatosensory cortex (Brodmann's area 3, 2 and 1) (Fig. 3.3). Recently Caulo *et. al.* classify different central sulcus shapes in a large papolation (257 subjects) founding 5 shapes variants of the central sulcus [Caulo 2007]. This landmark corresponding to the hand motor representation (see section 3.2) is often known as the *"hand-knob"*.

The post-mortem study of Geyer [Geyer 1996] evidenced a subdivision of Brodmann area 4 (M1) into an anterior part (4a) and a posterior one (4p) on the basis of cytoarchitecture and of

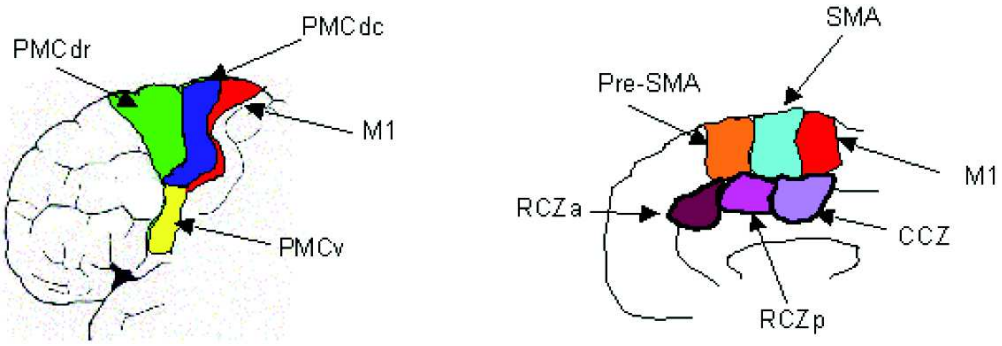

Figure 3.2: *General scheme used for classifying subunits of the human motor system. Left: lateral view; right: medial view. M1=primary motor cortex; PMC=premotor cortex; SMA=supplemetary motor area; RCZ=rostral cingulate zone; CCZ=caudal cingulate zone; d=dorsal; v=ventral; r=rostral; c=caudal; a=anterior; p=posterior (mod. from [Johansen-Berg 2001])*

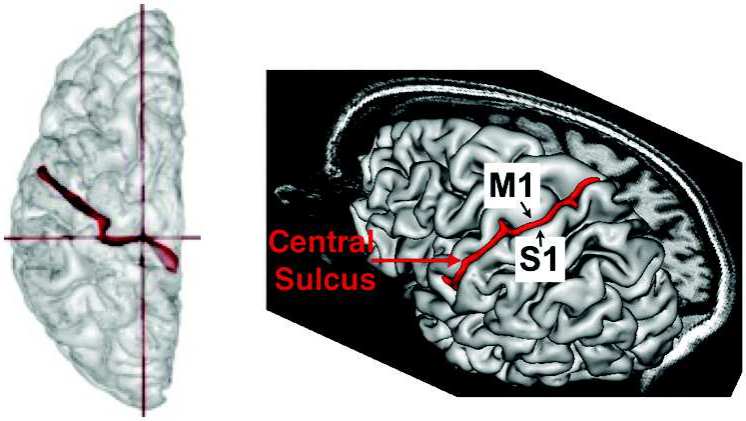

Figure 3.3: *Axial view of the cortical surface for the left hemisphere (Left). 3D reconstruction of the left hemisphere cortical surface where the central sulcus, M1 and S1 are indicated (Right). The central sulcus (red) and the cortical surface have been automatically extracted from our data using BrainVISA (brainvisa. info/).*

the quantitative distribution of transmitter-binding sites. Additionally, Geyer *et al.* found a double representation of thumb and index flexion in M1a and M1p –whose functional roles remain to be precised– using PET and manual tasks in 4 healthy subjects. Hilbig *et. al.* also confirm Geyer's results using neuron markers [Hilbig 2001] .

Cykowski *et al.* [Cykowski 2008], using automatic methods, define several structural landmarks of the central sulsus (CS) (Fig. 3.4), as the "*pli de passage fronto-pariétal moyen*" (PPFM), first described by Broca [Broca 1888], in order to study CS asymmetry.

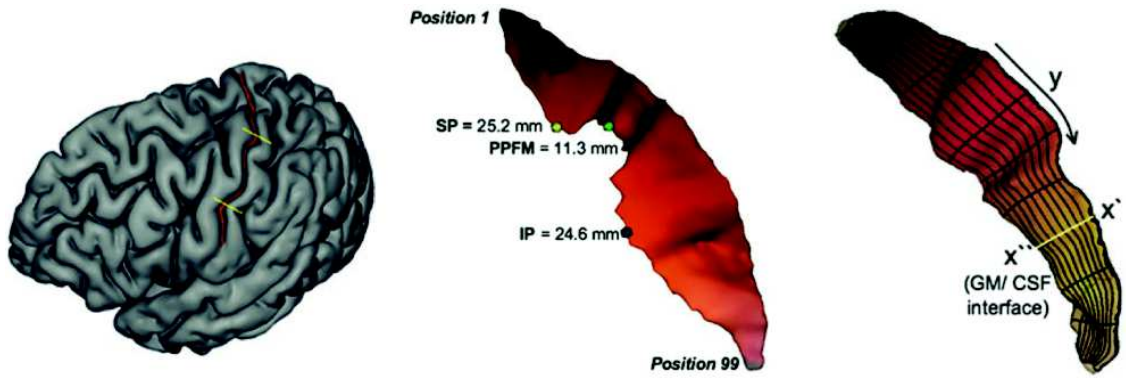

Figure 3.4: *From left to right: superficial appearance of the CS, landmarks of the CS and sulcal surface parameterization. Adapted from [Cykowski 2008].*

3.1.2 Premotor cortex (PMC)

The premotor cortex, a nonprimary motor area, lies in the frontal lobe. It is involved in action planning and influences the motor output. It is located on the lateral part of the Brodmann area 6 and it is divided into the dorsal portion, rostral and caudal **PMCdr** and **PMCdc** respectively [Picard 2001], and the ventral portion **PMCv** (Fig. 3.2).

3.1.3 Supplementary motor area (SMA)

It is located in the medial part of Brodmann area 6 (Fig. **??**) and was discovered by Penfield and Rasmussen [Penfield 1950]. They could elicit motor responses not only stimulating the classical sensorimotor area, but also from this part of the cortex. On the basis of cytoarchitecture and neurochemistry **SMA** and **pre-SMA** can be differentiated (Fig. 3.2) [Zilles 1995]. Vorobiev *et al.*

[Vorobiev 1998] found a further subdivision of the SMA into rostral (**SMAr**) and caudal (**SMAd**) regions. VCA line represents the boundary between the SMA (SMAr+SMAd) area and the pre-SMA area (Fig. 3.5).

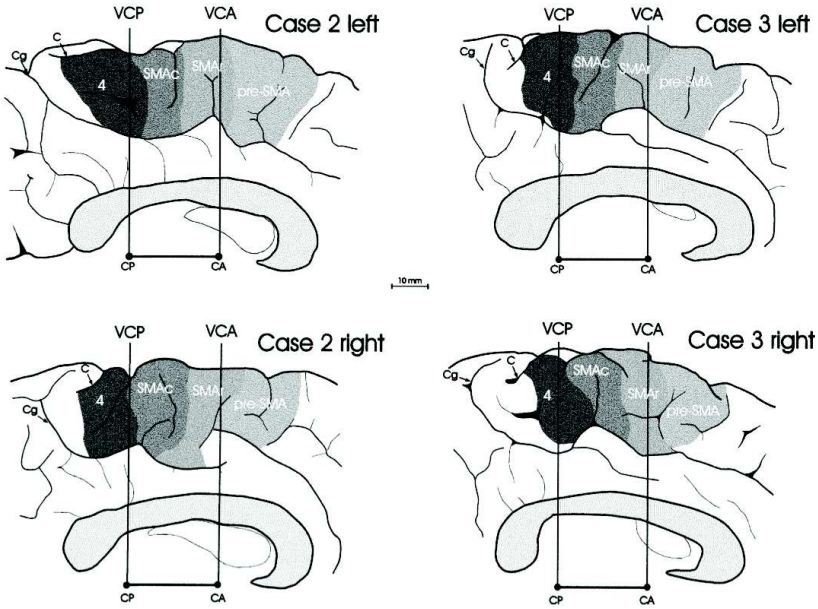

Figure 3.5: *Mesial view of four human hemispheres, shown as the left hemisphere, showing the location and extent of the agranular frontal areas. The VCA and VCP lines are indicated in order to show the topographic relationships of these areas with anatomical landmarks.C=central sulcus; CA=anterior commissure; Cg=cingulate sulcus; CP=posterior commissure; VCA=vertical line transversing the anterior commissure; VCP=vertical line transversing the posterior commissure. (Adapted from [Vorobiev 1998]).*

3.1.4 Cerebellum

The cerebellum is an anatomical structure located at the posterior base of the skull. A midline portion, the vermis, separates two lateral lobes, or cerebellar hemispheres. A schematic representation of the cerebellum parts is represented in figure. (Fig. 3.6a). The lobes are ranging from I to X [Schmahmann 1999, Stoodley 2009] (Fig. 3.6b).

The cerebellum consists of the cerebellar cortex and the underlying cerebellar white matter. Four paired deep cerebellar nuclei are located within the white matter of the cerebellum.

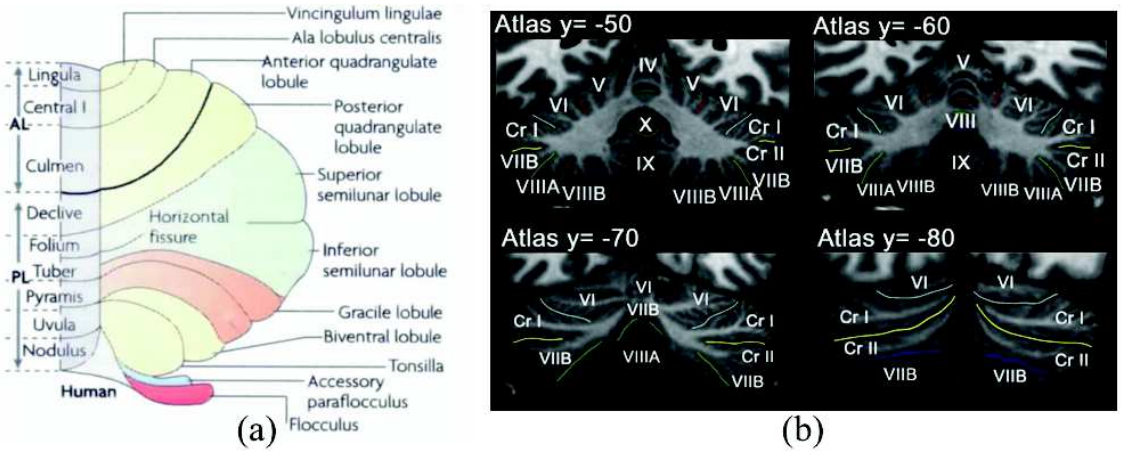

Figure 3.6: *(a) Hemicerebellar anatomical parts representation. (b) Coronal view of the cerebellar anatomical atlas in which fissures and lobules demarcated and labelled. Adapted from [Stoodley 2009].*

3.1.5 Thalamus

The ventrolateral part of the thalamus is involved in sensory and motor mechanisms. The thalamus is located in the diencephalon and comprising of four parts (the hypothalamus, the epythalamus, the ventral thalamus, and the dorsal thalamus). Thalamic nuclei project to one or a few well-defined cortical areas [Herrero 2002]. Multiple cortical areas receive afferents from a single thalamic nucleus and send back information to different thalamic nuclei. The cortico-efferent projection provides positive feedback to the "correct" input, while at the same time suppressing irrelevant information. Topographical organisation of the thalamic afferents and efferents is contralateral, and the lateralisation of the thalamic functions affects both sensory and motoric aspects.

3.1.6 Basal ganglia

Basal ganglia form a major centre in the complex extrapyramidal motor system, as opposed to the pyramidal motor system (corticobulbar and corticospinal pathways) [Herrero 2002]. Basal ganglia are involved in many neuronal networks having emotional, motivational, associative and cognitive functions as well. The striatum (caudate nucleus, putamen and nucleus accumbens) receive inputs from all cortical areas and, throughout the thalamus, project principally to frontal lobe areas (prefrontal, premotor and supplementary motor areas) which are concerned with motor planning.

These circuits: (i) have an important regulatory influence on cortex, providing information for both automatic and voluntary motor responses to the pyramidal system; (ii) play a role in predicting future events, reinforcing wanted behaviour and suppressing unwanted behaviour, and (iii) are involved in shifting attentional sets and in both high-order processes of movement initiation and spatial working memory. Basal ganglia-thalamo-cortical circuits maintain somatotopic organisation of movement-related neurons throughout the circuit.

3.2 Some key elements on the functional organization of the primary motor area (M1)

Our current knowledge on hand movement control relies mainly on investigations performed by pre-surgical investigations (Penfield, 1935), by electrophysiological recordings on monkeys [Humphrey 1986, Kakei 1999, Rathelot 2006a] or by post mortem cytoarchitectonic studies [Geyer 1996].

3.2.1 Somatotopy and overlapping

Beginning in the mid-twentieth century, work that used low-intensity electrical stimulation to map output functions of **M1** revealed a somatotopically ordered representational map for movements (or muscles) that resembled a distorted cartoon of the body [Penfield 1950, Woolsey 1952b]. Doctor G.D. Schott in his editorial of the Journal of Neurology, Neurosurgery, and Psychiatry in 1993 [Schott 1993] described the huge work performed by Penfield and Rasmussen (Fig. 3.7). This map commonly depicted body-part joints or movements as a continuous representation laid out upon the surface of electrically excitable M1. The principal organizing feature incorporated a general medial-to-lateral topography of leg (hindlimb in quadripedal mammals), arm (forelimb, including digits), and head and face. Although the general medial-to-lateral leg, arm, and face representation appeared consistently in all early studies, one doubts that the level of somatotopic detail was ever intended by the near omnipresent homunculus cartoon [Schott 1993]. The homunculus plan suggests that representations for each body part are orderly and point-to-point and that each part occupies nonoverlapping cortical space.

Current data obtained from contemporary methods have upheld the results showing the seg-

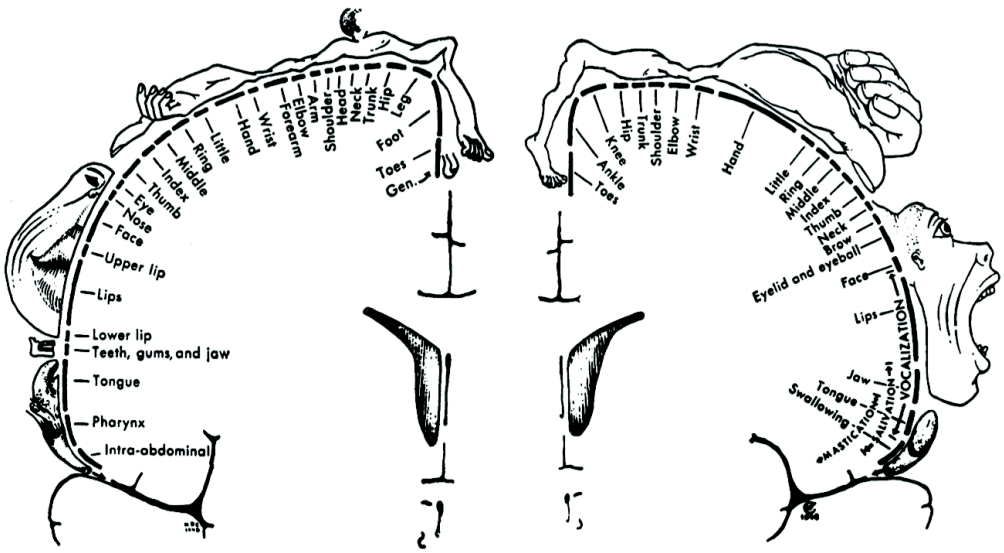

Figure 3.7: *The motor and sensory homunculus: the first map. Penfield and Rasmussen, 1950. Reprinted by Schott [Schott 1993].*

regation within M1 of functional subregions for legs, arms, and heads but soundly reject the idea of a precise topography. Instead, the internal organization of each subregion is best described as a network with broadly distributed functions involving large populations of neurons within a subregion [Sanes 1995]. The most complete data for this departure from a simple topography has been obtained for the M1 arm region, and the most extensive maps of this region have been realized with intracortical electrical stimulation techniques. This influential method, developed by [S. D. Jr Stoney 1968], provided a means to evaluate the movement or muscle coupling of a site focally stimulated by electrical stimulation via a microelectrode inserted among cortical neurons. New movements were evoked when the electrode moves in small steps across cortex suggesting the existence of an underlying pattern of organization. However, when assembled into a comprehensive map, sites for any particular body part appear widely distributed, multiple, and overlapped [Sessle 1982, Gould 1986, Nudo 1992, Sanes 1995]. The artificial nature of electrical stimulation is clearly questionable when defining the organizing features of the motor map. However, evidences from neural recordings, pharmacological inactivation, and connectional studies reveal that the distributed nature of M1 subregion organization is consistent with that identified by intracortical electrical stimulation mapping.

In addition, recordings of single M1 neurons show that they rarely modulate with the action of a single joint or part. Each neuron appears to participate in multiple hand motor actions, and neurons influencing different digits or the wrist appeared to have a seemingly random distribution [Schieber 1993]. This pattern does not easily find reconciliation with a discrete, topographically segregated organization for M1. As predicted by the distributed functional relationship of M1 to movement and muscle control, focal inactivation of monkey M1 produces more global effects on arm actions but does not block the action of individual parts [Schieber 1998].

In healthy subjects, different recent fMRI studies of the cortical representation of fingers revealed highly overlapping maps, together with an arrangement of finger-specific hot spots that follows a somatotopic organization [Sanes 1995, Rao 1995, Kleinschmidt 1997, **?**, Beisteiner 2001, Dechent 2003]. More recently, Meier and collaborators [Meier 2008] found activated patterns in human for which the representations of the different body parts are intermingled, and a complex organization for the arm and hand, with fingers emphasized in a core region surrounded by a dorsal and ventral representation of the arm Fig. 3.8.

All noninvasive studies in human M1 proposed to date have been limited by the considerable inter-individual variability in subject's response, degree of somatotopy and the exact localization of their motor maps [Kleinschmidt 1997, Meier 2008]. Moreover, some analysis techniques, as the "*winner-take-all*" [Meier 2008, Olman 2011], hide the concomitance of different movement coded in the same cortical region.

This results reveal a pattern of M1 organization that has discrete gross subdivisions. However, each subdivision has an internal distributed network in which control emerges from broad activity patterns. This organization provide not only the immense storage capability and richness of function characteristics of distributed networks, it also provides a basis for flexibility if the organization of this network is modifiable.

3.2.2 Coding of the hand movement direction

Many neurons in the primary motor cortex are selective for a particular direction of movement. A long standing debate concerns the role of cortical neurons: do they encode parameters of hand path rather than muscle activity? does the central nervous system uses spatial coordinates, rather than joint or muscle coordinates? Whether muscles or movements are represented in the motor cortex,

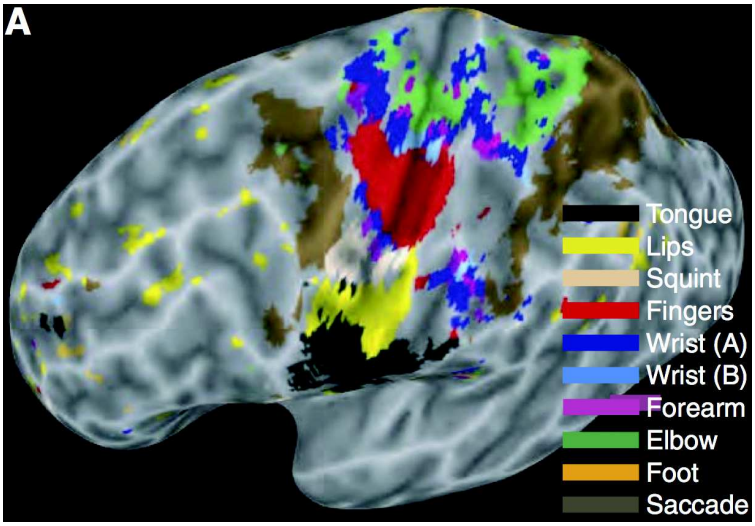

Figure 3.8: *Somatotopy representation. Voxels were selected if the regression was positive and significant at the P<0.0001 level. These selected voxels were assigned to the movement that resulted in the largest F value. The results were projected onto the inflated cortical sheet, in which dark shading indicates the floor of a sulcus and light shading indicates the crown of a sulcus. The map shows the overall somatotopic progression in the primary motor cortex (anterior to the floor of the central sulcus) and in the primary somatosensory cortex (posterior to the floor of the central sulcus). [Meier 2008].*

is related to the distinction between planning and execution of movements [Mussa-Ivaldi 2000].

Neurophysiological studies in monkeys show that activity of neurons in primary cortex (M1) [Georgopoulos 1982, Kakei 1999], pre-motor cortex (PMC) [Caminiti 1991, Kakei 2001], and cerebellum [Fortier 1989] varies systematically with the direction of reaching movements.

In humans, Z'Graggen *et al.* [Z'Graggen 2009], by using TMS, found a segregation of the functional aspect in M1 of thumb movement, in particular for extension and flexion tasks. Toxopeus *et al.* [Toxopeus 2011] found a movement direction coding in M1 by fMRI experiments. Both of these studies highlight a more lateral activation for extension movements and more medial activation for flexion movements.

How the command of the 27 extrinsic and intrinsic muscles of the hand can be triggered by informations located on a 2D surface? This question suggest some dimension reduction.

One scope of this thesis is also to investigate the functional patterns corresponding to extension and flexion movements of thumb, fingers and wrist.

A deeper knowledge of movements coding in the brain cortex represents an important aspect for any developmental approach of motor cortex self-organization.

3.2.3 Hand dominance

Handedness (also referred to as chirality or laterality) is a human attribute defined by unequal distribution of fine motor skills between the left and right hands.

Links exist between handedness and morphological features of the central sulcus [Mangin 2004a, Hopkins 2010]. Indeed, controlateral CS of the dominant hand results longer, or deeper, than the non-dominant one. Sun *et al.* [Sun 2011] evaluate how the shape of the central sulcus differs between consistent dextrals and sinistrals and they studied the sulcal shape of individuals with acquired dextrality. They suggest that late plasticity induced by forced hand use mainly influences the folding process through fold elongation or deepening, while the global shape of the sulcus is more resistant to change, because its shape is sculpted early during human development. Whether links exist between handedness and functional activation remains an open question which will be investigate in the context of this thesis.

3.3 Functional organization of the Cerebellum

The cerebellum is an integral part of the motor system, playing a role in maintaining posture and movement coordination. Thanks to the progress of neuroimagine and of the clinical cases studied, the role of the cerebellum is emerging, in cognitive [Schmahmann 1998, Ravizza 2005], and emotional [Schmahmann 1998, Scheuerecker 2010] mechanisms.

Knowledge of the functional implications of the different cerebellar lobules comes mainly from studies of functional MRI. Like the motor cortex, a somatotopic organization in the cerebellum has been hypothesized. Grodd *et. al.* [Grodd 2001] confirm by fMRI the "*homunculi*" obtained by Snider and Eldred (1951) (Fig. 3.10). Two homunculi could be highlighted: the first located in the anterior lobulse V and VI (Fig. 3.6), the second one in the posterior lobe. The existence of the third homunculus is still unproved [Buckner 2011]. Recently, the correlation of activa-

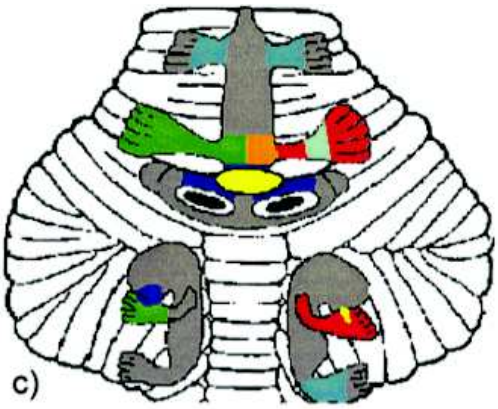

Figure 3.9: *Cerebellar homunculi as represented by Snider and Eldred (1951) [Grodd 2001].*

tion between the cerebellum and the primary motor area has been studied. Connectivity studies have shown a cerebello-thalamocortical network [Voogd 2003]. Thus, the cerebellum plays a role in the movement organization, modulating the motor cortex activity by inhibiting or exciting it [Daskalakis 2004]. Connection between motor cortex and vermis has been studied by using the attenuated rabies virus [Coffman 2011]. The cerebellum may also play a role in brain plasticity and learning, specifically in the motor adaptation to environment. Doyon and Benali [Doyon 2005] have proposed a model showing the existing relations between the cortico-striatal and cerebellar areas with the motor cortex during motor sequence learning.

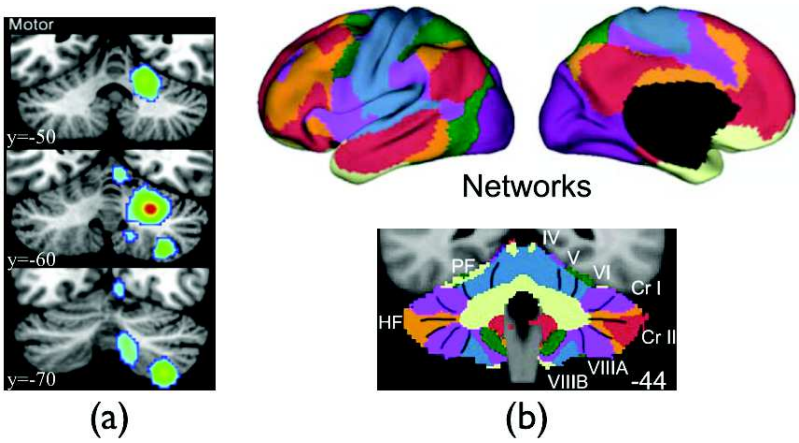

Figure 3.10: *(a) Meta-analysis of simple right-handed finger movement tasks, which yelded 7 publications. Adapted from [Stoodley 2009]. (b) Functional connectivity maps between the cerebellum and the brain cortical cortices regions. Correletions can be seen in blue between the central sulcus ares (motor area) and the lobules IV and V. Adapted from [Buckner 2011].*

Part II

State of the art

CHAPTER 4

High spatial resolution fMRI

We hypothesized that the combination of a perfect alignment of all *hand-knobs* across subjects with high resolution fMRI, insuring each functional voxel to be attributed to a single gyrus location, could thus improve the functional areas overlap and increase the significance of statistical parametric maps.

Given the high tortuosity of the cortical ribbon, Hyde and coworkers [Hyde 2001] found that an isotropic spatial resolution of 1.5 mm was optimal, for a finger-tapping paradigm, to detect robust cortical activation. This spatial resolution can be achieved by decreasing plane thickness, increasing the in-plane acquisition matrix using multi-shot EPI sequences while restricting the acquired volume to encompass the areas under study.

In this chapter the Echo-Planar Imaging (EPI) technique, proposed by Mansfield [Mansfield 1977] and its multi-shot EPI version to obtain high spatial resolution fMRI are described.

4.1 EPI sequence

4.1.1 Description

Traditional methods for acquiring images was to fill up *k-space* in a line-by-line fashion, which necessitated a certain number of separate excitations for even a moderate-resolution image.

In 1977, Mansfield [Mansfield 1977] proposed a new method, known as echo-planar imaging, or EPI, in which the entire *k-space* is filled using rapid gradient switching following a single excitation. The gradients are commutated so rapidly that sufficient gradient echoes ("echos-train") are created to allow measurement of all the phase-encoding steps required for an image. However, to achieve reasonable spatial resolution, a relatively large *k-space* must be sampled, which takes time.

The basic EPI pulse sequence is shown in figure 4.1. All the *k-space* must be filled following a single excitation pulse, the data must be acquired before significant transversal relaxation time

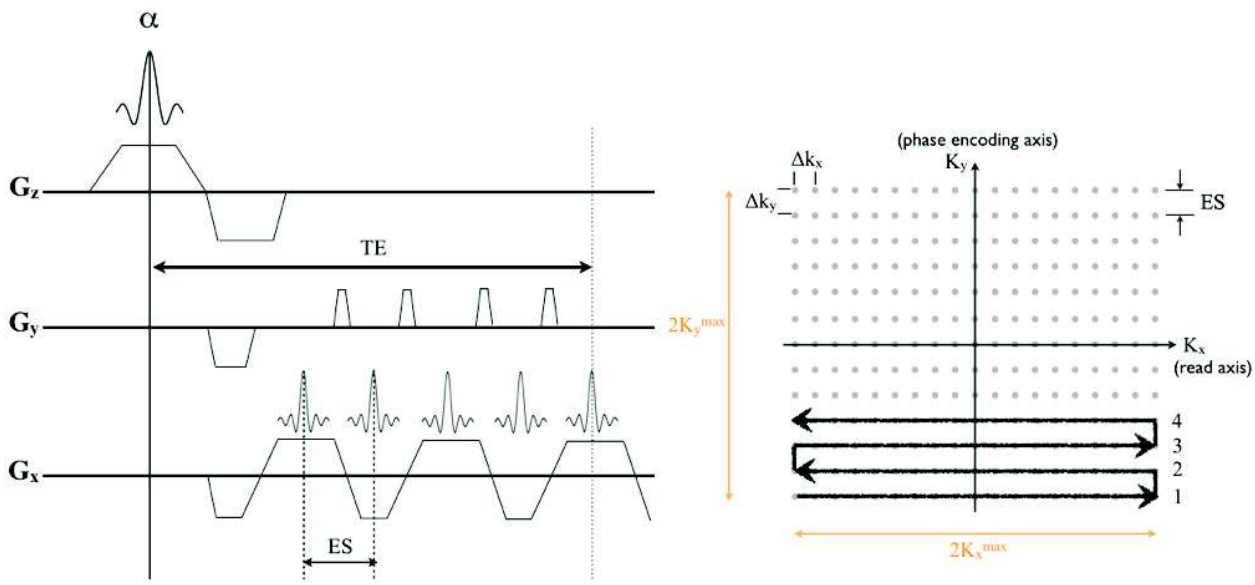

Figure 4.1: *Simplified representation of a 2D GRE-EPI sequence. ES = echo spacing*

T_2^* or T_2 decay occurs. Firstly an *RF* pulse (α) and a slice selection gradient G_z are applied. Then a sequence of phase-encoding gradient G_y and frequency-encoding gradient G_x allow to fill the *k-space*; in practice the G_y (called "blips") move from one line to another and G_x sample each line.

Echo planar imaging fills all *k-space* lines in a single TR period ("shot") and it can be combined with two kinds of sequences sensitive to T_2 contrast (Spin-Echo) or T_2^* contrast (Gradient Recalled Echo (GRE)). While two radio-frequency (RF) pulses (90°and 180°) are used for spin refocusing and spin echo generation, GRE imaging is based on only a single RF pulse, typically <90°, in combination with readout gradient reversal, each one generating a gradient echo. This sequence allows to reduce the acquisition time and to obtain a T_2^*-dependent signal. Indeed we know that

$$\frac{1}{T_2^*} = \frac{1}{T_2} + \frac{1}{T_2'} \tag{4.1}$$

where T_2 represents the **spin-spin relaxation time** which depends on the chemical environment and T_2' represents the transversal relaxation time due to the non-uniformity of the static magnetic field. This effect can be reversed with the spin-echo pulse sequence obtaining a signal dependent on T_2. But the local magnetic field changes are exactly what we want to capture to measure the BOLD signal. Hence the GRE-EPI sequence is the suitable method for T_2^*-weighted

images acquisition. It can be shown that at the echo peak the detected signal S will be proportional to the T_2^* as follow

$$S(TE) \sim e^{-TE/T_2^*} \tag{4.2}$$

where TE represents the *echo-time*, that is the time between the gradient reversal and the peak of the echo. T_2^* decay due to dephasing starts with the excitation and progresses with time. The longer the TE, the greater the signal loss. Hence, as TE increases, T_2^* sensitivity of the GRE sequence increases because of more dephasing. With a low flip angle, excitation longitudinal magnetization remains close to the fully relaxed state, independent of different longitudinal relaxation time T_1 values. Hence, a low flip angle reduces the T_1 influence, and the T_2^* differences become dominant [Nitz 1999]. A long TR also reduces the T_1 effect.

Other factor increasing the T_2^* sensitivity of the sequence include increased field strength. This allows a gain in terms of signal to noise ratio (SNR) [Triantafyllou 2005]. However as the field strength increases, the susceptibility effect also increases because it is directly dependent on the main field. Thus the artifacts becoming more important with higher magnetic fields, as we will see in the next sections.

4.1.2 Spatial resolution

In EPI, for each TR, a set of *k-space* lines are acquired. N_x point are collected along the frequency encoding direction k_x (**read axis**) *per* N_y times, that are the phase-encoding steps required (along the **phase encoding axis**, k_y), to sample the *k-space*, or a part of it.

It is known that to "move" from a point at time 0, $k(0)$, in the *k-space* to another point $k(t)$ we can apply a gradient magnetic field G for a period t following the relation

$$k(t) = \frac{\gamma}{2\pi} \int_0^t G(t')dt' \tag{4.3}$$

where γ is the gyromagnetic ratio.

Thus, denoting FOV_x and FOV_y as the fields of view along x an y directions in the image domain, the relationship between the spatial frequency and the spatial size in the image domain is given by:

$$\Delta k_x = \gamma G_x \Delta t_x = \frac{1}{FOV_x}$$
$$\Delta k_y = \gamma G_y \Delta t_y = \frac{1}{FOV_y} \tag{4.4}$$

where G_x and G_y are the gradients amplitude, Δt_x is the time between adjacent points in the frequency-encoding direction and Δt_y is the time between two points in the phase encoding direction. So the discrete steps in *k-space* define the image FOV, whereas the maximum extents of *k-space* define the image resolution (small in *k-space* determines big in image space, and *vice versa*). For an $N_x \times N_y$ image we acquire $N_x/2$ and $N_y/2$ values of *k-space* either side of zero, making the total span of *k-space* equal to $2k_x^{max}$ and $2k_y^{max}$. So the spatial resolution is given by

$$\Delta x = \frac{FOV_x}{N_x} = \frac{1}{N_x \Delta k_x} = \frac{1}{2k_x^{max}}$$
$$\Delta y = \frac{FOV_y}{N_y} = \frac{1}{N_y \Delta k_y} = \frac{1}{2k_y^{max}} \tag{4.5}$$

Experimentally getting more resolution in the image requires larger k values, requiring either larger amplitude or longer gradient episodes (or some combination of the two) according to equations 4.3, 4.4.

The gradients have to be drive harder (larger amplitude) or leave them on for longer to attain smaller pixels. Indeed, this is probably the biggest single limit to MRI performance.

The 2D GRE-EPI sequence represents the in-plane acquisition. To acquire a volume the third dimension (*z-direction*) is provided by *RF* pulses that are applied during a slice-selective gradient.

4.1.3 EPI artifacts

EPI suffers from three major artifacts: **Nyquist ghosts** (N/2), **geometric distortion** and **signal loss**. Each artifact will usually vary across an image. Some parts of the brain - occipital and parietal cortices, for example - can be imaged relatively free of major artifacts whereas other parts of the brain - orbitofrontal and inferior-temporal lobes - will be plagued by them. Moreover these artifacts become more apparent at higher magnetic field strengths where local variations in magnetic field caused by susceptibility gradients cause severe phase distortions in the signal.

Nyquist ghosts

These artifacts are a consequence of the back and forth sampling trajectory in *k-space*. Indeed they occur in the phase encoding dimension. The sampling frequency being lower in this direction compared to frequency encoding direction. A small lag in the sampling therefore results in a line to line *k-space* discrepancy with alternate lines being properly phased. This will result in the introduction of ghost artifacts into the image. The misalignment of odd and even *k-space* lines cause the shifting of ghosts of about $N/2$ from the main image reducing the image quality and the signal-to-noise ratio (SNR).

Geometric distortion

Despite the suitable homogeneity of the static magnetic field B_0, the magnetic susceptibility of the biological tissue inside an MR scanner produces some field inhomogeneities ΔB_0. These are more important in the boundary between different tissues or between tissues and air. If we consider the signal coming from an elementary point (x, y, z) is

$$\partial S(x, y, z, t) \propto \rho(x, y, z) \cdot exp[i\gamma \cdot \int_0^t B(x, y, z, t)dt] \cdot exp(-t/T_2^*) \tag{4.6}$$

where ρ is the local spin density, γ the gyromagnetic ratio and $t = 0$ at the RF pulse excitation beginning. If we consider an homogeneous field: $B(x, y, z, t) = B_0$ and the first exponential is equal to 1 in the Larmor's frequency rotating frame, obtaining the equation 4.2 if $t = TE$.

In MRI the first exponential can be written as follow

$$exp\left\{ i\gamma \cdot \left[\int_0^t G_x(t)xdt + \int_0^t G_y(t)ydt + \int_0^t \Delta B_o(x, y, z, t)dt \right] \right\} \tag{4.7}$$

where G_x the readout gradient (frequency encoding), G_y the phase-encoding gradient and $\Delta B_0(x, y, z, t)$ the field inhomogeneities in a point (x, y, z). From equation 4.7 it can be seen that the distortion depends on the *k-space* filling method.

Being DW ("dwell time") the acquisition time between two point in k_x direction and τ_{ramp} the commutation time of G_y (*i.e.* the time needed to move to another line in k_y direction) we can express the phase evolution in the *k-space* from the equation 4.7 as

$$\Delta\phi_x = \gamma \cdot \left[\int_0^{DW} G_x(t)xdt + \int_0^{DW} \Delta B_0(x,y,z)dt\right]$$
$$\Delta\phi_x = \gamma \cdot [G_x \cdot x \cdot DW + \Delta B_0(x,y,z) \cdot DW] \tag{4.8}$$

in the frequency-encoding direction k_x and

$$\Delta\phi_y = \gamma \cdot \left[\int_0^{T} G_y(t)ydt + \int_0^{T} \Delta B_0(x,y,z)dt\right]$$
$$\Delta\phi_y = \gamma \cdot \left[G_y \cdot y \cdot \frac{\tau_{ramp}}{2} + \Delta B_0(x,y,z) \cdot (\tau_{ramp} + N_p \cdot DW)\right] \tag{4.9}$$

in the phase-encoding direction k_y. T is the time between the acquisition of 2 points in the k_y direction and N_p is the number of points sampled in one line of the *k-space* ($T = \tau_{ramp} + N_p \cdot DW$).

From equations 4.8 and 4.9, one can see that the most important dephasing due to the field inhomogeneities occurs in the phase-encoding direction k_y. It is about $(\tau_{ramp}/DW + Np)$ times higher than in k_x direction.

The echo spacing (***ES***, Fig. 4.1), which is the time between each phase encode blip, defines the bandwidth in the phase encoding axis. A typical echo spacing might be 0.5 ms, yielding a bandwidth of 2kHz defined, for example, by 64 pixels. That corresponds to around 30 Hz per pixel. If we have a 100-300 Hz error arising from magnetic susceptibility gradients then we can have a spatial distortion in this dimension that could be up to 3-10 pixels.

Geometric distortions could effect the fMRI results leading to an erroneous interpretation of the data. The frequency encoding dimension suffers only modestly from distortion compared to the phase encoding dimension. For a review of geometrical distortion sources refer to [Jezzard 1999]. In [Jezzard 1995] and [Cusack 2003] fields map characterizing the inhomogeneities were acquired allowing to unwarp the distorted images. Even if it is not a common strategy in fMRI multi-shot EPI can reduce the geometrical distortions as we see later.

Signal loss

The signal loss artifact arises because of spurious dephasing caused by magnetic susceptibility gradients. In fMRI we have a requirement to generate BOLD contrast by setting the TE within a certain range of values; the optimum BOLD contrast occurs when the TE matches the local T_2^*

of the tissue of interest. Thus, we don't typically minimize the TE in order to minimize the signal loss, we instead set our TE to provide the BOLD contrast we want. But the T_2^* change from one region to another causing a signal attenuation in some parts of the brain.

Studies as [Gorno-Tempini 2002] investigated the compromise between the echo-time, the BOLD signal quality and the signal loss.

4.2 Multi-shot EPI

Many of the problems related to single-shot EPI described above can be overcome by accumulating the data over multiple excitations using multishot EPI. Acquiring additional lines in the k-phase direction is easily done by simply extending the pulse sequence for a longer period, allowing to reduce the geometrical distortions, the signal loss and to reach higher spatial resolution.

Unfortunately the transversal relaxation time T_2^* limits the acquisition time. In fact the typical T_2^* of brain tissue is ~ 30 ms at 3 Tesla. Thus, after 100-150 ms the signal level is rapidly approaching zero, and an increasing level of noise would be detected. Assuming, for example, that we want to acquire an EPI that is 256x256 pixels with a field-of-view of 224 mm. That is equivalent to a nominal pixel resolution of 0.875 mm. Now, to acquire each line of k_x (the read direction) it will take four times longer for 256 readout points as for 64 readout points. If 64 points causes an echo-space time (ES) of 0.5 ms then each line of k_x takes 2 ms to be acquired. So we can't acquire all 256 phase-encoded readout points in a single shot in the T_2^* range. But if we consider four echoes of 64 readout points each, and combine the four shots before doing the 2D FT, then we can produce a final image with appreciable SNR at the target nominal resolution.

Multi-shot EPI acquires all the data points required to make up the image in several FIDs. A variety of *k-space* encoding schemes are available. In Figure 4.2 the *k-space* is covered by a two shot EPI sequence.

With regard to **geometrical distortions** the critical parameters to consider is the echo-space time (ES), *i.e.* the time between each line of k_x sampling, and the size of the step in k_y between each echo. For single-shot EPI, each new echo in the train defines a step in k_y (the phase encode dimension) of size Δk_y. Any change that decreases the ES time or increases the k_y step size between each echo will tend to decrease the distortion, all other parameters remaining constant. For example, we could simply skip every other k_y step, *i.e.* make the step size $R \cdot \Delta k_y$, as is done

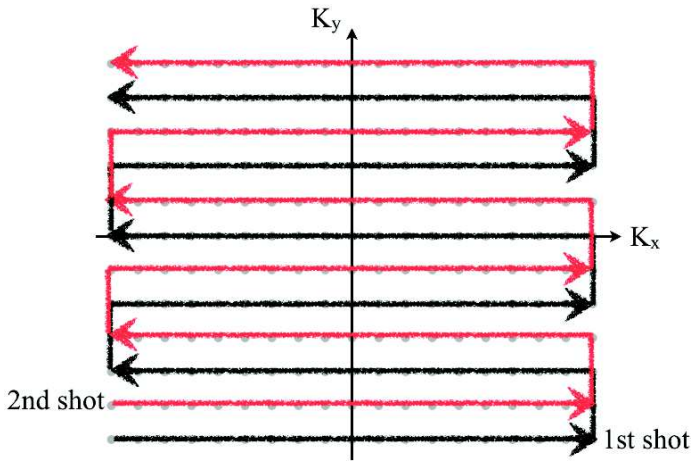

Figure 4.2: *k-Space trajectories for 2 shots EPI.*

in parallel imaging methods such as GRAPPA for R-fold acceleration [Griswold 2002] where the amount of phase evolution between k_y samples has been reduced by a factor R, thereby reducing the distortion by a factor R. Likewise, if one does an interleaved multi-shot EPI scheme then similar n-fold reduction of distortion for an n-shot acquisition can be achieved, but only if the ES time is maintained and the k_y step size is increased by the factor n, to $n \cdot \Delta k_y$.

Our aim was to acquire fMRI images with a voxel size of $1.5 \times 1.5 \times 1.5 mm^3$, the optimum spatial resolution with a magnetic field of 3T [Hyde 2001], in a reasonable acquisition time. Thus not the entire brain is acquired in our experiments but only two packs relatives to the primary motor area (M1) and to the cerebellum (Section 7.1, Fig. 7.2).

To aquire all the slices the SNR can be improved by employing a **multi-shot** technique. The first shot of every slice is acquired before returning to acquire the second interleave. This increases the steady state transverse magnetisation available after each pulses, and therefore increases the SNR.

The benefits are slightly offset by the risk of subject movement during the acquisition. If the movement occurs between the first and second shot of one slice, that image will contain artefacts. The probability of this occurring is much greater if there is a long delay between shots, as is the case in the multi-slice experiment. The comparison between high spatial resolution and low spatial resolution EPI is summarised in Table 4.2.

	Low Resolution	**High resolution**
Voxel volume (mm^3)	few tens	few
TR	$< 3s$	$> 3s$
tSNR	good	poor
Activation spatial localisation	poor	good
Partial Volume effect	important	low
Geometric distortions	high sensitivity	low sensitivity
Intra-subject movements sensitivity	resonable	important

Table 4.1: *Comparison between low spatial resolution and high spatial resolution EPI sequences.*

CHAPTER 5

Image Registration

5.1 Introduction

Medical imaging plays a central role in a large number of clinical applications. Among several image modalities two main categories that can be identified: *anatomical* and *functional*. Anatomical modalities include all techniques characterising the morphology of the system, *i.e.* X-ray, CT (Computed Tomography), MRI (Magnetic Resonance Imaging). Functional modalities characterise the metabolism of the underlying anatomy, *i.e.* SPECT (Single Photon Emission Computed Tomography), PET (Positron Emission Tomography) and fMRI (functional MRI).

All the mentioned techniques are complementary and a proper **combination** of data is often desirable. This combination is made possible by **Image registration**. First, a common reference system is defined for all the images under study. Additionally, the images are spatially aligned by founding the transformation parameters, based on certain **similarity measures** and **cost functions**.

The objective of this thesis was to find the best registration pipeline for our neuroscientific aims (Chapter 1). It is out of the scope of this work to detail the ”image registration" theory, which is subject for many books and publications. However, the main components of a registration algorithm will be introduced and general applications of the methods, and their classification, will be depicted. Finally, four representative registration methods will be described. In the results section (Chapter 10) these methods will be experimentally compared.

5.2 General applications

It is now common for patients to be repeatedly imaged either with a single modality or with different modalities. Therefore, the number of images becomes more and more important and it is highly desirable to relate each image to the others using the registration process.

Registration of medical image data sets presents the problem of identifying an homology or a geometric transformation which maps the coordinate system of one data set to that of another one. In other words, the problem consists of finding the spatial correspondence between homologue input data sets. Three classes can be distinguished:

1. **Intra-subject uni-modal** case: same subject, one imaging modality.
2. **Intra-subject multi-modal** case: same subject, two or more imaging modalities.
3. **Inter-subject uni-/multi-modal** case: different subjects (group study), one or more imaging modalities.

The **first class** of registration (**Intra-subject/uni-modal**) perhaps represents the simplest registration scenario that arises when we want to register images of the same subject, acquired with the same type of imaging modality. It is the case of, for example, the **motion correction** of the functional time-series images in a fMRI study [Friston 1995, Kim 1999], or the **correction for geometric distortion in EPI (Echo Planar Imaging) sequences** by registering the distorted EPI images to undistorted images [Hellier 2000, Li 2008].

The **second class** (**Intra-subject multi-modal**) of registration concerns the same subject imaged with several types of modalities. For example, MRI *vs* fMRI or PET image in order to integrate functional and anatomical informations. It is the case of the fMRI study of McGoniugle *et al.*, where brain activations due to supernumerary phantom limb were investigated, in a case study [McGonigle 2002].

The **third class** (**Inter-subject/uni- and multi-modal**) is relevant when, for example, structural [Rueckert 2003, Draganski 2004] or functional [Jaillard 2005] images are compared to investigate anatomical and functional changes at a group level and/or in a longitudinal study. It includes also the atlas creation where several healthy brains were imaged with different modalities [Roberts 1998, Rohlfing 2010].

All these registration scenarios required different approaches depending on the “difficulties” to register the images. First, the appropriate transformation domain needs to be identified;

secondly, a special function (or an objective function or a similarity metric) needs to be defined, which evaluates the quality of the current alignment; and thirdly, an optimisation algorithm has to be selected.

For the first class of problems, generally a *rigid-body* transformation, *i.e.* translation in x, y and z + rotation around the three axis, could be enough to achieve a good registration. A mean-squared is then used as metric.

The second class requires a more detailed analysis of the observed images because the corresponding anatomical structures might have significantly different intensity profiles. Moreover, the intensities that are compared refer to a set of different physical properties. In this case a mutual information similarity metric is usually used.

The third class of registration techniques, concerning the comparison between different subjects, is a more ambitious task involving complex assumptions that should describe the differences between the input images. This requires *non-rigid* (or *elastic*) transformations in order to take into account the high anatomical variability between subjects. In this case, the sum of squared differences (SSD) can be used as similarity measure.

In the following section the general registration framework is presented and the principal parts of a registration algorithm are briefly described.

5.3 Image Registration Components

The main components of a registration process, as represented in Figure 5.1, are:

- **Fixed image**: reference image (*i.e.* target image)
- **Moving image**: image to be transformed (*i.e.* source image)
- **Transform**: it correlates the fixed image and the moving image
- **Metric**: a similarity criterion defining how well the *moving image* match the *fixed image*
- **Optimiser:** methods used to find the *Transform* parameters that optimise the *Metric*
- **Interpolator:** technique used to resample the object after *Transform*

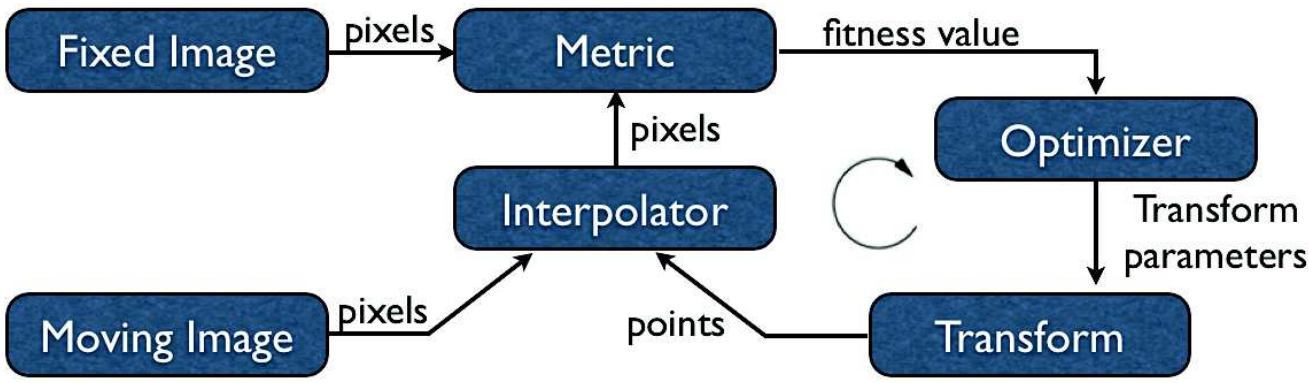

Figure 5.1: General registration algorithm framework (Extracted from ITK Software Guide, http://www.orfeo-toolbox.org/SoftwareGuide/).

5.3.1 Transformations

To **register** means to find a spatial transformation mapping the points in one image (*i.e. moving image* or *source image*) with the homologous points of another image (*i.e. fixed image* or *target image*). We can formalise as following:

$$\mathbf{T} : \mathbf{x}_P \longmapsto \mathbf{x}_Q \Longleftrightarrow \mathbf{T}(\mathbf{x}_P) = \mathbf{x}_Q \tag{5.1}$$

where **P** and **Q** are the moving and the fixed images respectively, **T** the transformation and **x** the positions (Fig. 5.2). The sets of image points $\{\mathbf{x}_P\}$ and $\{\mathbf{x}_Q\}$ are involved in registration algorithms that work with geometrical features. Methods working on images intensity estimate a similarity parameter between $\mathbf{x}_P$ and $\mathbf{x}_Q$.

Typical transformation methods can be rigid, affine, piecewise affine or non-rigid (elastic) . In the following sections we briefly describe these methods.

A representation of identity, rigid, affine and non-rigid transformation is shown in Figure 5.3.

5.3.1.1 Rigid transformation

Rigid transformations preserve all distances, straightness of lines and non-zero angles between straight lines. Rigid transformations are simple to specify and they have two components: a **translation**, $\mathbf{t} = (t_x, t_y, t_z)^T$, and a **rotation R**, which can be applied to any point $\mathbf{x} = (x, y, z)^T$ in the

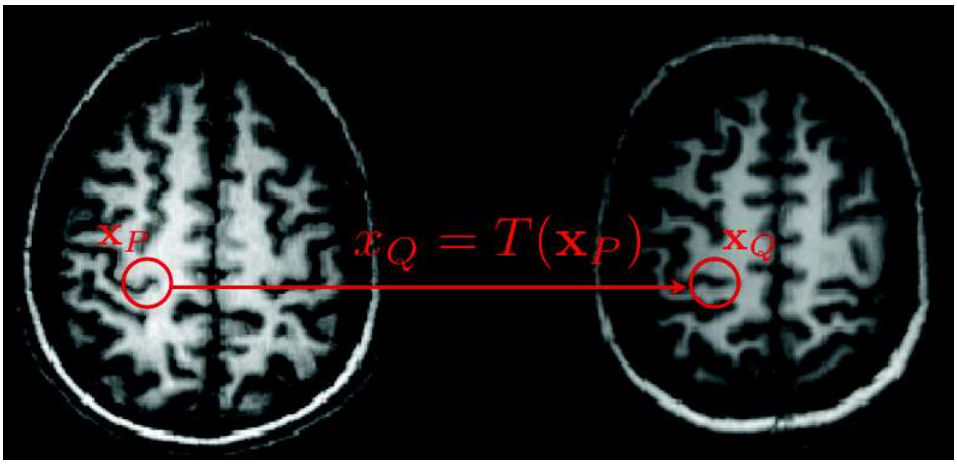

Figure 5.2: Registration problem: T is the transformation to be found in order to establish a spatial correspondence between homologue points (x_P, x_Q) in different images P and Q.

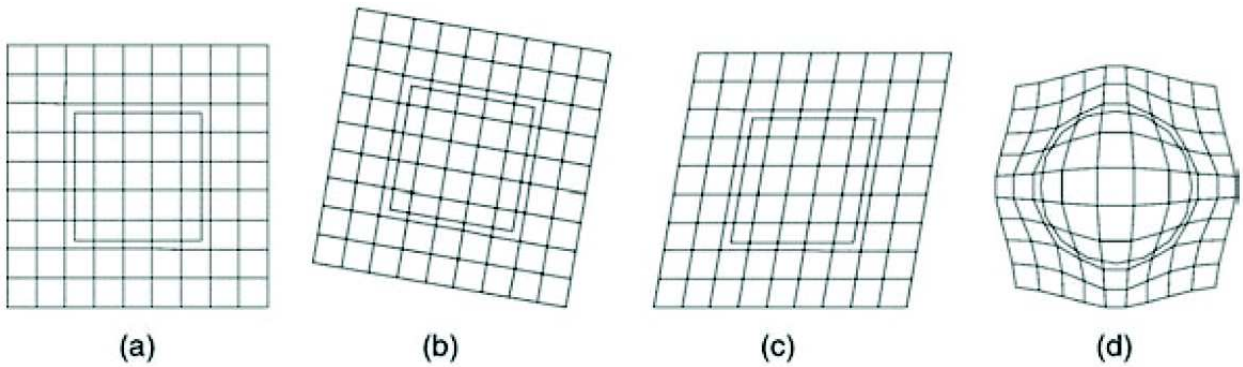

Figure 5.3: *Example of different types of transformations of a square: (a) identity transformation, (b) rigid transformation, (c) affine transformation, and (d) non-rigid transformation* [Hajnal 2001].

image:

$$\mathbf{T}_{rigid}(\mathbf{x}) = \mathbf{Rx} + \mathbf{t} \tag{5.2}$$

t is a three-dimensional vector that may be specified by giving its three coordinates or by giving its polar spherical coordinates. If α, β and γ are the pitch, roll and yaw angles respectively, we can represent the rigid transformation as a 4x4 matrix, whose components are:

$$\mathbf{T}_{rigid} = \begin{vmatrix} 1 & 0 & 0 & t_x \\ 0 & 1 & 0 & t_y \\ 0 & 0 & 1 & t_z \\ 0 & 0 & 0 & 1 \end{vmatrix} \times \begin{vmatrix} 1 & 0 & 0 & 0 \\ 0 & cos\alpha & sin\alpha & 0 \\ 0 & -sin\alpha & cos\alpha & 0 \\ 0 & 0 & 0 & 1 \end{vmatrix} \times \begin{vmatrix} cos\beta & 0 & sin\beta & 0 \\ 0 & 1 & 0 & 0 \\ -sin\beta & 0 & cos\beta & 0 \\ 0 & 0 & 0 & 1 \end{vmatrix} \times \begin{vmatrix} cos\gamma & sin\gamma & 0 & 0 \\ -sin\gamma & cos\gamma & 0 & 0 \\ 0 & 0 & 1 & 0 \\ 0 & 0 & 0 & 1 \end{vmatrix} \tag{5.3}$$

Thus, the transformation has 6 DOF: 3 translations and 3 rotations. It is linear and it can be represented as a 4x4 matrix.

5.3.1.2 Affine transformation

An affine transformation is achieved by coupling a scaling factor (S) to the rigid transformation:

$$x' = \mathbf{SRx} + \mathbf{t} \tag{5.4}$$

where $S = diag(s_x, s_y, s_z)$ is a diagonal matrix whose elements represent scale factors along the three coordinate axes. This is a crude approximation to a fully non-rigid transformation that preserves the lines straightness and the angles between them. There are 6 more components than in rigid transformation: 3 stretches and 3 shears. So this method includes 12 DOF. If the scaling is isotropic, the transformation is a similarity transformation,

$$x' = s\mathbf{Rx} + \mathbf{t} \tag{5.5}$$

where s is a positive scalar, known as *dilatation*, that has values less than unit. The affine transformation is effective when registrations must account for erroneous or unknown scales in the image acquisition process.

5.3.1.3 Piecewise-affine transformation

It is a simple extension of a fully non-rigid transformation and strictly speaking it is non-linear. The registration approach based on the Jean Talairach and Pierre Tournoux atlas of brain anatomy [Talairach 1988] falls in this category. They define a coordinate system used for the stereotaxic space. The Talairach system establishes the maximal dimensions of the brain in three planes of space (Fig. 5.4):

- X axis: a horizontal line running through the anterior and posterior commissures (AC-PC line)
- Y axis : vertical lines passing through the anterior commissure (VAC line) and the posterior commissure (VPC line) (verticalfrontal lines)
- Z axis: A line forming the interhemispheric sagittal plane (midline)

The Tailarach registration method maps the brains into a template (the Talairach atlas) by applying affine transformations to the single cells (piecewise registration) (Fig. 5.5).

There are some important difficulties when the Tailaraich atlas is used:

1. it is developed for stereotaxic surgery of deep structures and not for the brain cortex.
2. it is based on post-mortem sections of 60-year-old female's brain (single subject and not necessarily representative).
3. spatial normalisation based on AC-PC does not accommodate most variable brain structures.
4. it is defined for one hemisphere ignoring the inter-hemispheric variability.
5. the cerebellum and the brainstem are not considered.

Some improvement has been done by using more representative atlas like the Montreal Neurological Institute atlas (MNI) including the International Consortium for Brain Mapping atlas (ICBM) where 152 subjects are registered on the MNI[1] .

To take into account local variations Collins *et al.* performed a linear transformation, in order to globally align the source image with the target image, followed by a non-linear transformation

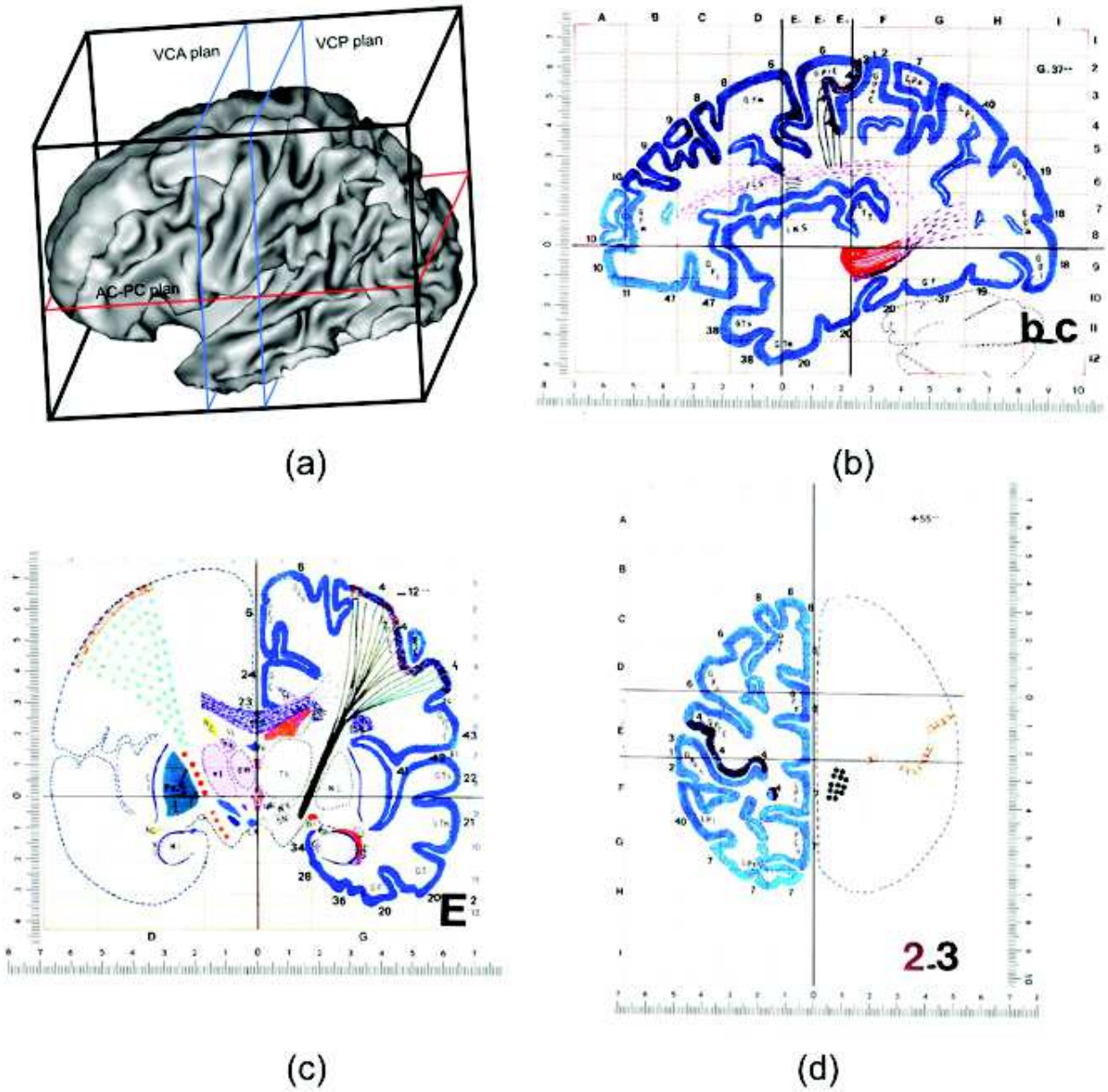

Figure 5.4: (a) Talairach referential plans representation. Example of sagittal (b), coronal (c) and axial (d) view from the Tailarach's atlas. Extracted from [Talairach 1988].

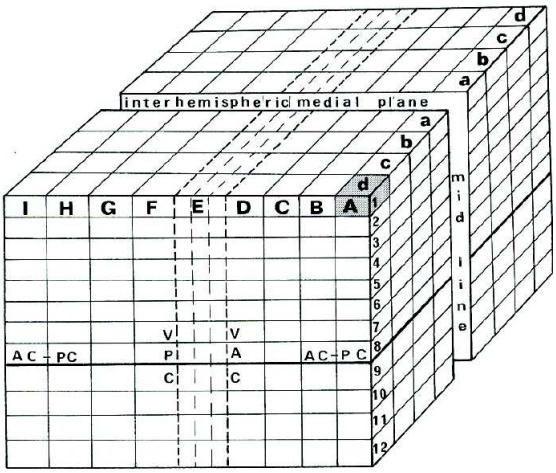

Figure 5.5: Volumetric subdivision of the Thalairach space: each cerebral hemisphere is divided into six associated blocks (inter-hemispheric plane, AC-PC axial plane, 2 coronal planes through AC and PC). Extracted from [Talairach 1988].

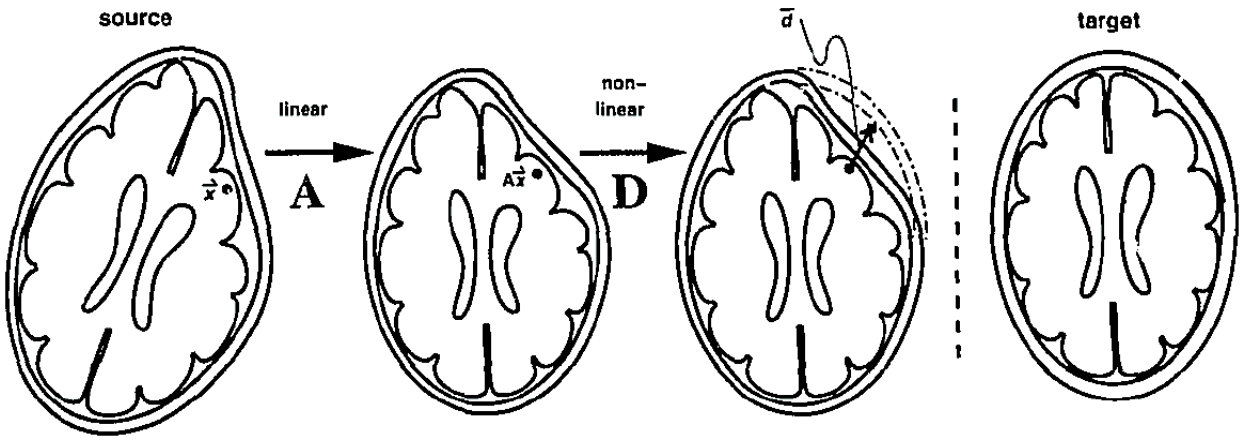

Figure 5.6: Linear transformation (A) + non-linear transformation (D) registering the source image with the target image. Extracted from [Collins 1994].

for local correction, as schematically shown in Fig. 5.6 [Collins 1994]. This method pretends to find a global minimum of an error surface. Unlucky, it is computationally expensive and it may find undesirable local solutions.

To avoid these problems, Friston *et al.* [Friston 1995] used an approach based on an explicit and unique solution that can be obtained by solving just one equation. They considered that for the registration of two images, $\Omega(x)$ and $\Gamma(x)$, two components can take into account: 1) the voxel-by-voxel intensity values when the images are hypothetically aligned, and 2) the structural differences due to misalignment, or gaps in size, of the object scanned. Thus, the relation between the two images can be expressed as

$$f_x\{\Gamma(x)\} = \Omega(q(x)) + e(x) \tag{5.6}$$

where f_x is the operator that transforms the intensity of the source image to the target image intensity, $q(x)$ is the spatial transformation and $e(x)$ is an error term. Imposing local constraints (no significant structural and intensity variations in the local contiguity are permitted) the linearisation of the equations 5.6 is performed by using some smooth basis functions.

5.3.1.4 Non-rigid transformation

In medical imaging, non-rigid registration was initially used to standardise MR and CT brain images with respect to an atlas [Bajcsy 1983, Bohm 1983].

These transformations allow changes in shape and size as well as grosser changes in topology. Some registration algorithms are based on approximation of physical phenomena like the elastic properties of solids or dynamics of viscous fluids.

Their characteristic is the high number of DOF, introduced to the transformation via polynomial functions. By adding additional degrees of freedom (such as higher order polynomial) to the rigid transformation eq. (5.2), we can obtain non-rigid transformation models. For example, the quadratic transformation model is defined by second order polynomials:

[1] http://imaging.mrc-cbu.cam.ac.uk/imaging/MniTalairach

$$T(x,y,z) = \begin{pmatrix} x' \\ y' \\ z' \\ 1 \end{pmatrix} = \begin{pmatrix} a_{00} & \dots & a_{08} & a_{09} \\ a_{10} & \dots & a_{18} & a_{19} \\ a_{20} & \dots & a_{28} & a_{29} \\ 0 & \dots & 0 & 1 \end{pmatrix} \begin{pmatrix} x^2 \\ y^2 \\ \vdots \\ 1 \end{pmatrix} \tag{5.7}$$

where the a_{ij} coefficients determine the 30 DOF of the transformation [Hajnal 2001].

Cachier *et al.* [Cachier 2003] proposes a classification of various non-rigid image registration methods.

5.3.2 Metric

To establish the goodness of the registration process we need to measure some kind of difference between the target image and the source image we want to register. This *similarity measure* is implemented in the registration algorithm and adapted to the images features that we want to register. The common metrics are the following:

Sum of Square Differences (SSD)

$$SSD = \frac{1}{N} \sum_{x_A \in \Omega_{A,B}} |A(x_A) - T(B(x_A))|^2 \tag{5.8}$$

where A and B are the images, T the transformation, x_A the voxel location in A within the overlap domain $\Omega_{A,B}$ comprising N voxels. It is only valid for the same modality with properly normalised intensities in the case of MRI.

Normalised Correlation Coefficient (NCC)

$$NCC = \frac{1}{N} \sum_{x_A \in \Omega_{A,B}} \frac{[A(x_A) - \bar{A}][T(B(x_A)) - \bar{B}]}{\sigma_{A(x_A)} \sigma_{T(B(x_A))}} \tag{5.9}$$

where $\bar{A}$ is the mean voxel value in image A, $\bar{B}$ is the mean of $T(B)$ within $\Omega_{A,B}$. $\sigma_{A(x_A)}$ and $\sigma_{T(B(x_A))}$ are the respective standard deviations. This metric models the linear relationship between voxel intensities and it is especially useful for rigid body registration using the properties of the Fourirer transform in the k-space [Kassam 1996].

Mutual information

It is a more general metric which maximises the clustering of the *joint histogram* (Fig. 5.7) and it does not assume any type of relationship of intensities.

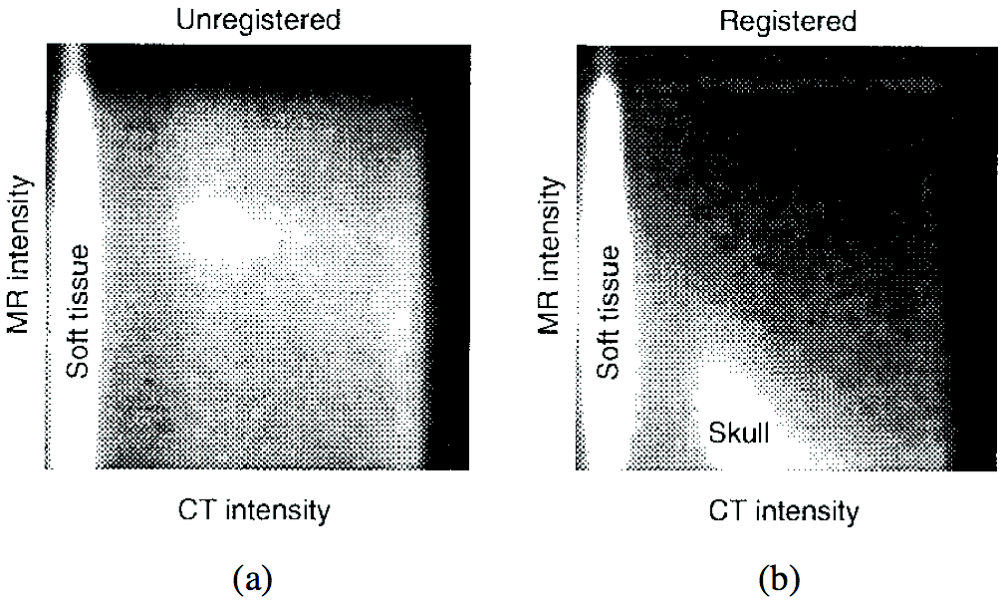

Figure 5.7: *Joint histogram of the overlapping volume of the CT and MR brain images: (a) Initial position, (b) registered position*. Extracted from [Maes 1997].

The *joint histogram* is a 2-D histogram where each axis is the number of possible greyscale values in each image. Figure. 5.8 shows an example of joint histogram of an MR image with itself when it is identical or rotated with respect by different angles [Pluim 2003].

From the information theory the Shannon entropy's measure H (Shannon-Wiener entropy) is used to evaluate and maximise the shared information in two images:

$$H = \sum_{i}^{n} p_i \log \frac{1}{p_i} \tag{5.10}$$

where H is the average information coming from i objects whose probabilities are given by $p_1, p_2, p_3, \ldots p_n$. An infrequently occurring event provides more information than a frequently occurring event. A system with one frequent event has less entropy than a system with many equally probable events.

(a) (b) (c) (d)

Figure 5.8: *(a) Histogram showing the situation of two registered identical images. Since the images are the same, all gray value correspondences lie on the diagonal. (b), (c), and (d) show the resulting histograms when one MR image is rotated with respect itself by an angle of 2°, 5°, and 10°, respectively*. Extracted from [Pluim 2003].

It was observed that a link exists between histogram dispersion and image matching. The *joint entropy* is a measure of the joint histogram dispersion. If A and B are two images, the joint entropy between them will be

$$H(A,B) = -\sum_{i,j \in \Omega_{A,B}} p_{i,j} \log p_{i,j} \tag{5.11}$$

A and B are registered when one is transformed relative to the other to minimise the joint entropy (*i.e.* the dispersion in the joint histogram is minimised). Since the eq. (5.11) is dependent on the overlap $\Omega_{A,B}$, we can compute the mutual information (I) that can be expressed as:

$$I = H(A) + H(B) - H(A,B) \tag{5.12}$$

Maximising the mutual information is equivalent to minimise the joint entropy (last term). It works better than simply joint entropy in regions of image background (low contrast), where the joint entropy is low.

5.3.3 Optimisation

A process of optimisation is required in almost all registration algorithms to obtain an efficient iterative computation. Several parameters need to be found in a registration algorithm, depending on the transformation (6 parameters for the rigid transformation, 12 for the affine, etc). Optimisation

concerns the choice of initial parameters (*i.e.* a starting point, defined within the "capture range", that is the optimal portion of the parameters space) and the search of optimal parameters. This is done by a cost function, or a similarity measure, computation. The more appropriate numerical methods are used to efficiently converge towards a solution.

5.3.4 Interpolation

Once the transformation and the registration parameters are defined, it is necessary to transform the source image to the new reference system. This requires the interpolation of the intensity values and, in this case, the choice of the good method it is crucial for not introducing undesirable correlations between voxels. The widely methods used are the **neighborhood** interpolation, **trilinear** interpolation and **B-spline** interpolation of different orders.

5.4 Classification of registration methods

The number of registration methods is growing with the applications in medical imaging. There are several ways to classify the large set of registration procedures introduced in the literature [Cachier 2003] . The *nature of the transformations* and consequently the DOF (*i.e.* the number of parameters needed to describe a registration transformation) can classify a registration method. A high number of DOF allows strong deformations as in non-rigid registration techniques for inter-subject registration [Klein 2009] and can give purely performance.

In addition, we can identify *volumetric-based* methods, which are those that use features in the 3D coordinates space, and *surface-based* methods, which need the reconstruction of the tissues in the 2D space before the registration process. The high variability of the brain cortex between subjects make arduous to find correspondences among the images. Thus, it becomes useful to analyse data on the surface using some characteristics like shape descriptors [Mangin 2004a]. While volumetric approaches perform well at aligning the deep subcortical structures of the brain, they often fail to correctly align the sulcal folding patterns of the cortex. By contrast, surface-based registration techniques align the sulcal folds but they do not always define a volumetric correspondence between points in the interior part of the brain. The surface representation can be simply a point set (*i.e.* a collection of points on the surface), a faceted surface (*e.g.* triangle set), an implicit surface, or a parametric surface (*e.g.* B-spline surface). Extraction of a surface such as the skin or

bone is relatively easy and fairly automatic for head CT and MR images. Extraction of many soft tissue boundary surfaces is generally more difficult and less automatic.

We call *features-base registration* (*i.e.* label-based) algorithms those techniques that consider geometrical features (or landmarks) and we call *intensity-based registration* (*i.e.* non-label based) those methods that use the intensity levels to match two images [Friston 1995]. The former requires the definition of specific features (landmarks) that should be matched. The latter suppose a relation (correlation) to be determined between the two images, quantified for example by entropy or mutual information.

A registration method can be **global** if it is applied to the entire image, and **local** if subsections of the images are forced to be aligned. Figure 5.9 shows examples of a global and a local 2D registration for a rigid and an affine transformation types.

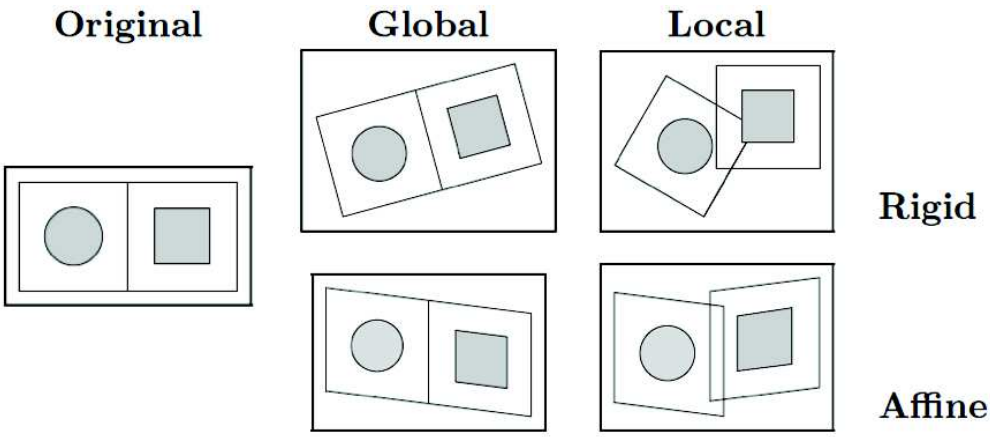

Figure 5.9: *Representation of a global and a local registration for a rigid and an affine transformation. Extracted from [Maintz 1998].*

5.4.1 Local registration methods

As shown in Figure 5.9, local registration methods concern the alignment of particular "features" of two or more images. These features can be a set of points, segmented structures or regions of interest (*e.g.* Demons, [Vercauteren 2009]). The goal is to register local parties of the images, even if the rest will be poorly aligned. For example DISCO [Auzias 2009], as we will see later, uses the sulci imprint as landmarks for the brain registration. The idea comes from previous works of

J.F. Mangin and colleagues [Régis 2005, Perrot 2011]. Their hypothesis is that despite the high variability of the sulci between formed adult brains (Fig. 5.10), the primary sulci, appearing at the

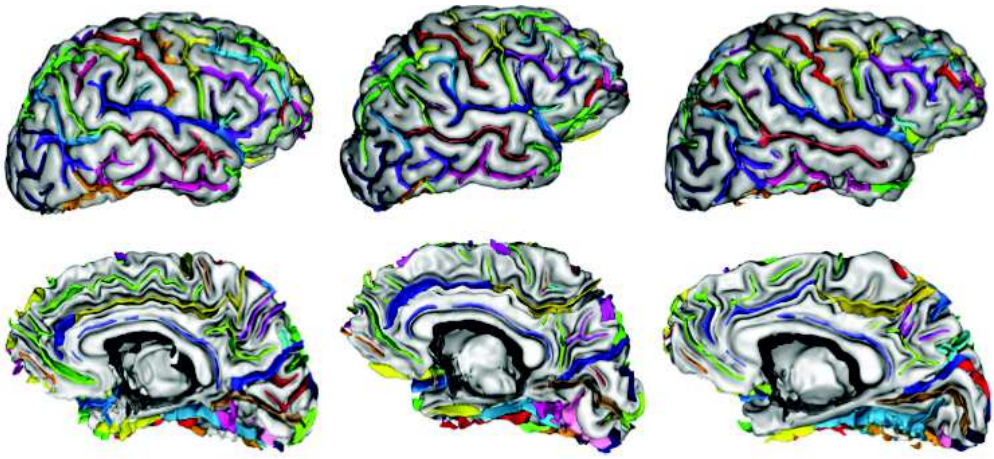

Figure 5.10: *Representation of the extracted sulci, of 3 different subjects, superimposed on the relative cortical mesh. The inter-subject structural variability can be valued. Adapted from* [Perrot 2011].

early stage of brain maturation [Dubois 2008], are stable and well localised in all subjects. These labelled sulci [Régis 2005] can be the reliable landmarks for brain matching. Thus Perrot *et al.* combine the registration procedure with the classification (*i.e.* labelling) in a Bayesian framework [Perrot 2011].

Yassa and Stark [Yassa 2009] showed that focusing on a particular region of interest and forcing to realign that regions can improve the registration results in respect consider the global image. It is also called "ROI-AL" (Region Of Interest Alignment) method.

5.4.2 Global registration methods

Global methods look for the transformation parameters evaluated from the whole images. For example SPM8-type registration ("Unified Segmentation" framework) [Ashburner 2005], DARTEL [Ashburner 2007] or ART (Automatic Registration Toolbox) algorithm [Ardekani 2005], which are ranked among the top in the Klein study that compares a large set of registration methods [Klein 2009].

5.5 Some representative registration methods

Hereafter a description of some representative methods of the current state of the art, introduced above, is presented.

SPM8-type , a method widely used in the neuroscience community [Ashburner 2005].

DARTEL , representatives of standard diffeomorphic methods, where the deformation constraints, estimated globally on the whole brain scan [Ashburner 2007].

DISCO + DARTEL (DiDa) , representative of a class of methods where explicit sulcal landmarks are used to constraint the 3D deformation [Auzias 2011].

Demon (DDe) , representative of diffeomorphic methods where deformations can be estimated locally to align predefined three-dimensional ROIs [Vercauteren 2009].

These methods will be compared in the results section (Chapter 10).

5.5.1 SPM8-type (Unified Segmentation)

This is a method implemented in the **S**tatistical **P**arametric **M**apping software (SPM). It is based on the "Unified Segmentation" framework [Ashburner 2005]. It is a global and volumetric method based on the intensities of the image voxels. It combines the registration, the bias correction and the segmentation (*i.e.* classification) steps in a single generative model.

This approach works by minimising the average across voxels of the squared difference between the volume to be normalised and a template volume. The intensity contrast of both images should be similar to produce an unbiased estimate of the spatial transformation.

The first step of the registration finds the optimum 12 parameters of the affine transformation by appropriate weighting of the template voxels. The affine registration is followed by non-linear deformations defined by linear combinations of $8 \times 8 \times 8$ discrete cosine transform basis functions [Friston 1995, Ashburner 1999]. This option results in each of the deformation fields being described by almost 10^3 parameters representing the coefficients of the deformations in three orthogonal directions (83 for each one).

Limitations

One limitation of this method it is the template dependence of the approach. The MNI template provided by SPM has a voxel size of $(2 \times 2 \times 2)mm^3$ in comparison with the typical high resolution anatomical (*i.e.*T1-weighted images) MRI, which has a voxel size of $(1 \times 1 \times 1)mm^3$. Furthermore, changing the template may changes the results.

Another problem is the DOF number. It allows the global registration of the images but it is too low to permit the alignment of brain subregions (Fig. 5.11).

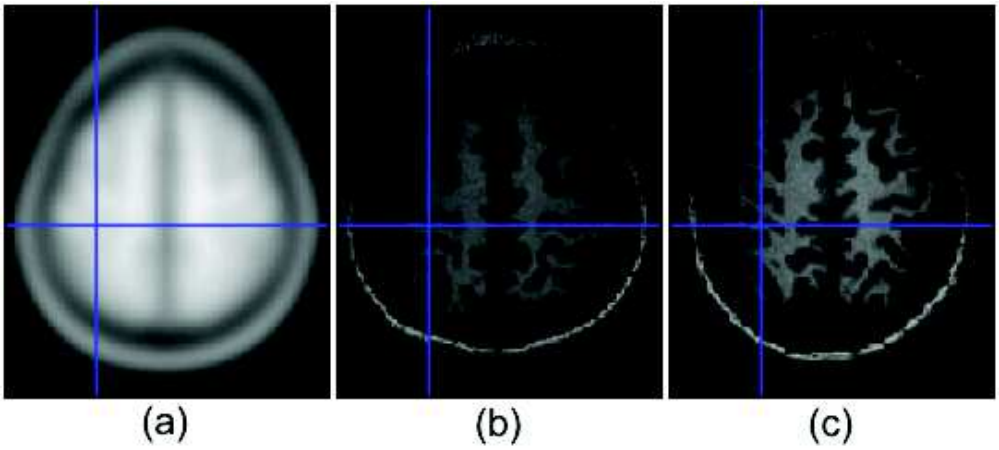

Figure 5.11: *Axial view of the MNI T1 template (a) and two different anatomical images (b,c) registered with the SPM registration method. The images are globally well registered with the MNI template but the local correspondence between homologues points is not guaranteed.*

Finally, the registration performance is not homogeneous over the brain, as it has been shown by Klein *et al.* [Klein 2009] (Fig. 5.12).

5.5.2 DARTEL

Diffeomorphic **A**natomical **R**egistration **T**hrough **E**xponentiated **L**ie Algebra (DARTEL) [Ashburner 2007] is a registration method using a nonlinear and diffeomorphic transformation function with 6.4 M of DOF. It is a **global**, volumetric and intensity-based method. It creates a **custom template** adapted for the population under study and spatially close to the MNI template. As we can see in Fig. 5.13, the homologue anatomical points seem to be in a good correspondence. DARTEL optimises the overlap of grey and white matter tissue masks between subjects through

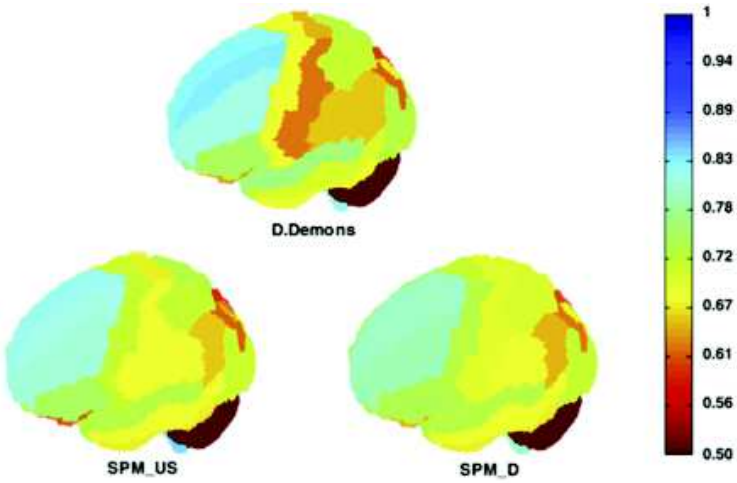

Figure 5.12: *Overlap ranking of different registration methods tested by Klein et al. (blue indicates higher accuracy; D.Demons=DDe, SPM_US= SPM8-type, SPM_D=DARTEL)*. Extracted from [Klein 2009].

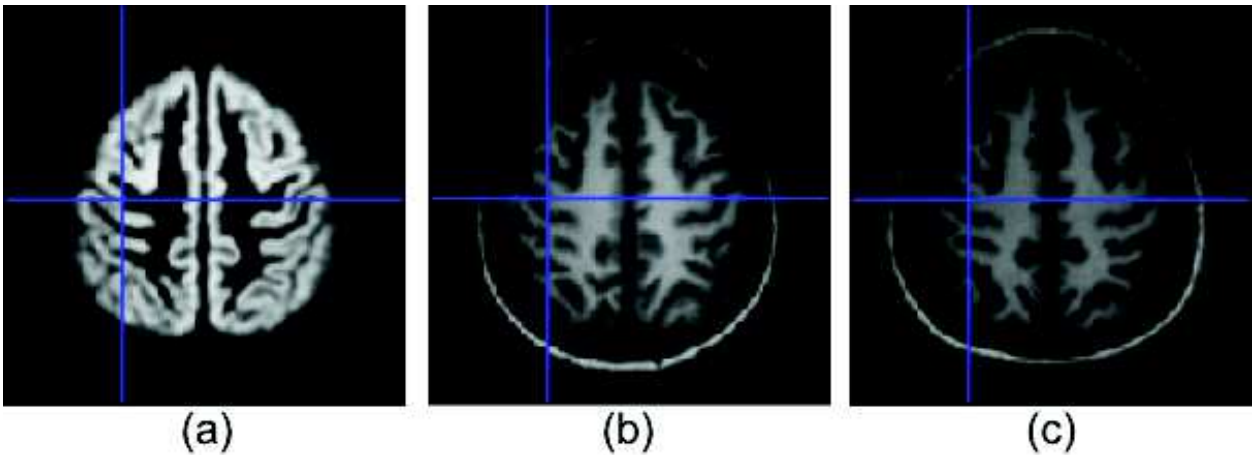

Figure 5.13: *Axial view of the DARTEL template using 13 different subjects (a); (b,c) two subjects deformed by DARTEL.*

a large deformation technique where deformations are parametrised by a velocity field that is constant in time. The algorithm embeds the construction of an average image template. The technique has been already applied in different VBM studies with good performance. It uses a multinomial model as similarity measurement ("congealing") with a linear elasticity and multi-resolution (recursive) regularisation function [Klein 2009].

The idea is to register images by computing a "flow field" which can then be "exponentiated" to generate both forward and backward deformations. Processing begins with the images segmentation. then, the tissues images, are rigidly registered so that they are in as close alignment with the tissue probability maps.

The next step is the registration itself. This involves the simultaneous registration of *e.g.* GM with GM, WM with WM and 1-(GM+WM) with 1-(GM+WM). This procedure begins by creating a mean of all the images, which is used as an initial template. Deformations from this template to each of the individual images are computed, and the template is then re-generated by applying the inverses of the deformations to the images and averaging. This procedure is repeated a certain number of times. Finally, warped versions of the images (or other images that are in alignment with them) can be generated.

Limitations

DARTEL is based on the tissue segmentation of the anatomical images and the results may change with different segmentation methods. Moreover the quality of the registration is not homogeneous over the brain's regions, as it has been shown by Klein *et al.* (Fig. 5.12).

5.5.3 Demon (DDe)

Demon uses a deformable, diffeomorphic and nonlinear transformation with 21M DOF. It is an efficient algorithm for the nonparametric diffeomorphic registration of N dimensional images [Vercauteren 2009]. It adapts the optimisation procedure on the entire space of displacement fields proposed in [Thirion 1998] to the space (Lie group) of diffeomorphic transformations. This method outperforms other techniques when applied locally to align ROIs in the medial temporal lobe [Yassa 2009].

Even if it is developed to locally work inside ROIs, it is conceptually a global and intensity-based

method that does not use landmarks or other local constraints.

Limitations

One limitation is the high number of DOF and the completely non-parametric characteristic of the method, allowing important deformations often very hard to interpret. As shown in Fig. 5.14, a local miss-alignment can be produced between the pre-central and the central sulcus.

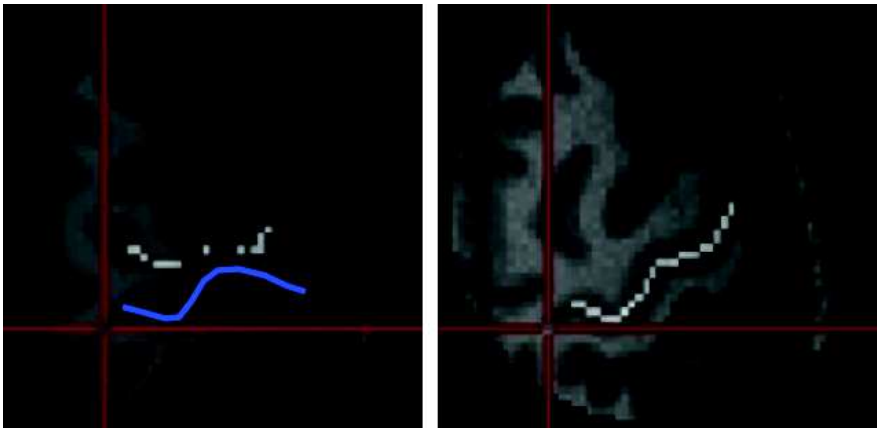

Figure 5.14: *Axial view of the ROI in the right hemisphere of one images (left) deformed by Demon on the target image (right). The blue line represents the pre-central sulcus erroneously registered with the central sulcus of the target image (white dotted line).*

Another critical point encountered with Demon is the choice of the target (*i.e.* template) image. Demon registered the moving image with the fixed image adding a bias due to the template choice. Furthermore, when Demon is applied globally, as in [Klein 2009], the quality of the registration is not homogeneous over the brain regions, as for SPM8 and DARTEL (Fig. 5.12).

5.5.4 DiDa (DISCO+DARTEL)

This method follows the idea of J.F. Mangin *et al* [Mangin 2004a]. They use individuals landmarks (*various elementary objects*) defined through automatic detection of the sulci and the parcellation of the cortical surface into gyri.

The **DI**ffeomorphic **S**ulcal-based **CO**rtical (DISCO) registration [Auzias 2011] explicitly forces the alignment of sulci in an iterative approach. Individual sulci are first segmented and modelled

with a set of points (Fig. 5.15). An empirical template is defined as the union of the entire set of

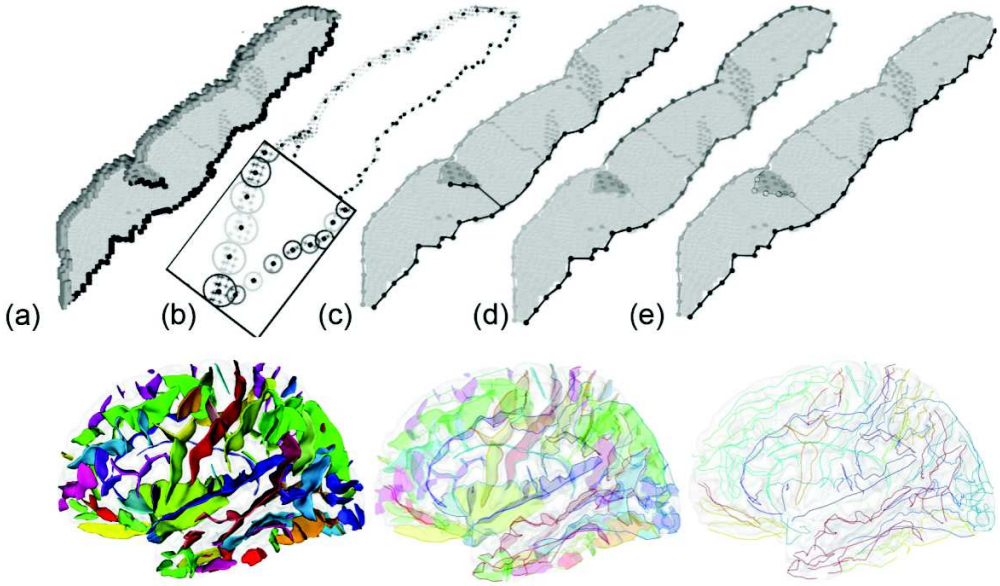

Figure 5.15: *Top row: (a) Each sulcus is decomposed into three subsets of voxels (fundus, outer edge and 'other' voxels) using BrainVISA (`http://brainvisa.info/`). The sulcal fundus is aline shown in black, the outer border in lighter gray and other voxels in lightest gray texture. Every sulcus is summarized by the fundus and outer border voxel subsets;(b) Because the voxel density of these 2 sets is generally very high, they are both down sampled as follows: 1) voxels are grouped into clusters (shown here as circles) and 2) each cluster is reduced to its barycenter (black dots). Finally, the resulting sulcal borders illustrated in (c) are decomposed into elementary components in (d) and reduced to simple lines through alongest-path approach (e). Bottom row: The automatic simplification of the original complex sulcal pattern (left) yields a distributed set of sulcal edges, thereby defining the sulcal imprint of an individual brain (right)* [Auzias 2011].

sulcal points through the set of subjects (Fig. 5.16).

For each sulcal label, the corresponding sulcal landmark in the template corresponds to the union of all points associated to this label for each subject. Diffeomorphic transformation of each individual data onto the empirical template is then proceeded in the general framework of the Large Deformation Diffeomorphic Metric Mapping theory. Improved mask overlap and reduction of sulcal dispersion can be reached through the sequential combination of DISCO and DARTEL (DISCO+DARTEL), with DARTEL being initialised using DISCOs outcome.

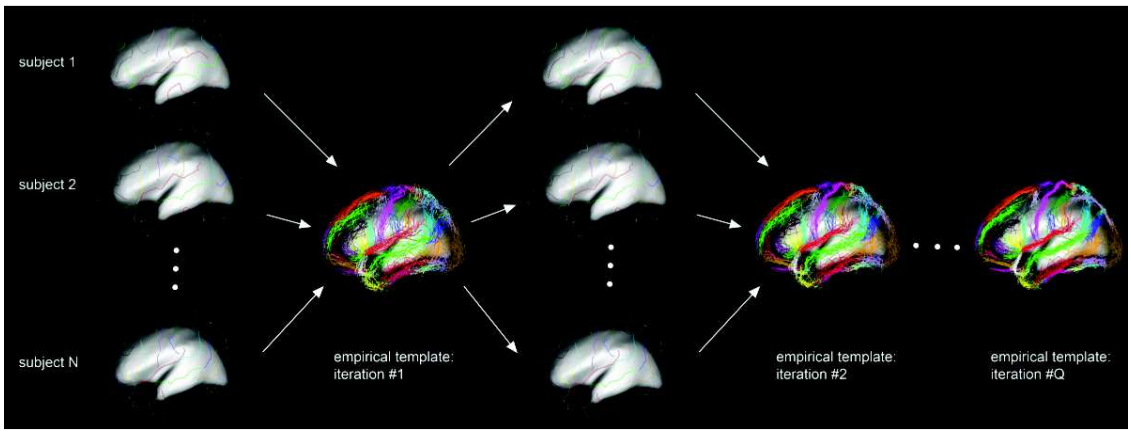

Figure 5.16: *Illustration of the iterative refinement of the empirical sulcal template. This latter is composed of the sample distribution of the entire set of sulcal points available in the group of subjects* [Auzias 2011].

Limitations

As DARTEL, DiDa is based on the tissue segmentation of the anatomical images and also the segmentation of the sulci could affect the results. Indeed sulci like the central sulcus are relatively simple to recognise [Yousry 1997]. But it is not the case for all the sulci, thus the manual interaction with the user is often required.

Part III

Material and methods

CHAPTER 6

Subjects under study

6.1 Patients who underwent a tendon transfer surgery

6.1.1 Tendon transfer surgery

Tendon transfer surgery is a type of hand surgery that is performed in order to restore lost hand functions. A functioning tendon is shifted from its original attachment to a new one to restore the action that has been lost.

Many different conditions can be treated by tendon transfer surgery. For instance, it is necessary when a certain muscle function is lost because of a nerve injury. If a nerve is injured and cannot be repaired, then the nerve no longer sends signals to certain muscles. Those muscles are paralysed and the corresponding functions are lost. Common nerve injuries that can be treated are spinal cord, radial nerve, ulnar nerve or median nerve injury.

Tendon transfer surgery may also be necessary when a muscle has been ruptured or been lacerated, due to rheumatoid arthritis or fracture.

There are 26 muscles animating the hand: 15 *extrinsic* and 11 *intrinsic* muscles. The extrinsic muscle groups are the long flexors and extensors. They are called extrinsic because the muscle belly is located on the forearm. Whilst the intrinsic muscles are located in the hand. Each muscle has a starting point (origin), and tapers down from its muscle belly into a tendon that then attaches onto bone (insertion) in a specific place; when the muscle fires (contracts), it causes a certain motion (action) (Fig. 6.1).

During tendon transfer surgery, the origin of the muscle, the nerve supply and blood supply to the muscle are left in place. The tendon insertion (attachment) onto bone is detached and re-sewn into a different place. It can be sewn into a different bone, or into a different tendon. After its insertion has been moved, when the muscle fires, it will produce a different action, depending on where it has been inserted.

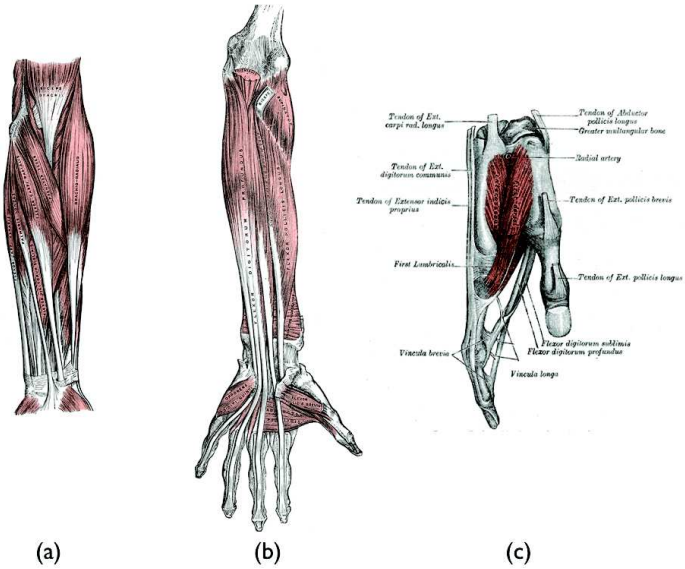

Figure 6.1: *Forearm muscles representation. (a) Front of the left forearm. Superficial muscles. (b) Front of the left forearm. Deep muscles. (c) Tendons of forefinger and vincula tendina. Source:* `http://www.bartleby.com`

We know that voluntary immediate active mobilisation, after tendon transfers reanimation of a loss function, shown its relevance by empirical ways. If it is done in a symmetrical way just after the surgical procedure, it allows quick motor scheme redistribution. After a 30 days immobilisation period, voluntary muscular function command is then present [Tsuge 1969, Zoccoli 1979, Tsuge 1980, Vigouroux 2007].

The tendinous surgery consists of transferring:

- the Pronator Teres (PT) terminal tendon was fixed on the Extensor Carpi Radialis Brevis (ECRB) to extend the wrist.

- the Flexor Digitorum Superficialis of the 4th finger (FDS IV) was fixed to the Extensor Pollicis Longus (EPL) to restore the thumb extension.

- the abduction of the thumb and the Flexor Carpi Radialis (FCR) was fixed to the Extensor Digitorum Communis (EDC) to restore digital extension.

6.1.2 Cases studied

Two patients were involved in our study and their characteristics are summarised in Tab. 6.2.

	Sex	Age	Height	Mass	Pathology	Surgery
Patient 1	M	71	1.68 m	64 Kg	Adicular cervical myelopathy (cervical spinal stenosis)	Right Hand
Patient 2	M	26	1.76 m	65 Kg	Section of the radial nerve after displaced of humerus fracture	Right Hand

Figure 6.2: *Characteristics of the patients who underwent the hand tendon transfer surgery.*

Patient 1, a healthy right handed 71 y.o. man, suffering for a complete high radial nerve classic palsy. He had a collapse of right hand wrist and fingers that do not permit to him to extend the fingers and the thumb ("Adam's hand of the Sistine Chapel ceiling").

Patient 2, a healthy right handed 26 y.o. man, without any osteoarticular, muscular or neurologic pathology underwent a downhill ski accident on 2005 April the 12th. He suffered a right humeral shaft fracture with a total radial nerve paralysis. The fracture was pegged according to Métaizeau [Metaizeau 2004] but suffered a non-union. During the second look surgical procedure, a complete radial nerve laceration was found. Osseous healing was complete after May 2006, but active extension of the wrist and digits were totally absent. Neuroelectromyographic examinations at 5th, 6th, 12th and 18th month post-operative showed no recuperation and concluded to the neural graft fail. So, palliative treatment of this high level radial nerve palsy was decided using tendon transfers. Passive articular motion was maintained by three times per week physical therapy sessions and wearing of a temporary pro extension dynamic splint ("radial-bis" splint). He presented a complete right high level radial nerve palsy resulting in a total loss of digital extension, extension and abduction of the thumb and wrist. To restore these three motor functions and the patient daily living, a reanimation procedure according to Tsuge [Tsuge 1980] was realized using transfers of tendons having normal innervation and function to restore fingers, thumb and wrist active voluntary extension.

A 30 days post-operative rigid immobilisation, in full correction position, was performed. During this period, daily symmetrical wrist and fingers extension exercises were performed mimicking the normal range of movement. After the 30th postoperative day, physical therapy sessions were realised to recover strength, range of movement and agility of the extension movements. Over the 45th postoperative day, the muscular electrical stimulation was used associated with increasing exercises difficulty and strength. The total physical therapy sessions represented 2 hours per day during a six months period.

One year after the surgery, Patient 2 recovered a totally normal daily activity. He returned to work 3 months postop, went back to sports 6 months postop, even for skiing and climbing.

The flexor/extensor inversion is an interesting point to investigate. This is the reason for choosing extension and flexion tasks during the fMRI sessions, even before the surgery. Patients were examined 5 times, in the course of one year. One more exam has been done after 2 years from the surgery (Fig. 6.3). Each exam is composed of two sessions: an high spatial resolution session and

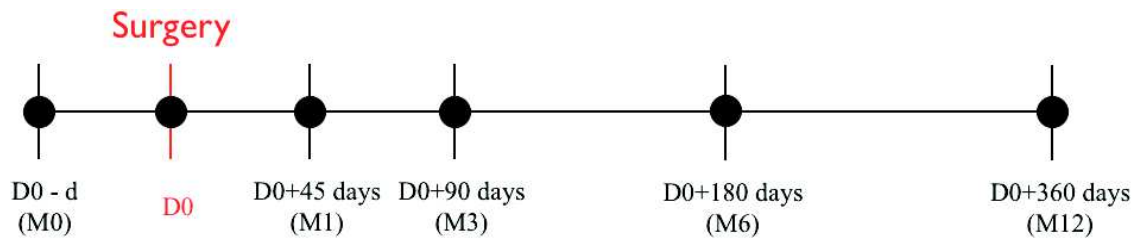

Figure 6.3: *Time line of the tendinous transfer longitudinal study. These patients were imaged 5 times, during one year, plus one more time after 1 year (almost 2 years from the surgery.)*

a low resolution one. In the low resolution session the whole brain was acquired with fMRI images voxel size of $3\times3\times3$ mm^3. During the high resolution session, the voxel size of fMRI images was $1.5\times1.5\times1.5$ mm^3 including only the primary motor area (M1) and the cerebellum. A structural (anatomical) image has been acquired at each session (Fig. 7.2).

6.2 Healthy subjects (control group)

Thirteen right-handed healthy subjects (8 females, 5 males, mean 27.5 y.o.) without past or current brain disease and no detected cognitive deficit, as assessed by the Edinburgh inventory (Oldfield,

Figure 6.4: *Set up of the patient acquisition. The movements were registered for each subject using a set of flexible sensors of flexion/extension (Flexpoint Sensor Systems, Inc., Utah®) fixed on the four hands' joints of interest: the metacarpophalangeal joint of the thumb, the carpometacarpal joint of the thumb, the metacarpophalangeal joint of the middle finger and the carpometacarpal joint of the wrist. These sensors were fixed on both hands with Hypafix®, to insure a close contact between the sensors and the skin. Additionally, this fixation method exerts a restoring force that helps the joints to passively return to the initial position during the relaxing time following each flexion or extension.*

1971), were involved in this study. All subjects gave written informed consent to participate in the study, which was approved by our institutional review board. They had the same tasks of the patients, that are extension/flexion of thumb, fingers and wrist with both hands.

Nine subjects of the control group has been acquired twice in one year, for a "Test"-"ReTest" study. We will test the hypothesis that the healthy subjects of the control groups do not change the functional activity relative to simply hand movements. This allow to study the reproducibility of the motor activation at a group level.

CHAPTER 7

Data acquisition

7.1 Anatomical images acquisition

High-resolution structural images ($1\times1\times1$ mm^3) were acquired on a Bruker 3T Medspec S300 whole body scanner equipped with a birdcage head coil using a T1-weighted 3D MP-RAGE (Magnetisation Prepared Rapid Gradient Echo) optimised sequence [Deichmann 2000].

The T1-weighted three-dimensional (3-D) MP-RAGE sequence is an *inversion-recovery* sequence that produces a T1 weighting. It was first used by Mugler *et al.* [Mugler 1990]. Their purpose was to acquire images with high spatial resolution and high contrast between grey and white matter in a short period of time. They were able to image a set of heads in 6 min with a voxel size of $1.0\times2.0\times1.4$ mm^3 (FOV: $180\times250\times250$ mm^3).

The sequence and the signals evolution are represented in Figure 7.1. The sequence can be described in three phases:

1. Inversion period (*i.e.* magnetisation preparation). It begins with an inversion pulse, 180°-RF, applied with a volume selection gradient (GS). The inversion time between the RF and the acquisition phase is selected in order to minimise the CSF signal.

2. Acquisition period (*i.e.* depth-encoding loop). A rapid gradient echo (RAGE) sequence, as the FLASH sequence [Haase 2011], is applied. It allows to fill the $k_x - k_y$ plane of the *k-space* in a short period of time.

3. Magnetisation recovery time. It is the necessary time for the tissue relaxation, before the next acquisition.

In our work 176 sagittal partitions in two segments with an image matrix of 256x112 (read x phase) were acquired for each subject. Other imaging sequence parameters used were:

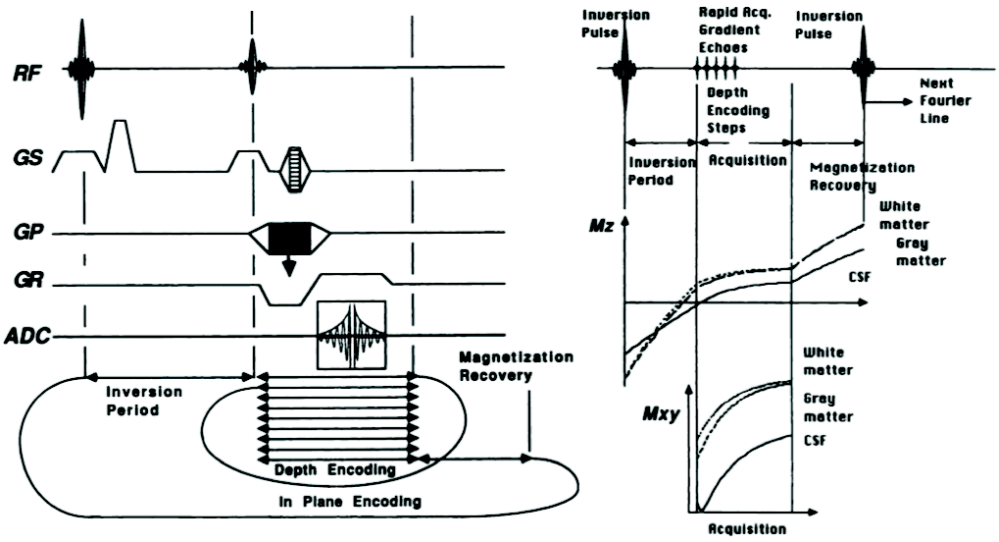

Figure 7.1: *MP-RAGE diagram (left) and magnetisation components evolution (right). RF = radio frequency, GS = slice selection, GP = phase gradient, GR = readout gradient, ADC = analog to digital conversion, M_z=longitudinal magnetisation, M_{xy} = transverse magnetisation. Extracted from [Brant-Zawadzki 1992].*

- TR/TE/TI : 16/4.96/903 ms.
- Excitation pulse angle : 8 deg.
- Acquisition matrix : 176×224×256 (x, y, z).
- Fast phase encoding in antero-posterior direction (112 steps per RAGE train, 2 segments), slow phase encoding in left-right direction.
- Isotropic nominal resolution = 1mm.
- BW = 130Hz/pixel.
- Readout in caudo-cranial direction.
- Number of averages = 1.
- Total measurement time = 14min 40s.

7.2 Functional images acquisition

fMRI functional images were acquired with high spatial resolution of ($1.5\times1.5\times1.5$ mm^3) using a 4 shot EPI sequence described in the Chapter 4. The acquisition parameters were:

- TR/TE : 1500/30 ms.
- flip angle : 77 deg.
- acquisition matrix : 72×64.
- 2 stacks of 15 adjacent contiguous slices of thickness 1.5 mm. The first stack encompassed the hand portion of the primary motor cortex and the second one was located on the upper part of the cerebellum (Fig. 7.2).

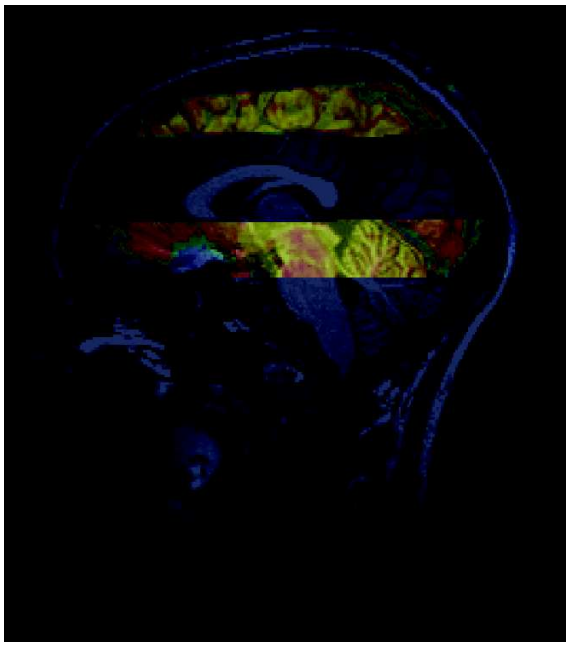

Figure 7.2: *Sagittal view of the acquired brain stacks for the functional acquisition. They encompass the primary motor cortex (M1) and superior part of the cerebellum. The stacks were separated with a processing step described later in Section 8.2.2.*

fMRI paradigm

Because of the high complexity of the motor command, we chose to study simple basic movements, namely repetitive **flexion** and repetitive **extension**, performed separately with either the **thumb** or the **fingers** or the **wrist** during a simple block-design fMRI protocol (Fig 7.3). These tasks were

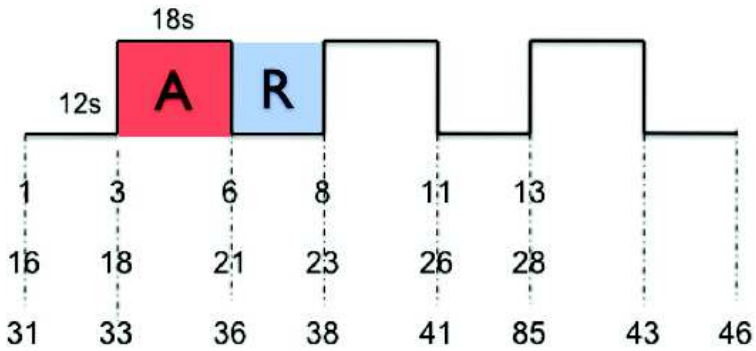

Figure 7.3: *Block fMRI paradigm. Alternating 12s-rest (R) and 18s-activation (A) blocks, repeated 9 times. The number of acquired volumes is represented, from 1 to 46.*

performed unilaterally with the dominant (right) and with the non-dominant (left) hand. The total number of basic movements equals to 12 (2 movement directions $\times$ 3 hand parts $\times$ 2 hands). For each basic movement, subjects were instructed to perform an alternation of a self-paced "movement and relax" during each activation block duration.

As described in Figure 6.4 for the patients, the movements were registered for each subject using a set of flexible sensors of flexion/extension (Flexpoint Sensor Systems, Inc., Utah) fixed on the four hands' joints of interest:

- the metacapophalangeal joint of the thumb.
- the carpometacarpal joint of the thumb.
- the metacapophalangeal joint of the middel finger (III)
- the carpometacarpal joint of the wrist

These sensors were fixed, on both hands, with Hypafix®, to insure a close contact between the sensors and the skin. Additionally, this fixation method exerts a restoring force that helps the hand joints to passively return to their initial position during the relaxing time following each

flexion or extension. Flexion and extension signals were recorded online at a frequency of 200 Hz using the LabView software package (National Instruments) and displayed on a screen in the acquisition room throughout the experiment, so that the tasks could be controlled in real-time by the experimenters.

In order not to mix all the twelve movements (2 directions $\times$ 3 hand parts $\times$ 2 hands), we presented the stimuli in four different functional runs for flexion or extension with the right hand or the left hand, respectively. The order was randomised among the subjects. Each run begins with the presentation of the type of stimuli (for instance: "Right hand flexion"), then 12s-rest and 18s-activation blocks alternated and this cycle was repeated 9 times (Fig 7.3).

Three activation blocks were performed respectively with each hand part, thumb, fingers and wrist, in a pseudorandom order to avoid possible motor preparation. Prior to their installation in the MR scanner, the subjects were trained to ensure that the tasks were properly executed. This short training period avoided any learning effect. We used the Presentation software (Neurobehavorial Systems®, Inc.) to display instructions back-projected using a video-projector (Epson 7250M, Epson Inc., Long Beach, CA®) on a translucent screen positioned at the rear of the magnet. Subjects viewed this screen through a mirror fixed on the head coil.

CHAPTER 8

Image data analysis

8.1 Introduction

We acquired a T_1-weighted image (*i.e. anatomical image*) and a set of T_2^*-weighted images (*i.e. functional images*) for each subject. To finely investigate the hand movement and the functional plasticity following the hand tendons transfer (see Chapter 1), the anatomical and the functional-series need to be processed. In particular, two kind of processing frameworks were necessary:

1. **Functional images pre-processing:** these are intra-subject pre-processing steps. The goal is to superimpose the statistical parametric maps on the corresponding anatomical image at individual level. For our fMRI images this involves a M1-CE separation step, a correction for the movement of the fMRI series and the registration on the corresponding anatomical image.

2. **Anatomical images processing:** it involves intra-subject processing steps, as the bias correction, the segmentation, the sulci extraction and the ROIs definition; and an inter-subject processing. This concerns the creation of a common reference system through inter-subject registration of anatomical images of the control group. Four different registration methods have been tested. Our assumption was that **an accurate inter-subject sulci registration should result in a precise alignment of corresponding functional regions and then improve the statistical significance of parametric maps**.

We were be able to investigate the quality of the registration pipelines relying on anatomical indices: grey matter overlap, Hausdorff distance and Jacobian of the deformation fields. Furthermore, the impact of the registration methods on the functional results was evaluated in terms of sensitivity of detection and accuracy of the localisation. Through a "Test-Retest" study the fMRI reliability were also investigated.

Through a statistical analysis of the activation maps three neuroscientific aspects, at a group level, were investigated:

1. The functional brain organisation of simple voluntary hand movement at a group level. In particular, handedness, the flexion/extension arrangement and the thumb/fingers/wrist localisation.

2. The reorganisation of the hand functions in the brain cortex in a patient who underwent a tendons transfer surgery.

3. The M1-cerebellum functional correlation.

The functional pre-processing is the same for each subject of the control groups ("Test" and "ReTest") as for the patient longitudinal study, at each acquisition time. The 1st level statistical analysis in made in the individual reference system (***Native Space***), whereas the 2nd level statistical analysis in performed in the common reference system (***Template Space***). This template was symmetrised, allowing the comparison between the dominant hand (operated hand in the patient) and the non-dominant hand. All the left-handed tasks were right/left flipped. Consequently, the ipsilateral activations are represented in the right hemisphere and the controlateral activations in the left one.

All the intra-subject pre-processing steps are valid also for the cerebellum analysis. For the inter-subject pre-processing, the *template* was created with the spatially unbiased atlas template of the cerebellum and brainstem (SUIT) [Diedrichsen 2006, Diedrichsen 2009] [1].

8.2 fMRI images pre-processing:

For the intra-subject pre-processing (*individual* study), the pipeline in Figure 8.1 was applied to each subject (control group subjects and patients), independently from the others. This allows to obtain the 1st-level statistical parametric maps, for each subject, in their own native space.

The different steps, forming this pipeline, are described in the next sections.

[1] http://www.icn.ucl.ac.uk/motorcontrol/imaging/suit.htm

Figure 8.1: *Intra-subject fMRI processing framework. The 1st-level (individual) statistical analysis was computed on the fMRI images registered between them and on the anatomical image (note: without smoothing).*

8.2.1 Slice timing

In multi-shot EPI slices of functional images are acquired throughout TR. Therefore the BOLD signal is sampled at different layers of the brain at different time points. But having the signal for the whole brain from the same time point is suitable. Time differences between different activated brain regions has been investigated suggesting a temporal order of activations [Bandettini 1995]. But this time shifting of the signal might be due to non-physiological effect, as the slice acquisition time difference [de Moortele 1997]. So a slice-timing correction is desirable. It consists, for each voxel, in interpolating, from its sampled time-course, the value at a specific reference time point. In that way we can make the assumption that every point in a given functional image is the actual signal from the same point in time.

Our fMRI volumes consist of 30 slices ($nslices$) acquired with a repetition time TR = 6 s. First the odd slices were acquired and then the evens. The 15th slice was chosen as a reference and the acquisition time TA was set to 5.8 s, computed as SPM documentation suggests: $TA = TR - (TR/nslices)$.

8.2.2 M1 and CE separation

The multi-slice multi-shot GRE-EPI we used for fMRI images acquisition consisted of acquiring 30 slices encompassing the primary motor cortex (M1) and the cerebellum. This means that these two regions are joined in the total reconstructed volume (Fig. 8.2). So, after slice-timing correction we need to separate this volume into two separate packs, formed by 15 slices each. A self-coded program uses the positions parameters taken from the Bruker's log files and automatically splits the volume into two packs, allowing to process separately M1 and the cerebellum. This is necessary in order to locate functional activations on the anatomical image. The result of this step is shown in

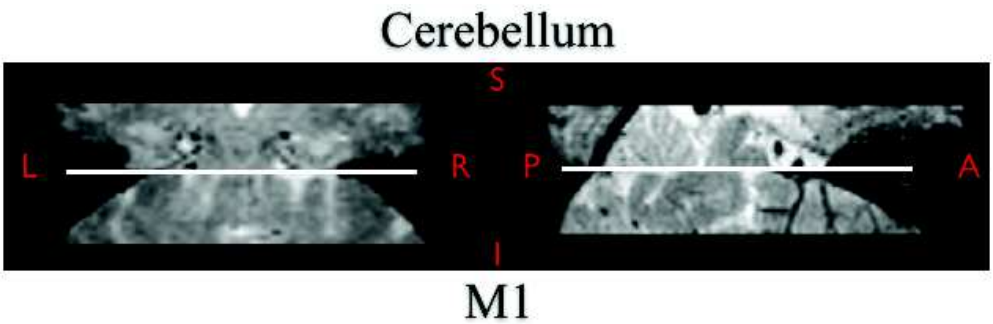

Figure 8.2: *EPI image. Coronal view (left) and sagittal view (right) of the total acquired fMRI volume. It consists of 30 slices encompassing the Cerebellum (upper part) and the primary motor cortex (M1, lower part).*

Figures 7.2, 8.3.

8.2.3 fMRI times-series registration

Subject head movement during the experiment is a major source of artifact in fMRI data. Changes in pixel intensity at the edges of the brain, upon even slight movement, can be greater than the BOLD activation response. It is common therefore in fMRI data analysis to perform some corrections to reduce this effect [Friston 1996].

In high-resolution imaging, even with cooperative subjects, head motion is a particularly limitative problem. In functional MRI, motion correlated to the stimulus can produce false activations [Hajnal 1994]; this is particularly problematic when motion is part of the study, such as movement tasks.

We registered the fMRI time-series using a rigid intra-subject registration. A least squares approach was used to compute the 6 parameters (3 translation parameters and 3 rotation) (see Section 5.3.1.1). Motion correction uses variance to check if images have a good match (smaller variance means better match).

8.2.4 fMRI-to-anatomical images registration

The T1-weighted image (*i.e.* anatomical image) and the T2*-weighted images series, for each subject, were registered. Our approach consists to: 1) compute the registration parameters between

the average fMRI image and the anatomical image; 2) to apply the registration parameters to the other images belonging the fMRI serie. To find the transformation parameters, Mutual Information similarity metric has been used. In Figure 8.3 an example of fMRI average image, for M1 (upper row) and cerebellum (lower row), registered and superimposed to the anatomical image is represented.

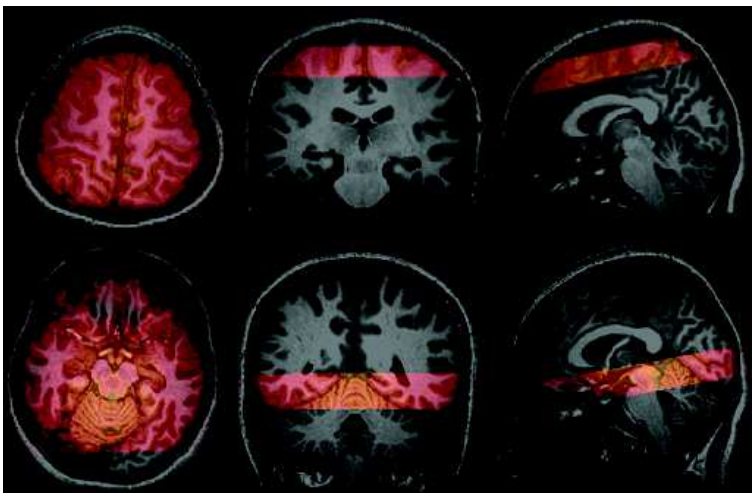

Figure 8.3: *Example of average fMRI image, computed from the functional series corrected for the head motion, registered and superimposed on the anatomical image. This is done for the fMRI images encompassing the primary motor cortex M1 (upper row) and the cerebellum (lower row).*

8.2.5 Spatial smoothing

Any reduction in the random noise will improve the ability of a statistical technique to detect true activations. Spatially smoothing each image improves the signal-to-noise ratio (SNR), but reduces the resolution. Thus a balance must be found between improving the SNR and maintaining the resolution benefits of the functional image. There is no straightforward answer to the question of which is the best smoothing width to use in the analysis of the data set. If we state that the best kernel is the one which matches the size of the activated region, a filter of FWHM= 3 mm (M1 cortex thickness) would be the optimum for regions of this extent, but the signal from smaller regions is not detected. A wider filter will reduce the noise to a greater extent, but will dilute the signal. For the group study, we applied to the contrast images, outcome from the 1st level

(individual) statistical analysis, a smooth of FWHM=1.5 mm and 3 mm. This allow us to investigate the impact of smoothness at the group level looking for the best compromise (see Section 10.3).

8.3 Anatomical images processing

Once an anatomical image is acquired, as described in Section 7.1, a series of processes need to be applied. Our goal here is to use the anatomical images in their own space (***Native space***) of the control group to define a ***Template space*** in which each subject will be moved. This involves a processing pipeline for each method used.

Individual anatomical images were firstly segmented and debiased using "Unified Segmentation" approach as implemented in SPM8[2] [Ashburner 2005] in considering two brain tissues (GM and WM) and four non brain tissues (CSF, large veins, scalp and meningia). We also used the BrainVISA[3] segmentation pipeline to automatically extract and identify the cortical sulci and, in particular, the CS in each individual brain. Then, the volumes were registered between subjects following four different strategies and software using their own default parameters values as briefly described hereafter: 1/ with mean square difference cost function on the MNI template using SPM8, 2/ DARTEL, 3/ DISCO+DARTEL (DiDa) and 4/ Diffeomorphic Demons (DDe). Each strategy provides a subject-related deformation field applied to functional data.

These pipelines need some common process as the **Segmentation** (SPM8, DARTEL and DiDa) and the **Bias correction** (all the methods), and other specific method as the **Sulci extraction** (DiDa) and the **ROIs definition** (DDe). So before the description of the registration pipelines we describe here these steps.

8.3.1 Bias correction

First, the non-uniform intensity bias, usually present in the T_1-weighted images, needs to be corrected (**Bias correction**). MR images are usually corrupted by a smooth, spatially varying artifact that modulates the intensity of the image (bias). Many medical image analysis methods, such as segmentation and registration, are highly sensitive to the spurious variations of image intensities, although this is not usually a problem for visual inspection. Correcting the bias should result in

[2] ('New Segment' SPM function)
[3] http://www.brainvisa.info

a more uniform intensities for each brain tissue. For a review of bias correction methods refer to [Vovk 2007]. Bias correction is performed by the BrainVISA T1-pipeline for the sulci extraction and by the "*Unified Segmentation*" framework for the registration pipelines (Section 8.3.5) and segmentation.

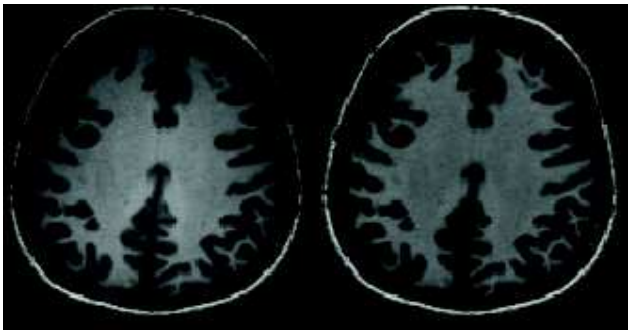

Figure 8.4: *Axial view of a single subject anatomical image. On the right side, the bias corrected image. The non-uniform intensity is slightly visible in the original image, on the left.*

8.3.2 Segmentation

Segmentation defines the probability, for a given voxel, to represent a particular type of tissue. We have adopted the "*Unified segmentation*" approach performed by Ashburner and Friston and implemented in SPM8 [Ashburner 2005] to obtain the grey matter (GM), white matter (WM) and cerebrospinal-fluid (CSF). It combines three components: registration (to the probabilistic tissue maps); segmentation; and the bias correction, in the same framework. Despite the higher computational cost (compared to the 3 components applied separately), this framework ensures a more robust tissue segmentation.

8.3.3 Sulci extraction

The process of sulci extraction begins with segmentation and automatic identification of the sulci with the method implemented in the BrainVISA [Mangin 2004b]. This method extracts the most elementary folds form the anatomical images [Mangin 1995] through several steps ([Mangin 2004b],Fig. 1). Sulci are represented as elementary shapes linked according to their topographical organisation. This is represented by a graph containing different attributes attached

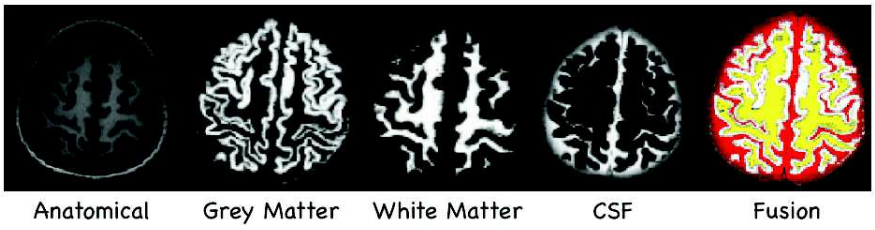

Figure 8.5: *Example of segmentation of an anatomical image belonging our data court. The "Unified Segmentation" framework [Ashburner 2005] was used.*

to the nodes, as the fold size or maximal depth, and to the links, as the length and average direction of the junction. All of the cortical folds can be represented as sets of voxels that are then labelled in accordance with a schedule composed of 60 different labels per hemisphere.

8.3.4 ROI definition

After a skull-stripping step [4] we manually defined individual **ROIs** surrounding the primary somatosensory cortical area and encompassing the hand-knob structure on each individual structural image registered in the MNI space (Fig. 8.6). We computed a common ROI as the union of all individual ROIs followed by morphological operations of closing and dilatation. This procedure was repeated for each hemisphere and resulted in two ROIs per subject (one per hemisphere). Using individual (inverse) transformation parameters, the two common ROIs were then put back in each individual referential.

8.3.5 Registration methods: SPM8, DARTEL, DiDa, DDeR1, DDeR2

As previously said, the group study needs a common reference system in which all the images will be registered. Each registration method finds the **deformation fields**, or the **transformation parameters**, able to map the images from the original space **Native space** to the common space **Template space** previously introduced (Chapter 8.3). We tested 4 different methods: SPM8-registration, DARTEL, DiDa, (DISCO+DARTEL) and Demon. DARTEL and DiDa define a custom template space, adapted to the population, SPM8 is based on the MNI template and Demon registers all the images (**Moving images**) on an image chosen (**Fixed image**) among the population

[4] We used the BrainVISA structural pipeline. It allows to separate brain tissues from non-brain tissues.

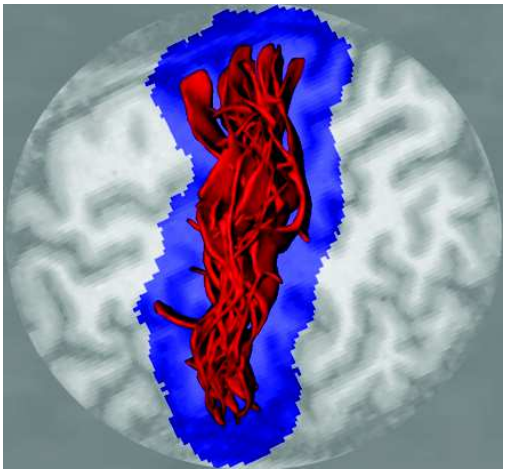

Figure 8.6: *Portion of the left hemisphere in which the extracted central sulci (red) of each subject is superimposed after a rigid transformation on the MNI space. The volumetric common ROI (blue) is defined encompassing all the sulci, for both hemispheres.*

under study. These methods are introduced in section 5.5. Here we want to describe the pipeline of each method and the steps necessary to obtain the deformation fields, or the registration parameters, allowing to move from the native space to the template space, for each method.

8.3.5.1 SPM8

The SPM8 algorithm allows to map the anatomical images from each relative native space to the template space (*e.g.* MNI) *via* the *Unified Segmentation* framework (Fig. 8.7).

The template space is defined by the MNI reference system, in which the TPMs (Tissue Probabilistic Maps) are defined. *Unified Segmentation* combines segmentation (*i.e.* classification), bias correction and spatial normalisation in a generative model. Being the segmentation dependent on the registration, and *vice-versa*, Ashburner and Friston [Ashburner 2005] enclose these processes in a single framework. The TPMs are deformed by a linear combination of a thousand cosine transform bases, and Gaussian distributions are used to model the intensity of each tissue class.

Each anatomical image has been then processed with this method obtaining a bias corrected image, the segmented white matter (WM), gray matter (GM) and cerebrospinal fluid (CSF) tissue maps, and the parameters for non-rigid and rigid registration into the template space.

As we will see in the next sections (Sections 8.3.5.2, 8.3.5.3, 8.3.5.4), the segmented images

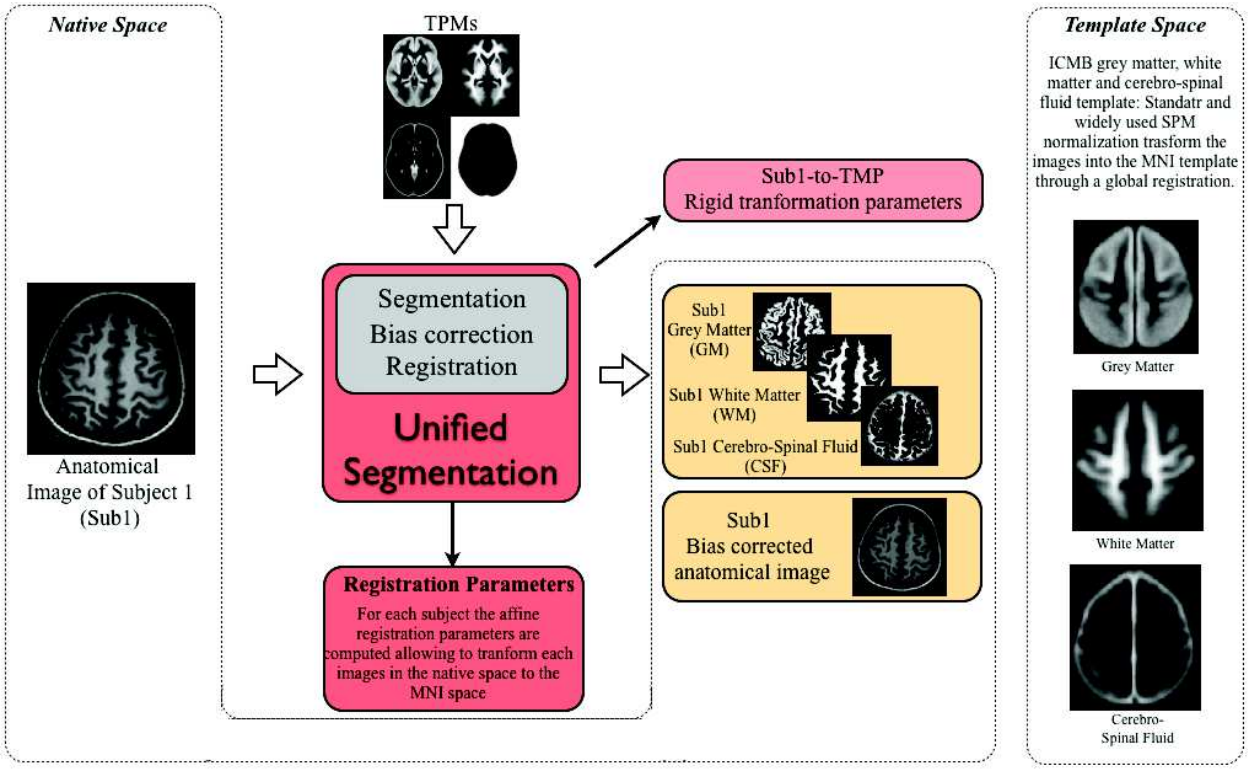

Figure 8.7: *Unified Segmentation framework. It combines a segmentation (i.e. classification) step with bias correction and registration. Based on the tissues priori maps (TPM), it consists of a single generative model allowing to segment an anatomical image into grey matter (GM), white matter (WM), cerebro-spinal fluid (CSF) and others tissues. It also permits to obtain a bias corrected anatomical image and the transformation parameters that register the original anatomical image into the MNI space (i.e. Template).*

were used also for the computation of the deformation fields with DARTEL and DiDa. The unbiased images and the affine transformation parameters were used for the initialisation of DDe.

8.3.5.2 DARTEL

DARTEL's pipeline is described in Figure 8.8. Anatomical images (T1-weighted images) were segmented into grey matter (GM) and white matter (WM) in the native space using the *Unified Segmentation* framework, previously described (Fig. 8.7). The segmented tissues have been then rigidly

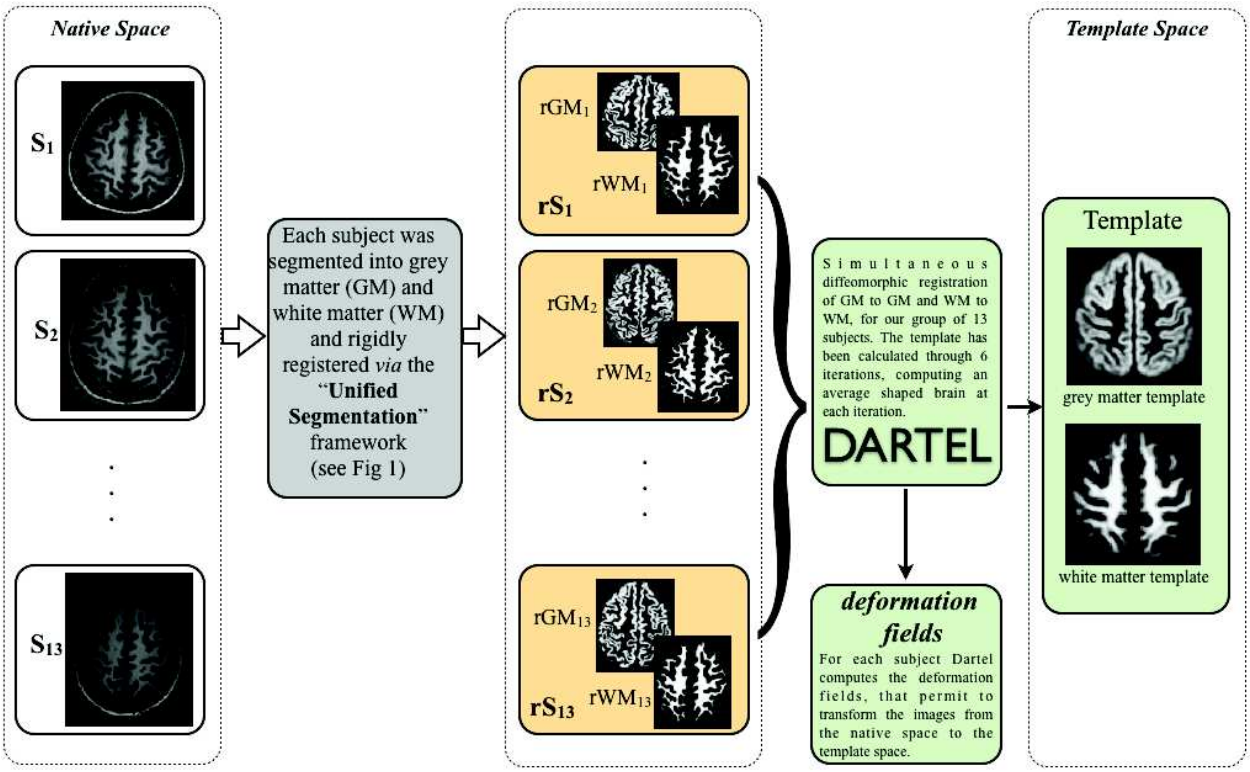

Figure 8.8: *DARTEL registration pipeline [Ashburner 2007]. The "Unified Segmentation" framework was used to segment each subject into grey matter (GM) and white matter (WM) and to rigidly register these tissues, obtaining rGM and rWM. DARTEL simultaneously registers the grey matter and white matter maps through 6 iterations to obtain an average template. This template represents the common reference system for the DARTEL group study. The deformation fields allow to map each individual from the* ***native space*** *to the* ***template space****.*

registered to the MNI template (DARTEL tools -> "Initial import" function) to make the computations easier for the non-linear registration. These images are the inputs for the DARTEL algorithm that simultaneously registers all the subjects (13) in several iteration (6) obtaining a final template for the grey matter and the white matter. These define the template space. The registration parameters are stored like a deformation field image, for each subject.

8.3.5.3 DiDa (DISCO+DARTEL)

DiDa is a combination of DARTEL and DISCO [Auzias 2011] (Fig. 8.9) and introduces a local characteristic to the registration. The anatomical images are segmented into WM/GM and the individual sulci are segmented and modelled as weighted sets of points. The DIffeomorphic Sulcal-based COrtical (DISCO) registration explicitly forces the alignment of sulci in an iterative approach. An empirical template is defined as the union of the entire set of sulcal points through the group of subjects. For each sulcal label, the corresponding sulcal landmark in the template corresponds to the union of all points associated to this label for each subject. Diffeomorphic transformation of each individual data onto the empirical template is then proceeded in the general framework of the Large Deformation Diffeomorphic Metric Mapping theory. Improved mask overlap and reduction of sulcal dispersion can be reached through the sequential combination of DISCO and DARTEL (DiDa), with DARTEL being initialized using DISCOs outcome.

8.3.5.4 DDe (Demon)

Demon [Vercauteren 2009] is representative for the local registration methods. In fact it is ROI-based, that is the regions of interest of each subject (*i.e.* the anatomical regions encompassing the central sulcus) are registered. The pipeline is shown in Figure 8.10.

The bias correction was applied to all anatomical images followed by skull-stripping using the "New Segment" tool of SPM. The left and right ROIs were defined and then all the images were affine registered to initialise Demon. The template space was defined by a subject chosen among the 13 belonging to the control group. Demon algorithm, implemented in MedINRIA software[5], was applied twice, with two different images chosen as a reference (DDe-R1, DDe-R2). As a result, we obtained two sets of deformation fields, one for the right and one for the left hemispheres, for

[5] http://www-sop.inria.fr/asclepios/software/MedINRIA/

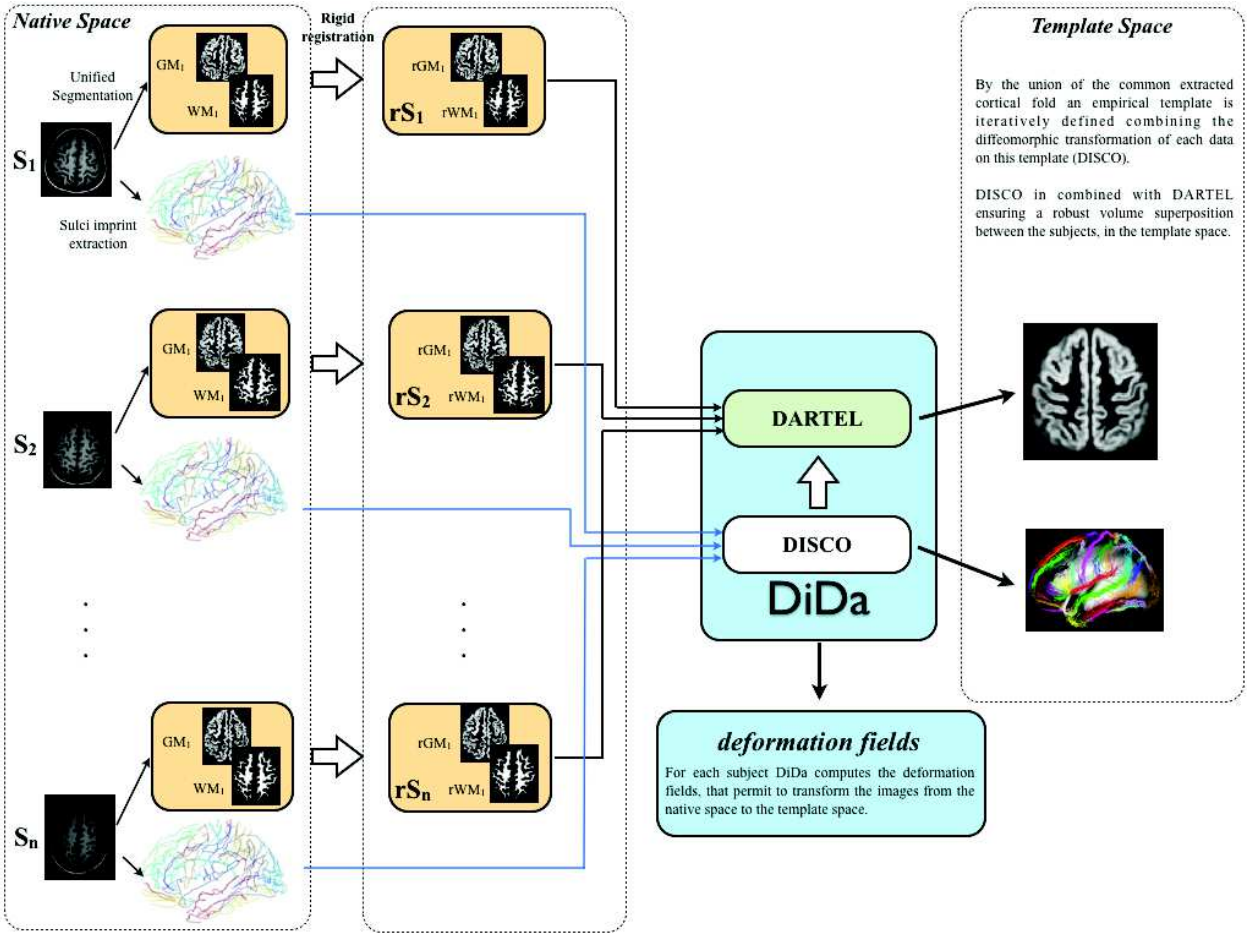

Figure 8.9: *DiDa registration pipeline. DiDa is the combination of DARTEL and DISCO [Auzias 2011]. For each subject, the DARTEL pipeline is applied (Fig 8.8). BrainVISA was used to automatically extract the central sulci that represents local landmarks, forced to be registered by DISCO. The deformation fields allow to map each individual from the* ***native space*** *to the* ***template space****.*

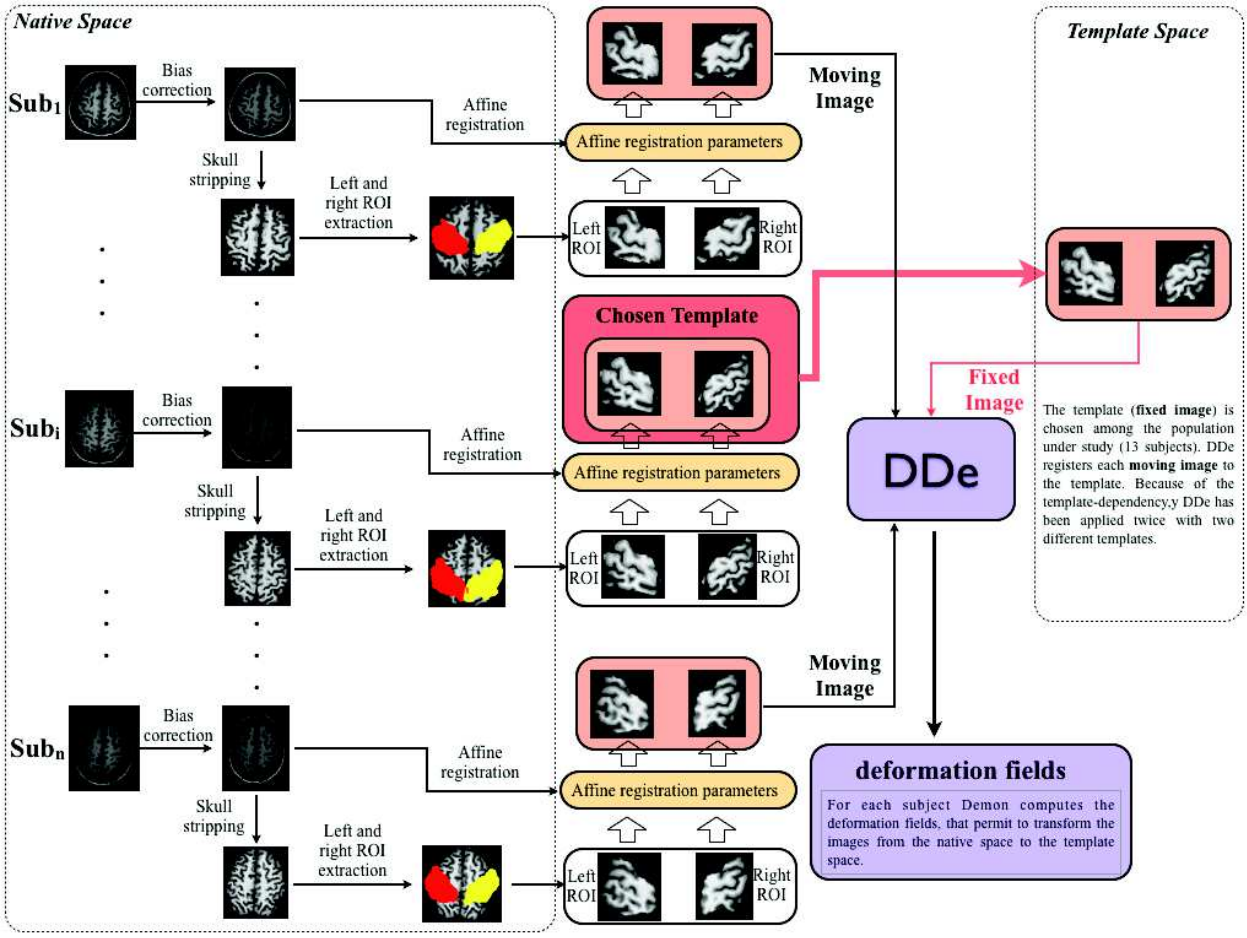

Figure 8.10: *Demon [Vercauteren 2009] registration pipeline. Each anatomical image was unbiased and affine-registered using the "Unified Segmentation". The unbiased images were skull-stripped and the left and right ROIs extracted and affine-registered. One subject was selected as reference (**template**) representing the **template** space. The ROIs of the other subjects were registered to the template using Demon and obtaining the deformation fields to map each individual from the **native space** to the **template space**.*

the two references.

8.3.6 DARTEL symmetrical template definition

In order to investigate the hand dominance, that is to compare the right and the left hand, the data need to be analysed in the same symmetrical reference system. So, in addition to define a template, as we have seen before, we have symmetrised it (Fig. 8.11). This has been done, for DARTEL, as

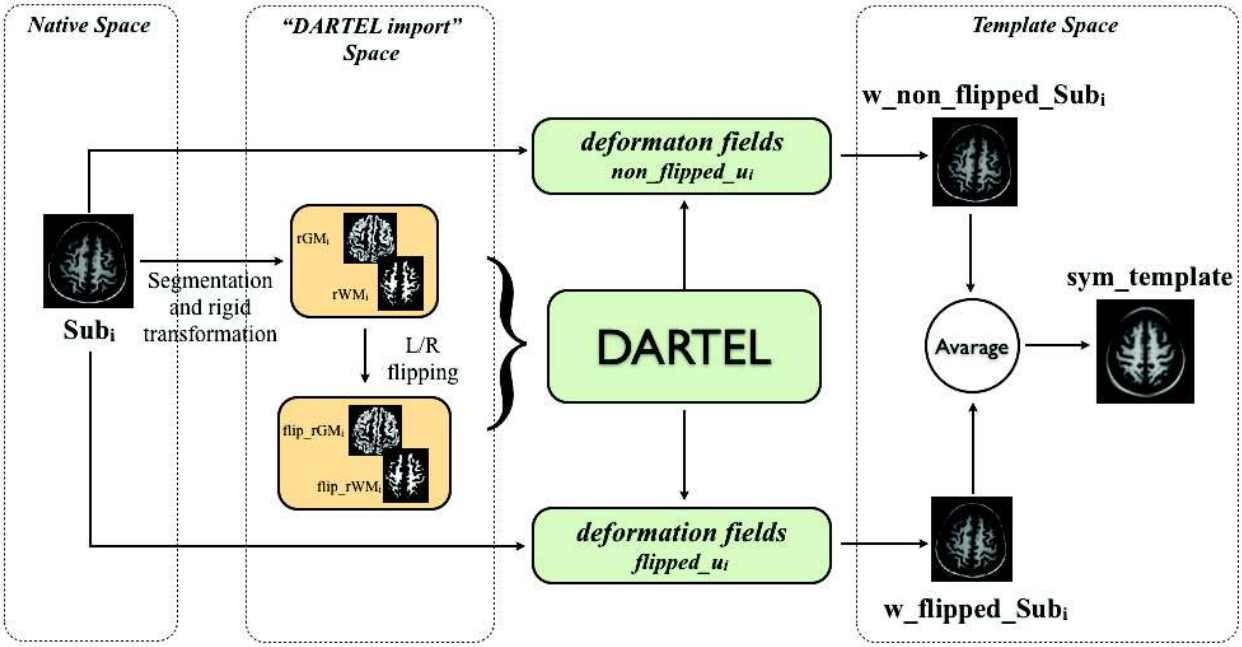

Figure 8.11: *DARTEL symmetrisation pipeline. DARTEL was applied to segmented images and flipped segmented images in order to obtain the symmetric template.*

follows: the anatomical images were debiased and segmented into GM and WM using the "*Unified Segmentation*" framework ("New Segment" SPM function). Then, these were affine registered[6] and the left and right side flipped (flipping along x direction). The flipped and non-flipped segmented images are the inputs for DARTEL that computes the deformation fields for the non-flipped images, *non_flipped_*u_i and for the flipped image, *flipped_*u_i. These deformation fields were applied then to the anatomical images, obtaining the *w_non_flipped_Sub*$_i$ and the *w_flipped_Sub*$_i$ anatomical

[6]DARTEL tools -> "Initial Import" function

images, in the template space. The average of the deformed images is our symmetrical template.

8.3.7 Registration pipelines for the cerebellum: SUIT

The individual functional analysis was performed on the cerebellar data as for the motor cortex data. SUIT toolbox[7], a spatially unbiased atlas template of the cerebellum and brainstem, was used to define a cerebellum template. The procedure that we have adopted to define our symmetrical templte is shown in Figure 8.12.

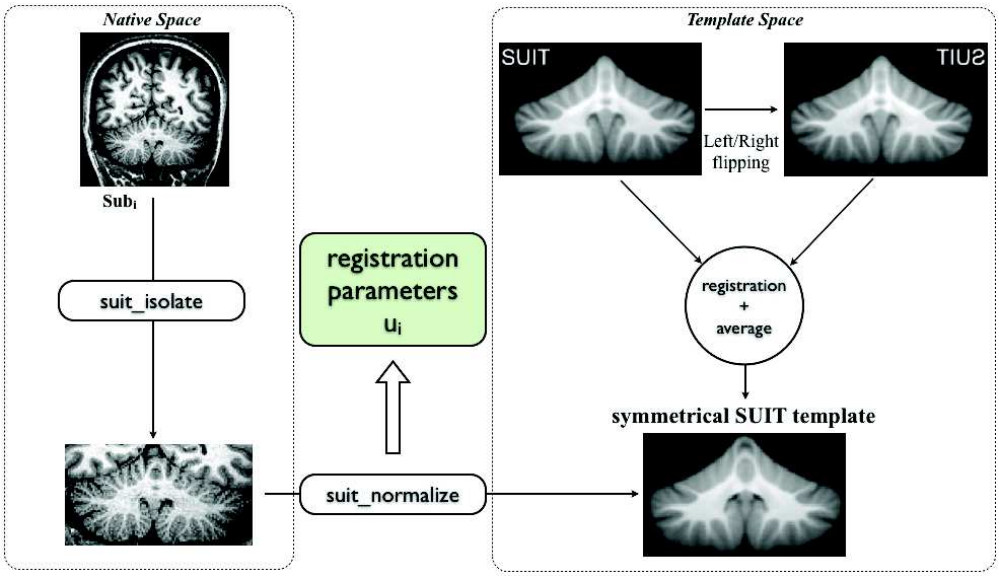

Figure 8.12: *The template provided by SUIT (http://www.icn.ucl.ac.uk/motorcontrol/imaging/suit.htm) was left/right flipped and affine registered ("Co-registration" SPM function) on the non-flipped SUIT template. The average of the non-flipped and flipped is our anatomical template for the cerebellum. Afterwards the cerebellum, of each subject, was separated from the rest of the brain using the suit_isolate function. Then the suit_normalize option registered each anatomical image to our template giving the registration parameters.*

The template provided by SUIT was left/right flipped and affine registered ("Co-registration" SPM function) on the non-flipped SUIT template. The average of the non-flipped and flipped is our anatomical template for the cerebellum.

[7] http://www.icn.ucl.ac.uk/motorcontrol/imaging/suit.htm

Afterwards we separate the cerebellum, of each subject, from the rest of the brain using the *suit_isolate* function. Then each cerebellum was registered to our template by using the *suit_normalize* option. These step gives the registration parameters.

8.3.8 Mapping from the native space to the template space

Once the registration methods were applied, the images for the statistical analysis at a group level need to be moved from *Native space* to the *Template space*, as summarised in Figure 8.13.

The 1st level of the statistical analysis allows to obtain a contrast image "**con**" relative to each tasks, extension/flexion of thumb, fingers and wrist for both hands. Thus, in total we get 12 contrast images *per* subject. Each contrast was masked to obtain the left and right contrast ROI, "**L_con**" and "**R_con**". These ROIs were then registered , "**Registration**", using the deformation fields, transformation parameters, obtained with each method (SPM8, DARTEL, DiDa and DDe-R1/DDe-R2[8]) (Fig. 8.13a). This pipeline permits to have each contrast of each subject in the *template* space relatives to each registration method. Finally, after a spatial smoothing of 1.5 and 3 mm (FWHM), the 2nd level statistical analysis were performed.

The grey matter segmented images, for each subject in the control group, were masked into left and right GM ROI, "**L_GM**" and "**R_GM**". Then they were registered obtaining the deformed images "**w_L_GM**" and "**w_R_GM**" (Fig. 8.13b).

The automatically extracted central sulci (CSs), for each subject in the control group, were masked into left and right CS ROI, "**L_CS**" and "**R_CS**". Then they were registered obtaining the deformed sulci "**w_L_CS**" and "**w_R_CS**"(Fig. 8.13c).

Cerebellum

For the cerebellum, we did not perform a ROI-based analysis, as we did for M1. The functional group analysis (2nd level statistical analysis) has be done registering the individual contrast images with SUIT after a smoothing of FWHM=1.5mm.

[8]For DDe we applied, to the contrast ROIs, the affine registration parameters used to initialize Demon.

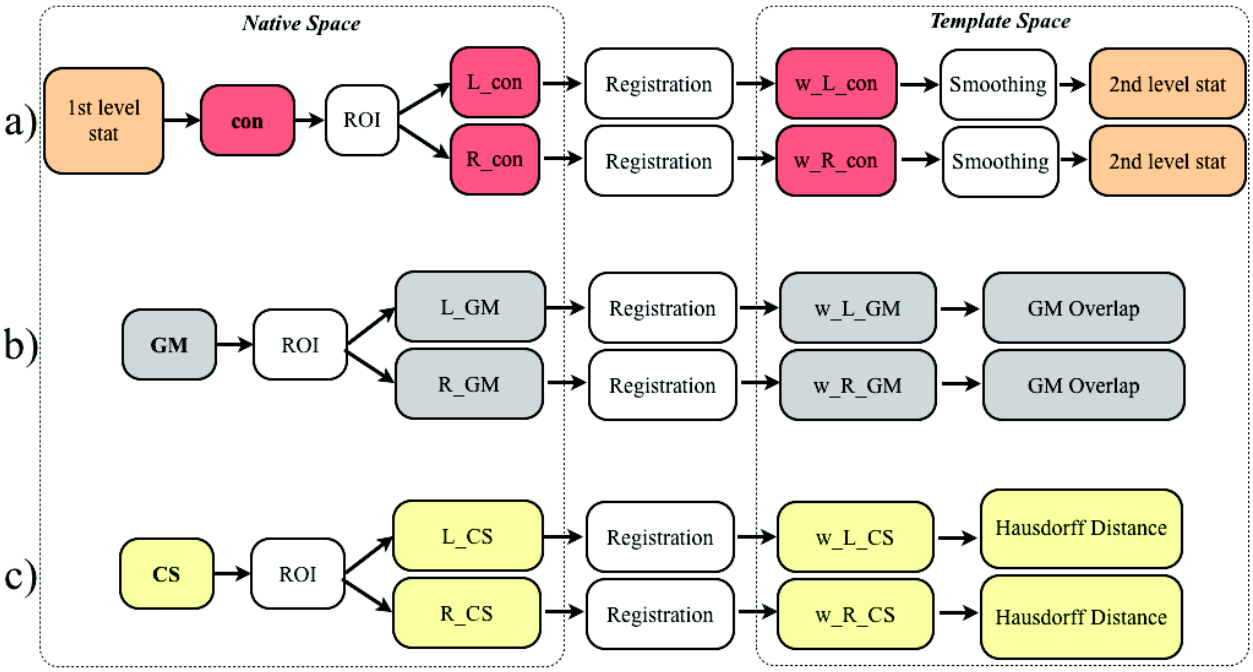

Figure 8.13: *Registration pipeline for the contrast images (a), the grey matter images (b) and the central sulci automatically extracted (c). The contrast images are the result of the 1st level statistical analysis, at individual level. To evaluate the registration methods a ROI-based analysis, for the anatomical and functional indices, were used.The ROIs were extracted from the contrast, for the left and right hemispheres (L_con,R_con; L_GM,R_GM; L_CS,R_CS). Then, they were registered with each method we used (SPM8-type, DARTEL, DiDa and DDe) (w_L_con,w_R_con; w_L_GM,w_R_GM; w_L_CS,w_R_CS). Finally, the 2nd level statistical analysis were performed on the non-smoothed contrasts and on the contrast with 1.5mm of smoothing and 3mm of smoothing (a). The overlap (b) and the Hausdorff distance (c) were computed on the registered GM ROIs and on the registered sulci, respectively.*

8.4 Registration methods evaluation

Which is the best registration method we can use for our applications? Several studies exploit custom registration methods and consequently the comparison between them is not simple.

Knowing the quality of the registration process in medical application is crucial. An erroneous interpretation of results could risk the patience's healthy. The validation process is usually performed by imaging physical phantoms or a volunteer and evaluating both robustness and accuracy. Maintz and Viergever [Maintz 1998] list different aspects of the performance of the registration algorithms as precision, accuracy, robustness/stability, reliability, resource requirement, algorithm complexity, assumption verification, and clinical use. Every work using the registration process encountered the problem to describe the quality of the algorithm and the success is estimated usually by visual inspection, by comparison with a gold standard (defined in some way) or by means of some self-consistency measure [Crum 2006, Gholipour 2007, Klein 2009].

8.4.1 Anatomical measurement

For each method, we applied the computed deformation field to the individual grey matter images and to the individual structural images. We computed for each pair of subjects (S^1, S^2): the **fuzzy Jaccard overlap** measure JO of grey-matter probability images [Auzias 2011, Crum 2006]; the **Hausdorff distance** between the CS; and the **Jacobian** of the deformation fields.

8.4.1.1 Grey matter overlap

Theoretically a perfect registration between two images leads up to a perfect alignment between them giving a 100% of superposition (overlap). That is a perfect correspondence between one point in one image with the homologous point in the other one. The two most common measures of region overlap are the Dice Similarity Coefficient (DSC) and the Jaccard overlap (JO) (or the Tannimoto Coefficient)

$$JO = \frac{N(A \cap B)}{N(A \cup B)} \qquad DSC = \frac{2N(A \cap B)}{N(A) + N(B)} \tag{8.1}$$

where $N(A)$ is the number of voxels in the image A and N(B) the number of voxels in the image B.A and B could be any kind of images. Here the grey matter (GM) segmented maps are

consideredand JO (eq. 8.1) becomes

$$JO(S^1, S^2) = \frac{\sum_{voxels,i} \min(GM_i^1, GM_i^2)}{\sum_{voxels,i} \max(GM_i^1, GM_i^2)} \tag{8.2}$$

where GM^1 and GM^2 are the grey matter maps for S^1 and S^2 respectively in the common ROI, defined as in Section 8.3.4 and deformed with each registration method used (See section 8.3.8).

Eq. 8.2 has been used in this work to evaluate the quality of the registration methods applied.

8.4.1.2 Hausdorff distance

In addition to the grey matter overlap, we can measure the distance between sulci of different subjects. The brain sulci are segmented and represented as a set of points. In Fig. 8.14 an example of sulci automatically extracted using BrainVISA[9].

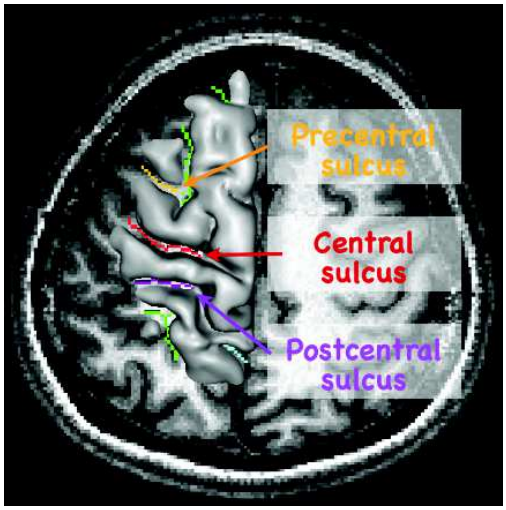

Figure 8.14: *Single subject axial view of the sulci automatically extracted by BrainVISA. The colored lines represent the sulci set of points.*

For each image of the population under study the sulci are extracted obtaining N sets of points, each of them representing a brain sulcus. In order to evaluate the registration algorithm, the distance between a pair of sulci is computed, iteratively among all the subjects. This is called **Hausdorff distance,** H. The H between two sets of points determines how close in space two point sets are. It is defined as follow:

[9] http://brainvisa.info

$$H(S^1, S^2) = \max(\max_i \min_j(||CS_i^1 - CS_j^2||), \max_j \min_i(||CS_j^1 - CS_i^2||))$$

where $[(CS_i^1)_{1 \leq i \leq n_1}$ (resp. $(CS_j^2)_{1 \leq j \leq n_2})]$ correspond to the voxels forming the central sulcus of the first (resp. second) subject. This measure is an indicator of the spatial dispersion of central sulcus.

8.4.1.3 Jacobian of the deformation fields

The deformation field produced is related the quality of the registration method [Leow 2007]. Indeed, two registration methods can achieve similar GM overlaps but with a different amount of dilatations and compressions. Unnecessary tissue stretching or compression should be avoided. A method that generates few deformation while providing an accurate alignment is always preferable. The Jacobian of the deformation field was computed to assess the regularity of the field and the amount of dilatation or compression for each voxel of the common ROI for the three diffeomorphic methods and for each subject. The Jacobian computation was straightforward for DARTEL and DDe methods. As DiDa is a sequential combination of DISCO and DARTEL we computed the following Jacobian measure for each voxel v,

$$Jacobian^{DI+DA}(v) = Jacobian^{DISCO}(v) \times Jacobian^{DARTEL}(v)$$

The spatial distribution of high compression and high dilatation rates in the ROI and among subjects illustrates the regularity of the field *a posteriori* and how the registration process has deformed the shape of anatomical structures.

8.4.2 Impact of the registration methods on the functional results

To qualitatively evaluate the registration methods we identify the main activated clusters derived from group analysis for extension and flexion respectively ($p \leq 0.0001$, voxel level uncorrected with no thresholding on cluster size), superimposed on the corresponding mean structural image computed for each method and restricted to the common ROI.

For the quantitative evaluation we compare the histograms of the T-value maps ($t \geq 4.0$, $p \leq 0.0001$ voxel level uncorrected) for extension and flexion respectively for each task and each hemisphere.

We further tested whether the four methods had significant effect on activation detectability whatever the task. We computed using Statistica 8 (StatSoft©), a 2-way (method, hemisphere) repeated-measure ANOVA with the total number of detected voxels as measures. A post-hoc Tukey-Kramer test was further computed to assess which methods performed significantly better in terms of activation detectability.

To asses the reproducibility of the our fMRI results we tested for an additional factor, the time effect,in the statistical analysis of the control groups (see Section 9.1.2).

For localization, we superposed the significantly activated voxels onto the corresponding mean structural image. The major part of activation should be precisely located in M1.

CHAPTER 9

Statistical analysis of hand movements

The registration process allows to accurately analyse the data in a common reference system. The anatomical differences among the subjects were minimised and tin consequence functional areas overlap was maximised. Three kinds of neuroscientific questions arise: **which is the organisation of the hand movements at a healthy population?**, **how cortical maps are reorganised in a patient after hand surgery? Are these maps different across time from healthy subjects?**

9.1 Statistical analysis for the control group

The central control of the movement could be different between the dominant and non-dominant hand. Moreover, it is known that pure flexion or pure extension do not exist because flexor and extensor muscles always cooperate. Some studies, on monkeys [Kakei 2001] and humans [Z'Graggen 2009], have shown that the movement direction is coded in the brain cortex. Finally, the somatotopy of the hand is still debated [Meier 2008].

The activation maps were evaluated using the symmetrical DARTEL template (see Sections 8.3.6 and 8.3.8). Indeed, comparing the registration methods (Section 10), DiDa and DARTEL give the best performances. Being DiDa not yet available for the neuroscientific community, DARTEL has been used to analyse the functional results. For the cerebellum (Ce) the images registered with SUIT have been analysed.

The contrasts concerning the left hand were left/right-flipped in order to be able to compare the left hand tasks with the right hand tasks. As a consequence, the *controlateral* activations will be represented in the left hemisphere and the *ipsilateral* activations in the right hemisphere (Chapter 11).

9.1.1 Effects of hand dominance, movement direction and hand segment in the control group

For the statistical analysis among all the tasks, we computed a 3-way ANOVA random effect analysis, on the control group. The three factors were:

1. The handedness with two levels: right hand (dominant) and left hand (non-dominant).
2. The movement direction with two levels: flexion and extension.
3. The hand parts with three levels: thumb, fingers and wrist.

The statistical significance of activation maps related to the movement of **left** and **right hand**, separately, has been tested against null hypothesis with Student t-test thresholded at a corrected p value < 0.01 (M1), < 0.05 (Ce) with an extent $k > 20$ voxels, as for the **extension** and **flexion** movement. For the activation maps related to **hand segments (thumb, fingers and wrist)**, the effects were tested with a Student t-test at a threshold of non-corrected p value < 0.0001 (M1), < 0.001 (Ce) with an extent $k > 20$ voxels.

The common activated regions (***conjunction***) and a ***predominance*** of one hand in comparison with the other (***left hand vs right hand***) were investigated with a Student t-test thresholded at a non-corrected p value < 0.001 and an extent higher than 20 voxels (M1) and corrected p value < 0.05 (Ce).

The *conjunctions* and the *predominance* were investigated also for the extension/flexion movements and for the hand segments. The *conjunctions* were analysed with a Student t-test thresholded at a non-corrected p value < 0.0001 (M1) and corrected p value< 0.05 (Ce) with an extent higher than 20 voxels, for **extension/flexion** and **hand segments**. The predominance with a Student t-test thresholded at a non-corrected p value < 0.0001 (M1) and corrected p value< 0.05 (Ce) with an extent higher than 20 voxels for **movement direction** (*extension vs flexion* or *flexion vs extension*) and non-corrected p value < 0.001 (M1) and non-corrected p value < 0.0001 (Ce) with an extent higher than 20 voxels for the **hand segments**.

9.1.2 fMRI reliability: Test-ReTest study

To investigate the reliability of our fMRI results we acquired for 9 healthy subjects of the control group, a second session one year later. A 4-way ANOVA was computed for the activations in the

primary motor cortex (M1). The four considered factors were: handedness, movement direction, hand segments and Group (Test or ReTest). The last factor represents our fMRI reproducibility index. Equal variances were considered for all factors but unequal for the Group factor. The reliability ("Test"-"ReTest" factor) were tested with a Fischer's test at a threshold of $p_{FWE} < 0.05$ and voxel extent $k > 20$ voxels.

9.2 Clinical investigation

The functional analysis of the control group gives a reference to study the functional brain plasticity of the subject who underwent a tendons transfer surgery.

Based on our data, two analysis were performed for the patient activation maps. A longitudinal study, for the investigation of the functional evolution, and a comparison analysis between the patient and control group results.

9.2.1 Longitudinal study

A 3-way ANOVA random effect analysis was computed, where the factors are:

1. time, with five levels: M0, M1, M3, M6 and M12.
2. hand, with two levels: right (operated) and left (non-operated) hand.
3. movement direction, with two levels: extension and flexion.

Since one movement direction is restored by surgery, we also studied the "hands by movements" interaction and the "hands by movements by time" interaction.

9.2.2 Patient vs Control group

To compare the patient with the control group results, the activation maps corresponding to the restored movement were displayed on the same anatomical template and visually compared with the activation maps of the control group.

Part IV

Results

CHAPTER 10

Registration methods evaluation

The common ROI considered for the analysis is superposed in red on one individual structural image in Figure 10.1. Figure 10.1 shows for a given subject (upper row) the deformed ROI after application of each registration method. The mean structural, restricted to the common ROI, obtained after registration of the 13 subjects using each method is displayed (lower row). The blurring obtained using SPM8 clearly indicates a poor realignment. Non-linear deformations introduced in SPM8 are clearly too limited to reach a satisfying registration of all brains for the considered population. The mean deformed ROI is sharper for the three diffeomorphic methods. For DDe, the mean shape is very close to the chosen reference image (not shown). Figure 10.2 displays the set of 13 deformed central sulci after registration. It illustrates how the four methods deform locally the individual left and right CS. Note the persistent large dispersion of sulci after realignment with SPM8 and DDe. As expected, we note the strong influence of the reference used with DDe (see DDE-R1 vs DDe-R2).

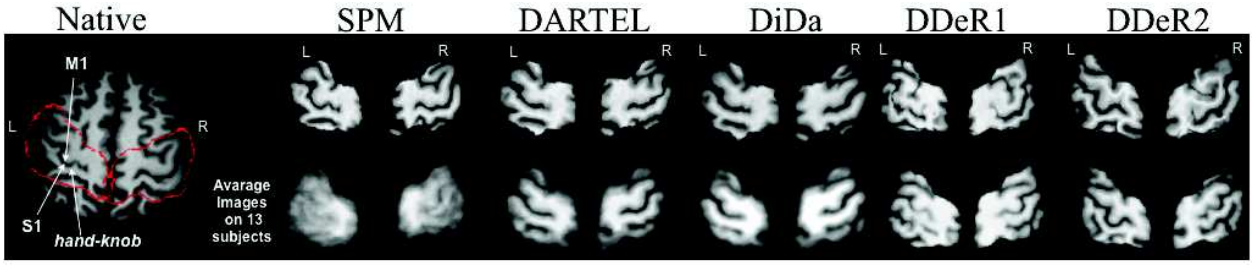

Figure 10.1: *Hand-knob region. Left: The common ROI surrounding the hand-knob is delineated by the red contour on each hemisphere of one subject. The top row shows for this subject, the ROI for each hemisphere after deformation with each registration method. On the bottom row: the mean image restricted to the common ROI after registration of the 13 subjects for each hemisphere and each method. L = left, R = right.*

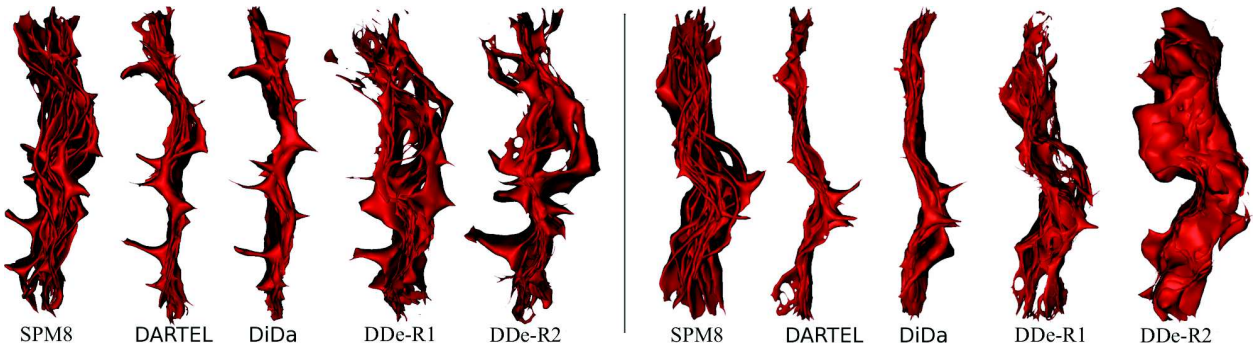

Figure 10.2: The deformed left (left) and right (right) sulci (13 subjects) after realignment by each method.

10.1 Anatomical alignment accuracy

Figure 10.3 shows the distribution across all pairs of subjects of the fuzzy Jaccard overlap for grey matter within the ROI and Hausdorff distance between CS. These quantitative measures confirm a clear improvement of the gray matter overlap when using diffeomorphic methods compared to SPM8. Both DARTEL and DiDa methods provided a low Hausdorff mean distance and a good overlap of the GM around the hand-knob. Concerning Demons, in spite of the obtention of a relatively high overlap score and the apparent preservation of the hand-knob structure shape, as showed on the mean images (Figure 10.1), the Hausdorff distances across CS remain relatively high compared to DARTEL and DiDa. We noted for some subjects (6) a local matching between central sulcus and precentral or postcentral sulci. This suggests that a local minimum in the energy term was achieved as a consequence of the large deformations tolerance without inserting explicit anatomical constraints. These quantitative measures also confirm the influence of the chosen reference on the accuracy of the method.

10.1.1 Deformation fields for diffeomorphic methods

Figure 10.4a illustrates the consistency of the spatial deformations across the subjects. For each voxel in the common ROI, we counted the number of subjects sustaining relatively large compression ($J<0.6$) or large expansion ($J>1.4$). Figure 10.4b depicts the histogram of the Jacobian values across all voxels in the common ROI for the 13 subjects and for each hemisphere.

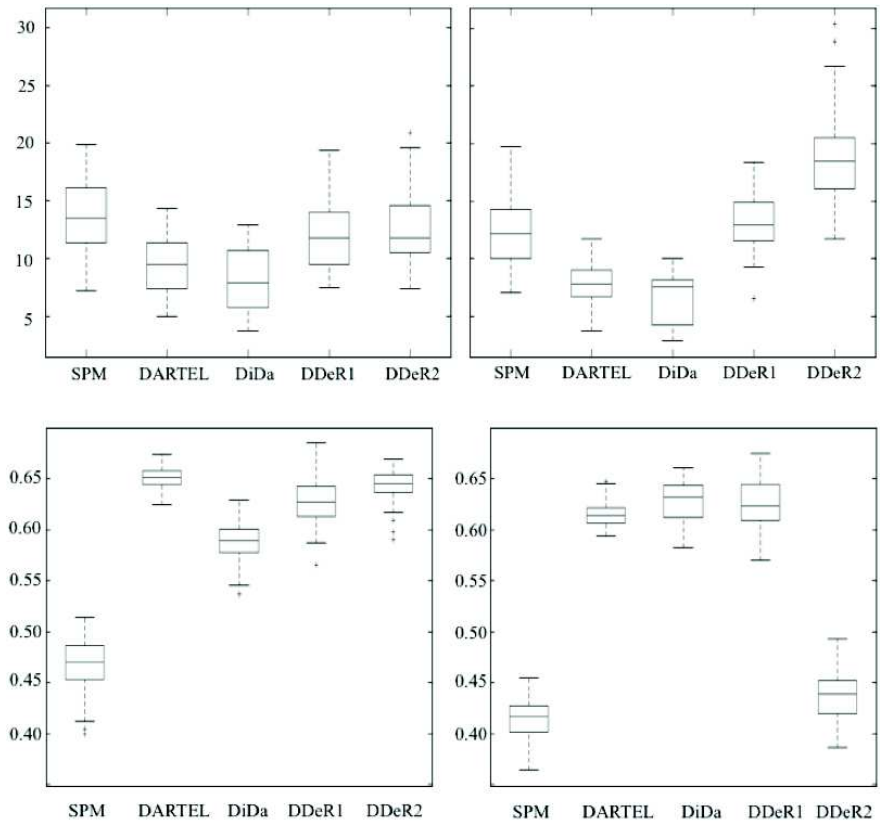

Figure 10.3: *Boxplot of Hausdorff distances (upper row) and fuzzy Jaccard overlap for grey matter (bottom row) obtained for the four methods. Left column: left hemisphere, Right column: right hemisphere.*

All Jacobian values are positive, a necessary condition for a transformation to be diffeomorphic. However, their distribution varies significantly depending on the method. The histograms and spatial distribution maps show clearly that DDe generates very strong deformations (especially compressions) distributed through the entire ROI. This is an expected outcome of the previously observed mismatch between the central sulcus and pre- and post-central sulci. Compare to DARTEL, more voxels sustained a deformation with DiDa, with similar compressions and more dilatations.

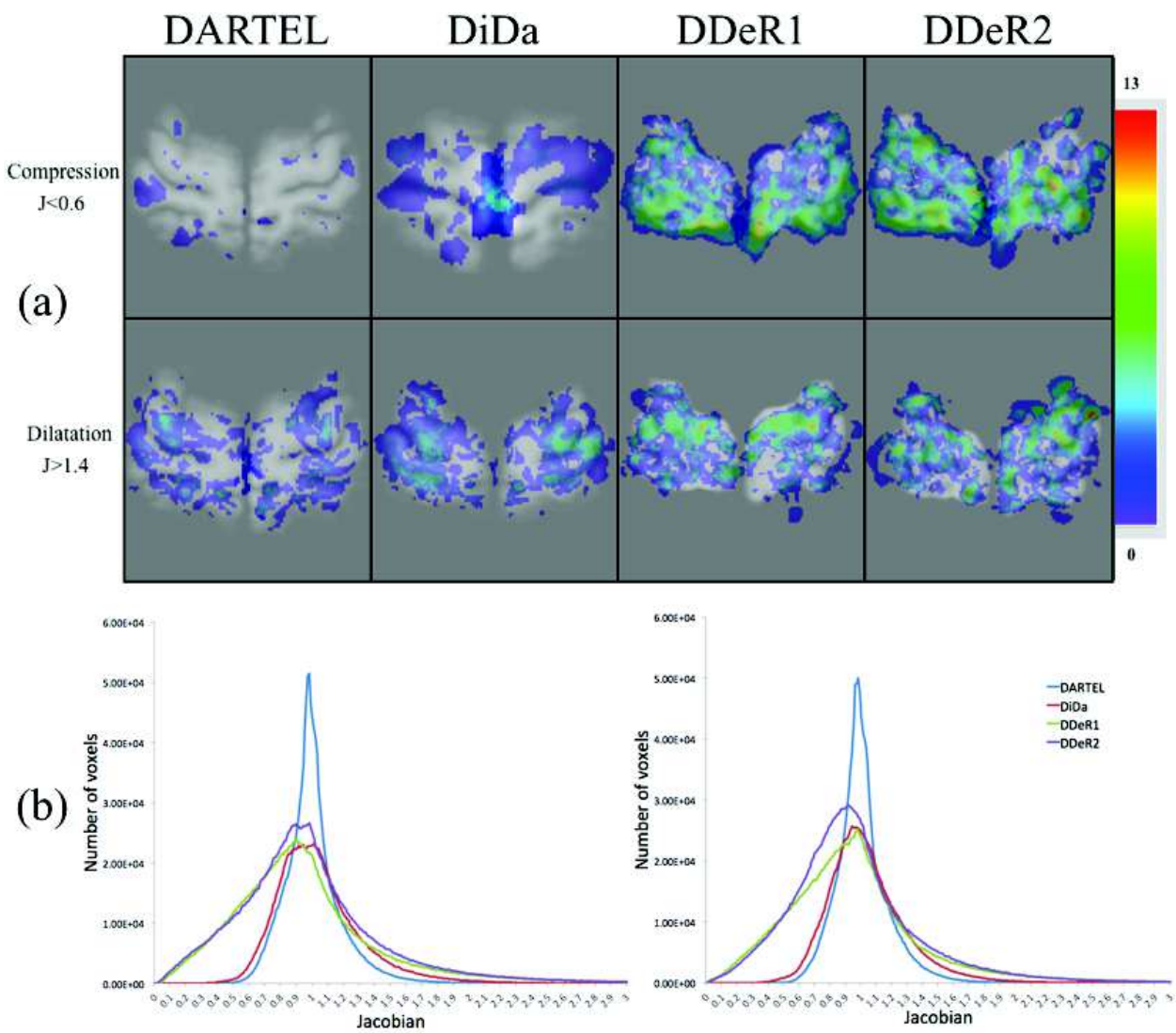

Figure 10.4: *Deformation fields for diffeomorphic methods. (a) The spatial distribution maps of the deformations across the subjects. They report for each voxel of the common ROI the number of subjects sustaining high compressions (J<0.6, top) and high dilatations (J>1.4, bottom) following DARTEL, DiDa, DDeR1 and DDeR2 registration. These values are superimposed on the corresponding mean structural image computed for each method and restricted to the common ROI. (b) Histograms of Jacobian values across every voxel in the common ROI and across all the subjects for the left hemisphere (left) and right hemisphere (right).*

10.2 Impact of the registration methods on the functional results

10.2.0.1 Qualitative evaluation

Figures 10.5 and 10.6 illustrate the localization of the main activated clusters derived from group analysis for extension and flexion respectively ($p \leq 0.0001$, voxel level uncorrected with no thresholding on cluster size), superimposed on the corresponding mean structural image computed for each method and restricted to the common ROI. With SPM8, activated spots cannot be identified as belonging to M1 or S1 because of the poor alignment. With DARTEL and DiDa, in all conditions, we could easily identify several spots along the hand-knob region which are coherent with the current knowledge about cortical representation of hand movement. Results provided by DDe-R1 seem coherent with the literature for the left hand (see especially the Figure 10.5) but incoherent for the right hand where activation foci are clearly found both along central and mostly along postcentral sulci. The activation pattern obtained with DDe (Figures 10.5 and 10.6) is highly dependent on the chosen reference (DDeR1 versus DDeR2).

Note that the representation of the activation on the reconstructed grey/white matter interface was less accurate than the classical volumetric representation (see Appendix 10.4)

10.2.0.2 Quantitative evaluation

Figures 10.7 and 10.8 compare the histograms of the T-value maps ($t \geq 4.0$, $p \leq 0.0001$ voxel level uncorrected) for extension and flexion respectively for each task and each hemisphere. These histograms confirm that the good alignment of CS obtained with DiDa and to a less extent with DARTEL is associated with a higher number of activated voxels compared to SPM8 and DDe. Jointly with the bad registration of CSs, DDe provides low T-values for the left and right hand flexion despite a relatively good overlap of gray-matter in the left hemisphere (Figure 10.3). The bias induced by the choice of the reference subject between DDe-R1 and DDe-R2 appears clearly.

Figure 10.9 shows the total number of statistically significant voxels detected at the group level across all the tasks in each hemisphere and for each method. There is a highly significant effect of the method on the activation detectability ($F_{4,20}=16$, partial eta-squared $\eta_p^2 = 0.76$, $p \leq 5.10^{-6}$), and a small but significant effect of the hemisphere ($F=7$, $\eta_p^2 = 0.59$, $p \leq 4.10^{-2}$) and a significant interaction between hemisphere and method ($F=19$, $\eta_p^2 = 0.79$, $p \leq 10^{-6}$). For the

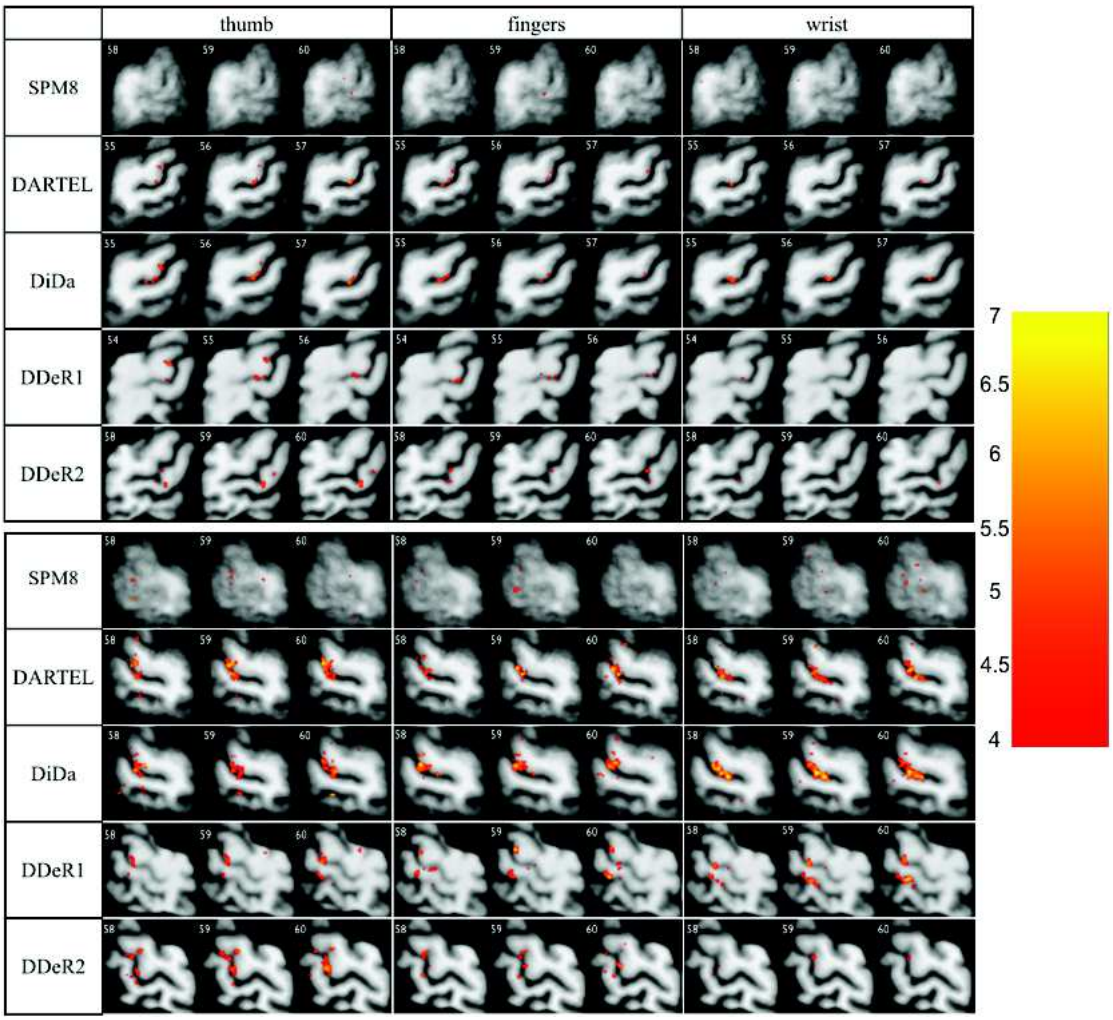

Figure 10.5: *Activation maps obtained for extension tasks for left hand (top, right hemisphere) and right hand (bottom, left hemisphere) for each method. Three contiguous transverse slices are displayed to show the largest clusters around the right (resp. left) central sulcus for each method. Maps are superimposed on the corresponding mean structural image computed for each method and restricted to the common ROI. $t \geq 4.0$, $p \leq 0.0001$ voxel level uncorrected with no thresholding on the cluster size.*

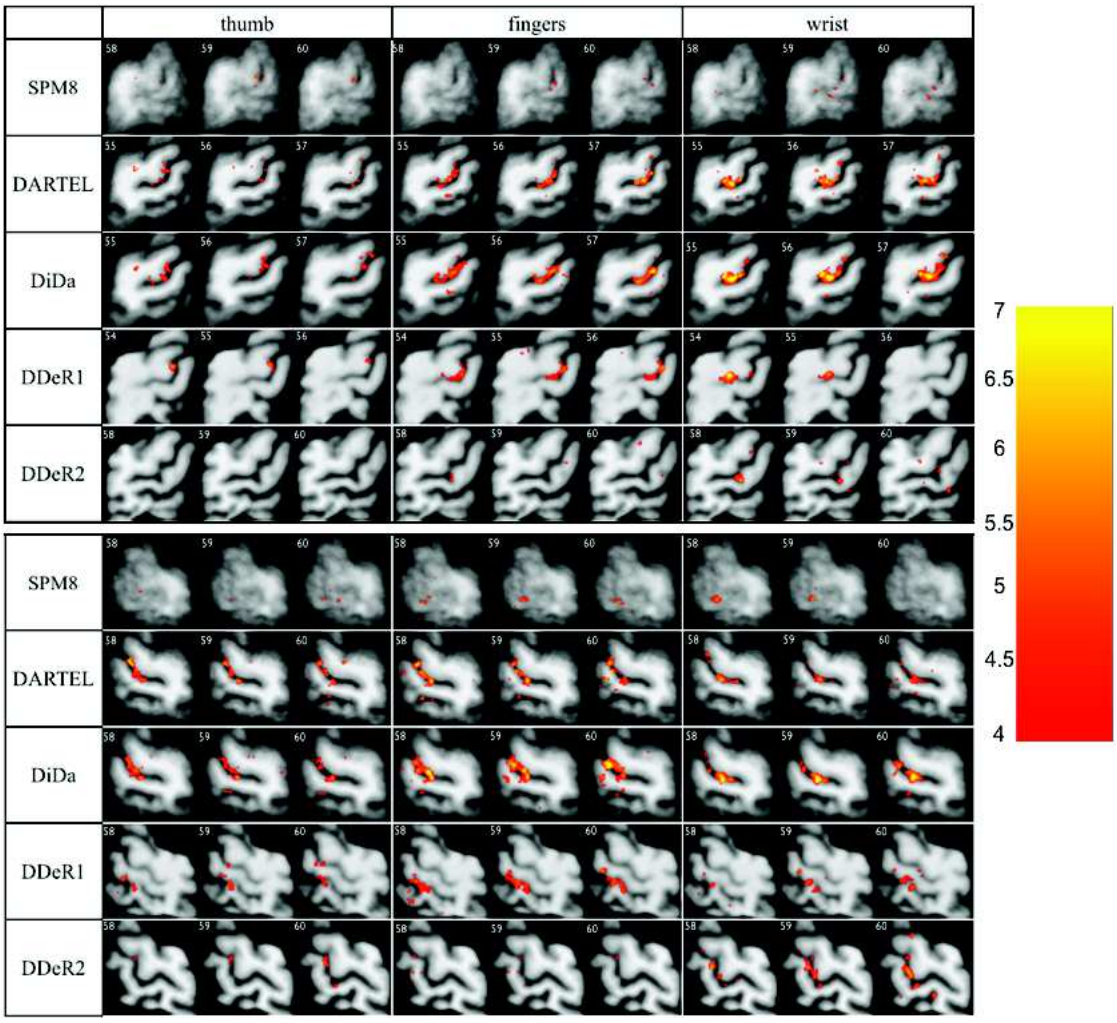

Figure 10.6: *Activation maps obtained for flexion tasks for left hand (top, right hemisphere) and right hand (bottom, left hemisphere) for each method. Three contiguous transverse slices are displayed to show the largest clusters around the right (resp. left) central sulcus for each method. Maps are superimposed on the corresponding mean structural image computed for each method and restricted to the common ROI. $t \geq 4.0$, $p \leq 0.0001$ voxel level uncorrected with no thresholding on the cluster size.*

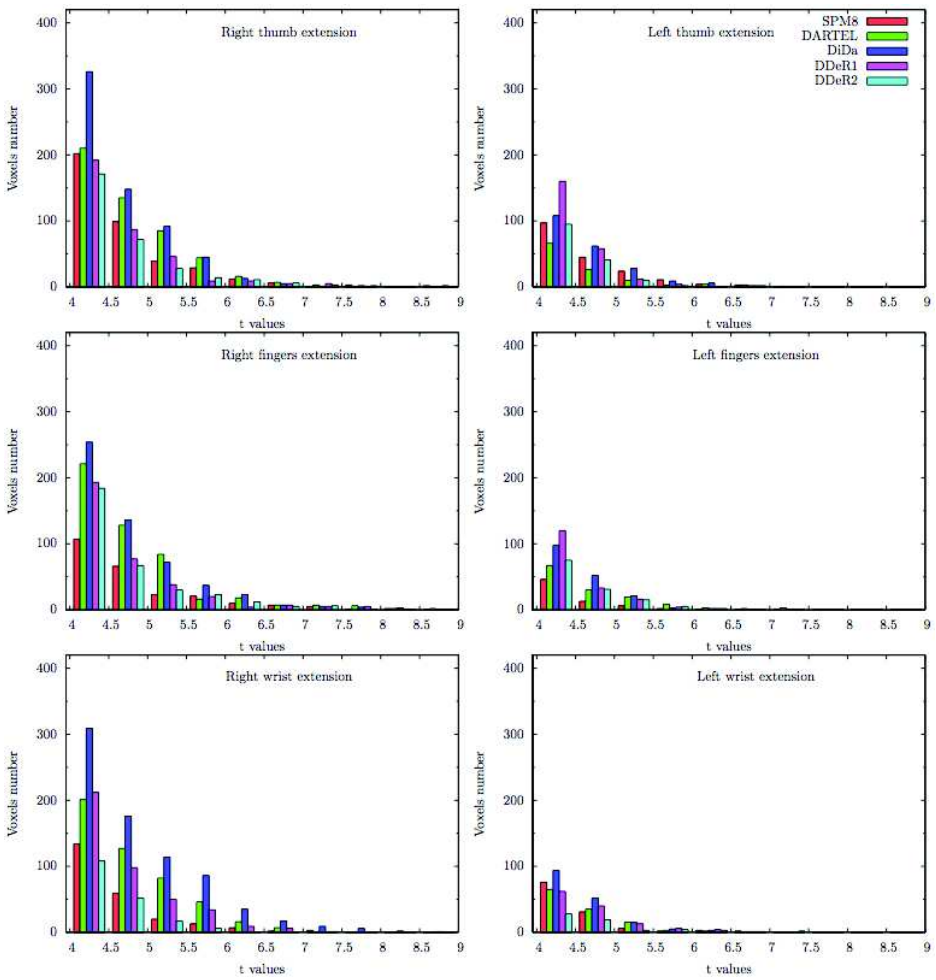

Figure 10.7: *Histograms of significantly activated voxels (t≥4.0, P≤0.0001 voxel level non corrected) using nine bins of T-values obtained by group mean effect for extension. Left hemisphere (left) and right hemisphere (right).*

left hemisphere, differences between the methods in term of activation detectability are highly significant but for SPM8 vs DDE-R1 or DDE-R2 and for DDE-R1 versus DDE-R2. For the right hemisphere, the differences between methods are less significant except for DiDa versus DDe-R2.

10.3 Effect of Smoothing

A gaussian kernel of 3x3x3mm^3 was applied on the functional data.

Figures 10.10 and 10.11 illustrate the localization of the main activated clusters derived from

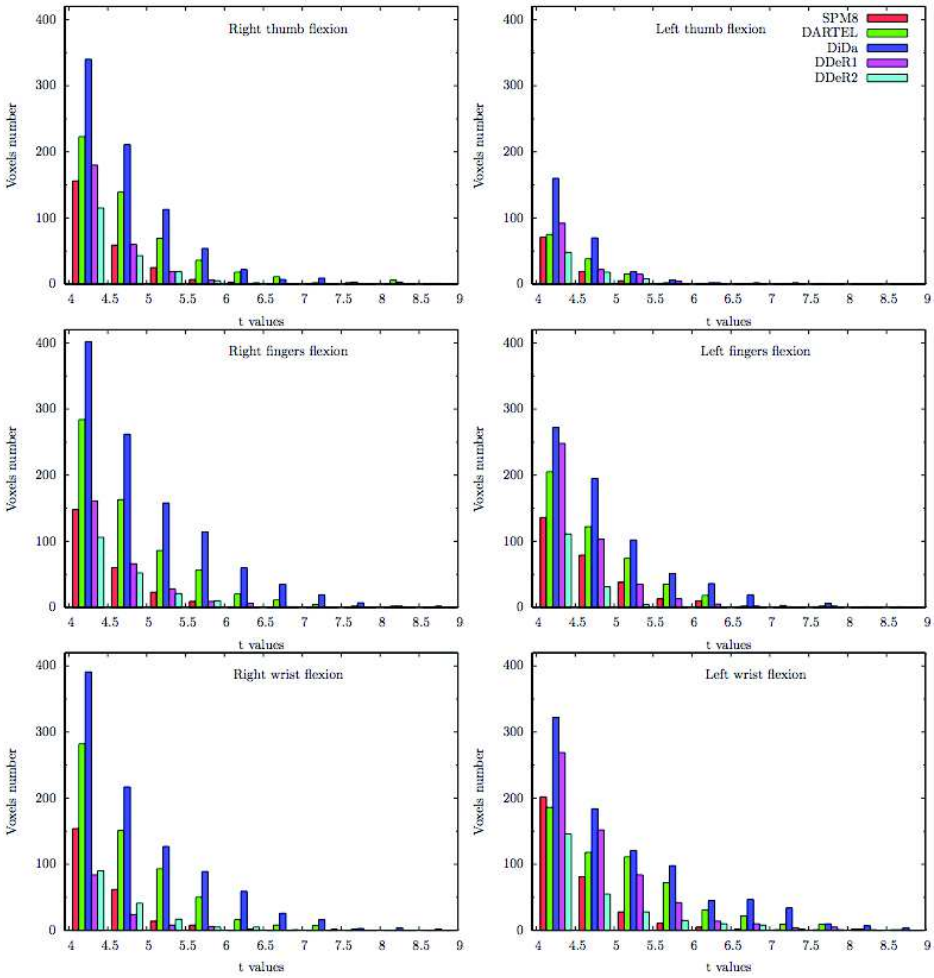

Figure 10.8: *Histograms of significantly activated voxels (t≥4.0, P≤0.0001 voxel level non corrected) using nine bins of T-values obtained by group mean effect for flexion. Left hemisphere (left) and right hemisphere (right).*

group analysis for extension and flexion respectively (p≤0.0001, voxel level uncorrected with no thresholding on cluster size), superimposed on the corresponding mean structural image computed for each method and restricted to the common ROI.

Figures 10.12 and 10.13 compare the histograms of the T-value maps (t≥4.0, p≤0.0001 voxel level uncorrected) for flexion and extension respectively for each task and each hemisphere.

Figure 10.14 shows the total number of statistically significant voxels detected at the group level across all the tasks in each hemisphere and for each method. There is a highly significant effect of the method on the activation detectability ($F_{4,20}$=12, partial eta-squared η_p^2 = 0.70, p≤ 4.10^{-5}

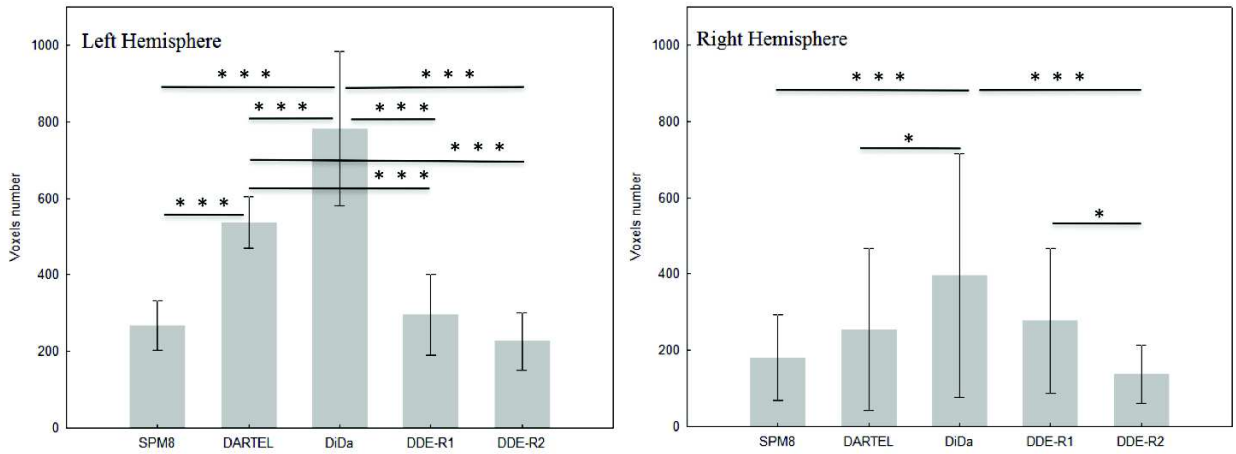

Figure 10.9: *Activation detectability. For each method, we show the mean and standard deviation of the number of voxels significantly activated at the group level ($t \geq 4.0$, $p \leq 0.0001$ voxel level uncorrected) across the tasks in each hemisphere. The p values corresponding to significant differences between methods are indicated as follows: * $p \leq 0.05$, *** $p \leq 0.001$.*

), and a high significant effect of the hemisphere (F=18, η_p^2 = 0.78, p$\leq 8.10^{-3}$) and a significant interaction between hemisphere and method (F=10, η_p^2 =0.67, p$\leq 10^{-4}$). Differences between methods for each hemisphere are similarly to those obtained with data smoothed with a 1.5mm^3 gaussian kernel. However, no difference between DARTEL and Disco appears significant for the right and the left hemisphere when using 3mm^3 smoothing .

10.4 Volumetric vs surface representation

Surface representation of the statistical parametric maps could be suitable for a global view of the brain activity.

Using BrainVISA we have reconstructed the cortical surface (*mesh*) of the anatomical average image computed with DARTEL. The t-contrasts resulting from the 2nd-level statistical analysis (group study) were then projected on the *mesh*. In Figure 10.15 there is and example of volumetric and surface representation, for the right fingers extension task ($p < 0.001$ *(uncorrected)*, $k > 20, t > 4.4$).

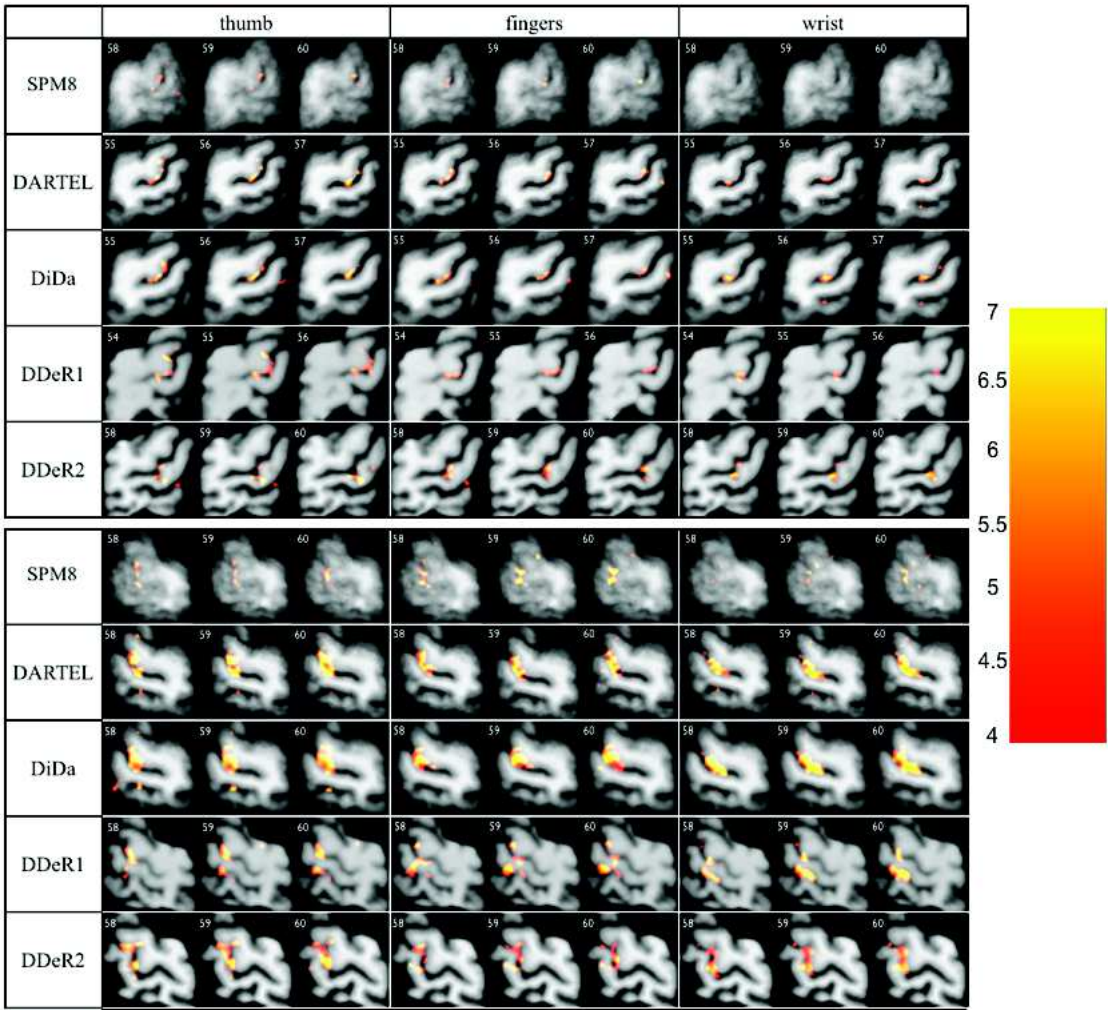

Figure 10.10: Activation maps obtained for extension tasks for left hand (top, right hemisphere) and right hand (bottom, left hemisphere) for each method. Three contiguous transverse slices are displayed to show the largest clusters around the right (resp. left) central sulcus for each method. Maps are superimposed on the corresponding mean structural image computed for each method and restricted to the common ROI. $t \geq 4.0$, $p \leq 0.0001$ voxel level uncorrected with no thresholding on the cluster size.

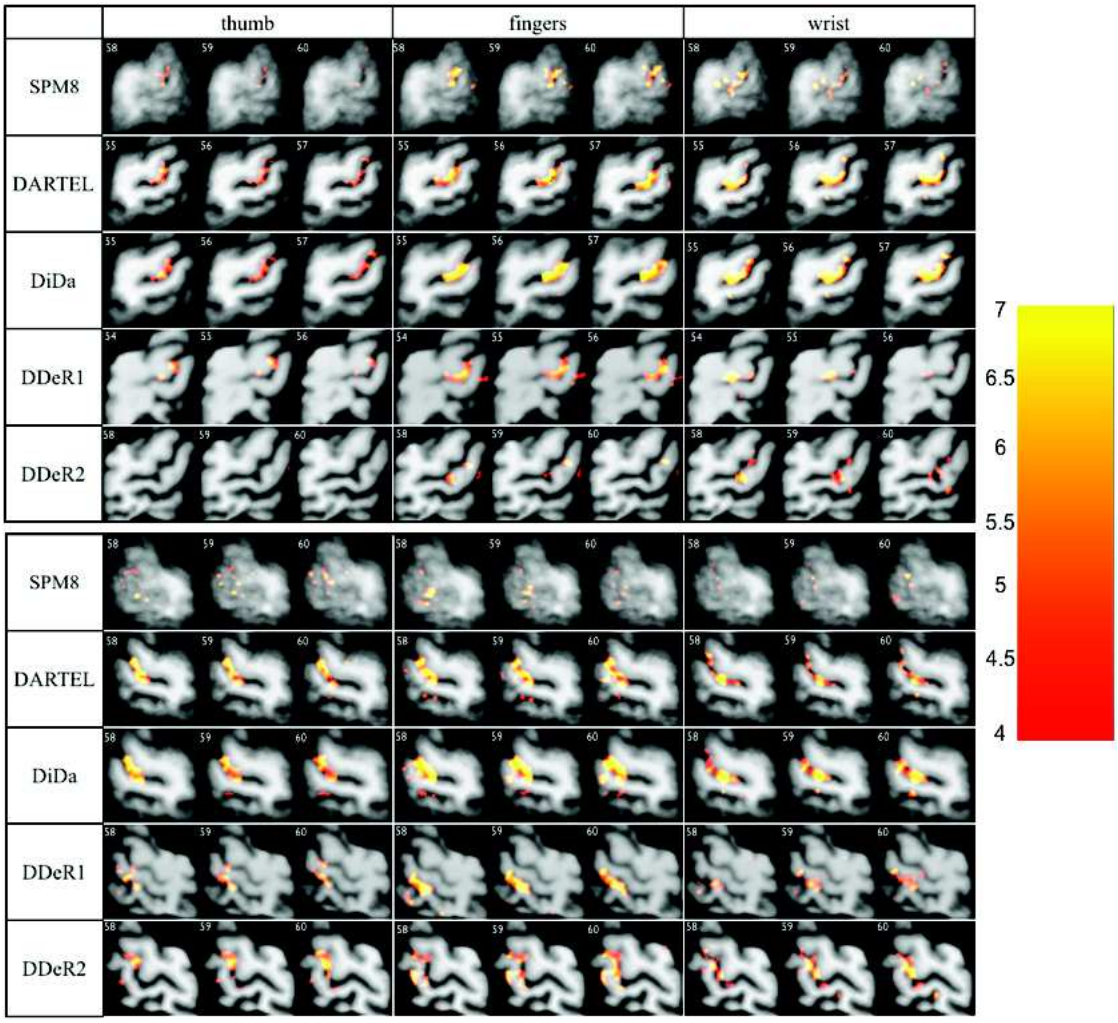

Figure 10.11: Activation maps obtained for flexion tasks for left hand (top, right hemisphere) and right hand (bottom, left hemisphere) for each method. Three contiguous transverse slices are displayed to show the largest clusters around the right (resp. left) central sulcus for each method. Maps are superimposed on the corresponding mean structural image computed for each method and restricted to the common ROI. $t \geq 4.0$, $p \leq 0.0001$ voxel level uncorrected with no thresholding on the cluster size.

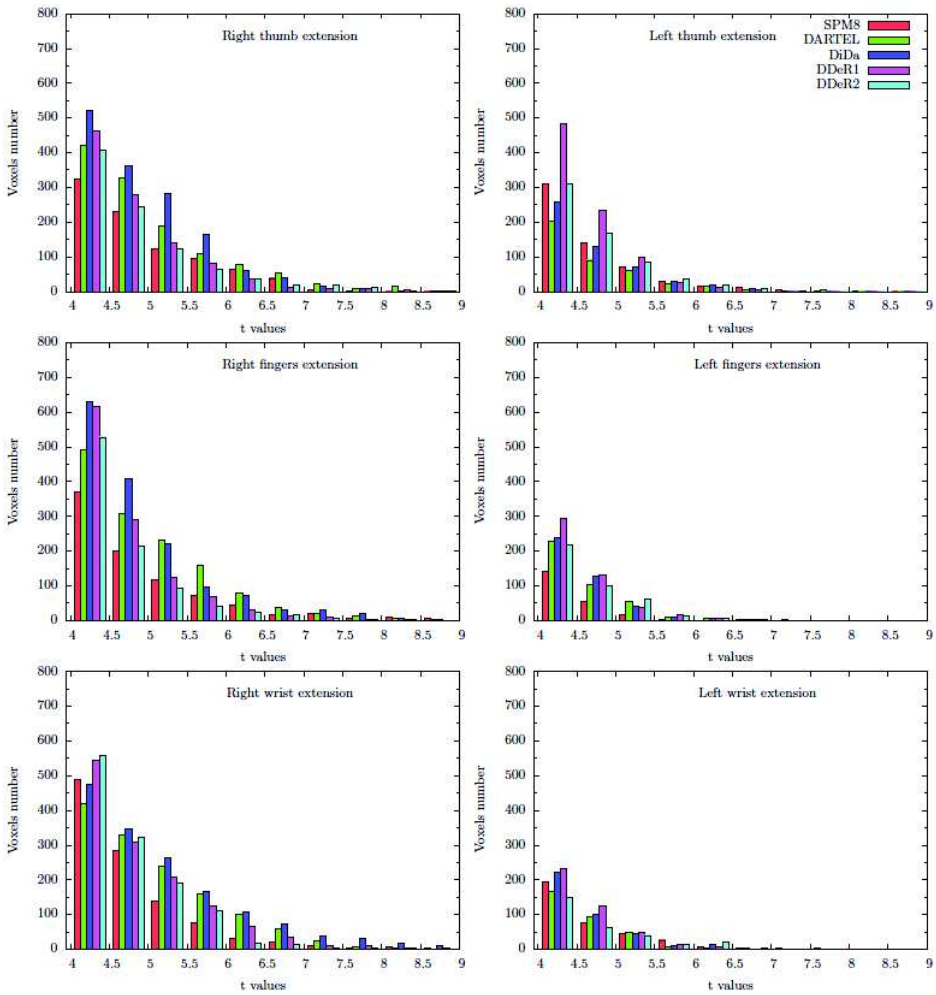

Figure 10.12: Histograms of significantly activated voxels (t≥4.0, P≤0.0001 voxel level non corrected) using nine bins of T-values obtained by group mean effect for extension. Left hemisphere (left) and right hemisphere (right).

On the left side of Figure 10.15 the volumetric representation shows 3 activated spots on M1. The two other images are shown with different angles of view with the coordinate z unchanged. The 3 spots are not well identified on the surface and the activation is projected more on the S1-side of the central sulcus than on M1.

Zooming on the axial view (Figure 10.16) shows that the *mesh* does not represent the cortical surface but rather the grey matter/white matter interface.

Another problem could come from the projection method used to assign activation to the cortical surface. Different methods produce different results. The procedure we used for the surface

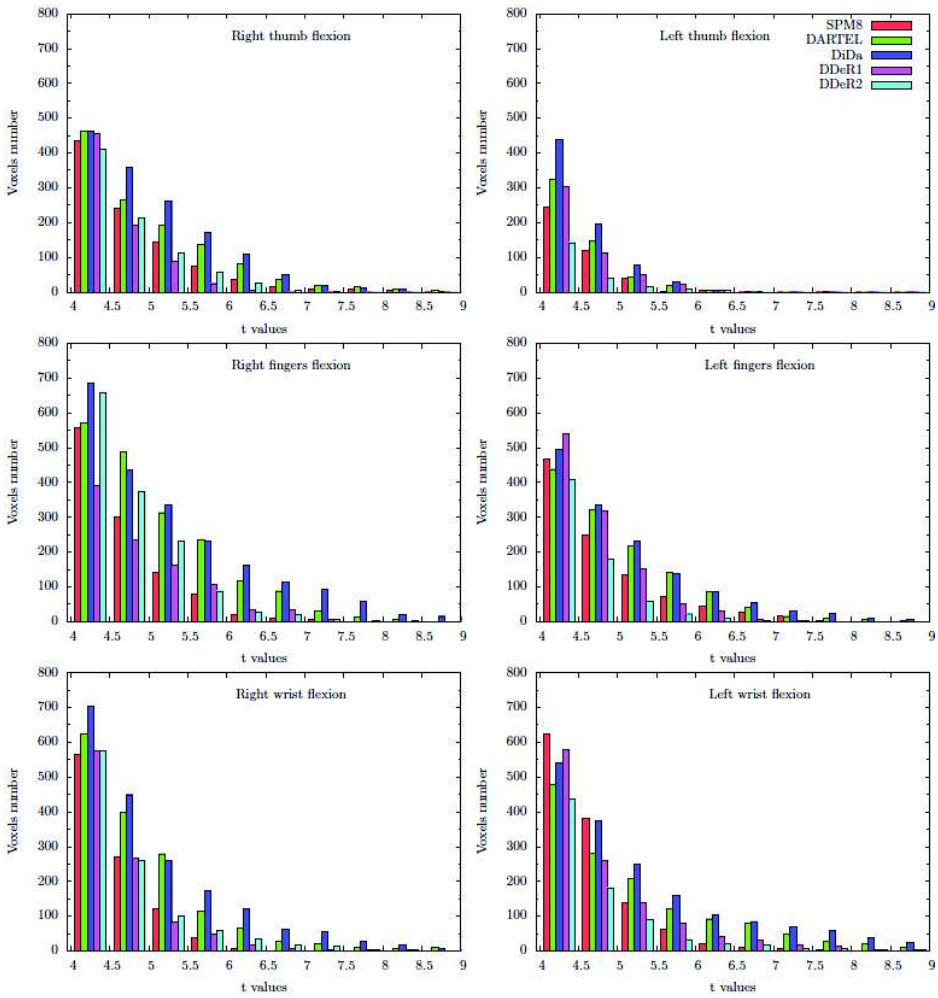

Figure 10.13: Histograms of significantly activated voxels (t≥4.0, P≤0.0001 voxel level non corrected) using nine bins of T-values obtained by group mean effect for flexion. Left hemisphere (left) and right hemisphere (right).

representation was to check the best projection method in accordance with the volumetric representation. The cons of this procedure are the time spent for checking every task under study and subjectivity in choosing the best method of projection.

Finally, to avoid misinterpretations, we chose to represent the results in an "old fashion" slice by slice manner.

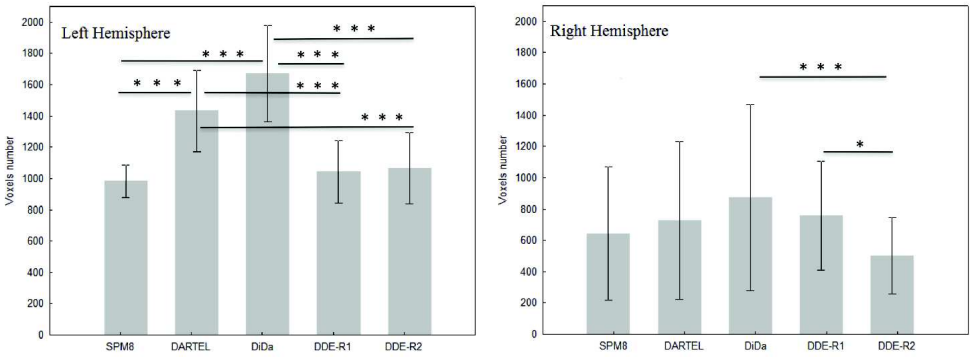

Figure 10.14: Activation detectability. For each method, we show the mean and standard deviation of the number of voxels significantly activated at the group level (t≥4.0, p≤0.0001 voxel level uncorrected) across the tasks in each hemisphere. The p values corresponding to significant differences between methods are indicated as follows: * p≤0.05, *** p≤0.001.

Figure 10.15: *Example of volumetric and surface representation, for the right fingers extension task ($p < 0.001, k > 20, t > 4.4$). On the left side the axial view highlighting 3 activated spots in M1. On the center and right side the same image, from different angle of view, but with the coordinate z unchanged, the M1 and S1 walls are visible respectively.*

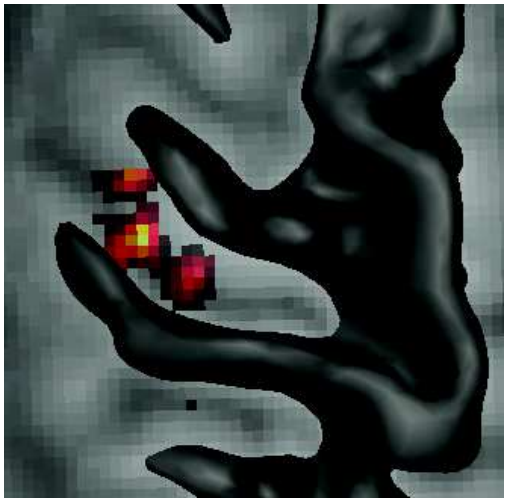

Figure 10.16: *Zoom of the left image in Figure 10.15 showing the limits of the reconstructed mesh.*

CHAPTER 11

Control group results

In this chapter the results concerning the motor representation of the elementary hand movement at group level are presented. The tasks and the fMRI acquisition paradigm are described in Section 7.2. Here we show the activation maps for the left and right hand movement, the movement direction (extension and flexion) and the the hand segments (thumb, fingers and wrist). These were obtained on the control group of 13 healthy subjects (Section 11). The results for the investigation of the common regions (*conjunction*) and the *predominance* between hand movement (extension/flexion) and the hand segments are also presented here.

The evaluation of the reliability of our fMRI results, computed with a 4-way ANOVA on 9 healthy subjects of the control group, who underwent a second acquisition session one year later after the first one, is shown in this chapter.

The activated maps for the left-hand tasks were flipped in the left-right direction, so that left sided results correspond to contralateral activity and right sided to ipsilateral activation. This flip was introduced to directly compare left and right hand activation. DARTEL deformation fields were applied to the individual anatomical images in order to compute an average anatomical image. This is the template used to localised the functional activations. We tested a surface representation extracting a mesh of the grey/white matter interface from the anatomical template. Because of uncertainty in the projection of activation onto the reconstructed surface, we finally adopt a volumetric representation. All views are shown in neurological convention. (see Section 10.4).

During the fMRI experiments we asked the subjects to perform the **extension** and **flexion** of **thumb**, **fingers** and **wrist**, for **both hands**. All the individual statistical analysis were registered in the same symmetric system using DARTEL registration method (see Section 8.3.6).

11.1 Areas involved in the hand tasks at group level

Motor cortex

In Figure 11.1 we show the significant activation[1] for all the tasks that all the subjects performed (ANOVA main effect). It can be seen that the activated cluster covers the *hand-knob* region, from the deeper part of the central sulcus (z=+42) to the upper part (z=+60) in M1 and S1 contralateral. We did not find ipsilateral activations.

The SMA involvement at $z = 50, 51$, is clearly displayed in sagittal view (Fig. 11.2). F-test, $p < 0.01$ *(corrected)* and *cluster size*> 20.

Cerebellum

In Figure 11.3 we show the significant activation for the cerebellum, for all the tasks that all the healthy subjects performed (ANOVA main effect). It can be seen that the activated cluster covers the ipsilateral part of the cerebellum. There are multiple activated foci in the IV V and VI lobules (see Figure 3.6). F-test, $p < 0.01$ *(corrected)* and *cluster size*> 20.

11.2 Hand dominance effects

Motor cortex

In Figure 11.4 the activations for the **right hand movement** are shown. Large activation cluster is located around the *hand-knob*, in M1 and S1, and several peaks can be distinguished. In particular at z=48,50, 51, 52, 54. We did not find SMA and ispilateral activation at our statistical thresholds. T-test: $p < 0.01$ *(corrected)* and *cluster size*> 20.

In Figure 11.5 the activations for the **left hand movement** are shown. An activated cluster is located around the *hand-knob*, in M1. Several peaks can be distinguished in the deeper part of the central sulcus (z=+44,+45,+46). The posterior part of the post-central sulcus appears activated at z=54,56,57. We did not find SMA and ispilateral activation at our statistical thresholds. T-test: $p < 0.01$ *(corrected)* and *cluster size*> 20.

In Figure 11.6 the **common activation (conjunction) between the right hand movement and**

[1] All coordinates are in the MNI reference system

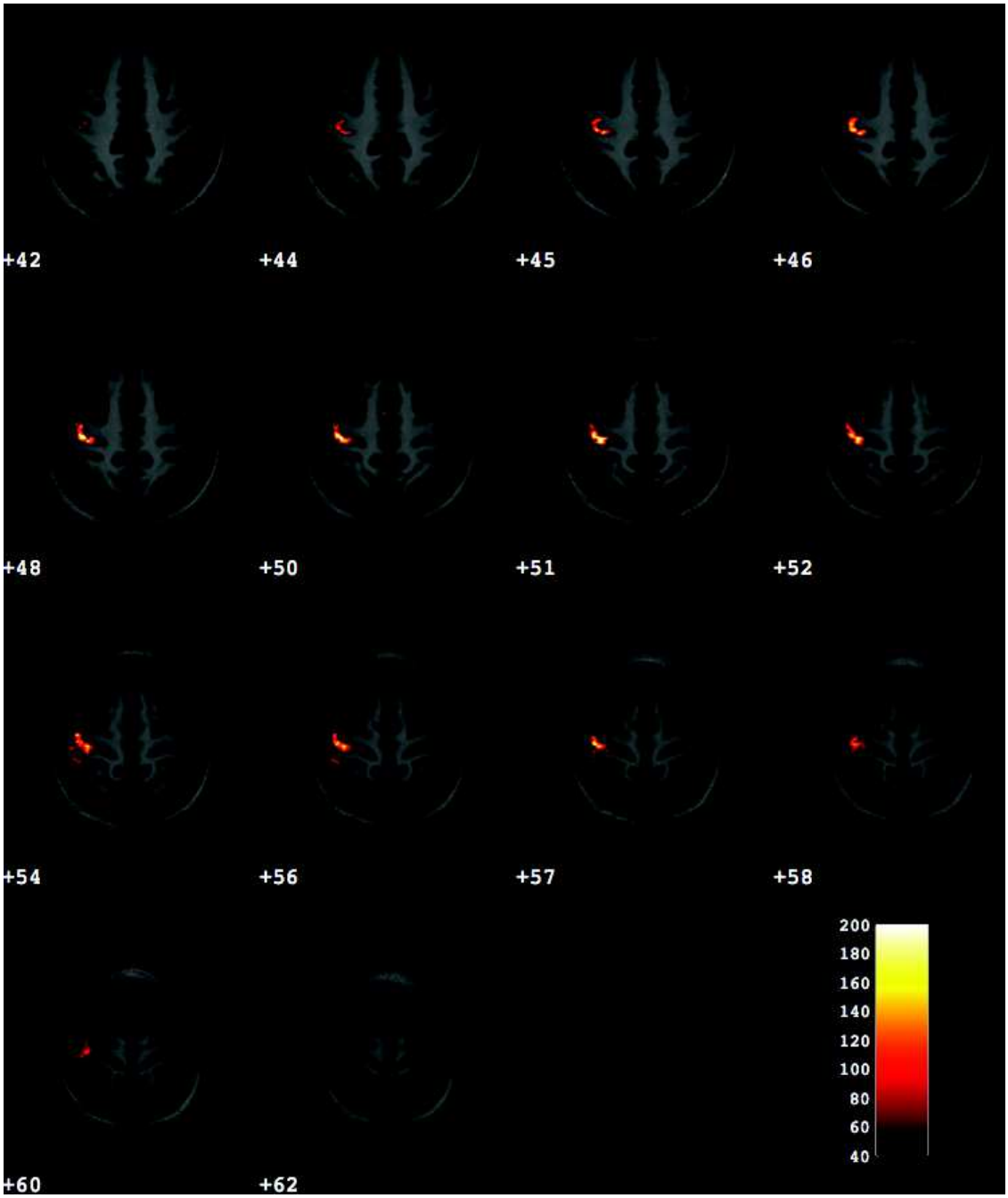

Figure 11.1: *Axial view of 14 slices in which the activation map corresponding to* ***all tasks*** *(ANOVA main effect) is superimposed to the symmetric DARTEL template. The left-hand activation maps are represented in the left hemisphere due to the symmetrization. We can see the role played by the hand-knob in every kind of movement and the involvement of the SMA and post-central suclus. F-test:* $p < 0.01$ *(corrected) and cluster size*> 20.

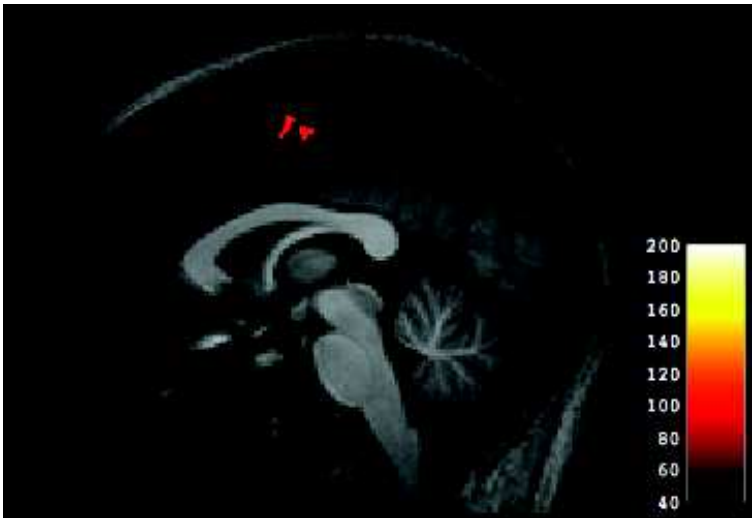

Figure 11.2: *Sagittal view showing the SMA recruitment at a group level for* ***all tasks*** *(ANOVA main effect) involved. F-test:* $p < 0.01$ *(corrected) and cluster size*> 20 .

the left hand movement is represented. It can be seen that the *hand-knob* M1 and S1 contralateral are the main activated regions for both hands. Also the SMA is involved at z=45,46,48,50,51,52 and the post-central sulcus at z=46,54,56,57. T-test: $p < 0.0001$ *(uncorrected)* and *cluster size*> 20.

Since subjects under study were all right-handed we looked for some difference in activation level between the right hand and the left hand (**Right hand > Left hand**). We found very tiny spots in M1, laterally in S1, in the deeper part of the central sulcus (Fig. 11.7). T-test: $p < 0.0001$ *(uncorrected)* and *cluster size*> 20.

We did not find activations for the left hand greater than the right hand. These results suggest a slightly higher functional extent with the dominant hand.

Cerebellum

In Figure 11.8 the activation maps corresponding to the right hand movement (red) and to the left hand movement (green). There is no contralateral activation. It seems that there is a shift between the right hand activation and the left hand activation with a multiple representation for both of them, in lobules IV, V and VI. T-test: $p < 0.05$ *(corrected)* and *cluster size*> 20.

In Figure 11.9 the **common activation (conjunction) between the right hand movement and the left hand movement** is represented. It can be seen that there is no contralateral activation (as

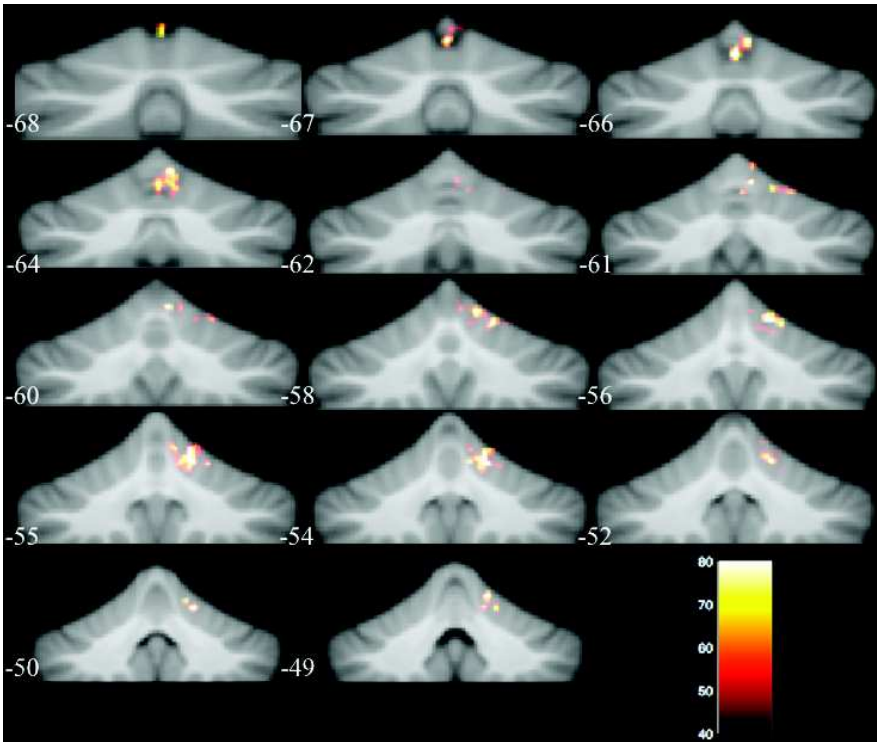

Figure 11.3: *Coronal view of 16 slices in which the activation map corresponding to* ***all tasks*** *(ANOVA main effect) is superimposed to the symmetric SUIT template. The right-hand activation maps are represented in the right hemisphere due to the symmetrization. It can be seen that the activated cluster covers the ipsilateral part of the cerebellum. There are several activated foci in the IV V and VI lobules (see Figure 3.6). F-test,* $p < 0.01$ *(un corrected) and cluster size*> 20.

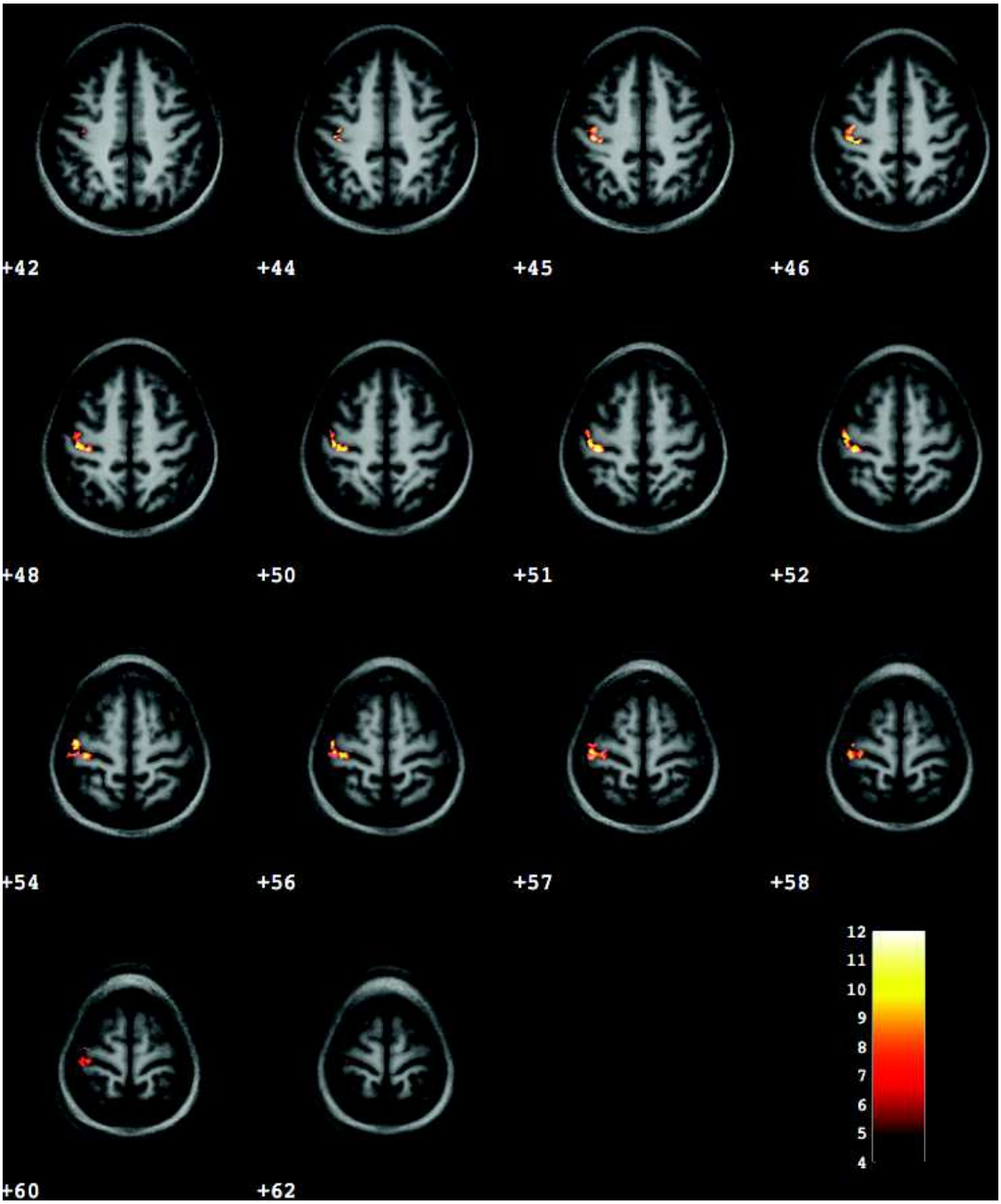

Figure 11.4: *Axial view of 14 slices. Activation map for the* ***right hand movement****, of both extension and flexion, is represented. An activated cluster is located around the "hand-knob" and several peaks can be distinguished. In particular at z=48,50, 51, 52, 54. T-test:* $p < 0.01$ *(corrected) and cluster size*> 20.

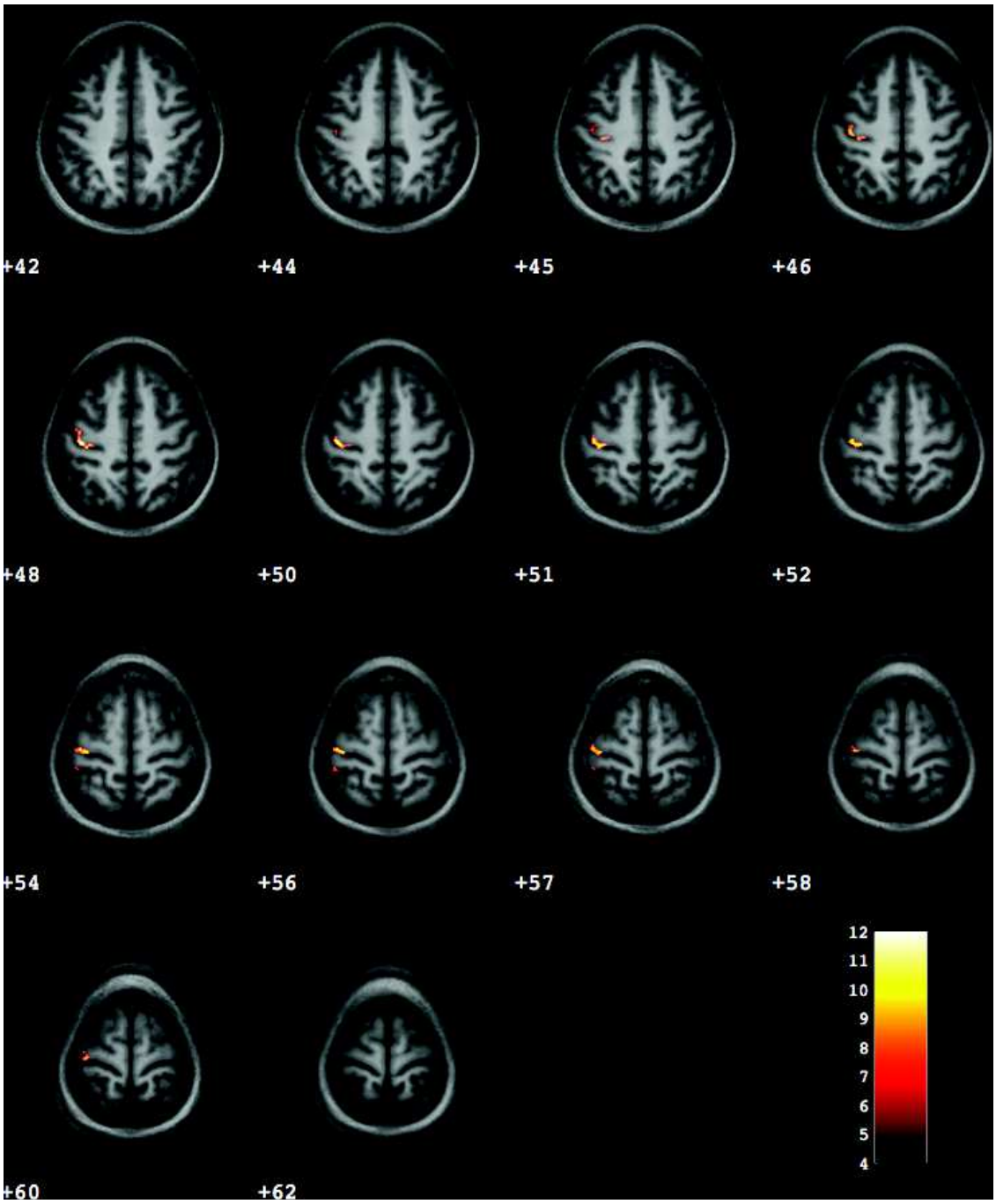

Figure 11.5: *Axial view of 14 slices. Activation map for the* ***left hand movement****, of both extension and flexion, is represented. An activated cluster is located around the "hand-knob" and several peaks can be distinguished in the deeper part of the central sulcus. T-test:* $p < 0.01$ *(corrected) and cluster size*> 20.

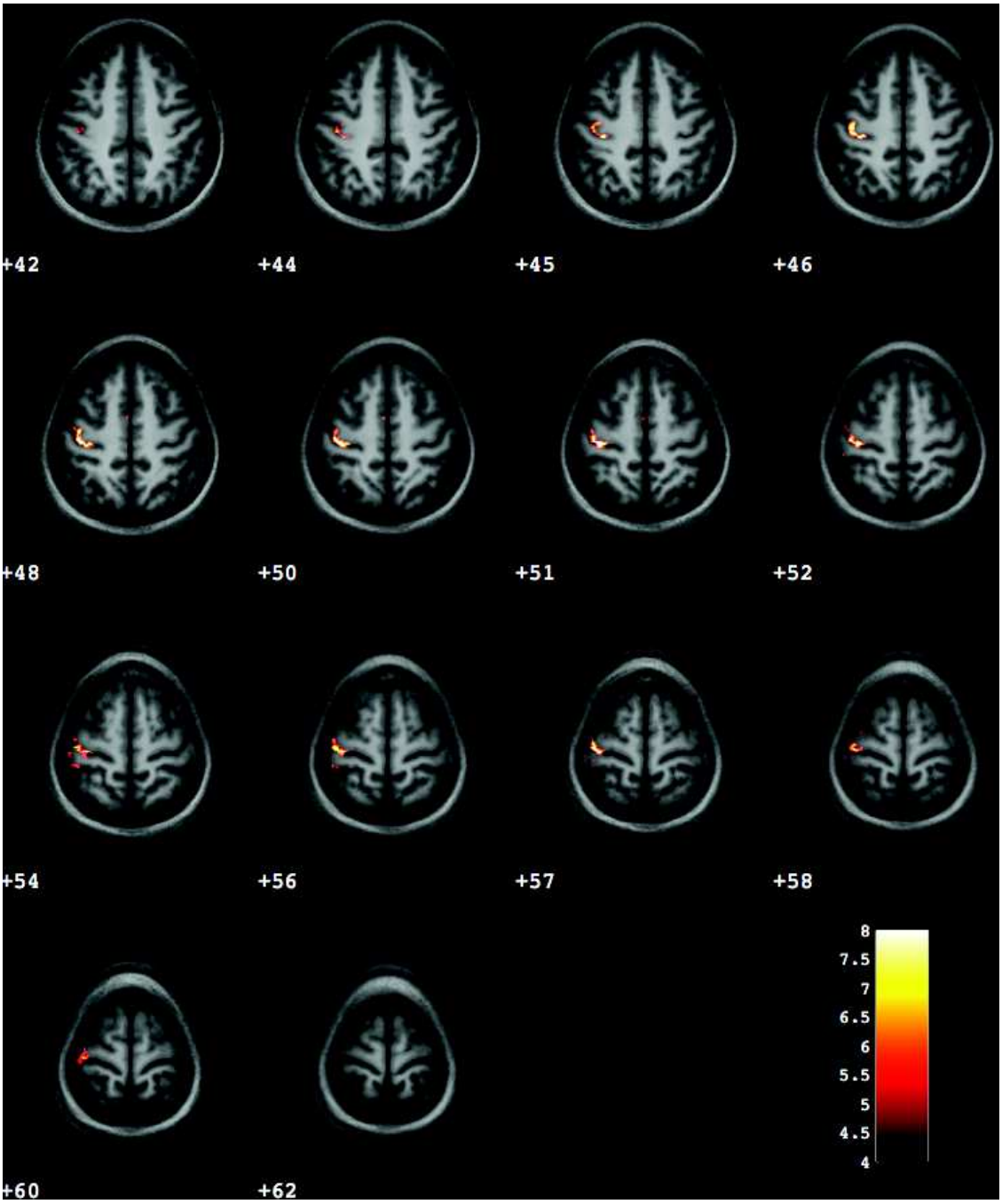

Figure 11.6: *Axial view of 14 slices. The* ***common map (conjunction) between the right hand and the left hand movement (extension/flexion)*** *is represented. The hand-knob is the principal activated region for both hands (as expected). Also the SMA is involved at z=45,46,48,50,51,52 and the post-central sulcus at z=46,54,56,57. T-test:* $p < 0.0001$ *(uncorrected) and cluster size*> 20.

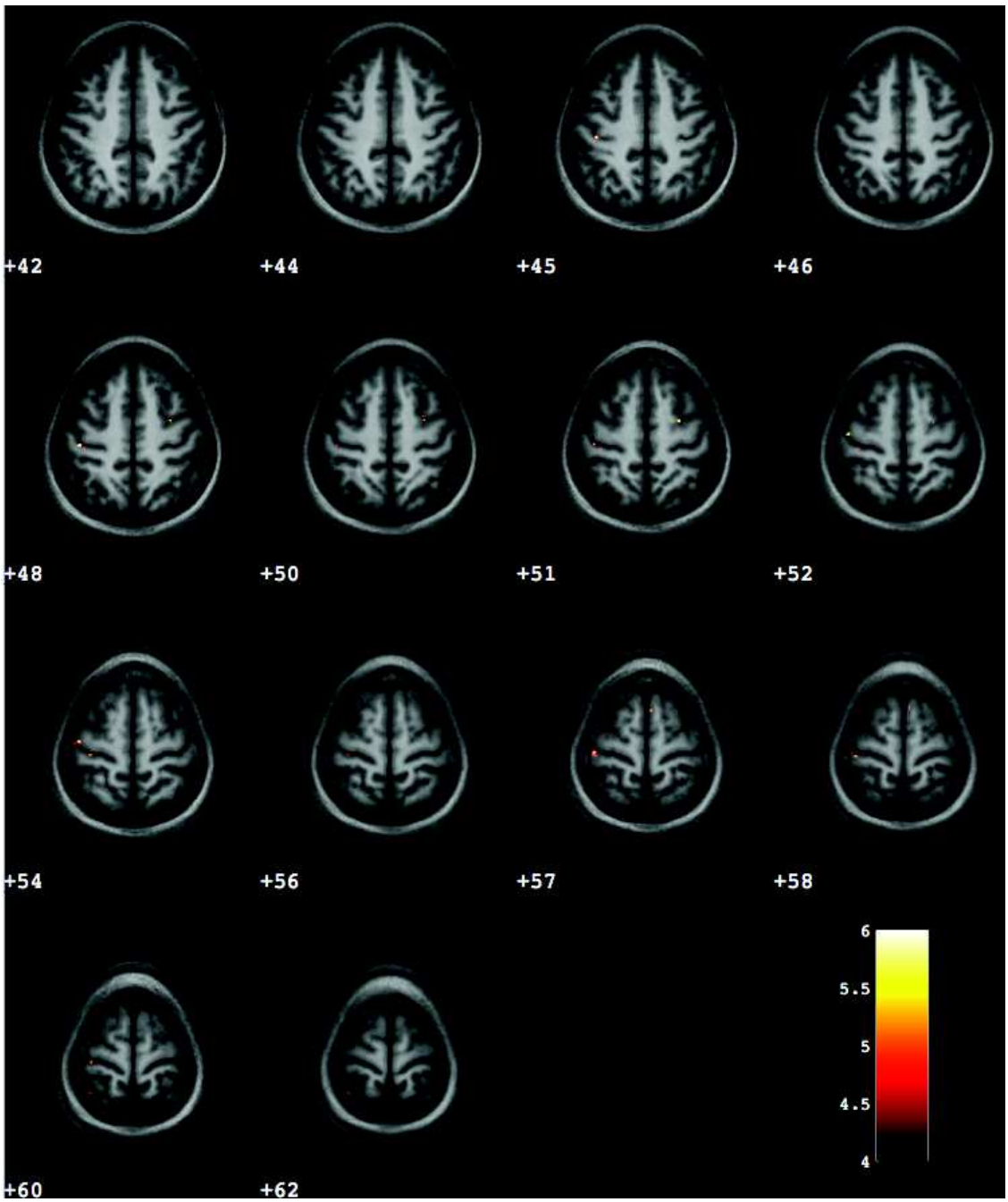

Figure 11.7: *Axial view of 14 slices. The T-test (**Right hand>Left hand**), for all the tasks and hand segments, at a group level, is represented. Activated spots are localized in M1, S1, in the deeper part of the central sulcus, in SMA and close to the ipsilateral pre-central sulcus. T-test:* $p < 0.0001$ *(uncorrected) and cluster size*> 20.

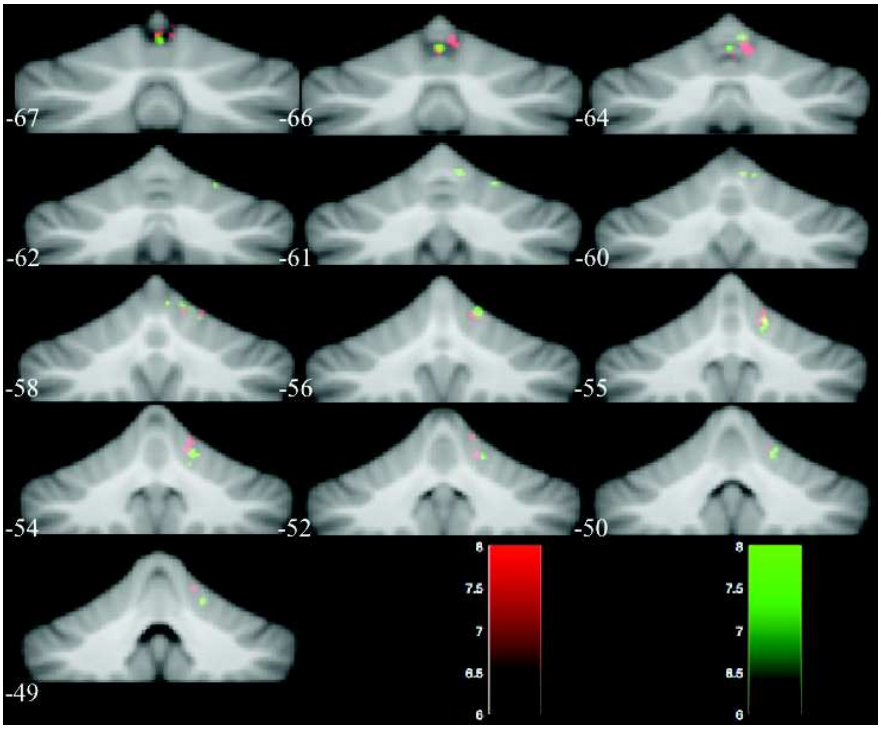

Figure 11.8: *Coronal view of 16 contiguous slices. Activated maps the* ***right hand movement*** *(red) and* ***left hand movement*** *(green), of both extension and flexion, are represented. There is no contralateral activation. It seems that there is a shift between the right hand activation and the left hand activation with a multiple representation for both, in lobules IV, V and VI (see Figure 3.6). T-test:* $p < 0.05$ *(corrected) and cluster size*> 20.

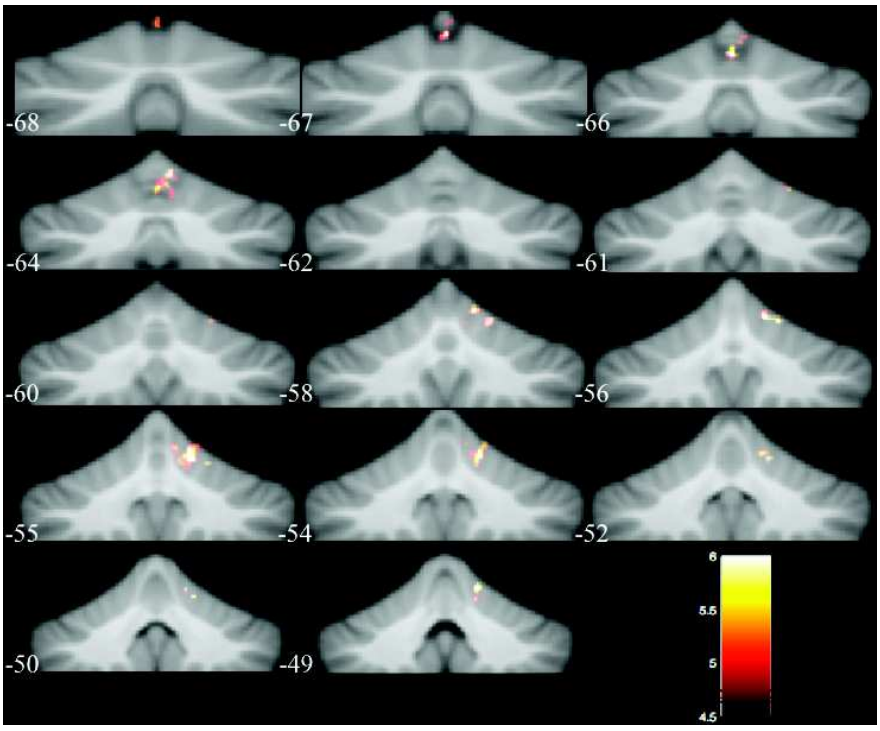

Figure 11.9: *Coronal view of 16 contiguous slices. Activated map the* ***common activation (conjunction) between the right hand movement and the left hand movement*** *(extension/flexion) is represented. There is no contralateral activation. There is a large cluster at* $y = -64$ *corresponding to the lobule V and at* $y = -55$ *corresponding to the lobule VI (see Figure 3.6). T-test:* $p < 0.05$ *(corrected) and cluster size*> 20.

expected). In can be seen a large cluster at $y = -64$ corresponding to the lobule V and at $y = -55$ corresponding to the lobule VI. T-test: $p < 0.05$ *(corrected)* and *cluster size*> 20.

Testing the differences between right and left hand movement, with a Student's T-test, does not give significant results.

11.3 Movement direction effects

Motor cortex

Since in patient the tendons transfer surgery inverts the extension/flexion functions we have investigated the direction encoding in the brain cortex in the control group. In Figure 11.10 the activation map corresponding to the **extension movement**, of both hands, is shown. It lies around the *hand-knob*, in M1 and S1, and in the post-central sulcus (z=+54,+56,+57). The activated cluster seems composed of several peaks, in particular at z=+45,+46,+48,+54,+56. T-test: $p < 0.01$ *(corrected)* and *cluster size*> 20.

In Figure 11.11 the the activation map corresponding to **flexion movement**, of both hands, is shown. It lies around the *hand-knob*, in M1 and S1. As for extension the activated cluster seems composed of several peaks, in particular at z=+45,+46,+48,+54. T-test: $p < 0.01$ *(corrected)* and *cluster size*> 20.

The **common region** (*conjunction*) between **extension and flexion** is shown in Figure 11.12. M1 seems to be activated form the deeper part to the upper part. SMA appears to be activated at z=45,46,48,50,51,52. And post-central sulcus at z=+52,+54,+56,+57,+58. T-test: $p < 0.0001$ *(uncorrected)* and *cluster size*> 20.

In Firgure 11.13 the extension is represented in red and the flexion movement in green. (T-test: $p < 0.01$ *(corrected)* and *cluster size*> 20.).

Cerebellum

In Figure 11.14 the activation maps of the **extension** (red) and the **flexion** (green) movement are represented. There is no contralateral activation. It seems that extension end flexion are more active in lobules VI at $y = -55, -56$. Whereas there is more flexion in lobules V-VI at $y = -66, -64$ and extension in lobules VI at $y = -50, -49$. T-test: $p < 0.05$ *(corrected)* and *cluster size*> 20.

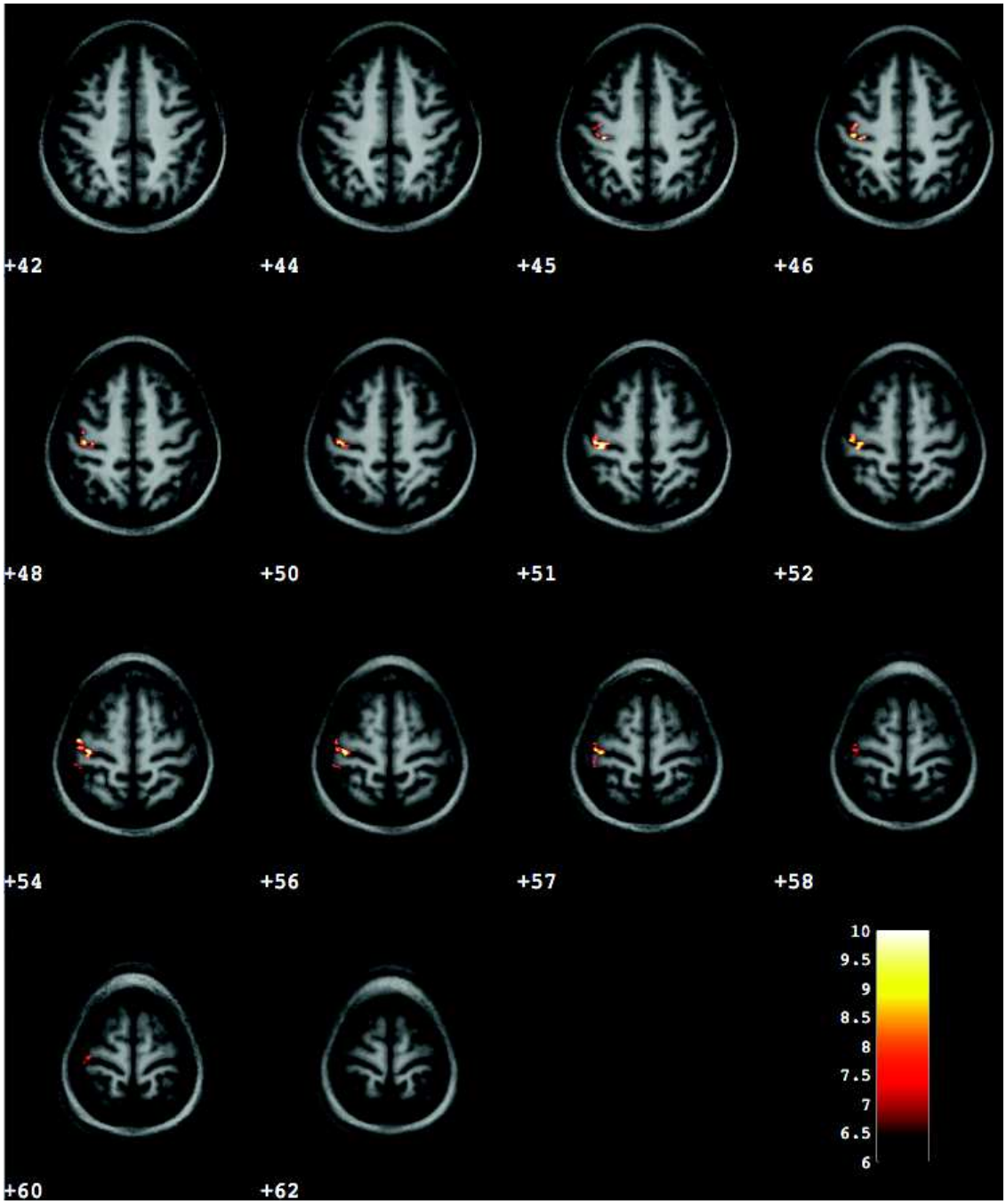

Figure 11.10: *Axial view of 14 slices. Activation map for* ***extension movement****, of both hands, is represented. Activated cluster lies around the hand-knob, in M1, and in the post-central sulcus. The activated cluster seems composed of several peaks. T-test:* $p < 0.01$ *(corrected) and cluster size*> 20.

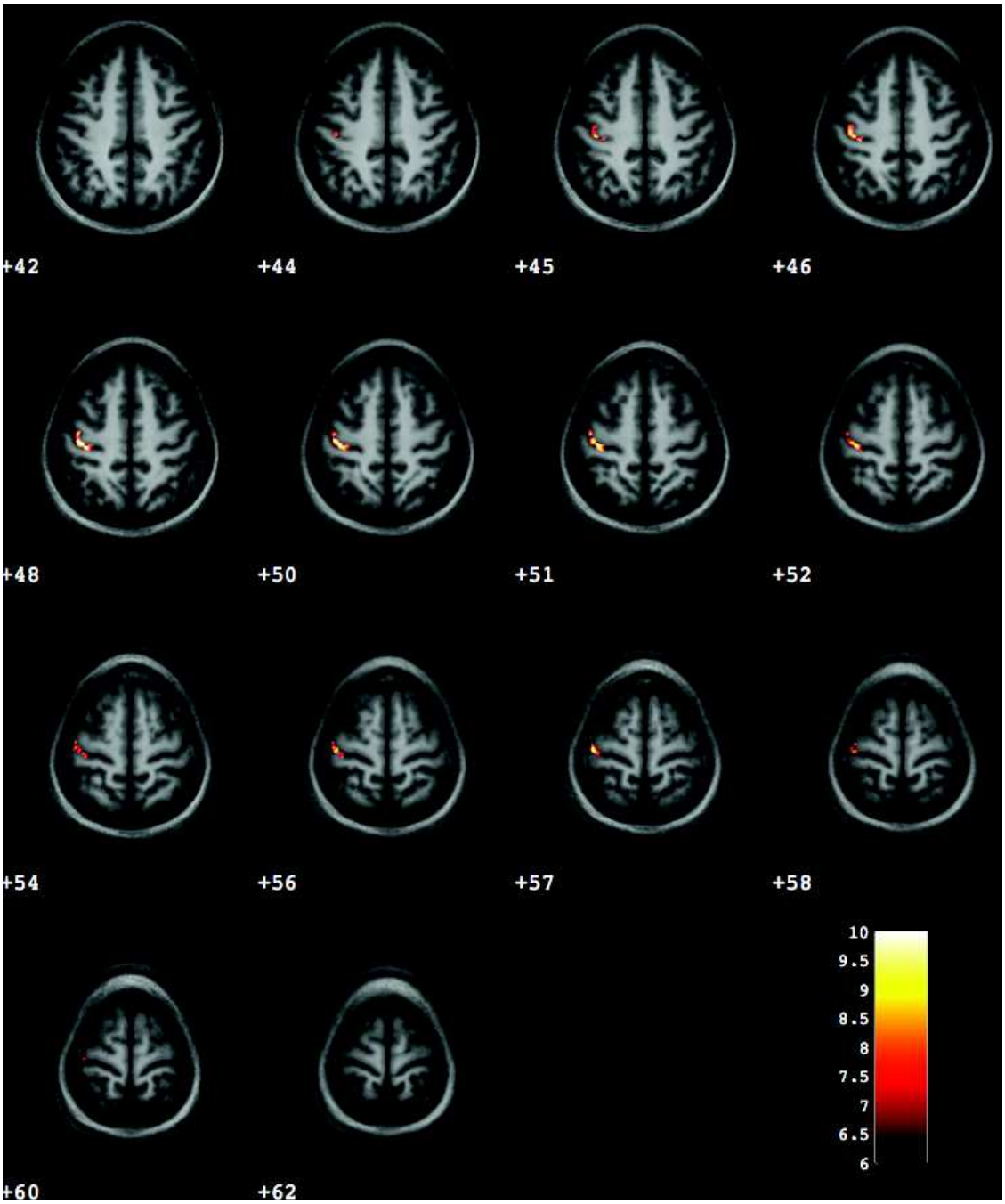

Figure 11.11: *Axial view of 14 slices. Activation map for* ***flexion movement****, of both hands, is represented. Activated cluster lies around the hand-knob, in M1. As for extension the activated cluster seems composed of several peaks. T-test:* $p < 0.01$ *(corrected) and cluster size*> 20.

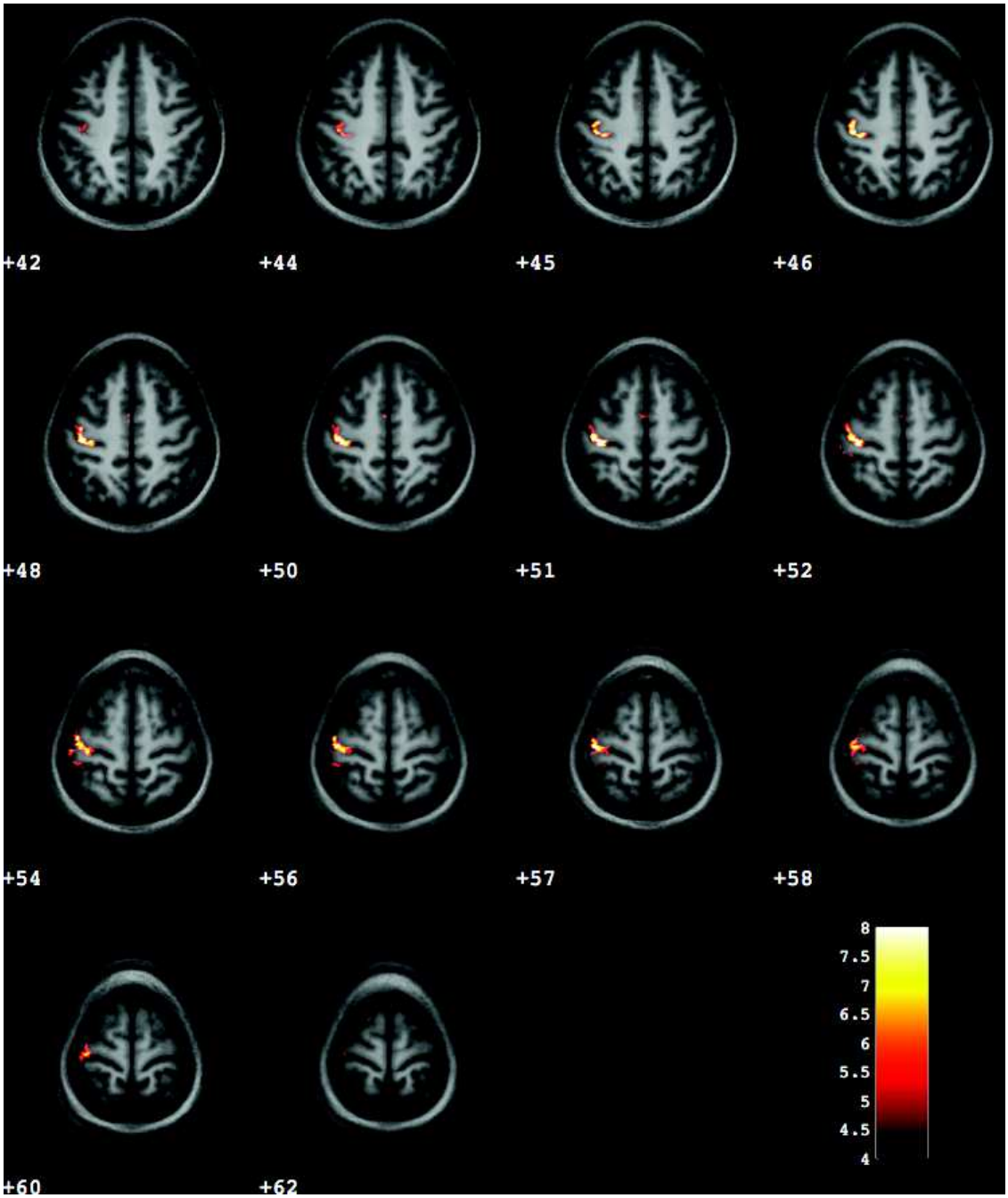

Figure 11.12: *Axial view of 14 slices. Activation map of the* ***common region (conjunction) between extension and flexion, of both hands, movement is represented****. M1 seems to be activated form the deeper part to the upper part. SMA is also involved. T-test:* $p < 0.0001$ *(uncorrected) and cluster size*> 20.

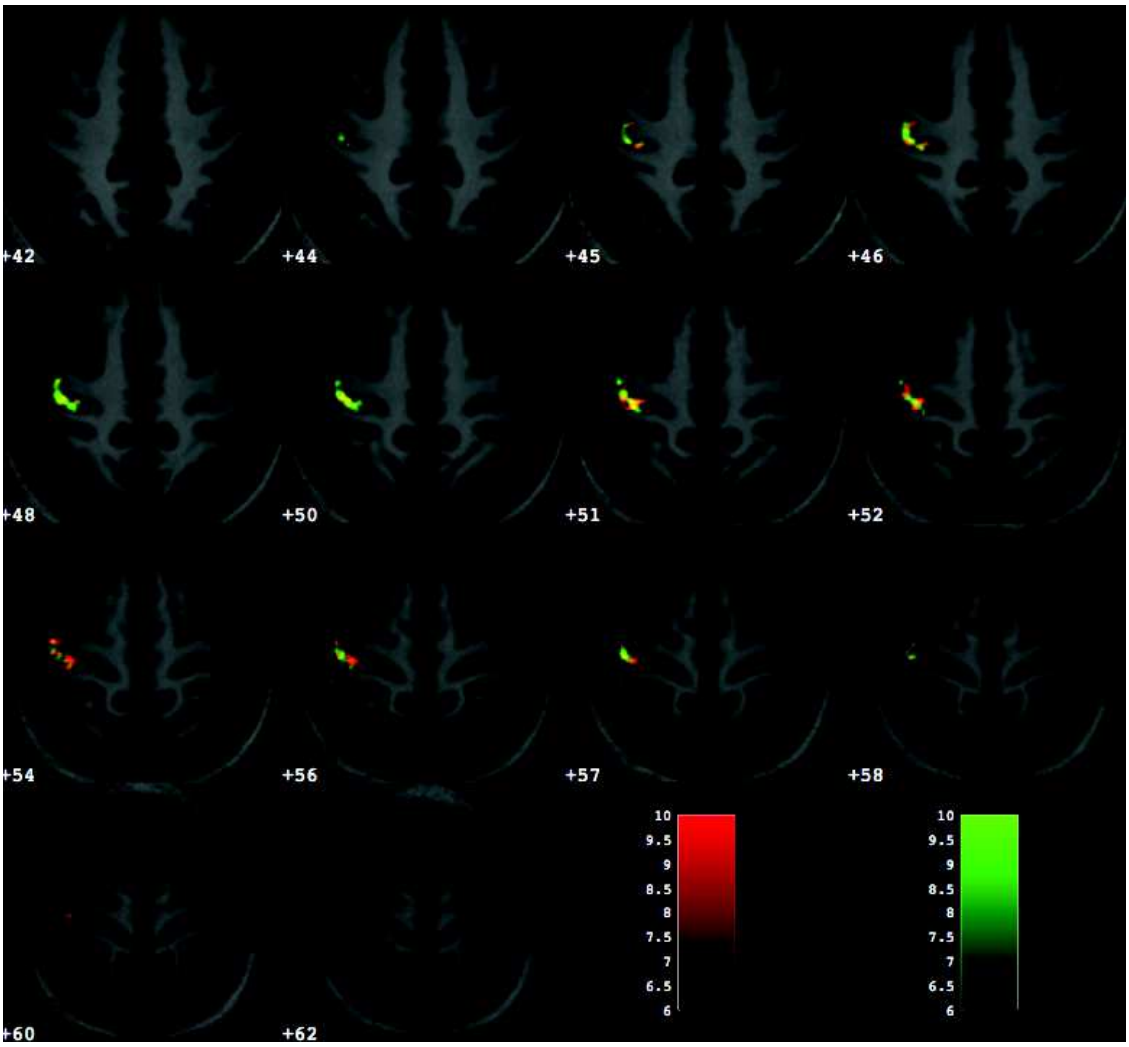

Figure 11.13: *Axial view of 14 slices. Activation map of the* ***extension (red)*** *and* ***flexion (green)****, of both hands, movement is represented. M1 seems to be activated form the deeper part to the upper part. T-test:* $p < 0.01$ *(corrected) and cluster size*> 20.

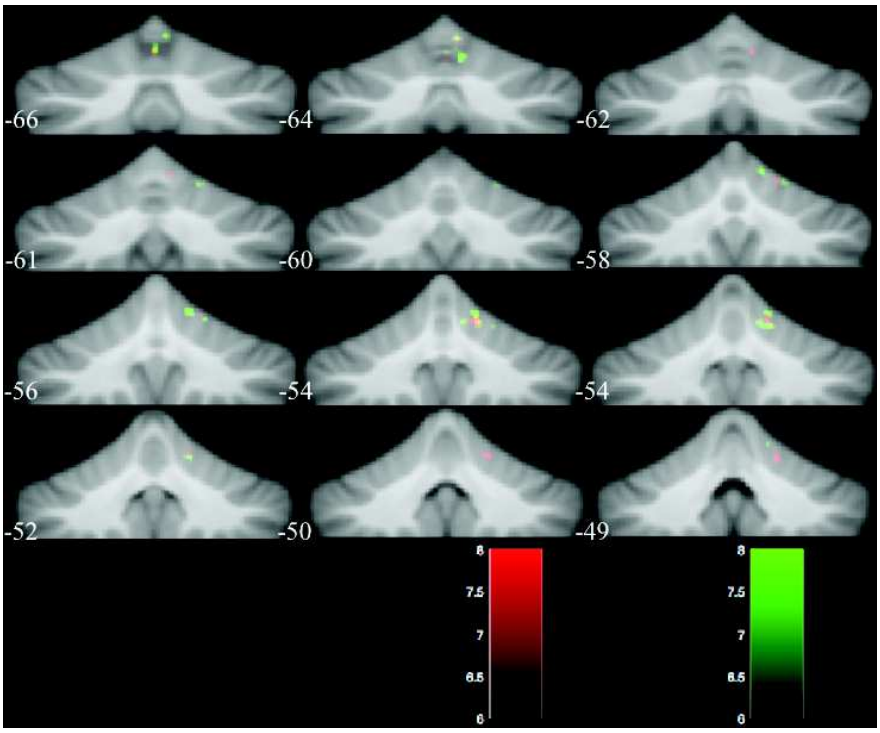

Figure 11.14: *Coronal view of 16 contiguous slices. Activated map of the* ***extension*** *(red) and the* ***flexion****, of both hands, movement are represented. There is no contralateral activation. It seems that extension end flexion are more active in lobules VI at* $y = -55, -56$*. Whereas there is more flexion activation in lobules V-VI at* $y = -66, -64$ *and extension activation in lobules VI at* $y = -50, -49$ *(see Figure 3.6). T-test:* $p < 0.05$ *(corrected) and cluster size*> 20*.*

Figure 11.15 represents the map concerning the common activated regions (*conjunction*) for extension and flexion, of both hands,. There is no contralateral activation. There is a large acti-

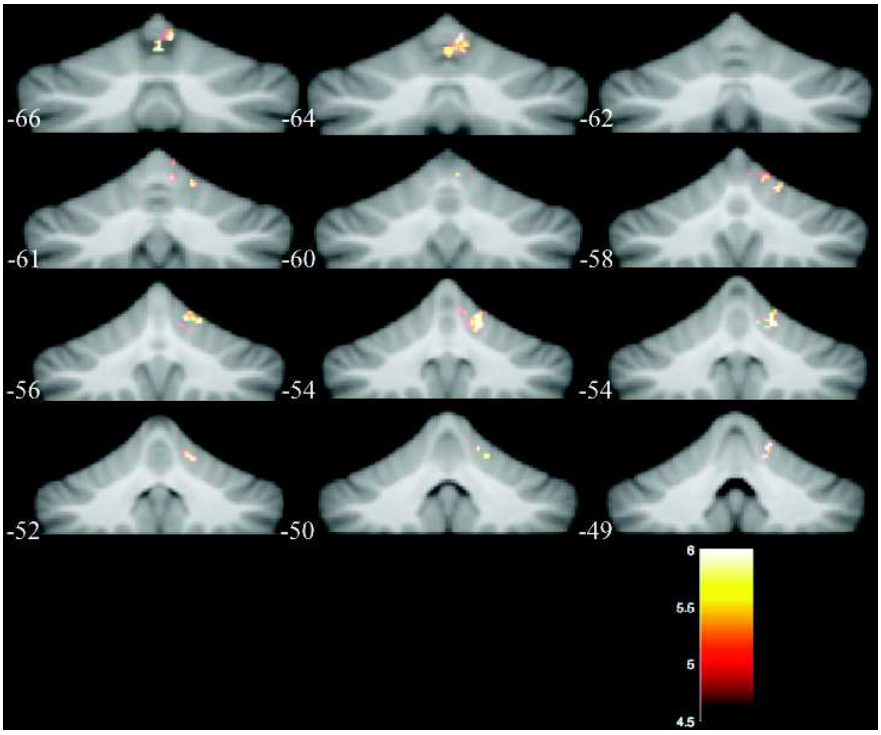

Figure 11.15: *Coronal view of 13 contiguous slices. Activated map of the* ***extension and flexion common activated regions (conjunction)****, of both hands, is represented. There is no contralateral activation. There is a large activation cluster across lobules V and VI at* $y = -64$*. Different activated spots appear in lobule VI at* $y = -58, -56, -55, -54$*. (see Figure 3.6). T-test:* $p < 0.05$ *(corrected) and cluster size*> 20*.*

vation cluster across lobules V and VI at $y = -64$. Different activated spots appear in lobule VI at $y = -58, -56, -55, -54$. T-test: $p < 0.05$ *(corrected)* and *cluster size*> 20.

Testing the differences between extension and flexion movement, with a Student T-test, does not give significant results.

11.4 Hand segments effect

Motor cortex

In Figure 11.16, 11.17 and 11.18 the **thumb, fingers and wrist** activation maps are respectively shown. Several spots appear in M1,S1 and SMA. T-test: $p < 0.0001$ *(uncorrected)* and *cluster size*> 20.

In Figure 11.19 the **common region** (*conjunction*) of activated voxels between **thumb, fingers and wrist**, of both hands extension and flexion, is represented. A large *hand-knob* region appears involved in all the hand's parts movements. T-test: $p < 0.0001$ *(uncorrected)* and *cluster size*> 20. The large overlap means that there is no specificity of the *hand-knob* for any part of the hand, nor for movement direction.

In Figure 11.20 the activated voxels for **thumb** (red), **fingers** (green) and **wrist** (blue), of both hands extension and flexion, is represented. T-test: $p < 0.0001$ *(uncorrected)* and *cluster size*> 20. A slight gradient appears, with the thumb activation located more laterally, the fingers in the middle part of the *hand-knob* and the wrist located more medially.

If we perform a T-test for wrist > thumb we found a spot medially at z=+48 in M1. T-test: $p < 0.001$ *(uncorrected)* and *cluster size*> 20 (Fig. 11.21).

Testing the interaction between factors gives no significant results.

Cerebellum

Figure 11.22 represents the activation maps for the thumb (red), fingers (green) and wrist (blue) movements, of both hands extension and flexion. The activation corresponding to the wrist seems more extended than thumb and fingers activations. The activation corresponding to the wrist seems more extended than thumb and fingers activations IV, V and VI lobule. T-test: $p < 0.001$ *(uncorrected)* and *cluster size*> 20.

11.5 fMRI reliability evaluation

Nine subjects of the healthy population was imaged twice in one year, forming a "Test" and a "ReTest" group. To assess the reliability of our fMRI results a 4-way ANOVA on the "Test"-"ReTest" groups, for all tasks, was computed. In Figure 11.23 the activation map of the common regions

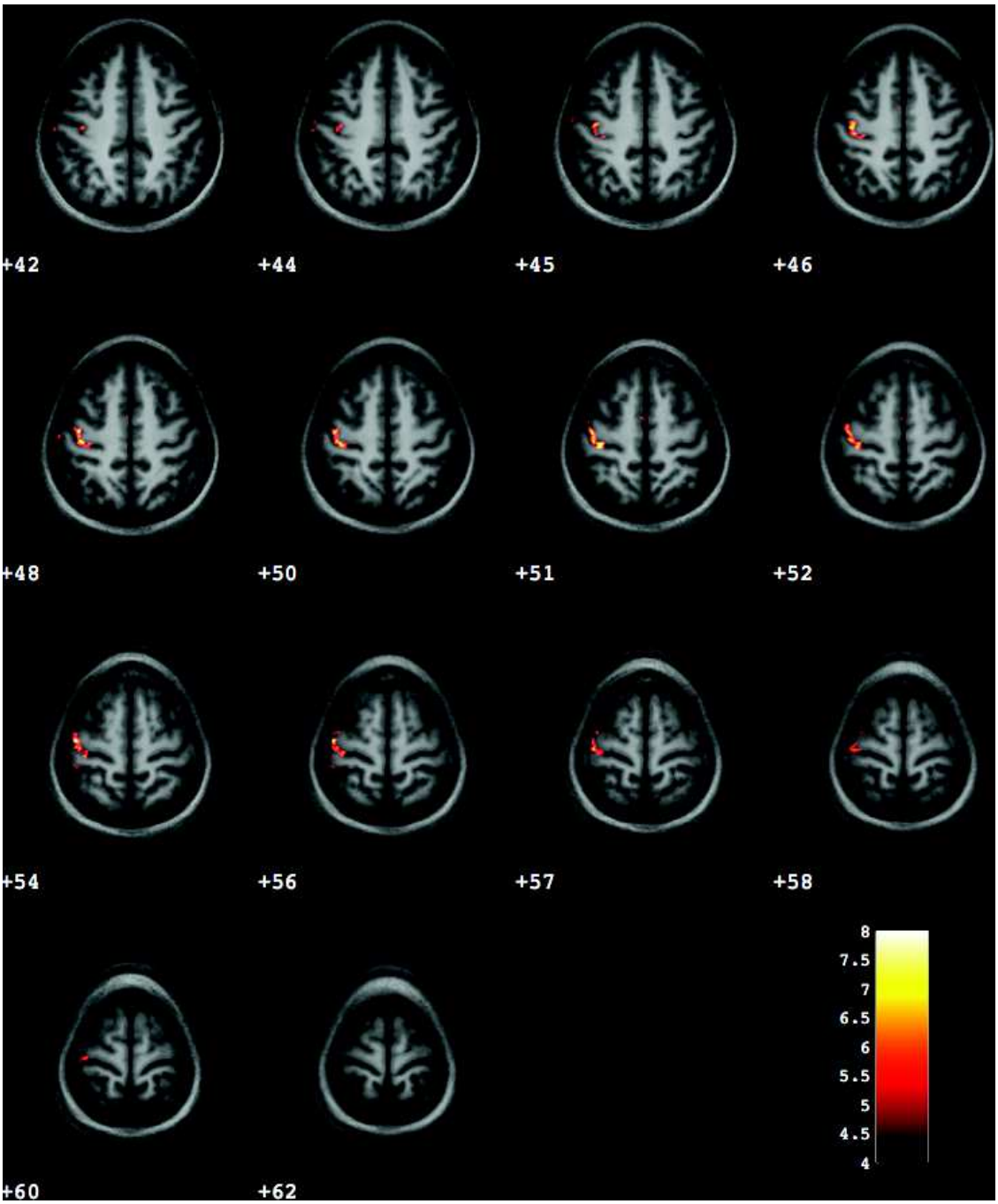

Figure 11.16: *Axial view of 14 slices. Activation map the the* ***thumb movement****, of both hands extension and flexion. T-test:* $p < 0.0001$ *(uncorrected) and cluster size*> 20 .

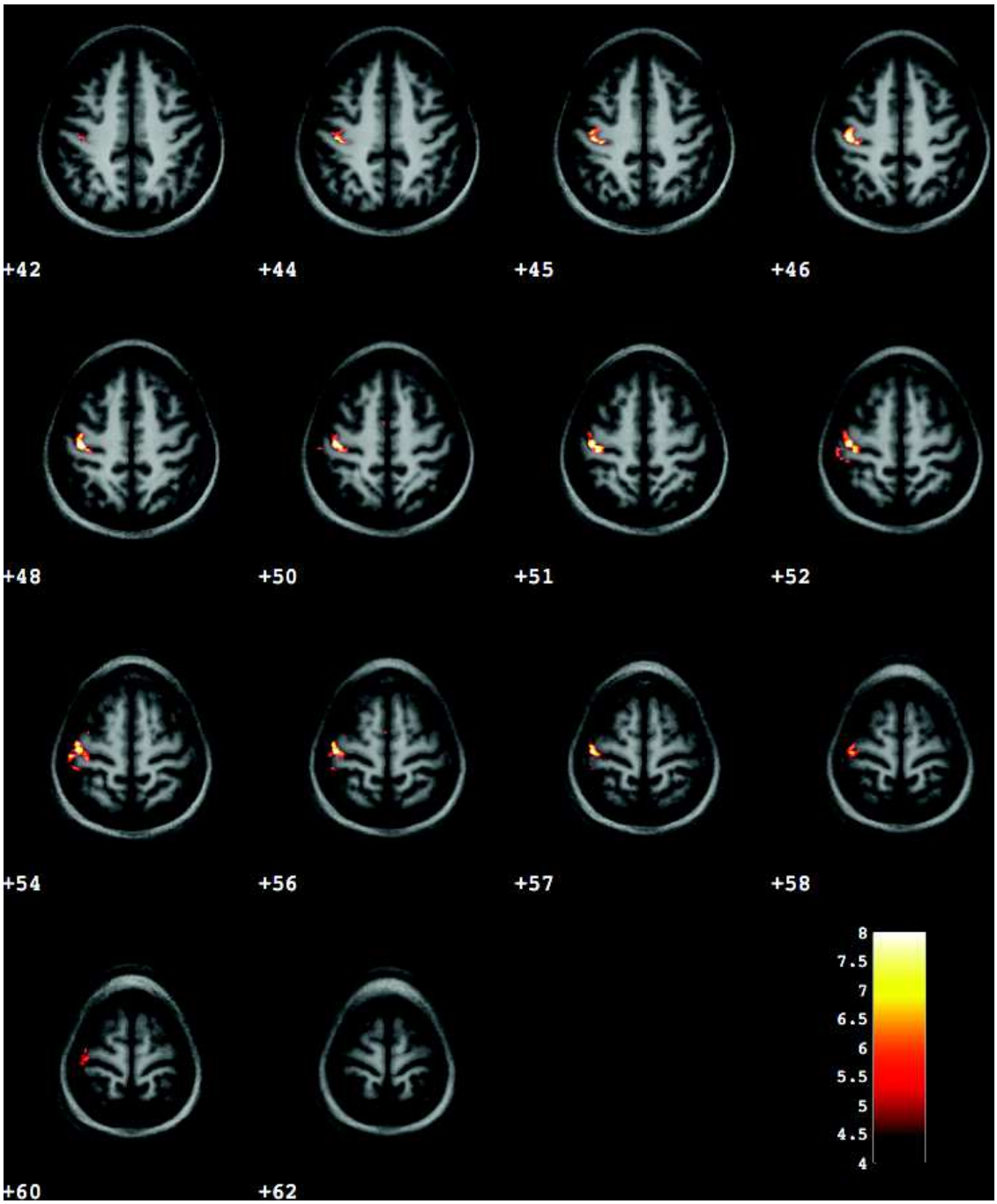

Figure 11.17: *Axial view of 14 slices. Activation map of the* ***fingers movement****, of both hands extension and flexion. T-test:* $p < 0.0001$ *(uncorrected) and cluster size*> 20 .

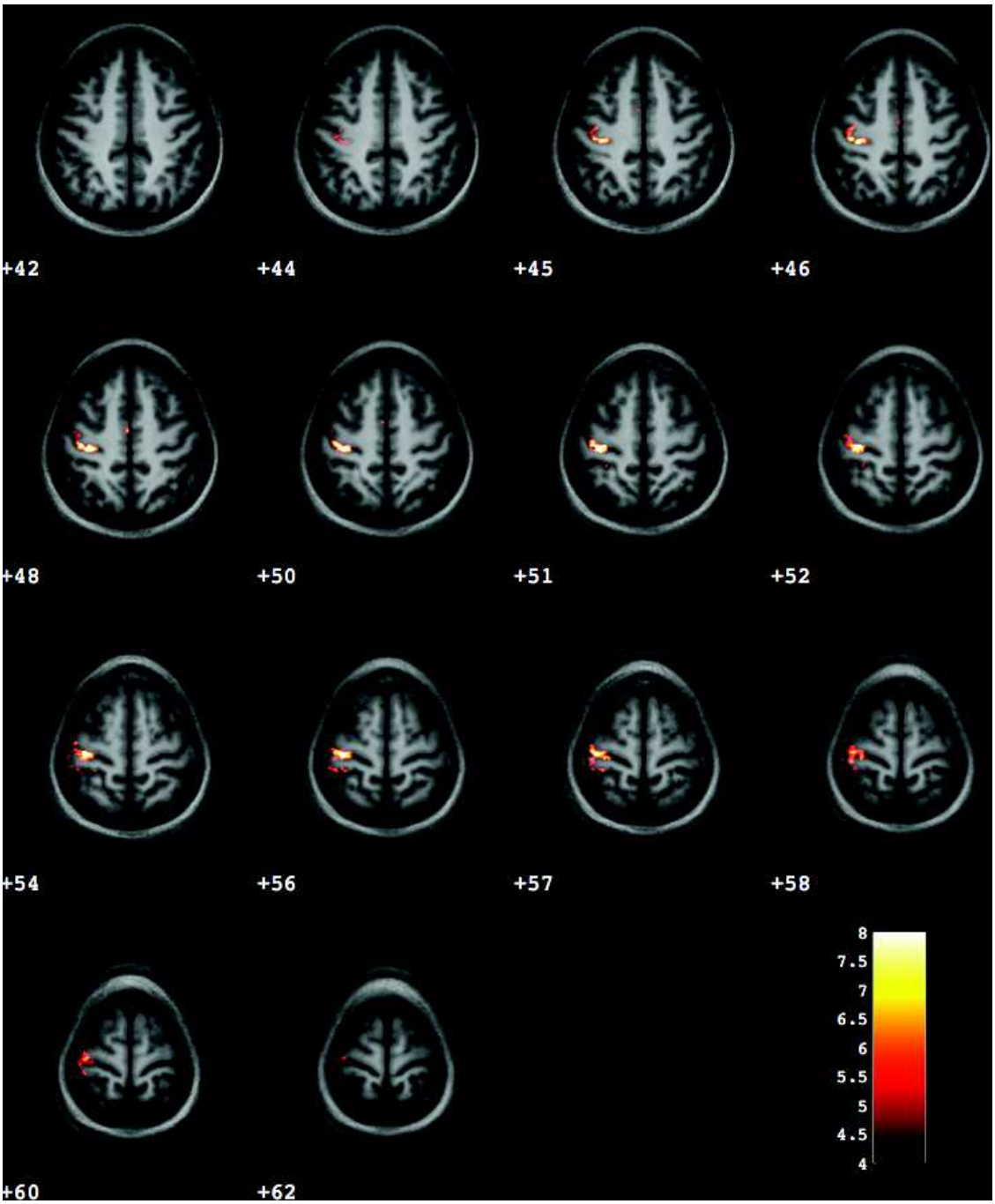

Figure 11.18: *Axial view of 14 slices. Activation map of the* ***wrist movement****, of both hands extension and flexion. T-test:* $p < 0.0001$ *(uncorrected) and cluster size*> 20.

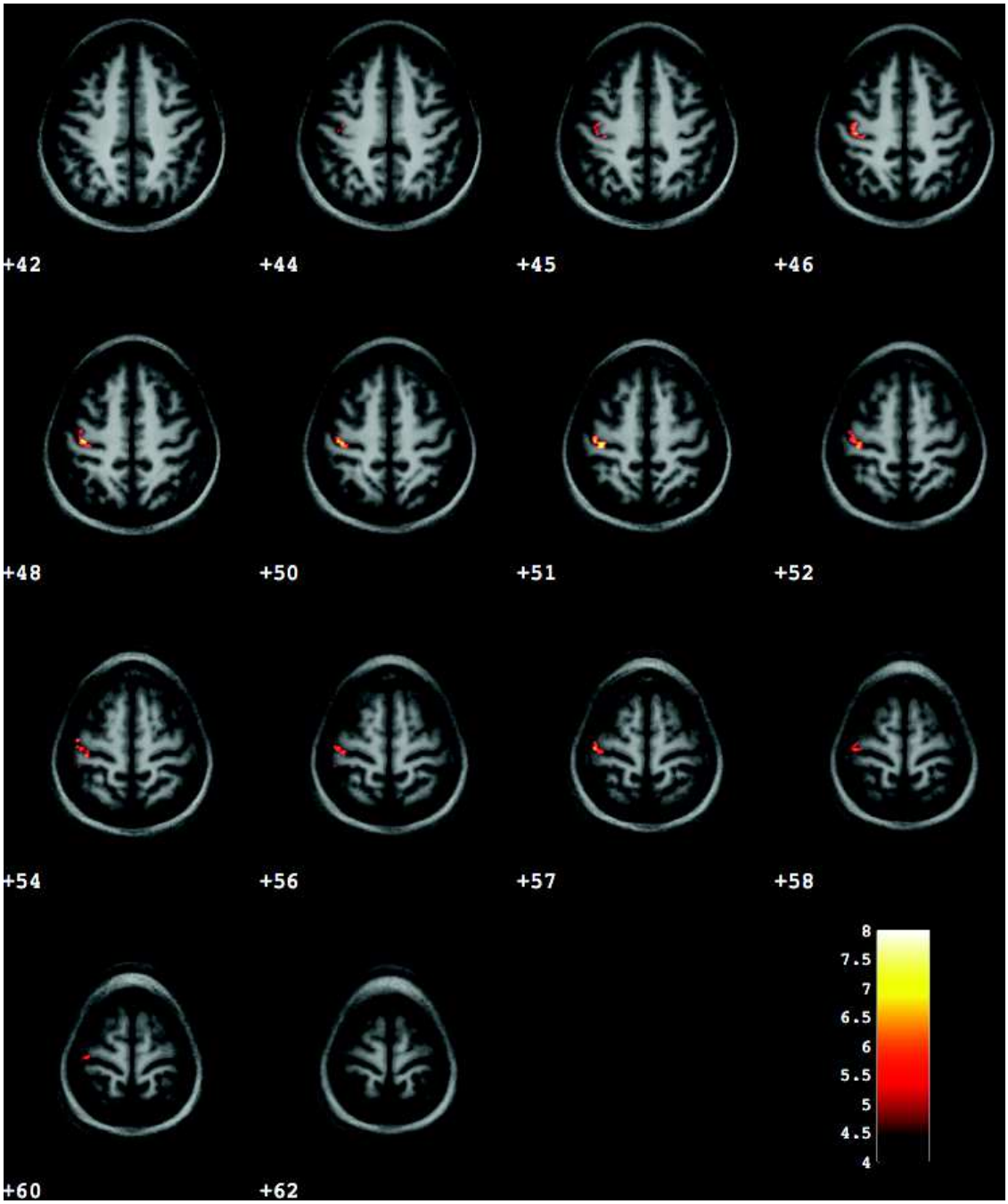

Figure 11.19: *Axial view of 14 slices. Activation map of the* ***common region (conjunction) between thumb, fingers and wrist*** *movement, of both hands extension and flexion. T-test:* $p < 0.0001$ *(uncorrected) and cluster size*> 20.

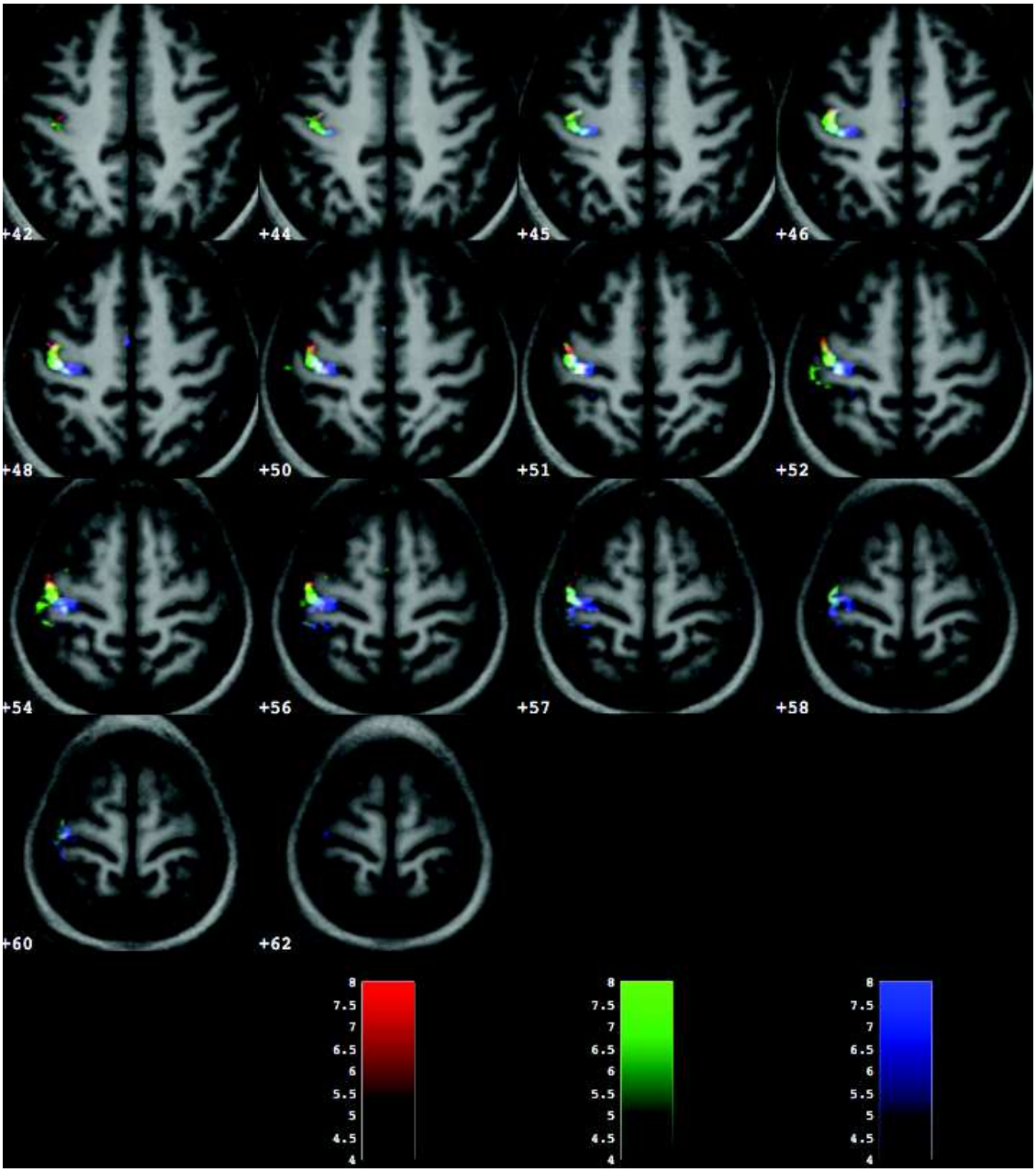

Figure 11.20: *Activation map for the* ***thumb*** *(red),* ***fingers*** *(green) and* ***wrist*** *(blues) movement, of both hands extension and flexion. T-test:* $p < 0.0001$ *(uncorrected) and cluster size*> 20.

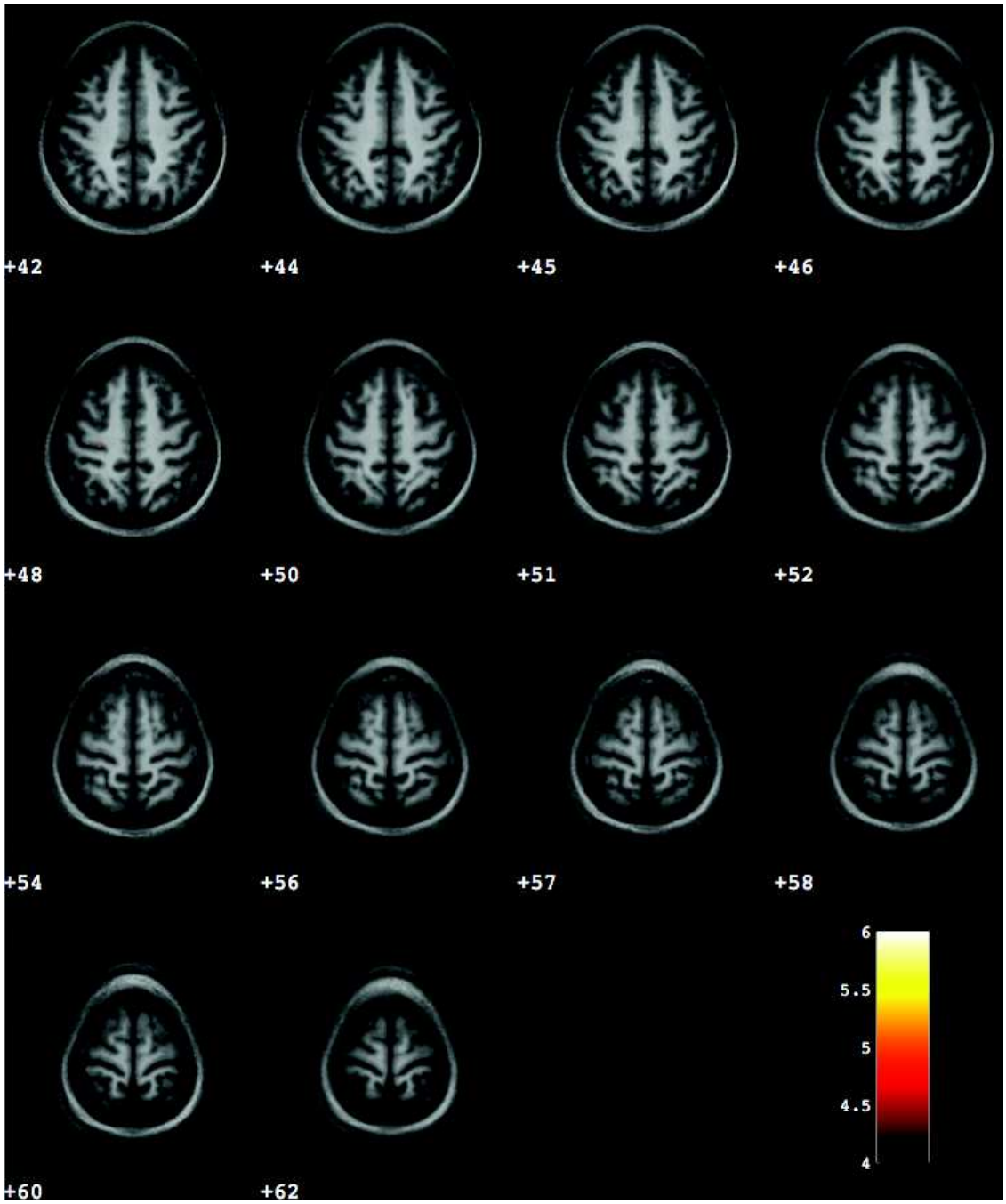

Figure 11.21: *Axial view of 14 slices. T-test for* ***wrist > thumb****, of both hands extension and flexion. A single spot has been found at z=+48 in M1. T-test:* $p < 0.001$ *(uncorrected) and cluster size*> 20 .

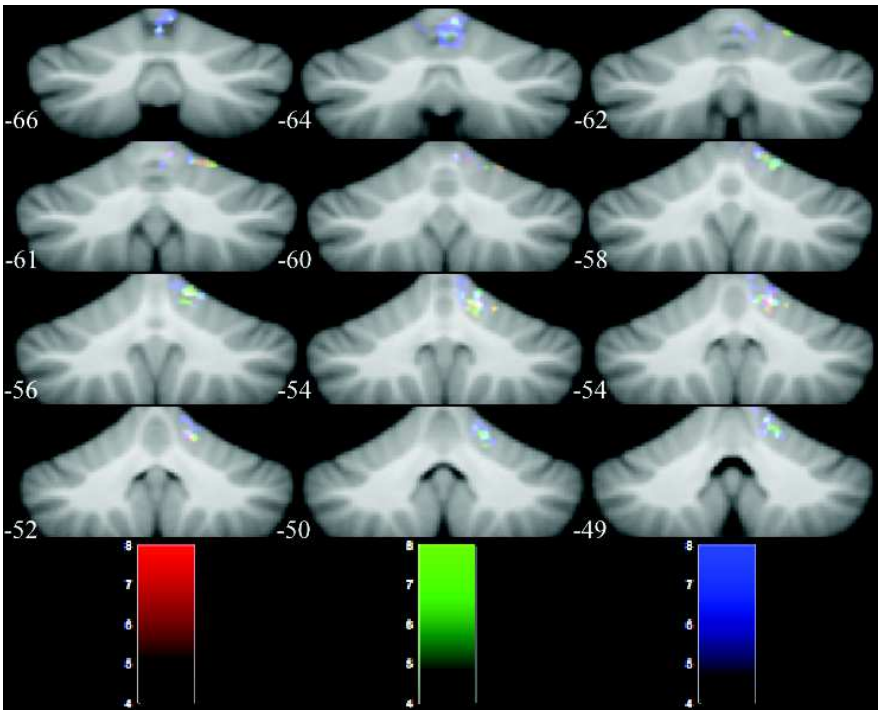

Figure 11.22: *Coronal view of 16 contiguous slices. Activated map of the* ***thumb*** *(red),* ***fingers*** *(green) and* ***wrist*** *(blue), of both hands extension and flexion. There is no contralateral activation. The activation corresponding to the wrist seems more extended than thumb and fingers activations IV, V and VI lobule. (see Figure 3.6). T-test:* $p < 0.001$ *(uncorrected) and cluster size*> 20.

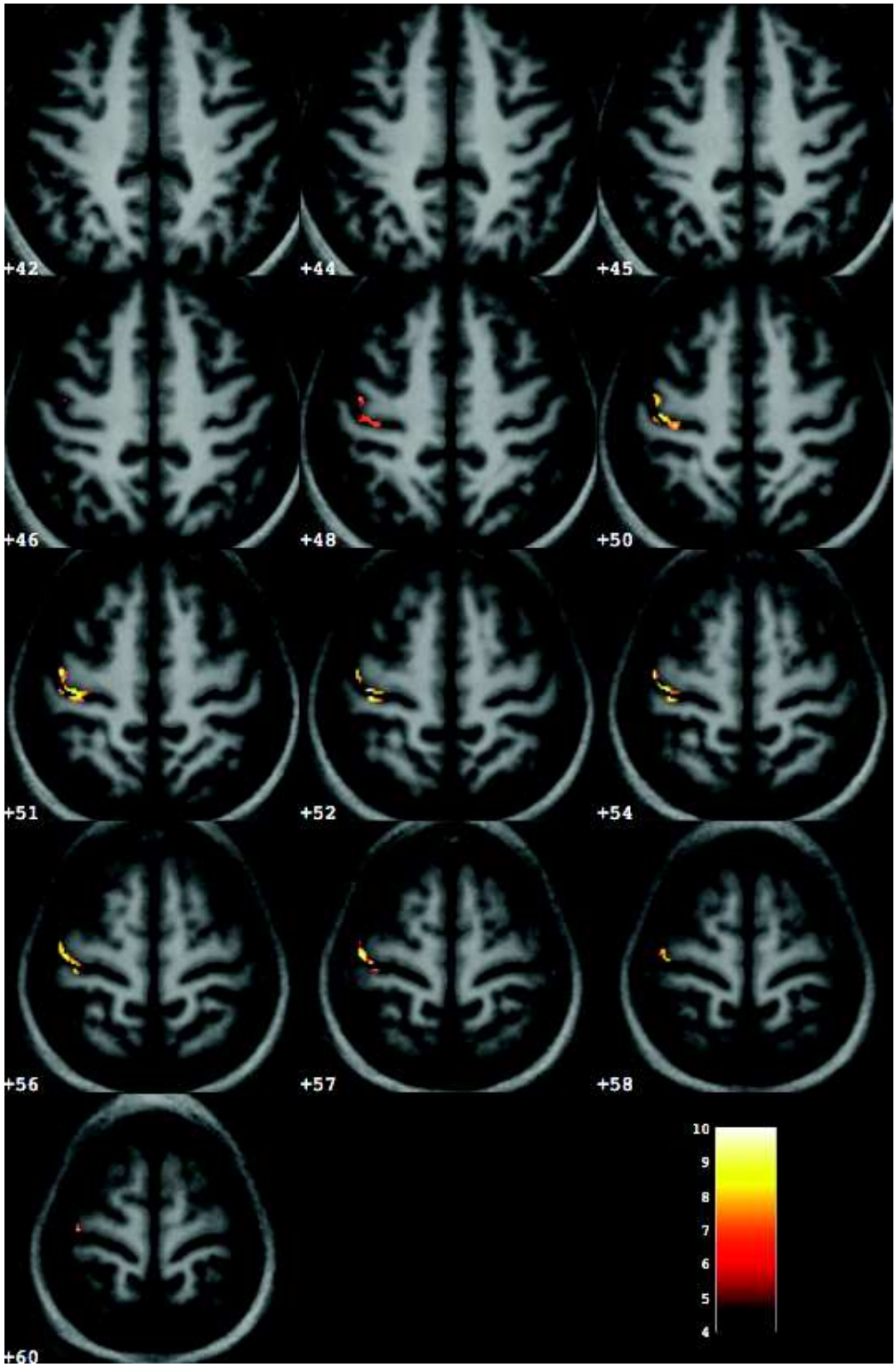

Figure 11.23: ***Activation relatives to the conjunction of the "Test" and "Re-Rest" tasks, for 9 subjects imaged twice. The common region (conjunction) appear well localised in M1 and S1***. *T-test:* $p < 0.05$ *(corrected) and cluster size*> 20.

(*conjunction*) relative to "Test"-"Re-test" factor is shown. T-test: $p < 0.05$ *(corrected)* and *cluster size*> 20. Functional activations are well localised in M1 and S1 proving the reliability of the localisation of our results.

Figure 11.24 show the results for a Student's T-test "*Test*" $>$ "*ReTest*". This result proves that

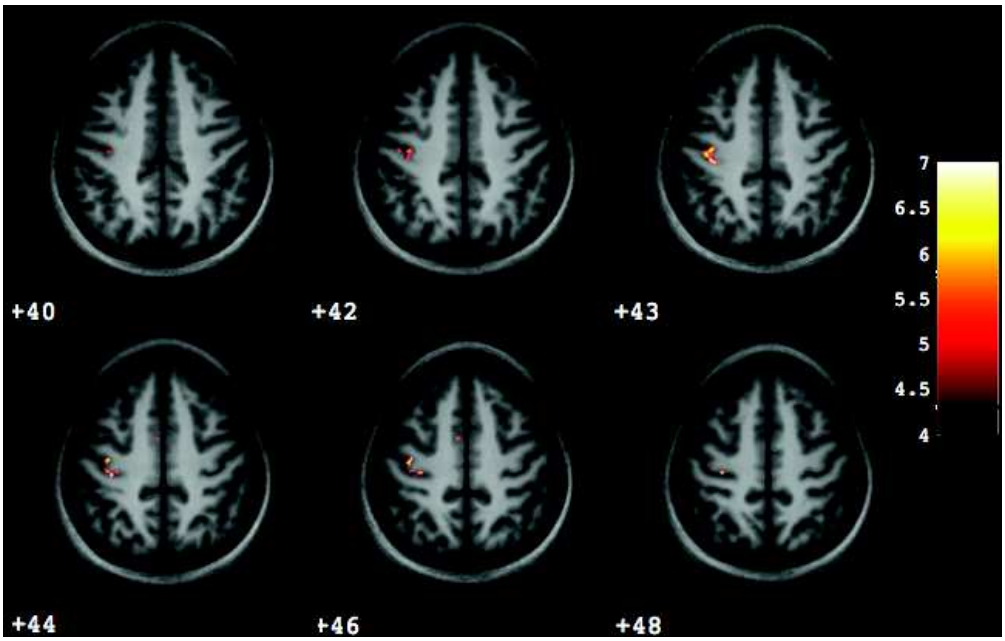

Figure 11.24: *Activation relatives to the Student's T-test* "***Test***" **>** "***Re-Rest***". *The activated foci appear well localised in M1 and S1. T-test:* $p < 0.05$ *(corrected) and cluster size*> 20.

differences between "Test" and "ReTest" groups concern the activation level, not the spatial localisation. We hypothesise that this might be due to differences in experimental conditions (experiments were separated by one year) but some learning effects as documented in Loubinoux *et al.* [Loubinoux 2001] can not be ruled out. No activation was detected for Re-Test $>$ Test with the same statistical threshold (p<0.01 *corrected*, *cluster size* > 20).

CHAPTER 12

Preliminary clinical results: rehabilitation study in patient

Two patients were acquired. In order to match the average age between the patient and the healthy population, only the patient 2 has been investigated (see Section 6.1.2). We explore the brain functional changes in a patient who underwent a tendons transfer surgery that restored the right hand movement extension functions. The patient was imaged 5 times during one year: before the surgery (M0) and at M1, M3, M6 and M12 after the surgery (see Section 9.2.1). The time-course of the restoration at the cortical level was studied using an intra-patient 3-way ANOVA, that includes the time factor, the hand factor (operated or healthy) and the movement direction (extension or flexion). The processing pipeline includes a symmetrisation of the two hemispheres so that both hands could be compared. In this analysis, the contralateral activations occur on the left side of the images and the ipsilateral activations on the right side of the images. Our preliminary results concern the **extension** movement, which is the restored function of the right hand.

12.1 Extension movement effect

In Figure 12.1 the activation for the extension tasks performed with the **operated (right) hand** (red) and **non-operated (left) hand** (green) is showed. A Student's t-test was computed for both hands, separately, with thresholds: $p < 0.0001$ *uncorrected* and *cluster size*> 20.

For the operated hand (red) we found an activation pattern that is much less lateralized than in the controls group. It includes contralateral activations mainly in S1 and SMA, and a little in M1 and contralateral S2 and ipsilateral activations in M1 and SMA. For the non-operated hand (green), the activation pattern includes contralateral M1 ($z = 54, 55$), bilateral SMA and ipsilateral pre-motor cortex (PM).

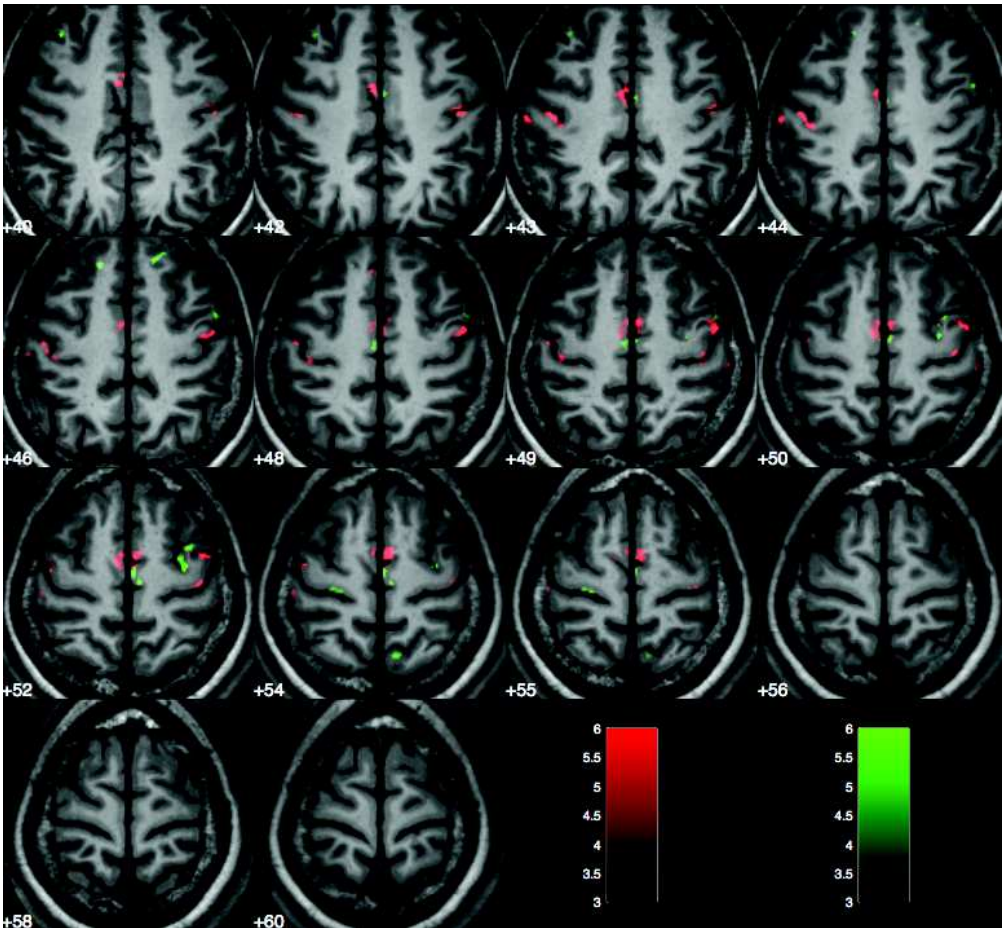

Figure 12.1: *Activation related to the* ***extension*** *tasks performed with the* ***operated (right) hand*** *(red) and the* ***non-operated (left) hand*** *(green). T-test:* $p < 0.0001$ *(uncorrected) and cluster size>* 20.

Testing a statistically higher activation for the extension movement with the operated as compared to the non-operated hand we obtain the results in Figure 12.2 for **non-operated > operated**

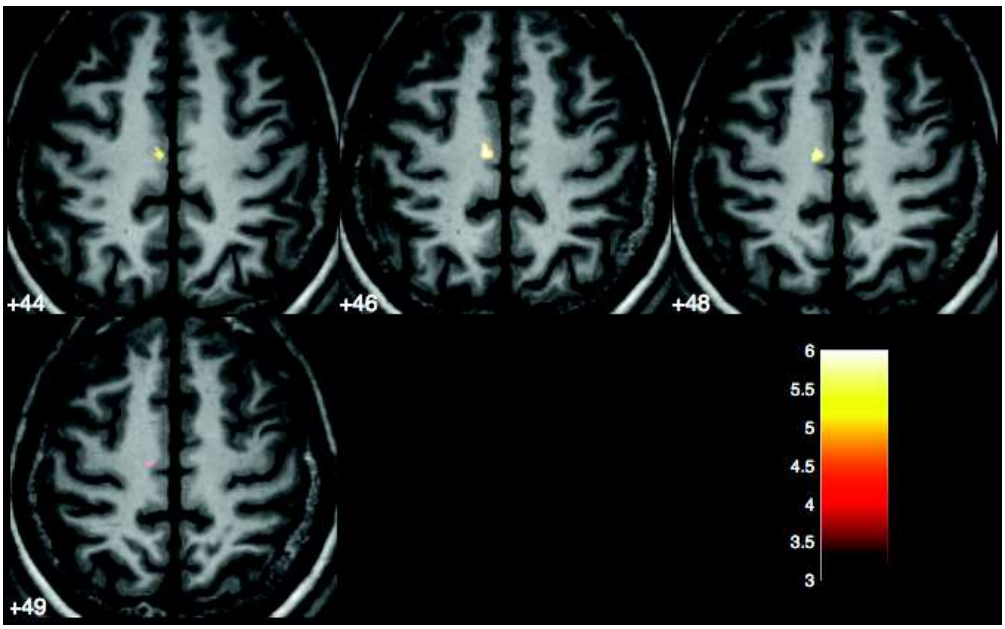

Figure 12.2: *Activation related to the* ***extension*** *tasks. The results were tested with a Student's t-test of* ***non-operated hand > operated hand****. T-test:* $p < 0.001$ *(uncorrected) and cluster size*> 20.

activations and in Figure 12.3 for **operated > non-operated** activations. The tests were performed with a Student's t-test, non-corrected $p < 0.0001, k > 20$. The contralateral upper SMA ($z = 44$ to 49) is more involved for the non-operated hand than for operated hand. The operated hand recruits more than the non-operated hand, the contralateral S1, ipsilateral M1 ($z = 48$), S1 ($z = 42$) and contralateralinferior SMA ($z = 40$).

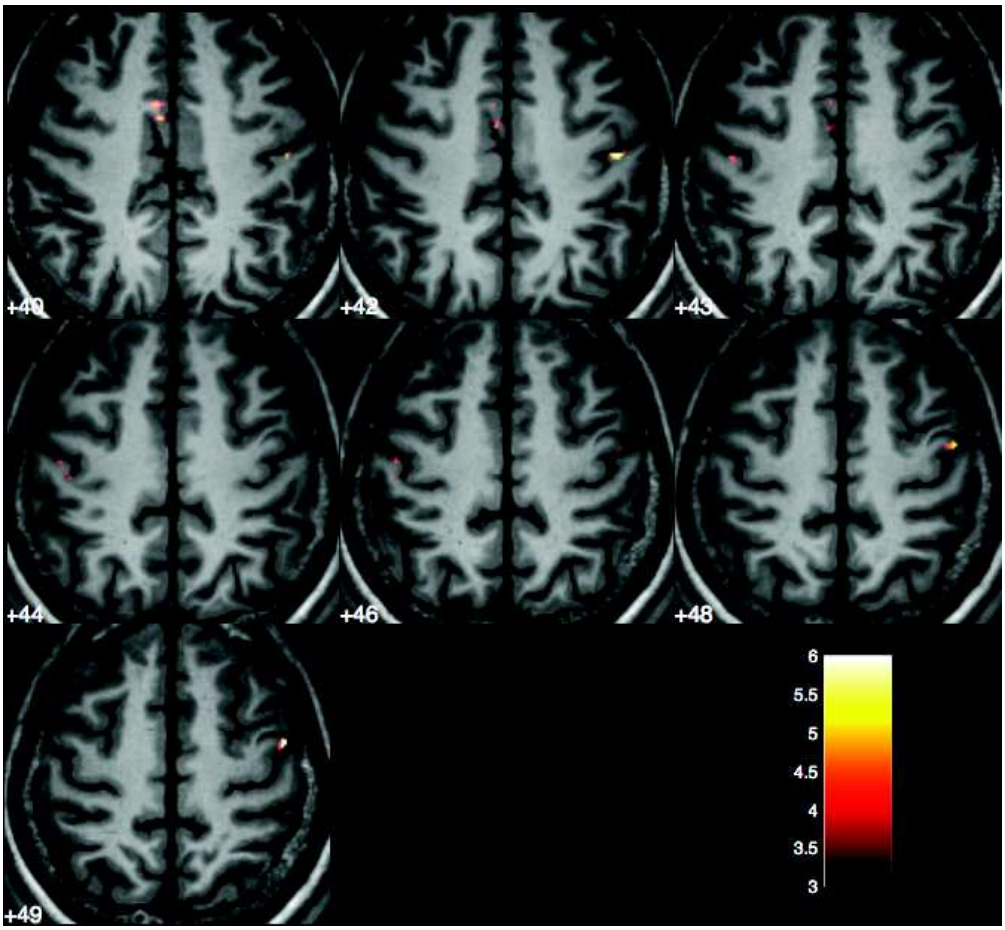

Figure 12.3: *Activation related to the* ***extension*** *tasks. The results were tested with a Student's t-test of* ***operated hand > non-operated hand****. T-test:* $p < 0.001$ *(uncorrected) and cluster size*> 20.

12.2 Comparison of the extension movement between the patient and the control group

Here we qualitatively compare the activation of the patient who underwent a tendon transfer surgery at each time point with the activations obtained in the 9 subjects of the controls group who repeated twice the experiment.

In order to find variations that could not be related to experiment repetition, we first look for a meaningful single-subject statistical threshold (see below). Then, we used this threshold at each time-point to find the pattern related to the extension of the operated hand that cannot be assigned to time repetition only but by recovery after surgery. Finally, at each time point, we compared these recovery patterns to the reference pattern provided by the control group. In two subjects from the control group that performed twice the experiment, we performed an intra-subject 3-way ANOVA similar to the patient's, with the same 3 factors (time, hand and movement direction). We tested for statistically significant differences between right-hand extension at first and second session. We retain as "meaningful threshold", the threshold such that no difference could be found between the two sessions. We found that the non-corrected $p < 0.0001$ *(uncorrected)* and $k > 20$ were meaningful.

The recovery patterns related to the **extension** of the operated hand are displayed in Figures 12.4, 12.5, 12.6, 12.7, 12.8 respectively before surgery and at **M1** (just after the plaster removal), **M3**, **M6**, **M12** after the surgery, for the patient (red) and for the control group (green).

Before surgery, the patient could not extent his right hand but the attempt to do so, activates a pattern that cannot be explained by mental imagery of movement. Rather it presents activations in the SMA bilaterally and in the ipsilateral M1, evidencing already a motor pattern reorganisation, probably due to long-term plasticity following his accident. At **M1**, the patient could not yet extent his operated hand and no activation could be evidenced at the meaningful threshold we used in M1, nor in S1. At **M3**, the patient had intensive reeducation training, could extent slightly his hand. At that time, an ipsilateral activation in M1 could be observed. At **M6**, the patient could extent much better his hand. We found at that time a contralateral S1 and S2 activation at our threshold. Note that when lowering this threshold to $p < 0.001$ *(uncorrected)* and *cluster size*> 20, we could also observe activation in S1. Finally, at **M12**, the patient has fully recovered his hand extension movement in daily life. The extension pattern presents significant ipsilateral activations in M1 and

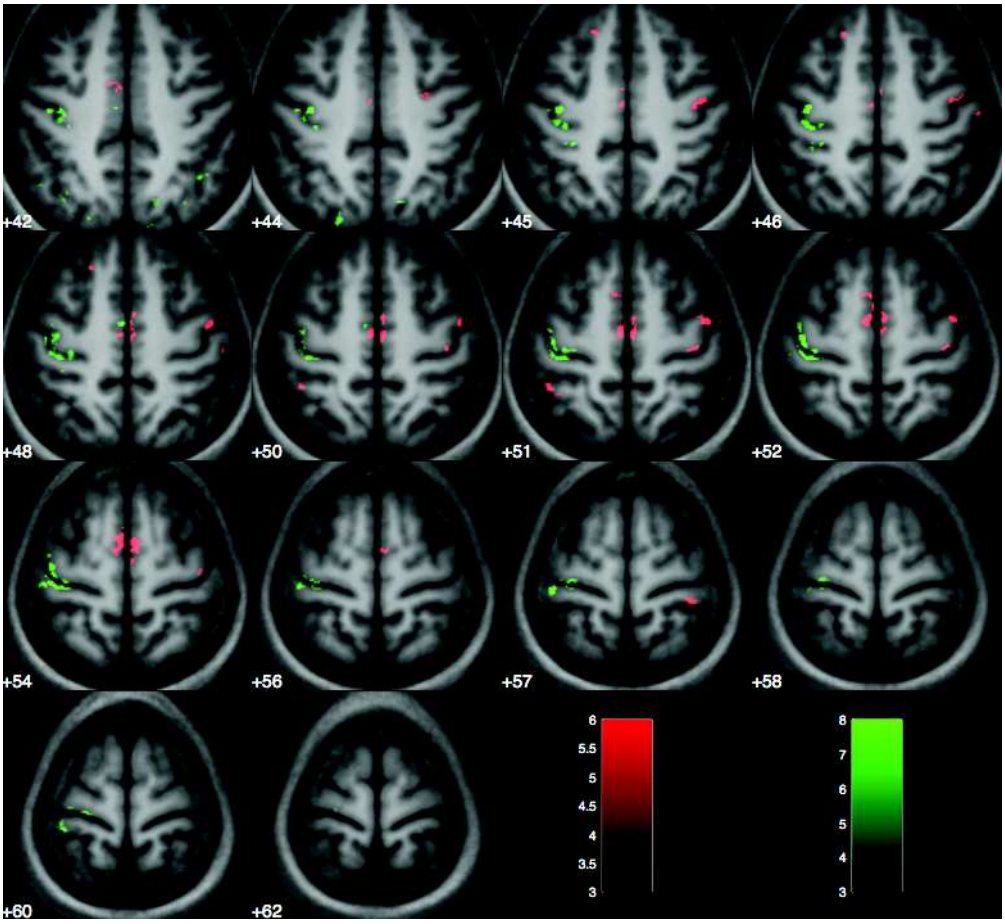

Figure 12.4: *Activation maps for the right hand extension, in patient* ***before the surgery*** *(red) and in the control group (green).T-test:* $p < 0.001$ *(uncorrected) and cluster size*> 20.

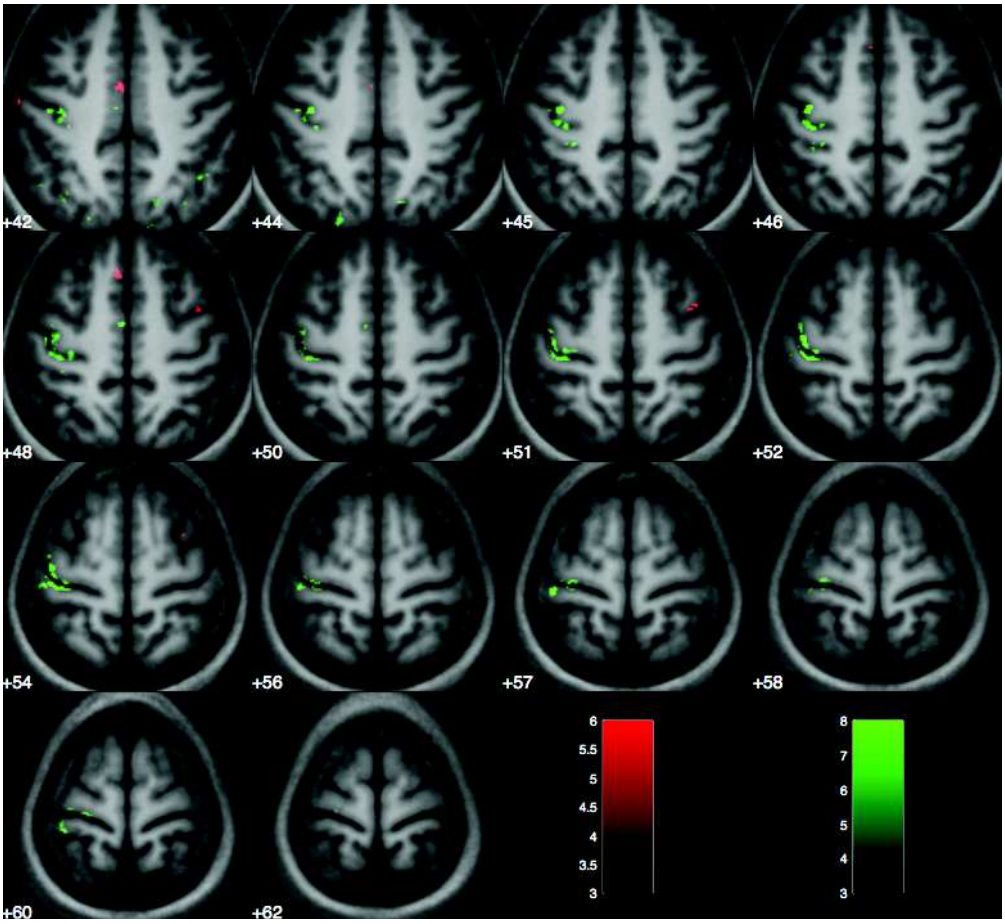

Figure 12.5: *Activation maps for the right hand extension, in patient at* ***M1*** *(red) and in the control group (green). T-test:* $p < 0.0001$ *(uncorrected) and cluster size*> 20.

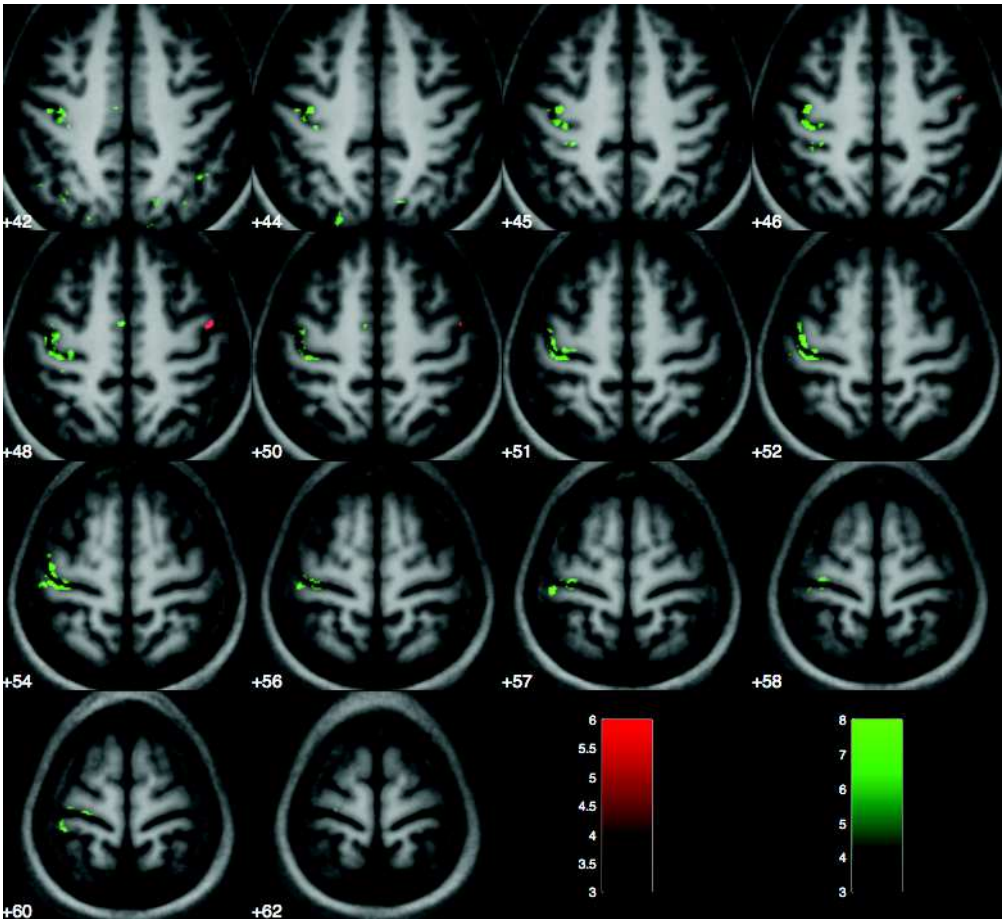

Figure 12.6: *Activation maps for the right hand extension, in patient at* ***M3*** *(red) and in the control group (green). T-test:* $p < 0.0001$ *(uncorrected) and cluster size*> 20.

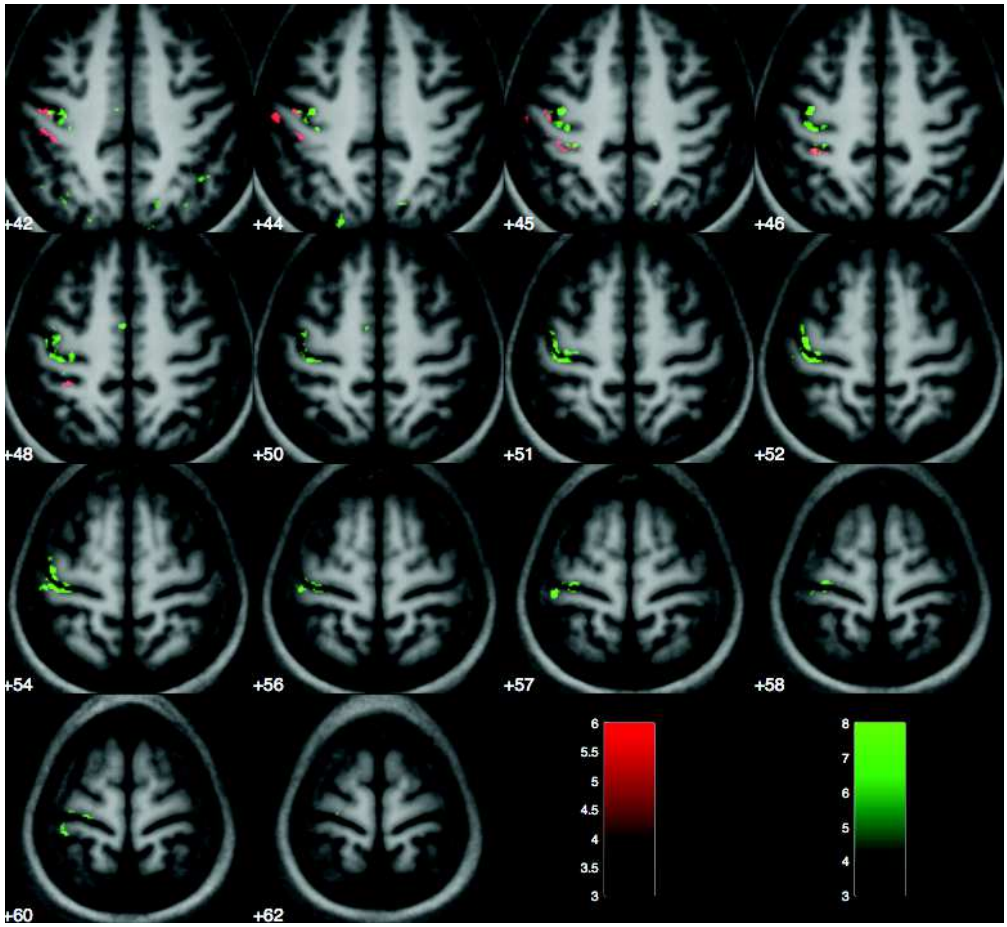

Figure 12.7: *Activation maps for the right hand extension, in patient at* ***M6*** *(red) and in the control group (green). T-test:* $p < 0.0001$ *(uncorrected) and cluster size*> 20.

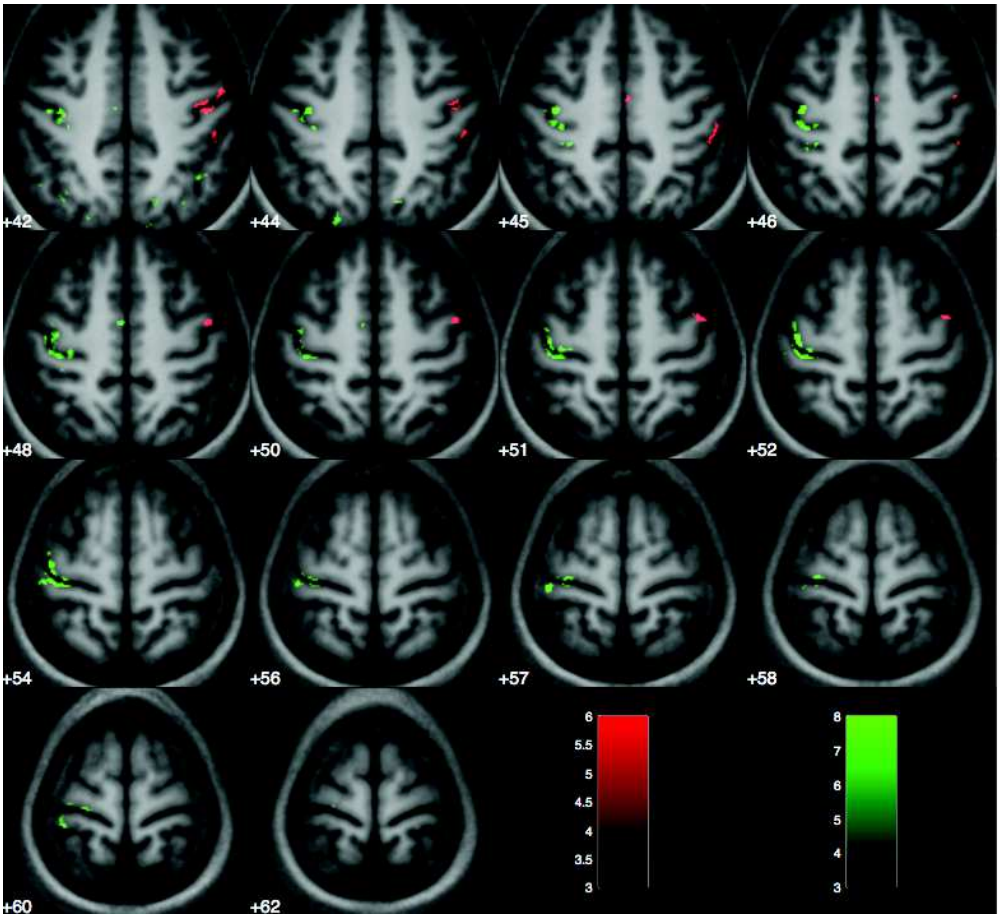

Figure 12.8: *Activation maps for the right hand extension, in patient at* ***M12*** *(red) and in the control group (green). T-test:* $p < 0.0001$ *(uncorrected) and cluster size*> 20.

S1. Note that when lowering this threshold to $p < 0.001$ *(uncorrected)* and *cluster size*> 20, we could also observe additionally activation in S1.

Globally, we find a global motor network reorganisation, much less lateralised than in the normal subjects, mainly involving the SMA and the ipsilateral hemisphere and the sensory areas.

Part V

Discussion and perspectives

CHAPTER 13

Methodological advancement

In an effort to improve the quality of the results provided at the population level using fMRI data, we have investigated the combination of state-of-the-art registration methods with high resolution functional MR data imaging to study the motor cortex. Our study demonstrates that the alignment accuracy provided by nonlinear methods has a direct and strong impact on the detection of activated clusters.

13.1 Reliability and improvement of HR-fMRI

High spatial resolution fMRI improves the localisation of the brain activation. For our study it allows to discriminate the primary motor area (M1) and the primary somatosensory area (S1). The localisation of the activations, relative to the voluntary movement organisation in M1, is more precise, along the anterior bank of the central sulcus from the upper part, corresponding presumably to M1-4a, down to the deeper portion, corresponding presumably to M1-4p, as were described by Geyer *et al.* [Geyer 1996].

We could not assign clearly our results to M1-4a nor to M1-4p (using the anatomy toolbox) because the authors registered the individual limits between both subareas in the MNI template using standard normalisation procedure. This limits de facto the interpretation of our results.

To obtain high spatial resolution we used a multi-shot EPI, encountering some difficulties (see Section 4.2 for multi-shot EPI pros and cons). We were unable to use some fMRI data due to some artefacts. With a TR= 6s head motions, intra-image and intra-shot, occur frequently and seven subjects over the acquired twenty were rejected. Using a multichannel coil can reduce the acquisition time, limiting the effects of head motion.

The benefits of the high spatial resolution fMRI are ascertained, at a group level, using a robust inter-subject registration method. Viceic *et al.* [Viceic 2009] compare to standard global affine and

non-rigid methods their local landmark based registration method developed specifically for the supra temporal plane and using sulci delimiting Heschl's gyrus. They show the importance of local constraints they introduced on the precision of the alignment of individual Heschl's regions. However, the standard spatial smoothing used (6-mm full width at half maximum) limits the precision the assignment to the anatomical regions of activated clusters. In [Tahmasebi 2009] the effect of the spatial smoothing was investigated in auditory cortex, showing for all studied methods that smoothing degrades spatial resolution then activation localisation and increases the magnitude of the peak activation. The resolution we had after smoothing (3x3x3mm^3) was comparable to their initial image resolution (3.3x3.3x4mm^3) which, used without smoothing, led to a more accurate activation loci localisation.

13.2 Improvement brought by non-linear registration methods

The complementarity of anatomical and functional measures indicates that both are necessary to evaluate the impact of nonlinear registration methods on the activation patterns.

Jointly to [Viceic 2009] or [Tahmasebi 2009, Tahmasebi 2011] for auditory cortex, our study demonstrates that the alignment quality provided by nonlinear techniques has a direct and strong impact on the functional activation detection (improvement of the statistical significance of the detected clusters) and localisation (improvement of the accuracy of the clusters position).

In accordance to [Hellier 2003, Klein 2009], anatomical measures showed that methods with high degree of freedom improve the alignment of specific brain areas and increase overlap of cortical ribbon as observed here with DARTEL and DiDa compared to SPM8 (Figure 10.3). The smoothness introduced by the realignment method is a direct effect of its performances: lower the realignment quality higher the smoothness is (see the different blurring in the mean image in Figure 10.1. However, in absence of explicit anatomical constraints (grey- and white- matter overlap for DARTEL and sulcal constraints for DiDa), the DDe results in unsatisfactory deformations despite relatively good measure of grey-matter overlap.

We provided additional data with the analysis of the Jacobian of the deformations. The spatial distribution of the deformation (Figure 10.4a) indicates clearly that in the absence of explicit anatomical constraints, such as gray- and white- matter overlap for DARTEL and sulcal constraints for DiDa, DDe computed unsatisfactory deformations despite of a relatively good measure of grey-

matter overlap. DARTEL deformations remain relatively smooth (Figure 10.4b) while associated with good anatomical and functional measures. This suggests that DARTEL provides deformations that respect the anatomo-functional organization of the cortex. DiDa generates stronger deformations compared to DARTEL. The additional compressions were mainly located between the left and right central sulci, indicating that the constraints from the two central sulci competed in this region (Figure 10.4b). Indeed, unlike DDe, DiDa and DARTEL were not restricted to the common ROI and covered the entire brain volume such that the constraints between hemispheres could interacted. More interestingly, voxels corresponding to relatively high dilatations were distributed on both banks of the central sulci and especially around the hand-knob structure. This suggests that DiDa did integrate the information from the shape of the central sulcus while registering the surrounding cortices between subjects.

Clearly, based on functional measures (Figure 10.7 and Figure 10.8), and clusters positions (Figure 10.5 and Figure 10.6), SPM8 and DDe can not be used to robustly detect and accurately localise hand movement cortical activation. On the contrary, based on anatomical and functional measures, DARTEL and DiDa show similar interesting performances. While anatomical measures shows that DARTEL and DiDa have similar performances (Figure 10.3), functional measures reveal some differences. The local constraints introduced in DiDa have a positive effect on T-values (Figure 10.7, Figure 10.8). Despite these differences are not statistically significant (Figure 10.9) the explicit sulcal constraints introduced by DiDa seem to improve slightly the already good overlap of individual primary motor areas provided by DARTEL, showing that any change in the deformations impacts on functional group analysis. Indeed, only these two methods allow to distinguish for the first time with fMRI multiple spots of activation embedded within M1 for the different hand movements.

13.3 Perspectives

Our study could be interestingly extended using efficient nonlinear methods such as IRTK, cortical-surface-based registration methods (e.g. FreeSurfer [Fischl 1999, Yeo 2009]) or recent combinations of volumetric and surface registration [Postelnicu 2009, Du 2011] . Indeed, surface based analysis is attractive especially for functional data analysis because it respects the essentially 2D-structure of the cortical ribbon facilitating for instance the affectation of activation to the right

side of the bank of a sulcus. However, for registration purpose, surface-based and volume-based methods seem to perform with similar accuracies [Klein 2010]. Note that a recent version of the Demons algorithm to a sphere is available [Yeo 2009]. When using surface analysis, the method used to assign functional activation onto the surface is a crucial step to guarantee the accuracy of the final results (see for instance Tucholka *et al.* [Tucholka 2012] to appear). Each method used its own template: the well-known ICBM template for SPM 8 [Mazziotta 2001] , a single subject for DDe and a custom-built group template for DARTEL and DiDa. We did not study the influence of the template (except for DDe) and then can not separate differences due to the template from those due to the alignment algorithm *per se*. Our results with DDe illustrate the bias induced by the choice of a single-subject as template and the lack of landmark constraints visible both through anatomical and functional measures. An extension of DDe to iteratively compute, similarly to DARTEL or DiDa, a mean as template might be an interesting alternative.

CHAPTER 14

Neuroscientific advancement

14.1 Hand movement cortical representation in human

Starting with the pioneering work of Penfield [Penfield 1935], several studies have investigated the motor cortex using various imaging techniques (see [Rowe 2012] for a review) and more precisely the cortical representation of hand movements. However, the fine functional organization of M1 remains poorly known in humans. The post-mortem study of Geyer [Geyer 1996] evidenced a subdivision of Brodman area 4 into an anterior part (4a) and a posterior one (4p) on the basis of cytoarchitecture and of the quantitative distribution of transmitter-binding sites. Additionally, Geyer et al. found a multiple representation of thumb and index flexion in M1a and M1p –whose functional roles remain to be precised– using PET and manual tasks in alive subjects. In healthy subjects, different fMRI studies of the cortical representation of fingers revealed highly overlapping maps, together with an arrangement of finger-specific hot spots that follows a somatotopic organisation [Sanes 1995, Rao 1995, Kleinschmidt 1997, Beisteiner 2001, Dechent 2003]. Our study demonstrates that combining high resolution fMRI with accurate realignment of the central sulcus of individuals provided by DARTEL or DiDa opens the way to non invasive functional exploration of the human hand motor cortex at the population level. It shows the feasibility to differentiate the multiple hot spots related to thumb movement in M1, consistent with the results found in sub-areas 4a and 4p by Geyer and co-workers using PET [Geyer 1996].

14.2 Functional overlap and lateralisation

Our results show that, at a group level, there is an important overlap between the movement direction activation, extension and flexion (Fig. 11.12), that may concern M1-4a and M1-4p. A large overlap is also present between the activation of the different segments of the hand, thumb,

fingers and wrist (Fig. 11.19), in M1 and in lobules IV, V and VI of the cerebellum (Fig. 11.22).

By using high spatial resolution fMRI, combined with a robust inter-subject registration method, we find a **non-specific activated area**, the *hand-knob*, **at a group level** (Fig .11.1). The activated cluster covers the *hand-knob* region, from the deeper part of the central sulcus to the upper part in M1, and so probably M1-4a and M1-4p subregions, and S1 contralateral. Also the SMA is recruited (Fig. 11.2). Importantly, we did not find any ipsilateral activation for the basic movements that where studied here. Thus, in the reference maps that are obtained from our control group, these movements are highly lateralised and do not need for the recruitment of areas from the ipsilateral hemisphere. This observation holds for motor cortex and for the cerebellum.

These observations are in line with the previous observations of primary motor representations [Beisteiner 2001, Hlustík 2001, Indovina 2001, Sanes 2001, Grodd 2001, Dechent 2003]. They highlighted the complexity of the hand movement arrangement in the brain cortex. More recently, Meier and collaborators [Meier 2008] found an overlapping somatotopy in human for which the representations of the different body parts are intermingled, and a complex organisation for the arm and hand, with fingers emphasised in a core region surrounded by a dorsal and ventral representation of the arm (Fig. 3.8).

Several authors argues that the overlap and intermingling of cortico-motoneural cells for different hand muscles enables M1 to create a wide variety of muscle synergies [Rathelot 2006b].

14.3 Handedness

Functional lateralisation in the human brain has been studied intensively, but significant controversy over the brain mechanisms that instantiate it remain. Anatomical characteristics of the handedenss have been investigated, concerning the central sulcus shape, by Sun *et al.* [Sun 2011]. They found a significant difference between dextrals and sinistrals, relative to the shape of the left central sulcus. This finding strongly support the idea of a different shape related to dominant *vs.* non-dominant hand. After removal of these potential CS shape differences using the symmetrisation procedure, we could further investigate whether there is or not functional differences between the activation of dominant and non-dominant hand, a feature that had never been investigated, to our knowledge.

Here, we investigated, at a group level, the difference between dominant and non-dominant

hand activation thanks to the acquisition (high spatial resolution fMRI) and image processing (robust inter-subject registration method and symmetrisation process) that we used. We registered all the images in the same reference system, with DARTEL and a symmetric template, so that the inter-subject and inter-hemispheric anatomical variability are minimised. Our functional results show a robust overlap between activation maps related to the left hand's and the right hand's movements, and the statistical analysis reveals a slight larger extent of activation for the dominant hand as compared to the non-dominant hand, at a group level (see Section 11.4).

14.4 Movement direction

At group level, we did not find any statistically significant difference between the patterns related to flexion and extension movements. However, the superimposition of both patterns seem to present a shifted representation for flexion and extension (Fig. 11.13) with a response more medial for the flexion and more lateral for the extension. This result first described by electrophysiology in monkeys [Kakei 1999], was recently found in humans using TMS [Z'Graggen 2009] and by fMRI by Toxopeus *et al.* [Toxopeus 2011]. The large overlap between the patterns of extension and flexion might be related to the co-activation of extensors and flexors during any flexion and extension tasks (at least to stop the movement).

14.5 Hand segments

At group level, we did not find any statistically significant difference between the patterns related to movements of the thumb, of the fingers and of the wrist, except a small difference between thumb and wrist movements, that elicit a more lateral representation for the thumbs and a more medial representation for the wrists. However, when the three patterns were superimposed, we could observe a gradient of activation, in which the wrist activation is represented more medially, the fingers in the middle part of the hand-knob and the thumb more laterally. This is what was also observed in the early fMRI literature in the field [Kleinschmidt 1997, Beisteiner 2001, Hlustík 2001, Sanes 2001, Grodd 2001, Dechent 2003].

14.6 Perspectives

At a group level our analysis can be performed in a new surface reference system describing the sulcus, based on anatomical landmarks of the central sulcus [Cykowski 2008]]. The functional activation can be then projected on the reconstructed surface of the CS and compared with other subjects. Our preliminary results using this method were part of a IEEE-EMBS 2011 proceeding [Coulon 2011] (see publication A.3, O. Coulon *et .al*, "*Two new stable anatomical landmarks on the Central Sulcus: definition, automatic detection, and their relationship with primary motor functions of the hand.*").

CHAPTER 15

Clinical advancement

15.1 Functional recovery of patient who underwent a hand tendons transfer surgery

In this study we explored the brain functional changes, across the time, due to the tendon transfer surgery. Two patients were imaged, before the surgery (M0) and at M1, M3, M6 and M12. The construction of an accurate probabilistic map of cortical representation of hand movement at the healthy population level gives a reference to study mechanisms of brain functional plasticity. In order to match the average age between the patients and the healthy population we investigate only the patient 2. During one year of functional recovery he recruits a larger network concerning the operated hand (right hand) in comparison with the non-operated hand (left hand). In particular contralateral S1, SMA and ipsilateral M1, S1 are the main regions involved in the functional plasticity of the operated hand. Compared to the control group the patient recruits different neural networks while gradually recovering his hand extension movement ability. Activation is mainly observed in the ipsilateral hemisphere. After a period of 360 days, the patients did not activate similar neural circuits observed in healthy subjects. Before surgery, we found that a functional plasticity has already occurred, resulting in a less lateralised motor network than the reference group and an important recruitment of the SMA.

These results support the view that the functional reorganisation in this patient occur mainly, not at a regional level, but rather at the motor network level. This is in line with the hypothesis that during recovery the inter-hemispheric inhibitory system is disinhibited, leading to a strong bilateralised pattern of activation.

15.2 Perspectives

For the functional changes investigation of the patient who underwent a tendons transfer surgery, we will include the analysis of the activation regarding the non-operated hand, of the extension/flexion tasks and we will quantitatively compared the patient with the control group. Moreover, our study could be extended including other patients and integrating the hand movements detector signals registered during the fMRI sessions (see publication A.4, O. Martin *et .al*, "*Neural Plasticity Correlates Of The Thumb Extension Recovery After Tendon Transfer. A Case Study.*"). During the study, the patients underwent two sessions, a high-resolution one presented in this manuscript, and a standard resolution one (single-shot EPI, 3s of repetition time, a 3mm isotropic voxel size, covering the whole brain) with the same tasks which is not presented in this thesis. The analysis of these later data could confirm (or infirm) the pattern related to functional recovery in the patient and could further permit to explore the potential implication of the basal ganglia along the recovery process.

It could be interesting to perform a brain structural plasticity study, longitudinally, on the patient who underwent the hand tendons transfer. This can be done by using methods such as the VBM [Thomas 2009], or the one performed by Sun *et al* [Sun 2011] to investigate the shape variations of the central sulcus between dominant and non-dominant hand. It could apply to study structural changes in patients after hand tendons transfer surgery and in comparison with a population of healthy subjects.

Part VI

Appendix

Appendix A

Publications

A.1 F. Pizzagalli *et al.*, Conf Proc ISBI, 2012

WHICH REGISTRATION METHOD FOR HIGH RESOLUTION FMRI TO EXPLORE HAND MOVEMENT CORTICAL REPRESENTATION ?

F. Pizzagalli[⋆], *G. Auzias*[†], *C. Delon-Martin*[⋆] *and M. Dojat*[⋆]

[⋆] INSERM U836-UJF-CEA-CHU (GIN), Grenoble, France
[†]LSIS Lab, UMR CNRS 6168, Marseille, France

ABSTRACT

Progress in our understanding of brain functions relies on our capability to explore the human cortical surface at a fine scale (typically 1.5 mm isotropic at 3T). For this purpose, high accuracy is required for all processing steps from image acquisition to data analysis. For group studies, the high inter-subject variability of the human cortices hampers their precise registration. Based on the hypothesis that function follows anatomy, accurate inter-subject sulci registration should result in precise alignment of corresponding functional regions and then improve the statistical significance of parametric maps. Converging evidence from intra-operative mapping, cytoarchitectony, and functional neuroimaging conclusively rely primary cortical regions to morphological landmarks. Thus, the so-called "hand knob" landmark, a specific feature of the central sulcus (CS), consistently separates the primary motor cortex (M1), on its anterior bank, from the primary sensory cortex (S1) on its posterior bank. In an effort to define a dedicated processing pipeline for a fine non-invasive exploration of human M1, we compared four nonlinear registration methods applied on high resolution fMRI of basic hand movements. First, based on anatomical measures, we show how recent local or global diffeomorphic techniques improve the alignment of sulcal folds in M1. Second, with functional measures, we quantitatively evaluate their effect on the detection and localization of activation clusters at the population level. Based on such measures, we show that two diffeomorphic methods working globally (DARTEL) or including sulcal constraints (DISCO+DARTEL) improve activation detection and localization opening the way to a non-invasive exploration of the human hand motor cortex.

***Index Terms*—** Human brain, Functional MRI, Spatial normalization, Central sulcus, Realignment.

1. INTRODUCTION

A large portion of M1 is devoted to the control of hand movements. Its fine exploration using fMRI cannot be achieved without high spatial resolution image acquisition (1.5 mm isotropic at 3T) and a dedicated processing pipeline. Because of high inter-individual variability of M1, one crucial step is the quality of the inter-individual M1 realignment. M1 lies on the anterior bank of CS and extends across the precentral gyrus. On the posterior bank of the CS, lies the postcentral gyrus where primary somatosensory cortex S1 is represented. The segment of the precentral gyrus, which is shaped like a hook in the sagittal plane and an inverted omega in the axial plane (generally referred as the *hand-knob*), is a reliable landmark for identifying the CS [1] (see Figure 4). For conventional group studies, the poor cross-participant alignment of M1 leads to activation underestimation. Moreover, spatial normalization and spatial filtering, performed prior to statistical analysis to reinforce the overlap between individual activated areas, introduce *per se* a functional blurring and a loss of a precise localization of fMRI signals. This clearly hampers the separation of activated clusters found in M1. Because *hand-knob* is a good predictor of M1, we hypothesized that the combination of an accurate alignment of all *hand-knobs* of all subjects with high resolution fMRI, insuring each functional voxel to be attributed to a single gyrus, could improve the functional areas overlap and increase the significance of statistical parametric maps. For image acquisition, the improvement of spatial resolution can be achieved by decreasing plane thickness, increasing the in-plane acquisition matrix using multishot EPI sequences, and restricting the acquired volume to encompass the motor area. For spatial alignment, it is well established that linear registration is inadequate for aligning brain structures such as sulci. Several studies have compared nonlinear brain image registration algorithms working on the whole brain [2, 3], on specific regions [4], or using volume versus surface-based approaches [5]. In all these studies a set of quantitative measures was used to compare deformed structural MR source image and one target. but the effects of the registration algorithm on brain activation detection were not reported. We take a different perspective: we are mainly interested in exploring the effects of non-linear registration methods on the robustness of activation detection applied here to motor cortex investigation. For this purpose we selected a set of four recent methods that address the problem of inter-subject correspondences through different strategies and are representative of the state of the art in this active research field. The performances of the methods were quantitatively evaluated using both anatomical and

high resolution fMRI data coming from thirteen healthy control subjects. It demonstrates the clear improvement provided by large deformations registration methods applied to high resolution functional MRI on the quality of inter-individual brain structure alignment and on the detection and localization of functional activation in M1 area.

First, we considered DARTEL [6] as representative of standard diffeomorphic methods where the deformation constraints, estimated globally on the whole brain scans, align the cortical valleys and crests but without guarantee that sulci of identical anatomical denomination would be properly aligned altogether. Then, we considered DISCO+DARTEL [7] as representative of a class of methods where explicit sulcal landmarks are used to constraint the 3D deformation. Finally, we considered Diffeomorphic Demons [8] as representative of diffeomorphic methods where deformations can be estimated locally to align segmentations of specific three-dimensional region of interests (ROIs), here the *hand-knob* region. Data were also processed using the SPM8 normalization procedure widely used in the neuroscientific community.

2. MATERIAL AND METHODS

2.1. Data Acquisition and Processing

Thirteen right-handed healthy subjects (mean 27.5 y.o.) underwent a block-design fMRI protocol while performing six different tasks for each hand: extension and flexion of fingers, wrist and thumb. BOLD functional images were acquired with a high spatial resolution of $1.5\times1.5\times1.5$ mm^3 using a multi-shot EPI sequence on a 3T whole-body MR scanner (Bruker, Medspec S300). T1-weighted structural images were acquired with $1\times1\times1$ mm^3 spatial resolution using a MDEFT sequence. All functional images processing was performed using SPM8. These images were corrected for motion and very slightly smoothed using a gaussian kernel ($3\times3\times3$ mm^3). Individual statistical contrast images were realigned to the corresponding structural scan in each subject's referential. Random effects statistical group analysis was further performed after contrast images registration in a common referential using the deformation fields derived from the four registration approaches applied to the corresponding structural images. T-values associated to active clusters for each task and each realignment method were computed.

2.2. Inter-subject Registration

Individual structural images were firstly segmented and debiased using unified segmentation approach as implemented in SPM8 [9]. Then, they were registered following four different strategies and software using their own default parameters values: 1/ with mutual information registration on the MNI template (spatial normalization) using SPM8, 2/ DARTEL, 3/ DISCO+DARTEL (DiDa) and 4/ Diffeomorphic Demons (DDe) as implemented in MedINRIA toolbox[1].

–DARTEL [6] optimizes the overlap of grey and white matter tissue masks between subjects through a large deformation technique where deformations are parametrized by a velocity field that is constant in time. The algorithm embeds the construction of an average template from images of the group. The technique has been already applied in different voxel-based morphometry studies with good performances.

–The DIffeomorphic Sulcal-based COrtical (DISCO) registration explicitly enforces the alignment of identified sulci in an iterative approach. Individual sulci are first segmented and identified. An empirical template of sulci is then defined from the set of subjects before diffeomorphic transformation of each individual data onto the empirical template which is proceeded in the general framework of the Large Deformation Diffeomorphic Metric Mapping theory. Improved mask overlap and reduction of sulcal dispersion can be reached through the sequential combination of DISCO and DARTEL (DiDa), with DARTEL being initialized using DISCOs outcome [7].

–Diffeomorphic Demons (DDe) is an efficient algorithm for the non-parametric diffeomorphic registration based on the sum of squared difference in voxels intensity between images [8]. This method has been shown to outperform other techniques when applied locally to align ROIs in the medial temporal lobe [4]. To assess the influence of the reference image on the alignment quality, we applied DDe two times, with two different reference subjects R1 (DDe-R1) and R2 (DDe-R2).

3. RESULTS

3.1. Anatomical measures

To estimate the resulting cross-participant cortex overlap, we considered the intersection of registered grey matter masks restricted to ROIs designed to encompass the motor region in all individuals. We used a fuzzy union overlap metric (see [7]) computed for all pairs of subjects. For each method, we then applied the deformation field to the corresponding individual left/right CS segmented using BrainVisa[2]. The Hausdorff distances for CS between every pair of subjects were computed for each method. The mean and standard deviation of these two anatomical measures are reported in Table 1 and Fig.1 illustrates how the four methods deform locally the individual CS to align them.

As expected, the standard registration procedure used in SPM8 did not allow for a good alignment of CSs because of the strong regularization of the deformations involved in this method. On the other hand, allowing large deformations without imposing explicit anatomical constraints leads to a local mismatch between central and postcentral sulci for some subjects with DDe, with the two reference subjects. The relatively high overlap score given by DDe is made possible by

[1] http://www-sop.inria.fr/asclepios/software/MedINRIA/
[2] http://brainvisa.info

Table 1: Evaluation measures on grey matter overlap (Overlap Score) and on mean distance to the central sulcus (Hausdorff distance) for each method and hemisphere (Left Hemisphere on the left).

Method	Overlap Score (grey matter)	Hausdorff Distance (mm)	Method	Overlap Score (grey matter)	Hausdorff Distance (mm)
SPM8	0.47 ± 0.02	13.77 ± 2.92	**SPM8**	0.41 ± 0.02	12.48 ± 3.11
DARTEL	0.65 ± 0.01	9.61 ± 2.59	**DARTEL**	0.62 ± 0.01	7.85 ± 1.79
DiDa	0.59 ± 0.02	8.19 ± 2.73	**DiDa**	0.63 ± 0.02	6.31 ± 2.20
DDe-R1	0.63 ± 0.02	11.99 ± 2.86	**DDe-R1**	0.62 ± 0.02	13.12 ± 2.45
DDe-R2	0.64 ± 0.02	12.80 ± 3.27	**DDe-R2**	0.44 ± 0.02	18.54 ± 3.57

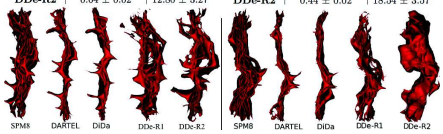

Fig. 1. Left (left) and right (right) central sulci superposition for each method.

the very low regularization of the deformations. When the alignment of CS was explicitly constrained (DiDa), we measured a clear improvement as compared to SPM8. Both DARTEL and DiDa methods provide a better superposition of the GM around the CSs with no significant difference between them. This highlights the fact that DARTEL achieves a good alignment of CS, as already observed in [3].

3.2. Functional measures

Group statistics on functional data indicate clearly that the alignment quality has a direct and strong impact 1) quantitatively on the statistical significance of the detected clusters (Figure 2) and 2) qualitatively on the activated clusters localization (Figure 4). As illustrated on Figure 2, the histograms of the T-value maps thresholded above t=5.0 ($p \leq 0.0001$ voxel level uncorrected) show that the a good sulci alignment obtained with DARTEL or DiDa provides larger activation with higher T-values than SPM8 and Demons do. Jointly with the bad superposition of CSs, Demons provide low T-values for the left and right hand flexion despite a relatively good overlap of gray-matter (Table 1 and Figure 1). Moreover, the bias induced by the choice of the reference subject appears clearly between DDe-R1 and DDe-R2. We further tested whether the four methods had significant effect on activation detectability whatever the task. We used a 2-way ANOVA followed by a Tukey-Kramer test for multiple comparisons on significant voxels ($t \geq 5$, $p \leq 0.0001$ uncorrected). This indicated that methods are different ($p=3x10^{-7}$) and are divided in two groups (SPM8, DDe-R1 and DDe-R2) and (DARTEL and DiDa) with significantly higher detectability performance for the latter (Figure 3). No statistically significant differences were found within each group. Figure 4 illustrates the localization of the main activated clusters at the group level for each method for flexion. In accordance to [10] we found with DARTEL and DiDa two main spots of activation both for flexion and extension tasks remarkably well separated for right hand (Figure 4). With SPM8 note the blurring of the mean structural image and the single large activation cluster that cannot be identified as belonging to M1. Using DDe some activations are localized on the wrong side of the sulcus bank and the double representation in M1 is not clearly elicited.

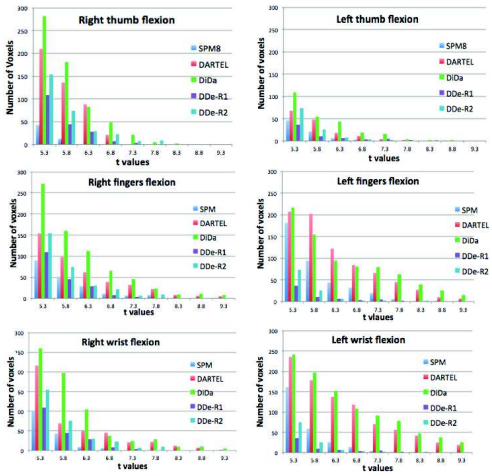

Fig. 2. Number of significantly activated voxels ($p \leq 0.0001$ voxel level non corrected) for nine bins of T-values obtained by group mean effect for flexion. Left hemisphere (left) and right hemisphere (right).

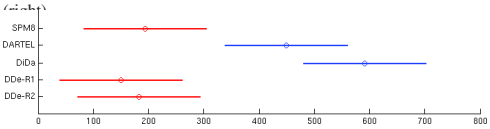

Fig. 3. Multiple comparison of means. Each group mean is represented by a circle and an interval around the circle. Two means are significantly different if their intervals are disjoint, and are not significantly different if their intervals overlap. Y axis: method, X axis: group mean.

4. DISCUSSION

Jointly to [11] or [12] for auditory cortex, our study demonstrates that the alignment quality provided by nonlinear techniques has a direct and strong impact on the functional activation detection (improvement of the statistical significance of the detected clusters) and localization (improvement of the accuracy of the clusters position). In accordance to [2, 3], anatomical measures showed that methods with high degree of freedom improve the alignment of specific brain areas and increase overlap of cortical ribbon as observed here with DARTEL and DiDa compared to SPM8 (Table 1 and Figure 1). However, in absence of explicit anatomical constraints (gray- and white- matter overlap for DARTEL and sulcal constraints for DiDa), the DDe results in unsatisfactory deformations despite relatively good measure of grey-matter

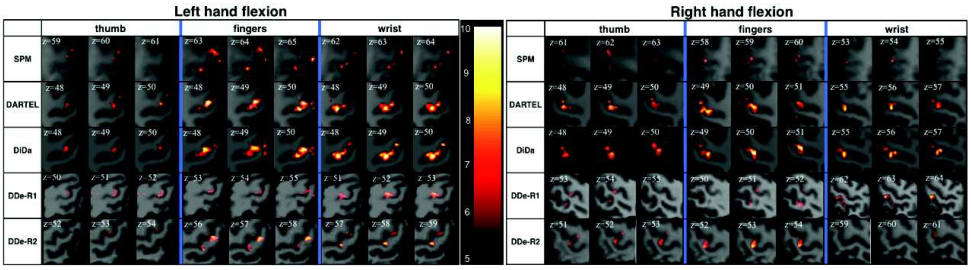

Fig. 4. Functional activation for T≥5 projected on the mean structural image obtained by each method. Three contiguous transverse slices are displayed to show for each method the largest clusters around the right central sulcus (Left) and left central sulcus (Right).

overlap. Clearly, based on functional measures and Figure 4, SPM8 and DDe can not be used to robustly detect and accurately localize hand movement cortical activation. On the contrary, based on anatomical and functional measures, DARTEL and DiDa show similar interesting performances. Despite the difference is not statistically significant, the explicit sulcal constraints introduced by DiDa seem to improve slightly the already good overlap of individual primary motor areas provided by DARTEL, showing that any change in the deformations impacts on functional group analysis. Indeed, only these two methods allow to distinguish for the first time with fMRI and without ambiguity two spots of activation in M1 for hand movements. Our study could be interestingly extended using efficient nonlinear methods such as IRTK, cortical-surface-based registration methods (e.g. FreeSurfer) or a combination of volumetric and surface registration [13]. Our results demonstrate that combining high resolution fMRI with high accuracy realignment of the central sulcus of individuals provided by DARTEL or DiDa opens the way to non invasive functional exploration of the human hand motor cortex under different normal, pathological or after rehabilitation conditions.

5. REFERENCES

[1] T. A. Yousry and al., "Localization of the motor hand area to a knob on the precentral gyrus. a new landmark," *Brain*, vol. 120 (Pt 1), pp. 141–57, 1997.

[2] P. Hellier and al., "Retrospective evaluation of intersubject brain registration," *IEEE Trans Med Imaging*, vol. 22, no. 9, pp. 1120–30, 2003.

[3] A. Klein and al., "Evaluation of 14 nonlinear deformation algorithms applied to human brain mri registration," *Neuroimage*, vol. 46, no. 3, pp. 786–802, 2009.

[4] M. A. Yassa and C. E. Stark, "A quantitative evaluation of cross-participant registration techniques for mri studies of the medial temporal lobe," *Neuroimage*, vol. 44, no. 2, pp. 319–27, 2009.

[5] A. Klein and et al., "Evaluation of volume-based and surface-based brain image registration methods," *Neuroimage*, vol. 51, no. 1, pp. 214–20, 2010.

[6] J. Ashburner, "A fast diffeomorphic image registration algorithm," *Neuroimage*, vol. 38, pp. 95–113, 2007.

[7] G. Auzias and et al., "Diffeomorphic brain registration under exhaustive sulcal constraints," *IEEE Transactions on Medical Imaging*, vol. 30, no. 6, pp. 1214–27, 2011.

[8] T. Vercauteren and al., "Diffeomorphic demons: efficient non-parametric image registration," *Neuroimage*, vol. 45, no. 1 Suppl, pp. S61–72, 2009.

[9] J. Ashburner and K J Friston, "Unified Segmentation," *NeuroImage*, vol. 26, pp. 839–851, 2005.

[10] S. Geyer and al., "Two different areas within the primary motor cortex of man," *Nature*, vol. 382, no. 6594, pp. 805–7, 1996.

[11] D. Viceic and al., "Local landmark-based registration for fmri group studies of nonprimary auditory cortex," *Neuroimage*, vol. 44, no. 1, pp. 145–53, 2009.

[12] A. M. Tahmasebi and al., "Reducing inter-subject anatomical variation: effect of normalization method on sensitivity of functional magnetic resonance imaging data analysis in auditory cortex and the superior temporal region," *NeuroImage*, vol. 47, no. 4, pp. 1522–31, 2009.

[13] J. Du and al., "Whole brain diffeomorphic metric mapping via integration of sulcal and gyral curves, cortical surfaces, and images," *NeuroImage*, vol. 56, no. 1, pp. 162–73, 2011.

A.2 F. Pizzagalli *et al.*, Conf Proc EMBS, 2011

Combination of nonlinear registration methods with high resolution fMRI for a fine exploration of human primary motor hand area

Fabrizio Pizzagalli, Guillaume Auzias, Chantal Delon-Martin, Michel Dojat

***Abstract*— Functional investigation of human hand representation in the motor area M1 requires high resolution functional imaging, to finely separate activation in M1, and a perfect alignment of individual central sulci to improve functional areas overlap and significance of statistical parametric maps obtained from different hand movements. Based on anatomical measures, we show how recent global diffeomorphic registration techniques impact positively on the alignment of sulcal folds in M1 area. With functional measures, we evaluate their effect on the robust detection and localization of group brain activation for flexion/extension of right and left thumbs/fingers and wrists. The methodology we propose opens the way to a non invasive functional exploration of the human hand motor cortex at the group level under different normal, pathological or after rehabilitative conditions.**

I. INTRODUCTION

Group analysis of neuroimaging data requires to register anatomical and functional individual data in a common space. This spatial registration should ensure a precise alignment of individual cortical grey matter tissues. Such an alignment becomes crucial for the functional investigation of human hand representation in the primary motor cortex M1. The primary motor cortex M1 is located on the anterior bank of the central sulcus (CS) in the precentral gyrus, while the primary somatosensory cortex S1 lies on the posterior bank of the CS in the postcentral gyrus. Folding is a good predictor of cytoarchitectonics especially for primary cortex areas [1] and could thus be a good predictor of functional specialization in the primary motor cortex. The segment of the precentral gyrus, generally referred as the *hand-knob*, is a reliable landmark for identifying M1 [2]. Although, its gross organization is somatotopic, the fine functional organization of M1 remains poorly known in humans [3], [4].

In humans, the functional analysis of M1 is limited by two factors:

- insufficient spatial resolution of functional MRI (fMRI). Typical spatial resolution (3x3x3 mm^3) leads to a mixing of functional BOLD responses within M1 subregions and between M1 and S1.
- high inter-individual variability of the hand motor area. For group analysis of fMRI, the poor cross-participant alignment leads to the underestimation or the lack of activation in M1. Moreover, spatial filtering performed prior to statistical analysis to reinforce the overlap between individual active areas, introduce *per se* a functional blurring and a loss of a precise localization of fMRI signals. This clearly impedes the separation of activated clusters found in M1.

Because *hand-knob* is a good predictor of M1, we hypothesized that the combination of a perfect alignment of all *hand-knobs* across subjects with high resolution fMRI, insuring each functional voxel to be attributed to a single gyrus, could improve the functional areas overlap and increase the significance of statistical parametric maps.

The achievement of a high spatial resolution in fMRI can be done by increasing the in-plane acquisition matrix, decreasing plane thickness and restricting the acquisition volume to the upper part of the brain encompassing the motor area. For inter-individual alignment of anatomical scans, it is well established that linear registration is inadequate for aligning cortical structures such as sulci. Several studies have compared nonlinear brain image registration algorithms working on the whole brain [5], [6], on specific regions [7], or using volume versus surface-based approaches [8]. In all these studies a set of quantitative measures was used to compare deformed structural MR source image and one target. The effects of the registration on brain activation detection was not reported. We take a different perspective: we are mainly interested in exploring the effects of nonlinear registration methods on the robustness of activation detection applied here to fine motor cortex investigation. For this purpose we selected 2 representative diffeomorphic methods, DARTEL [9] and DISCO+DARTEL [10]. Their performances were quantitatively evaluated using data coming from 13 healthy control subjects. Data were also compared with the standard procedure using the SPM8 normalization[1] widely used in the neuroimaging community.

II. MATERIAL AND METHODS

A. Data Acquisition

Thirteen right-handed healthy subjects (mean 27.5 y.o.) underwent a block-design fMRI protocol while performing 2 different movements (extension / flexion), with 3 hand parts (thumb / fingers / wrist) of the 2 hands (right dominant / left non-dominant), each separately. All along the task and rest periods, BOLD functional images were acquired with a high spatial resolution of $1.5\times1.5\times1.5$ mm^3 obtained using

F. Pizzagalli is with INSERM, U836, Grenoble Institut des Neurosciences, Grenoble, F-38700, France fabrizio.pizzagalli@ujf-grenoble.fr

G. Auzias is with the LSIS Lab, UMR CNRS 6168, Marseille, F-13000, France guillaume.auzias@gmail.com

C. Delon-Martin is with INSERM, U836, Grenoble Institut des Neurosciences, Grenoble, F-38700, France chantal.delon@ujf-grenoble.fr

M. Dojat is with INSERM, U836, Grenoble Institut des Neurosciences, Grenoble, F-38700, France michel.dojat@ujf-grenoble.fr

[1] http://www.fil.ion.ucl.ac.uk/spm/

a multi-shot EPI sequence on a 3T whole-body MR scanner (Bruker, Medspec S300). The acquisition volume covered the upper part of the brain with a repetition time of 6 seconds. A total of 222 functional volumes were acquired during 4 functional runs. T1-weighted structural images were acquired with $1\times1\times1$ mm^3 spatial resolution using a MDEFT sequence. In our experimental conditions, the measured time-serie SNR was 23, a value similar to those found at the same spatial resolution at 3T by others [11].

B. Structural Images Processing

Individual structural images were firstly segmented and debiased using unified segmentation approach as implemented in SPM8 [12]. Then, they were registered following three different strategies and software using their own default parameters values: 1/ with mutual information registration on the MNI template (spatial normalization) using SPM8, 2/ DARTEL and 3/ DISCO+DARTEL (DiDa).

1) DARTEL: Dartel [9] optimizes the overlap of grey and white matter tissue probabilistic masks between subjects through a large deformation technique where deformations are parametrized by a velocity field that is constant in time. To avoid the arbitrary selection of a single brain as a registration template, the algorithm embeds the construction of an average image template. The scheme involves iterations of DARTEL to map the scans above to their average, to form a new average. The initial smooth template become sharper each time it is re-generated, resulting in an iterative coarse-to-fine registration scheme. In the region of interest comprising the central sulcus, this method performs among the best registration techniques [6]. It has been applied in different voxel-based morphometry studies where accurate inter-subject realignment is required.

2) DISCO+DARTEL (DiDa): The DIffeomorphic Sulcal-based COrtical (DISCO) registration approach explicitly enforces the alignment of sulci in an iterative approach. Individual sulci are first segmented using BrainVisa[2] and modeled as weighted sets of points. An average sulcal template is defined as the union of the entire set of sulcal points through the group of subjects. For each sulcal label, the corresponding sulcal landmark in the template corresponds to the union of all points associated to this label for each subject. Diffeomorphic transformation of each individual data onto the empirical template is then proceeded in the general framework of the Large Deformation Diffeomorphic Metric Mapping theory. Improved mask overlap and reduction of sulcal dispersion can be reached through the sequential combination of DISCO and DARTEL (DiDa), with DARTEL being initialized using DISCOs outcome [10]. In the context of this study, a single sulcal template was computed for each hemisphere, corresponding to the central sulcus.

C. Registration Evaluation

To estimate the resulting cross-participant cortex overlap, we considered the intersection of registered grey matter masks restricted to ROIs designed to encompass the motor region in all individuals. We used a fuzzy union overlap metric (see [10]) computed for all pairs of subjects. For each method, we then applied the deformation field to the corresponding individual left/right CS. The Hausdorff distances for CS between every pair of subjects were computed for each method.

[2]http://brainvisa.info

D. Functional Images Processing

Functional images processing involved two steps. In a first step, individual images were computed in each subject's referential. It includes the following functional image preprocessing: a correction for motion, a registration on the structural image and a very slight smoothing using a gaussian kernel (FWHM 3mm). Individual statistical analysis was done with a single Generalized Linear Model. These computations were done with the SPM8 software. It provides a set of contrast images for each movement (extension or flexion), for each hand part (thumb or fingers or wrist) and for each hand (dominant or non-dominant). In the second step, a common referential is used to perform the group statistical analysis in a random-effect approach. Previous to the group analysis, all the individual contrast images are aligned to the common referential by applying to them the deformation fields derived from the structural images. A T-value map was thus derived for each contrast and for each realignment method. In order to compare the statistical results among these three registration approaches, the T-value maps are thresholded above t=5.0 ($p\leq0.0001$ voxel level non corrected) and their histograms are computed and compared for the three methods.

III. RESULTS

A. Anatomical measures

The registration results on the shape of the left and right CSs are displayed in Figure 1. As expected, the standard registration procedure used in SPM8 did not allow for an good alignement of CSs, compared to non-linear methods. When the alignment was locally constrained (DiDa) by relevant anatomical information, here CS delineating the M1 area, we measured only a slight improvement compared to DARTEL. This highlights the fact that DARTEL achieves a good alignment of CS, as already observed in [6]. Figure 2 quantifies the overlap of the grey matter volumes and the Hausdorff distance metric. It confirms that better alignment improves the grey matter overlap, as expected and reduces the distance of each individual's CS to the mean. Both DARTEL and DiDa methods provide a better superpimposition of the GM around the CSs with no significant difference between them.

B. Functional measures

Figure 3 displays the histograms of significantly activated voxels for flexion of left and right hands (right and left columns respectively), for the thumbs (upper row), the fingers (middle row) and the wrists (lower row). They show greater number of statistically significant voxels with

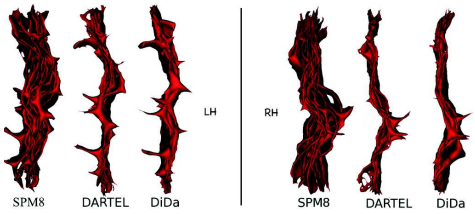

Fig. 1. Left (left) and right (right) central sulci superposition for each method.

DARTEL and DiDa as compared to SPM8. DiDa seems to improve slightly the number of activated voxels as compared to DARTEL.

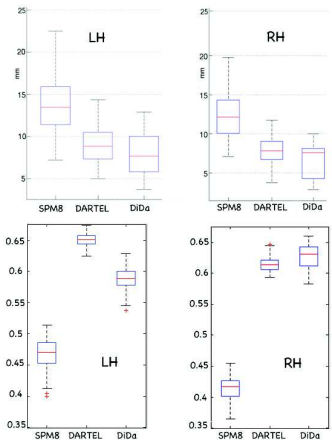

Fig. 2. Descriptive statistics of Hausdorff distance (upper row) and grey-matter tissue overlap (bottom row), obtained for the three methods. For each box, the horizontal mark indicates the median value; the upper and lower edges contain the data distribution within the first lower through the last upper quartile values; the whiskers cover values within 1.5 times this interquartile range.LH: Left Hemisphere, RH: right hemisphere

Figure 4 illustrates qualitatively the localization of the main activated clusters at the group level for each method. With SPM8 registration, we found smaller clusters, but for fingers where one spot was falsely assigned to S1. With DARTEL and DiDa, we found at least two spots of activation in the precentral gyrus, both for flexion and extension of right and left thumbs, fingers and wrists in accordance with Geyer

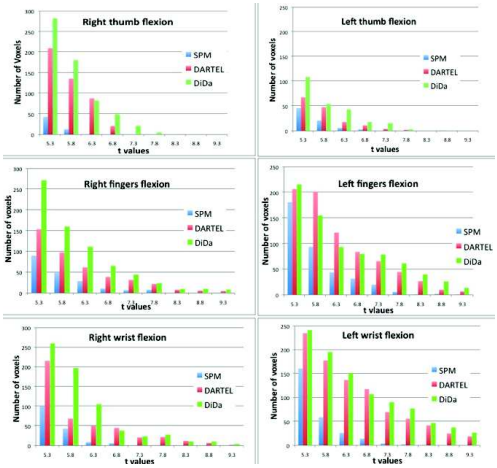

Fig. 3. Number of significantly activated voxels (P≤0.0001 voxel level non corrected) for nine bins of T-values obtained by group mean effect for flexion. Left hemisphere (left) and right hemisphere (right).

[3] who found evidences of M1 subdivision (M1-4p, M1-4a).

IV. DISCUSSION

The complementarity of anatomical and functional measures indicates that both are necessary to evaluate the impact of nonlinear (here diffeomorphic) registration methods on the activation patterns. As already mentioned in [5], [6], anatomical measures showed that methods with high degree of freedom improve the alignment of specific brain areas and increase overlap of cortical ribbon as observed here with DARTEL and DiDa compared to SPM8 (Figure 1 and Figure 2).

While anatomical measures shows that DARTEL and DiDa have similar performances, functional measures reveal some differences (Figure 3). Indeed, small anatomical differences induced by sulcal landmarks can generate significant variations in T-values. The local constraints introduced in DiDa have in general a positive effect on T-values (see Figure 3). We focussed our study on two diffeomorphic methods because of their nice topological properties particularly relevant with high resolution fMRI. Our study could be interestingly extended using other efficient nonlinear methods such as IRTK or cortical-surface-based registration methods (e.g. FreeSurfer). Note that the use of a specific EPI template such

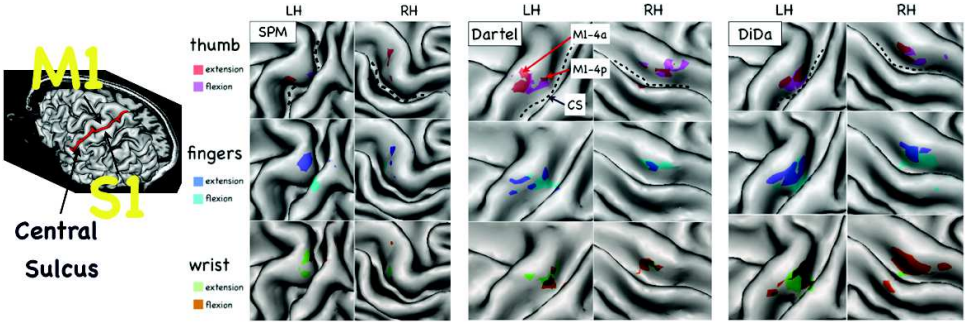

Fig. 4. Functional activation projected on the cortical surface of one subject warped on the average. Some overlap between flexion and extension activations is expected [15]. We used a T-value threshold of $\geq$5.0 ($p \leq 0.0001$ voxel level non corrected).

as proposed in [13] would not allow reaching the accurate localization we search for.

V. CONCLUSION

Our study demonstrates that the alignment quality provided by nonlinear (here diffeomorphic) registration techniques has a direct and strong impact on the functional activation detection (improvement of the statistical significance of the detected clusters) and the localization (improvement of the accuracy of the clusters position). We further show that when this alignment was locally constrained by sulcal information (using DISCO), an additional improvement was achieved whereas DARTEL permits a good anatomical alignment. In the motor area studied here, this improvement is not large because DARTEL already permits a good alignment of the central sulci as was reported by Klein [6]. In other brain areas, sulcal alignment with DISCO may provide higher improvement; for instance, in the Heschl's gyrus where nonlinear deformation techniques were efficient in fMRI studies of the auditory cortex [14].

Combining high resolution fMRI with high accuracy realignment of the central sulcus of individuals obtained using non-linear registration techniques, opens the way to the non invasive functional exploration of the human hand motor cortex under different normal, pathological or after rehabilitative conditions.

VI. ACKNOWLEDGMENTS

The authors gratefully acknowledge the contribution of the Cluster HVN of Région Rhône-Alpes, France.

REFERENCES

[1] B. Fischl et al., Cortical folding patterns and predicting cytoarchitecture, *Cereb Cortex*, vol.18, 2008, pp 1973-1980.
[2] T.A. Yousry et al., Localization of the motor hand area to a knob on the precentral gyrus. A new landmark,*Brain*,vol. 120, 1997, pp 141-157.
[3] S. Geyer et al.,Two different areas within the primary motor cortex of man, *Nature*, vol. 382, 1996, pp 805-807.
[4] W.J. Z'Graggen et al., Mapping of direction and muscle representation in the human primary motor cortex controlling thumb movements, *J. Physiol.*, vol. 587, 2009, pp 1977-1987.
[5] P. Hellier et al., Retrospective evaluation of intersubject brain registration, *IEEE Trans Med Imaging*, vol. 22, 2003, pp 1120-1130.
[6] A. Klein et al., Evaluation of 14 nonlinear deformation algorithms applied to human brain MRI registration, *Neuroimage*, vol. 46, 2009, pp 786-802.
[7] M.A. Yassa and C.E. Stark, A quantitative evaluation of cross-participant registration techniques for MRI studies of the medial temporal lobe, *Neuroimage*, vol. 44, 2009, pp 319-327.
[8] A. Klein et al., Evaluation of volume-based and surface-based brain image registration methods, *Neuroimage*, vol. 51, 2010, pp 214-20.
[9] J. Ashburner, A fast diffeomorphic image registration algorithm, *Neuroimage*, vol.38, 2007, pp 95-113.
[10] G. Auzias et al., Diffeomorphic brain registration under exhaustive sulcal constraints, *IEEE Transactions on Medical Imaging*, in press.
[11] C. Triantafyllou et al., Comparison of physiological noise at 1.5T, 3T and 7T and optimization of fMRI acquisition parameters , *NeuroImage*, vol.26, 2005, pp 243-250.
[12] J. Ashburner and K J Friston, Unified Segmentation, *NeuroImage*, vol.26, 2005, pp 839-851.
[13] C. M. Huang et al., Study-specific EPI template improves group analysis in functional MRI of young and older adults, *J Neurosci Methods*, vol. 189, 2010, pp 257-266.
[14] D. Viceic et al., Local landmark-based registration for fMRI group studies of nonprimary auditory cortex, *Neuroimage*, vol.44, 2009, pp 145-153.
[15] S. Kakei et al, Muscle and movement representations in the primary motor cortex, *Science*, vol. 285, 1999, pp 2136-9.

A.3 O. Coulon *et al.*, Conf Proc EMBS, 2011

33rd Annual International Conference of the IEEE EMBS
Boston, Massachusetts USA, August 30 - September 3, 2011

Two new stable anatomical landmarks on the central sulcus: definition, automatic detection, and their relationship with primary motor functions of the hand

Olivier Coulon Fabrizio Pizzagalli Grégory Operto Guillaume Auzias Chantal Delon-Martin Michel Dojat

***Abstract*— We present a method to automatically detect two new stable anatomical landmarks L_1 and L_2 on the Central Sulcus (CS). Those landmarks are shown to be representative of the Central Sulcus morphology and linked to the functional primary motor area of the hand. Detection is performed after introducing a new morphological characteristic, the sulcal profile. We show that when matching explicitly L_1 and L_2 across individuals the inter-subject matching of the central sulcus anatomy is improved , as well as the inter-subject matching of the primary motor area of the hand. This opens possibilities for morphological studies of the CS, more precise functional studies of primary motor function, and a better understanding of motor representations along the CS.**

I. INTRODUCTION

In human, the precise functional organisation of the primary motor cortex (M1) is largely unknown. Knowledge about its anatomical and functional organisation in healthy subjects could help understanding deficiencies related to specific pathologies (e.g Parkinson's disease) or cortical plasticity after surgery or amputation (phantom member representation). Structural and high resolution functional MR imaging are suitable non-invasive modalities for investigating hand representation in M1. M1 lies just anterior to the central sulcus (CS) and extends across the precentral gyrus. It appears that a part of the CS is shaped like an inverted omega or epsilon in the axial plane and like a hook in the sagittal plane (knob-like structure, Fig. 1). This 'knob' is a reliable landmark for identifying M1 [1]. In group studies, a perfect alignment of all individual "knobs" is a prerequisite for a robust detection of statistically significative cortical activation following hand movement. Clearly, such a registration is hampered by the high individual variability of the 'knob' structure (as shown on various indidual CS morphologies in Fig. 3). Another more local landmark associated to the hand representation in M1 is the 'Pli de passage fronto-parietal moyen' (PPFM, [2]), a buried gyrus associated to a local decrease of the CS depth [3]. Its detection is awkward and also suffers from the high inter-subject variability. In this paper, we propose the definition of two new anatomical landmarks of the CS. We introduce a morphological characteristic of the CS, the *sulcal profile*, and show that the two landmarks can be robustly detected using the sulcal profile. These landmarks are used to define a referential on the CS common to several individuals. We show that it provides a relevant anatomical inter-subject matching and that the hand representation in M1 is stable in this referential.

In the next section, we present the methods we proposed to extract the sulcal profile, detect the two landmarks and reparameterize the CS. Then we present experiments, for a group of 10 healthy subjects with anatomical and functional data, and the results we obtain..

II. METHODS

A. Sulcus Parameterization

In [3], [4] a method was presented to parameterize the CS and perform depth measurements. In this paper, we propose an extension to this method to define a CS-based referential and use it to analyze functional data. We briefly recall the idea behind the parameterization and the depth curve extraction. From T1 MR images, we extract the CS as a 3D mesh, by using BrainVisa[1]. On this mesh, the two extremities and the two ridges, at the fundus of the sulcus and at the convex hull, are automatically extracted. Using these landmarks, two coordinate fields are computed on the sulcus that indicate the depth between the two ridges (x coordinate) and the longitudinal position between the two extremities (y coordinate). For each value of $y \in [0; 100]$, we estimate the depth at this position by measuring the length of y iso-parameter lines. Depth as a function of the y position can then be computed, as shown in Fig. 1.

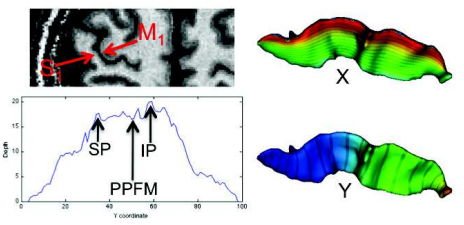

Fig. 1. The central sulcus 'knob' area with primary motor (M1) and sensori (S1) areas (top left), a CS mesh with X and Y coordinate field (right, with iso-parameter lines in dark) and depth curve (bottom left)

O. Coulon and G. Auzias are with Laboratoire des Sciences de l'Information et des Systèmes, UMR CNRS 6168, Marseille, France, olivier.coulon@univmed.fr

F. Pizzagalli, C. Delon-Martin and M. Dojat are with Institut des Neurosciences de Grenoble, Grenoble, France,

G. Operto is with Neurospin Center, CEA, Gif-Sur-Yvette, France,

[1]http://brainvisa.info

978-1-4244-4122-8/11/$26.00 ©2011 IEEE 7795

It has been shown that the parameterization available via the x and y coordinate fields provides a good inter-subject matching for morphological statistical studies. In particular, depth curves have been showing left-right asymetries related to handedness depth asymetries in humans [3], as well as in chimpanzees [4]. The depth curve has also been used to localize the PPFM, defined as the point of least depth between the inferior peak (IP) and superior peak (SP), as illustrated in Fig. 1. Although visible on an average depth curve computed from a group of subjects ([3], [4] and Fig. 5), the PPFM is sometimes difficult to detect on individuals, as shown in Fig. 3. Furthermore, although it is thought to be related to hand-related primary motor area, to what extent this statement is true is not very well known. This motivates the definition and detection of mode robust anatomical landmarks common to individuals.

B. A new morphological characteristic: the sulcal profile

The CS clearly has a main dorso-ventral direction ($\sim$the direction along the y coordinate), and apart from depth variations, its morphology can be described in terms of how much it bends along this direction. We introduce the *sulcal profile* in order to provide such information. The sulcal profile aims at measuring shape variations along the sulcus (y coordinate) in terms of deviation from the inertia plane, i.e. the plane that defines the main orientation of the sulcus. For a given sulcus mesh, defined as a vector of nodes $\mathbf{S} = (\mathbf{n}_i)_{i=1\ldots N}$, with $\mathbf{n}_i = (n_{xi}, n_{yi}, n_{zi})^T$ the nodes of the mesh, let us define the centered mesh $\mathbf{S_c} = (\mathbf{n}_i - \overline{\mathbf{n}})$, with $\overline{\mathbf{n}}$ the barycenter of $\mathbf{S}$. We then compute $\mathbf{A} = \mathbf{S_c}.\mathbf{S_c}^T$. After diagonalization, let $\mathbf{u}_1$, $\mathbf{u}_2$, and $\mathbf{u}_3$ be the 3 eigenvectors of $\mathbf{A}$ ordered by decreasing eigenvalue. The inertia plane (Fig. 2) is defined by $(\overline{\mathbf{n}}, \mathbf{u}_1, \mathbf{u}_2)$, and the signed distance of any node $\mathbf{n}_i$ to this plane is :

$$d_i = (\mathbf{n}_i - \overline{\mathbf{n}}).\mathbf{u}_3 \quad (1)$$

Fig. 2 shows a color representation of d_i at every node of a sulcus. At each position y, the sulcal profile function is then defined as the average value of d_i on the mesh at position y (i.e. along the y iso-parameter line). A sulcal profile as a function of y is presented on Fig. 2, showing how it represents shape information along the sulcus.

C. Automatic detection of anatomical landmarks and sulcal reparameterization

The central sulcus has been defined as being omega-shaped or in certain cases epsilon-shaped [1]. In both cases, when following the sulcus from the dorsal to the ventral extremities (y increasing), in the 'knob' area it first bends to an extremum in the posterior direction before coming back to another extremum towards the anterior direction. This shape corresponds to a large minimum of the sulcal profile, followed by a local maximum, as can be observed on Fig. 2 and 3. The latter clearly shows that the sulcal profile provides a more consistent information across subjects than the depth curve. Therefore, we propose to define two landmarks on the y axis, corresponding to the position of those two

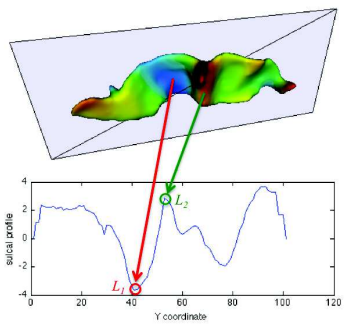

Fig. 2. Sulcus with inertia plane and color-coded (from negative in blue to positive in red) distance-to-plane information (top) and corresponding sulcal profile curve (bottom), with the two anatomical landmarks L_1 and L_2.

extrema. The first landmark L_1 is defined at the position y_1 corresponding to the global minimum of the sulcal profile in the inferior two thirds of the central sulcus ($y \in [0; 66]$). The second landmark L_2 is then defined at the position y_2 corresponding to the first local maximum of the sulcal profile after y_1. Prior to the detection, the sulcal profile is smoothed with a small Gaussian smoothing of variance $\sigma^2 = 3$ in order to remove spurious local extrema due to noise. Fig. 3 shows an example on the left central sulcus of four subjects, with the smoothed sulcal profiles and the automatically detected landmarks, illustrating the robustness of their definition.

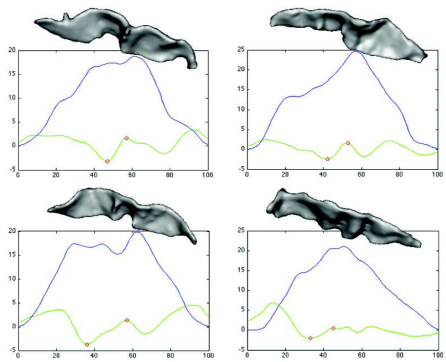

Fig. 3. Smoothed depth (blue) and sulcal profile (green) of 4 subjects with two landmarks automatically detected for each subject (red circles)

A new parameterization is computed by rescaling the Y coordinate in a piecewise linear fashion, such as to match exactly the coordinate of the two anatomical landmarks L_1 and L_2 across subjects. For a given subject, let $\overline{y_1}$ (resp. $\overline{y_2}$) be the mean of y_1 (resp. y_2) across subjects. In order to minimize metric distortions after reparameterization, we

therefore perform the following rescaling:

$$\begin{aligned} \text{if } y \leq y_1, \quad & y_{new} = \frac{y_1}{\overline{y_1}}.y, \\ \text{if } y_1 < y \leq y_2, \quad & y_{new} = \frac{y_2 - y_1}{\overline{y_2} - \overline{y_1}}.y + \frac{y_1.\overline{y_2} - y_2.\overline{y_1}}{\overline{y_2} - \overline{y_1}}, \\ \text{if } y_2 < y \leq 100, \quad & y_{new} = \frac{100 - y_2}{100 - \overline{y_2}}.y + \frac{y_2.100 - 100.\overline{y_2}}{100 - \overline{y_2}}, \end{aligned} \quad (2)$$

In the next section, this reparameterization is applied to a group of ten subjects after anatomical landmark detection.

III. EXPERIMENTS

Ten right-handed healthy subjects (mean 27.5 y.o.) underwent a block-design fMRI protocol while performing 2 different movements (extension / flexion), with the thumb of both hands (right dominant / left non-dominant), each separately. Due to paper length limitation, left thumb movements and consequently right CS, were not considered. During task and rest periods, BOLD functional images were acquired with a high spatial resolution of $1.5 \times 1.5 \times 1.5$ mm^3 obtained using a multi-shot EPI sequence on a 3T whole-body MR scanner (Bruker, Medspec S300). The acquisition volume comprised 15 1.5mm-thick slices covering the upper part of the brain containing the hand knob, with a repetition time of 6 seconds. A total of 222 functional volumes were acquired during 4 functional runs. T1-weighted structural images were acquired with $1 \times 1 \times 1$ mm^3 spatial resolution using a MDEFT sequence. Anatomical images were processed through the BrainVisa T1 Pipeline[2], in order to extract the left CS mesh. Each mesh was parameterized [3], then sulcal profile was computed, L_1 and L_2 detected and the mesh reparameterized. Meshes were finally resampled using the parameterization in order to provide an inter-subject node-to-node matching. This inter-subject matching was used to compute a mean left CS for the group of subject (Fig. 6).

Functional images were processed using SPM8[3] for realignment, slice-timing, and co-registration with anatomy. A trilinear interpolation was then performed to compute functional information at each node of the left CS mesh. Finally, a surface-based statistical t-map was computed for each subject by computing a GLM over the surface [6]. Using the node-to-node inter-subject matching, a Random Effect (RFX) group map [7] was also computed on the mean CS.

IV. RESULTS AND DISCUSSION

A. Anatomical inter-subject matching

On the 10 subjects, we found average positions of the two landmarks at $\overline{y_1} = 41$ and $\overline{y_2} = 54$. A visual inspection of the results showed that L1 and L2 were properly detected on all 10 subjects and reparameterization was performed using these average values.

The sulcal profiles of the 10 subjects before and after reparameterization are shown in Fig. 4. The variability of localization of the two landmarks is visible before reparameterization. Indeed y_1 varies between positions 32 and 47, and y_2 varies between positions 44 and 62. The good match of both landmarks is visible after reparameterization.

[2]http://brainvisa.info
[3]http://www.fil.ion.ucl.ac.uk/spm

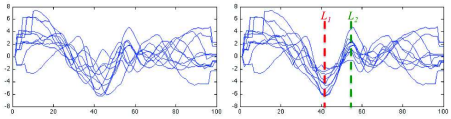

Fig. 4. Sulcal profiles of the ten subjects before (left) and after (right) reparameterization.

This effect also has consequences when using the inter-subject matching provided by the parameterization of the sulcus. When used to compute a mean CS, the quality of this inter-subject matching can be assessed. Fig. 6 shows the mean CS before and after reparameterization. After reparameterization the match of $L1$ and $L2$ is such that the knob has preserved its shape and appears clearly despite the effect of the averaging. Before parameterization , on the other hand, the variations of sulcal profile have been partly smoothed out.

Interestingly, the improvement does not only concern the bent part of the sulcus between L_1 and L_2 but also other features of the sulcus. The mean sulci and the corresponding sulcal profiles on Fig. 6 show that the curved part of the sulcus after L_2, very often present on individuals (see Fig. 3), is preserved on the mean SC only after reparameterization. The PPFM, a depth-related landmark that is not taken into account by the reparameterization process, is also better matched across subject. Fig. 5 shows the mean depth curve before and after reparameterization. The decrease of depth corresponding to the PPFM between SP and IP is a lot clearer after reparameterization.

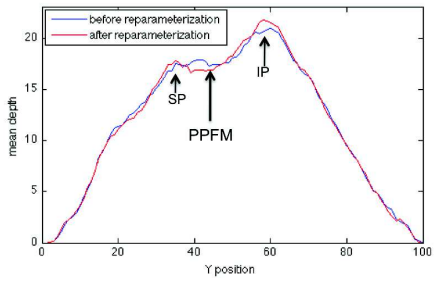

Fig. 5. Mean depth curve. The PPFM is better defined after reparameterization.

These elements show a overall better matching of CS morphology across subjects when explicitly taking into account L_1 and L_2.

B. Link with primary motor functions of the hand

Individual statistical maps were first computed on the CS mesh of each subject. A search for maxima after a threshold at $p < 0.001$ uncorrected, a standard threshold, showed that 9 out of the 10 subjects had activation peaks located

between L_1 and L_2. The tenth subject, with an overall poorer functional response, also had two activation peaks between L_1 and L_2 but just below the threshold. This link between the thumb primary motor activation and our two landmarks is confirmed by the RFX group analysis. On Fig. 6 one can see the results of this RFX analysis, thresholded at $p < 0.001$ uncorrected, before and after reparameterization. Due to the variability of the primary motor focus along the CS, the RFX analysis yielded no significant result. The RFX after reparameterization, on the other hand, showed a clear activation focus between L_1 and L_2 with a very strong significance ($p < 2.10^{-5}$)

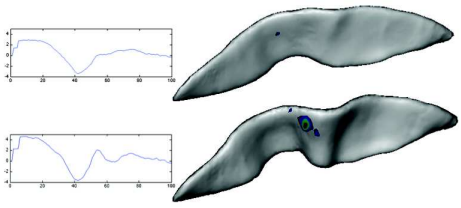

Fig. 6. Mean left central sulcus with RFX map thresholded at $p < 0.001$ uncorrected, before (top) and after reparameterization (bottom). Corresponding sulcal profiles are shown on the left. The effects of the reparameterization is visible with thumb related activations surviving the threshold and a mean anatomy that has better preserved morphological features.

This shows the strong link between anatomical landmarks L_1 and L_2 and the hand-related primary motor area in M1.

V. CONCLUSION

Based on the parameterization of each individual central sulcus, we defined two specific landmarks L_1 and L_2 that seem stable across healthy individuals. We provided an automatic detection method for these landmarks after introducing a new morphological characteristic for the central sulcus, the sulcal profile. These landmarks are used for the computation of a new parameterization of individual central sulci and the constitution on an anatomically-based common referential where individual functional activations can be accurately localized. Clearly, our study demonstrates that such a parameterization has a direct and strong impact at the group-level on functional activation detection. The implications of such process are manifold. From the functional point of view, the proposed CS parameterization allows us to study in depth, in healthy volunteers, the cortical representation of various hand movements (fingers and wrists). Pathological hand movement, after surgery or rehabilitation could be explored in this context to support a theory of adult brain plasticity. From an anatomical point of view, L_1 and L_2 provides more information to pursue studies such as those presented in [3], [4] and investigate possible morphologies of the CS. Finally, the link between morphology and function can be studied by investigating the correlation between functional specificities such as handedness and left/right CS asymmetries measured with the positions of L_1 and L_2.

VI. ACKNOWLEDGMENTS

O. Coulon is funded by the Agence Nationale de la Recherche (ANR-09-BLAN-0038-01, 'BrainMorph')

REFERENCES

[1] T.A. Yousry, U.D. Schmid, H. Alkadhi, D. Schmidt, A. Peraud, A. Buettner, P. Winkler, Localization of the motor hand area to a knob on the precentral gyrus. A new landmark, *Brain*, vol. 120 (Pt 1), 1997, pp 141-157.
[2] P. Broca, Mémoires d'anthropologie, Paris: Reinwald, 1888.
[3] M.D. Cykowski, O. Coulon, P.V. Kochunov, K. Amunts, J.L. Lancaster, A.R. Laird, D.C. Glahn, P.T. Fox, The central sulcus: an observer-independent characterization of sulcal landmarks and depth asymmetry, *Cerebral Cortex*, vol. 18(9), 2008, pp 1999-2009.
[4] W. Hopkins, O. Coulon, J.-F. Mangin, Observer-Independent Characterization of Sulcal Landmarks and Depth Asymmetry in the Central Sulcus of the Chimpanzee Brain, *Neuroscience*, vol. 171(2), 2010, pp 544-551.
[5] A. Roche, P.-J. Lahaye, J.-B. Poline, Incremental Activation Detection in fMRI Series using Kalman Filtering. *In Proc. 2nd IEEE ISBI, Arlington, VA*, 2004, pp 376-379.
[6] S.Kiebel, A.J. Holmes, ?The general linear model, *In Human Brain Function, Chap. 7, Academic Press*, 2004.
[7] W.D. Penny, A.J. Holmes, Random Effects Analysis, *In Human Brain Function, Chap. 12, Academic Press*, 2004.

A.4 O. Martin *et al.*, Conf Proc OHBM, 2011

Abstract submission for the 17th Annual Meeting of the Organization for Human Brain Mapping to be held in Québec City, Canada, June 26-30, 2011 is now open.
http://www.humanbrainmapping.org/i4a/pages/index.cfm?pageID=3421
The deadline to submit has been extended to January 10, 2011. Please note that this deadline is firm, there will be no further extensions.
Submit an Abstract : **http://ww4.aievolution.com/hbm1101/**

Title :
Neural Plasticity Correlates Of The Thumb Extension Recovery After Tendon Transfer. A Case Study.

Authors :
Martin O. (1,2), Pizzagalli F. (2,3), Delon-Martin C. (2,3), Dojat M. (2,3), Quaine F.(1,2), Moutet F.(2,4)

(1) GIPSA Laboratory, Control System Department, CNRS UMR 5216, Grenoble, France
(2) Grenoble Universities, Grenoble, France
(3) INSERM, U836, Grenoble, France
(4) Grenoble University Hospital A.Michalon, Unit of Hand Surgery, Grenoble, France

Introduction. Although some interesting studies have shown cortical changes and the increase in hand functional score following tendon transfer procedure (Cavadas et al. 2009; Silva et al., 2006; Viswanathan et al., 2006), our study questions more specifically the adaptive cortical plasticity associated to the reconstruction of the peripheral hand motor function after a palliative tendon transfer surgery. The goal of this longitudinal study, during a 12-months period of pre- and post-surgery, is to characterize the changes of brain neuromotor activation associated to the recovery of the thumb extension after the flexor-to-extensor tendon transfer.
Methods. One 28-years old male patient with a radial nerve palsy benefits of a right-hand thumb extensor tendon transfer by the Tsuge technique (Tsuge, 1980). The fourth digit flexor tendon was transferred on the right thumb extensor tendon in order to restore the thumb extension. The hand functional evaluation synchronized with MRI bloc-session acquisition allowed to score of thumb extension, one month before surgery (S-M1) and every three month after surgery (S+M1, S+M3, S+M6, S+M12). Hand motor tasks and protocol corresponded to blocs of trials of repetitive self-triggered flexion and extension of the thumb, the four fingers and the wrist, for both the right- and left-hand, executed with maximum joint amplitude and velocity. Here, are presented the results comparing neurobehavioral data of right-thumb extension with MRI data of cortical maps of motor area.
Results. Regarding the hand performance, the amplitude and the frequency of thumb extension increase significantly over post-operative sessions, compared to the first one (figure 1). The thumb flexion-extension co-ordination and timing improves regularly and becomes closer to the left-valid-thumb over successive sessions. Questioning patient reveals an increase of comfort in the everyday life hand-tasks, leading to the automatization of the more common gesture. At cortical level, the session's comparison shows a significant increase of activation in the primary motor area dedicated to the sensorimotor control of the right-thumb (figure 2). The coupled changes observed at both behavioural and cortical levels shows that a correlated functional adaptation emerges and leads progressively to the sensorimotor effectiveness of the hand extensions motor commands.
Conclusions. This study shows the clear cortical reorganisation of the sensitive-motor neural network associated to the adaptive thumb motor behaviour over a 12-months period. The improvement of the right-thumb extension performance coupled to the increase of the activation in the corresponding cortical loci in the primary motor area indicates that a functional neural network piloting the extension of the right-thumb, from the neuromotor activation of the antagonist flexor muscle, is growing. It demonstrates, for the first time, the extreme functional potential of the cortical plasticity induced by the inversion of the peripheral muscular function, due to the tendon transfer between agonists and antagonists thumb muscles. This functional plasticity succeeds to reverse the original central motor commands of the thumb extension to be able to execute a new well-coordinated thumb movement for which neither muscles nor neural commands had been initially intended for.

References
Silva, J.G. et al. (2006), 'Changes in cortical relative power in patients submitted to a tendon transfer: a pre and post surgery study', Arquives of Neuropsiquiatry Vol. 65, no. 3, pp. 628-632.
Cavadas P.C., Landin L., Ibañez J. (2009), 'Bilateral hand transplantation: result at 20 months', Journal of Hand Surgery (European volume), Vol. 34, no. 4, pp. 434-443.
Viswanathan V, Chmayssani M, Adams DJ, Hirsch J. (2006), 'Cortical reorganization following intradigital tendon transfer', Neuroreport, Vol. 17, no. 16, pp. 1669-1673.
Tsuge, K. (1980), 'Tendon transfer for radial nerve palsy', Australian and New Zealand Journal of Surgery, vol. 50, no. 3, pp. 267-272.

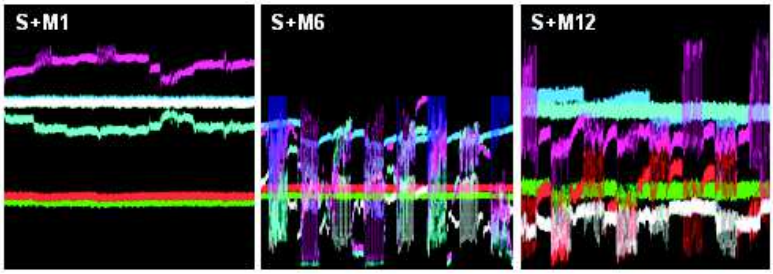

Figure 1. Time-series data of the right-hand extension amplitude for the wrist, thumb and finger, executed during a complete MRI bloc-session at S+M1, S+M6, S+M12 (raw data). Note the quick right-hand functional restoration after tendon transfer showed by the increasing of the amplitude, frequency and stability of extension movements.

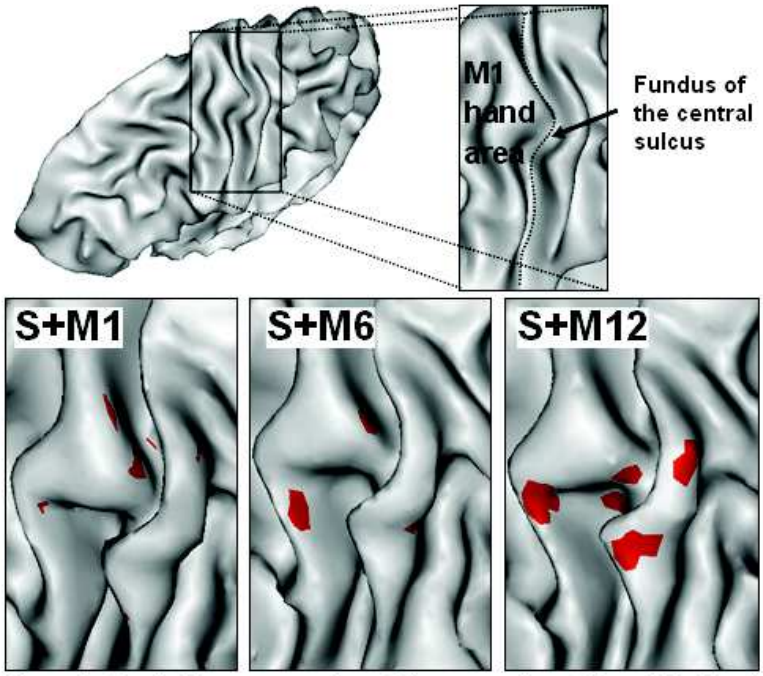

Figure 2. Cortical representation of the extension of the right thumb (in red, from S+M1 to S+M12). Note the loci increasing dedicated to the active extension of the right thumb.

A.5 F. Pizzagalli *et al.*, Conf Proc OHBM, 2010

Hand representation in human M1 revealed using 3T high resolution fMRI and diffeomorphic registration

Abstract No:

3015

Authors:

Fabrizio Pizzagalli[1], Michel Dojat[2], Irene Tropres-Broux[3], Chantal Delon-Martin[4]

Institutions:

[1]INSERM, Grenoble, France, [2]INSERM U836, Université Joseph Fourier, Institut des Neurosciences, Grenoble, France, [3]UJF, Grenoble, France, [4]INSERM, Grenoble Cedex 9, France

Introduction:

Hand representation occupies a large cortical area in M1 and its fine organization is largely unknown. The organization of primate M1 is not exclusively somatotopic but functional aspects of movement such as direction or velocity are also encoded. fMRI is a good tool for an accurate non-invasive investigation of human M1 but two main difficulties are encountered: insufficient spatial resolution and high inter-individual variability of the hand motor area. Typical spatial resolution (3x3x4mm3) leads to a mixing of functional BOLD responses in M1 and S1. For group analysis, registration to a common referential leads to a mixing of M1 and S1. Spatial smoothing performed prior statistical analysis per se reinforces functional blurring. We propose to overcome these difficulties by improving functional image resolution and using diffeomorphic image registration algorithms to realign all subjects' M1 areas, based on the « hand knob» landmark, before statistical analysis.

Methods:

Sixteen right-handed healthy subjects (mean 27,5 y.o.) underwent a block-design fMRI protocol while performing 2 different tasks: extension and flexion of the right thumb. BOLD functional images were acquired with a 1.5x1.5x1.5 mm3 spatial resolution using a multi-shot EPI sequence on a 3T whole-body MR scanner (Bruker, Medspec S300). Individual anatomical images were registered following three different strategies and software: 1/ with mutual information registration on the MNI template (normalisation) using SPM8 (http://www.fil.ion.ucl.ac.uk/spm/), 2/ with a spatial global registration by warping to their average using DARTEL (Ashburner, 2007) and 3/ with a spatial local registration on a reference subject hand knob using MedINRIA (http://www-sop.inria.fr/asclepios/software/MedINRIA/). Functional images were corrected for motion and slightly smoothed using a kernel gaussian (1.5x1.5x1.5mm3). Individual statistical contrast images were realigned to the corresponding anatomical scan separately for each registration strategy. Random effect statistical group analysis was further performed using SPM8 for all three approaches.

Results:

Group brain activation for the set of subjects for extension of the right thumb (red) and for flexion of the right thumb (yellow) are superimposed for SPM8 (Fig.1), DARTEL (Fig.2) and MedINRIA (Fig.3) on the corresponding average anatomical scan. Orange represents the overlap of the two tasks. Contrary to SPM8 normalisation, diffeomorphic registrations allow an accurate anatomical overlap of the central sulci with a clear distinction between M1 and S1. Note that the average hand knob shape seems closer to its known geometry after MedINRIA local registration.
SPM8 normalisation leads to undifferentiated functional activation in M1 or S1. At the contrary, DARTEL and MedINRIA both allow for extension, to distinguish two distinct clusters of activation in the hand knob: one in the lateral part and a second one more medial. For flexion, the two clusters partially overlapped extension clusters and are slightly more lateral and anterior. However, with DARTEL a spot of activation is falsely found in S1.

Conclusions:

High resolution fMRI and local or global diffeomorphic registration algorithm allow to detect robust statistical group brain activation, coherent with expectations: double representation for thumb movement, probably corresponding to 4p and 4a, (Geyer et al. 1996), and a flexion representation of the thumb more anterior than the extension representation, a result previously found using TMS (Z'Graggen et al., 2009). Local diffeomorphic registration as implemented in MedINRIA seems to be more accurate than global diffeomorphic registration as implemented in DARTEL. Individual M1 registration can certainly be refined (for instance using DISCO (Auzias et al. 09)). However the present methodology is suitable for a fine non invasive fMRI exploration of hand cortical representation.

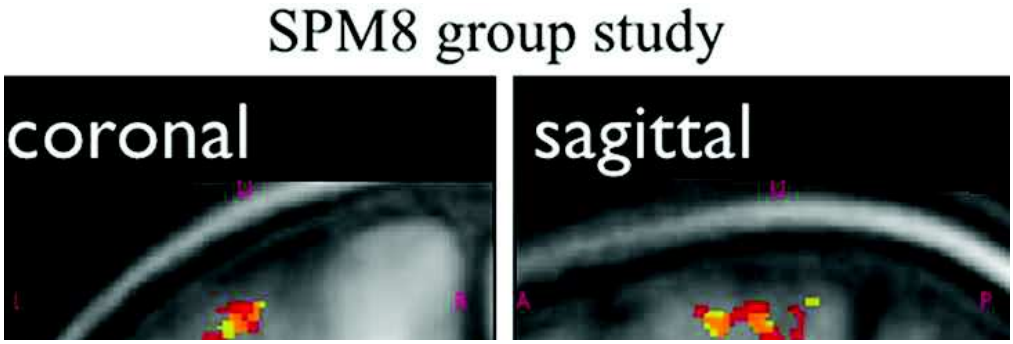

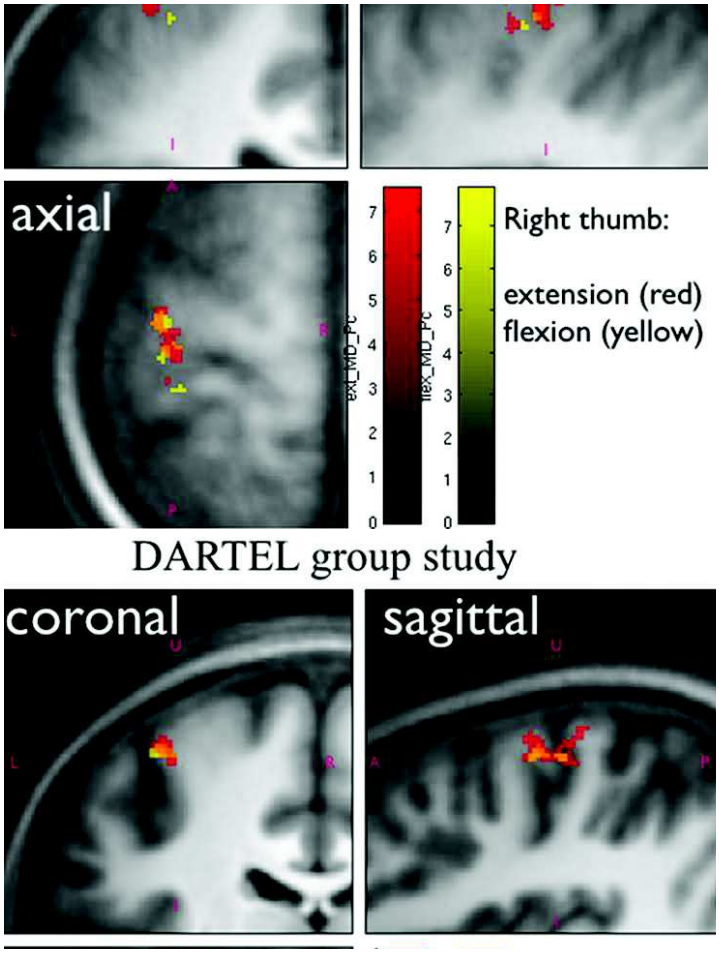
axial
Right thumb:
extension (red)
flexion (yellow)
DARTEL group study
coronal
sagittal

Hand representation in human M1 revealed using 3T high resolution fMRI and diffeomorphic registration

Abstract No:

3015

Authors:

Fabrizio Pizzagalli[1], Michel Dojat[2], Irene Tropres-Broux[3], Chantal Delon-Martin[4]

Institutions:

[1]INSERM, Grenoble, France, [2]INSERM U836, Université Joseph Fourier, Institut des Neurosciences, Grenoble, France, [3]UJF, Grenoble, France, [4]INSERM, Grenoble Cedex 9, France

Introduction:

Hand representation occupies a large cortical area in M1 and its fine organization is largely unknown. The organization of primate M1 is not exclusively somatotopic but functional aspects of movement such as direction or velocity are also encoded. fMRI is a good tool for an accurate non-invasive investigation of human M1 but two main difficulties are encountered: insufficient spatial resolution and high inter-individual variability of the hand motor area. Typical spatial resolution (3x3x4mm3) leads to a mixing of functional BOLD responses in M1 and S1. For group analysis, registration to a common referential leads to a mixing of M1 and S1. Spatial smoothing performed prior statistical analysis per se reinforces functional blurring. We propose to overcome these difficulties by improving functional image resolution and using diffeomorphic image registration algorithms to realign all subjects' M1 areas, based on the « hand knob» landmark, before statistical analysis.

Methods:

Sixteen right-handed healthy subjects (mean 27,5 y.o.) underwent a block-design fMRI protocol while performing 2 different tasks: extension and flexion of the right thumb. BOLD functional images were acquired with a 1.5x1.5x1.5 mm3 spatial resolution using a multi-shot EPI sequence on a 3T whole-body MR scanner (Bruker, Medspec S300). Individual anatomical images were registered following three different strategies and software: 1/ with mutual information registration on the MNI template (normalisation) using SPM8 (http://www.fil.ion.ucl.ac.uk/spm/), 2/ with a spatial global registration by warping to their average using DARTEL (Ashburner, 2007) and 3/ with a spatial local registration on a reference subject hand knob using MedINRIA (http://www-sop.inria.fr/asclepios/software/MedINRIA/). Functional images were corrected for motion and slightly smoothed using a kernel gaussian (1.5x1.5x1.5mm3). Individual statistical contrast images were realigned to the corresponding anatomical scan separately for each registration strategy. Random effect statistical group analysis was further performed using SPM8 for all three approaches.

Results:

Group brain activation for the set of subjects for extension of the right thumb (red) and for flexion of the right thumb (yellow) are superimposed for SPM8 (Fig.1), DARTEL (Fig.2) and MedINRIA (Fig.3) on the corresponding average anatomical scan. Orange represents the overlap of the two tasks. Contrary to SPM8 normalisation, diffeomorphic registrations allow an accurate anatomical overlap of the central sulci with a clear distinction between M1 and S1. Note that the average hand knob shape seems closer to its known geometry after MedINRIA local registration.
SPM8 normalisation leads to undifferentiated functional activation in M1 or S1. At the contrary, DARTEL and MedINRIA both allow for extension, to distinguish two distinct clusters of activation in the hand knob: one in the lateral part and a second one more medial. For flexion, the two clusters partially overlapped extension clusters and are slightly more lateral and anterior. However, with DARTEL a spot of activation is falsely found in S1.

Conclusions:

High resolution fMRI and local or global diffeomorphic registration algorithm allow to detect robust statistical group brain activation, coherent with expectations: double representation for thumb movement, probably corresponding to 4p and 4a, (Geyer et al. 1996), and a flexion representation of the thumb more anterior than the extension representation, a result previously found using TMS (Z'Graggen et al., 2009). Local diffeomorphic registration as implemented in MedINRIA seems to be more accurate than global diffeomorphic registration as implemented in DARTEL. Individual M1 registration can certainly be refined (for instance using DISCO (Auzias et al. 09)). However the present methodology is suitable for a fine non invasive fMRI exploration of hand cortical representation.

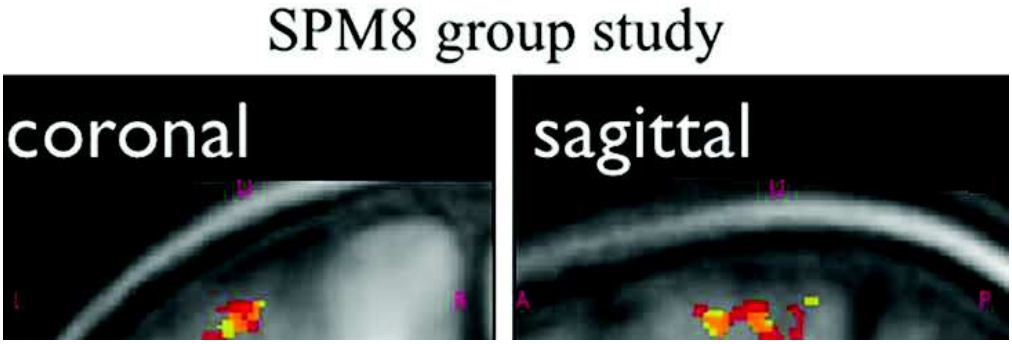

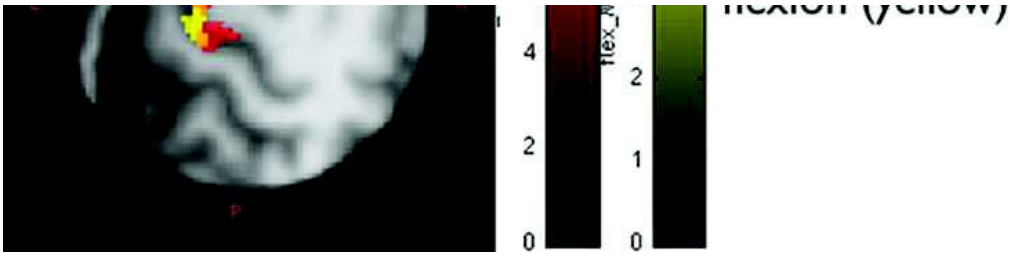

References:

Ashburner, J. (2007), 'A fast diffeomorphic image registration algorithm', Neuroimage, vol. 38, no. 1, pp. 95-113.
Auzias, G. (2009), 'Disco: A coherent diffeomorphic framework for brain registration under exhaustive sulcal constraints', Proc Miccai09, pp. 730-737.
Geyer, S. (1996), 'Two different areas within the primary motor cortex of man', Nature, vol. 382, pp. 805-807.
Z'Graggen, w. (2009), 'Mapping of direction and muscle representation in the human primary motor cortex controlling thumb movements', J Physiology, vol. 587, no. 9, pp. 1977-1987.

Categories

- Functional MRI (Imaging Techniques and Contrast Mechanism)
- Motion Correction/Spatial Normal, Atlas Construction (Modeling and Analysis)
- Hand Movements (Motor Behavior)

Appendix B

Tables of functional results

B.1 Control group results

Tables for motor cortex functional results

Group **Test**
Condition **All tasks**
Figure 11.1 - 11.2
3-way ANOVA F-Test
p <10^-2 (corrected)
cluster size >67.5 mm^3 (20 voxels)

	Hemisphere	cluster size (mm3)	pFWE-corr	Fmax	x (mm)	y (mm)	z (mm)
Cluster 1		4570					
Region							
M1	contralateral			227.91	-33	-27	48
S1	contralateral			159.37	-30	-30	47
M1	contralateral			154.34	-35	-25	57
M1	contralateral			151.67	-35	-23	46
S1	contralateral			106.36	-36	-28	51
Cluster 2		125					
Region							
SMA	contralateral			71.16	-2	-10	49
SMA	contralateral			58.17	-4	-7	45

Group **Test**
Condition **Right hand**
Figure 11.4
3-way ANOVA T-Test
p <10^-2 (corrected)
cluster size >67.5 mm^3 (20 voxels)

	Hemisphere	cluster size (mm3)	pFWE-corr	Tmax	x (mm)	y (mm)	z (mm)
Cluster 1		2845	<10^-4				
Region							
M1	contralateral			12.92	-37	-20	54
S1 (depth)	contralateral			12.58	-34	-28	45
S1	contralateral			12.54	-31	-31	51
S1	contralateral			11.19	-36	-28	51
M1	contralateral			9.45	-33	-20	46
M1	contralateral			9.43	-28	-28	56
S1	contralateral			8.88	-34	-31	58

Group **Test**
Condition **Left hand**
Figure 11.5
3-way ANOVA T-Test
p <10^-2 (corrected)
cluster size >67.5 mm^3 (20 voxels)

	Hemisphere	cluster size (mm3)	pFWE-corr	Tmax	x (mm)	y (mm)	z (mm)
Cluster 1		1620	<10^-4				
Region							
M1 (hand-knob)	contralateral			13.37	-33	-27	48
M1 (hand-knob)	contralateral			10.99	-34	-26	52
M1	contralateral			10.95	-30	-28	52
M1	contralateral			9.86	-31	-27	56
S1	contralateral			9.18	-30	-30	48
M1	contralateral			8.67	-35	-19	48
M1	contralateral			8.46	-29	-25	60

Tables for motor cortex functional results

Group	**Test**
Condition	**Left and right hand conj.**
Figure	11.6
3-way ANOVA	T-Test
p	<10^-4 (non-corrected)
cluster size	>67.5 mm^3 (20 voxels)

	Hemisphere	cluster size (mm3)	pFWE-corr	Tmax	x (mm)	y (mm)	z (mm)
Cluster 1		3233	<10^-4				
Region							
M1	contralateral			9.85	-32	-28	50
M1	contralateral			9.01	-30	-28	55
S1	contralateral			8.84	-30	-30	47
M1	contralateral			8.61	-34	-26	57
Cluster 2		243	<10^-4				
Region							
Post-central sulcus				6.04	-38	-38	55
Post-central sulcus				5.78	-34	-39	55
Cluster 3		125	<10^-4				
Region							
SMA	contralateral			5.32	-2	-11	49
SMA	contralateral			5	-4	-7	46
Cluster 4		74	<0.015				
Region							
Post-central sulcus	contralateral			5.02	-42	-29	54
Cluster 5		98	<0.002				
Region							
Pre-central sulcus	contralateral			4.83	-29	-14	58

Tables for motor cortex functional results

Group	**Test**
Condition	**Right hand > left hand**
Figure	11.7
3-way ANOVA	T-Test
p	<10^-4 (non-corrected)
cluster size	>67.5 mm^3 (20 voxels)

	Hemisphere	cluster size (mm3)	pFWE-corr	Tmax	x (mm)	y (mm)	z (mm)
Cluster 1		95	<0.003				
Region							
S1	contralateral			7.26	-37	-29	48
S1	contralateral			4.77	-33	-31	48
Cluster 2		172	<10^-4				
Region							
Pre-central sulcus	ipsilateral			5.86	25	-11	49
Cluster 3		68	<0.028				
Region							
S1	contralateral			5.27	-32	-31	52

Group	**Test**
Condition	**Extension**
Figure	11.10
3-way ANOVA	T-Test
p	<10^-2 (corrected)
cluster size	>67.5 mm^3 (20 voxels)

	Hemisphere	cluster size (mm3)	pFWE-corr	Tmax	x (mm)	y (mm)	z (mm)
Cluster 1		2106	<10^-4				
Region							
M1	contralateral			11.1	-30	-28	55
S1	contralateral			10.49	-31	-30	51
M1 (depth)	contralateral			9.65	-29	-29	45
M1/S1	contralateral			9.61	-35	-28	47
M1	contralateral			9.49	-37	-20	54

Tables for motor cortex functional results

Group **Test**
Condition **Flexion**
Figure 11.11
3-way ANOVA T-Test
p <10^-2 (corrected)
cluster size >67.5 mm^3 (20 voxels)

	Hemisphere	cluster size (mm3)	pFWE-corr	Tmax	x (mm)	y (mm)	z (mm)
Cluster 1		2028	<10^-4				
Region							
M1 (hand-knob)	contralateral			11.92	-33	-27	48
S1	contralateral			10.23	-30	-30	48
M1	contralateral			10.12	-31	-28	52
M1	contralateral			9.58	-35	-25	57
M1	contralateral			8.93	-37	-20	51
S1	contralateral			8	-28	-32	52

Group **Test**
Condition **Extension and Flexion conj.**
Figure 11.12
3-way ANOVA T-Test
p <10^-4 (non-corrected)
cluster size >67.5 mm^3 (20 voxels)

	Hemisphere	cluster size (mm3)	pFWE-corr	Tmax	x (mm)	y (mm)	z (mm)
Cluster 1		4269	<10^-4				
Region							
M1	contralateral			10.12	-31	-28	52
M1	contralateral			9.48	-35	-26	51
M1/S1	contralateral			9.45	-34	-27	47
S1	contralateral			8.72	-30	-30	47
M1	contralateral			8.32	-34	-26	57
Cluster 2		314	<10^-4				
Region							
Post-central sulcus	contralateral			5.66	-39	-37	55
Cluster 3		145	<10^-4				
Region							
SMA	contralateral			5.27	-2	-10	49
SMA	contralateral			5.23	-4	-7	45
Cluster 4		91	<0.004				
Region							
Pre-central sulcus	contralateral			4.86	-29	-14	58

Tables for motor cortex functional results

Group **Test**
Condition **Thumb**
Figure 11.16
3-way ANOVA T-Test
p <10^-4 (uncorrected)
cluster size >67.5 mm^3 (20 voxels)

	Hemisphere	cluster size (mm3)	pFWE-corr	Tmax	x (mm)	y (mm)	z (mm)
Cluster 1		2373	<10^-4				
Region							
M1	contralateral			7.80	-35	-19	48
M1	contralateral			7.67	-30	-28	51
M1	contralateral			7.61	-37	-20	54
M1(hand-knob)	contralateral			7.32	-33	-27	48
M1 (depth)	contralateral			5.92	-33	-23	42
Cluster 2		115	<10^-4				
Region							
S2	contralateral			5.16	-50	-19	44
Post-central sulcus	contralateral			4.77	-51	-25	43
Cluster 3		105	<10^-4				
Region							
Post-central sulcus	contralateral			5.13	-39	-37	55
Cluster 4		101	<0.002				
Region							
SMA	contralateral			4.81	-2	-10	51

Group **Test**
Condition **Fingers**
Figure 11.17
3-way ANOVA T-Test
p <10^-4 (uncorrected)
cluster size >67.5 mm^3 (20 voxels)

	Hemisphere	cluster size (mm3)	pFWE-corr	Tmax	x (mm)	y (mm)	z (mm)
Cluster 1		4357	<10^-4				
Region							
M1	contralateral			10.50	-35	-26	49
M1/S1	contralateral			8.74	-34	-27	45
M1	contralateral			8.28	-34	-26	57
S1	contralateral			7.83	-32	-31	51
M1	contralateral			7.66	-37	-20	54
M1	contralateral			7.43	-29	-29	45
Pre-central sulcus	contralateral			7.25	-42	-29	54
Cluster 2		71	<0.021				
Region							
Pre-central sulcus	contralateral			5.02	-29	-12	54
Cluster 3		81	<0.009				
Region							
Pre-central sulcus	contralateral			4.97	-29	-16	55

Tables for motor cortex functional results

Group **Test**
Condition **Wrist**
Figure 11.18
3-way ANOVA T-Test
p <10^-4 (uncorrected)
cluster size >67.5 mm^3 (20 voxels)

	Hemisphere	cluster size (mm3)	pFWE-corr	Tmax	x (mm)	y (mm)	z (mm)
Cluster 1		4928	<10^-4				
Region							
M1	contralateral			9.76	-33	-27	49
M1	contralateral			9.57	-27	-28	51
M1/S1	contralateral			9.01	-29	-30	48
M1	contralateral			7.31	-34	-26	57
S1	contralateral			6.80	-27	-31	58
Cluster 2		105	<10^-4				
Region							
SMA	contralateral			5.53	-2	-17	48
Cluster 3		118	<10^-4				
Region							
Post-central sulcus	contralateral			5.33	-25	41	52

Condition **Thumb, fingers and wrist conj.**
Figure 11.19
3-way ANOVA T-Test
p <10^-4 (non-corrected)
cluster size >67.5 mm^3 (20 voxels)

	Hemisphere	cluster size (mm3)	pFWE-corr	Tmax	x (mm)	y (mm)	z (mm)
Cluster 1		2373	<10^-4				
Region							
S1	contralateral			7.50	-31	-30	51
M1 (hand-knob)	contralateral			7.32	-33	-27	48
M1	contralateral			6.35	-35	-23	46
M1	contralateral			6.30	-35	-25	57
M1	contralateral			5.91	-30	-28	56
Cluster 2		95	<0.003				
Region							
Post-central sulcus	contralateral			5.13	-39	-37	55

Condition **Wrist >thumb**
Figure 11.21
3-way ANOVA T-Test
p <10^-3 (non-corrected)
cluster size >67.5 mm^3 (20 voxels)

	Hemisphere	cluster size (mm3)	pFWE-corr	Tmax	x (mm)	y (mm)	z (mm)
Cluster 1		236	<10^-4				
Region							
M1/S1	contralateral			4.40	-23	-29	48
M1	contralateral			3.91	-27	-28	53

Tables for motor cortex functional results

Group **Test- ReTest 9 subjects**
Condition **Test Retest conj.**
Figure 11.73
3-way ANOVA T-Test
p <5x10^-2 (corrected)
cluster size >67.5 mm^3 (20 voxels)

	Hemisphere	cluster size (mm3)	pFWE-corr	Tmax	x (mm)	y (mm)	z (mm)
Cluster 1		1333	<10^-4				
Region							
M1	contralateral			10.95	-35	-24	58
M1	contralateral			10.50	-32	-27	53
M1	contralateral			9.94	-35	-26	50
S1	contralateral			9.01	-29	-30	51
Cluster 2		122	<10^-4				
Region							
Post-central sulcus	contralateral			7.41	-42	-32	53
S1	contralateral			6.90	-37	-27	54

Group **Test- ReTest 9 subjects**
Condition **Test > Retest**
Figure 11.24
3-way ANOVA T-Test
p <5x10^-2 (corrected)
cluster size >67.5 mm^3 (20 voxels)

	Hemisphere	cluster size (mm3)	pFWE-corr	Tmax	x (mm)	y (mm)	z (mm)
Cluster 1		975	<10^-4				
Region							
M1	contralateral			7.43	-27	-28	47
M1/S1 (depth)	contralateral			7.01	-30	-30	44
M1	contralateral			6.87	-32	-20	46
S1	contralateral			6.49	-35	-25	43
Cluster 2		71	<0.072				
Region							
SMA	contralateral			5.27	-4	-8	46

Tables for cerebellum functional results

Group **Test**
Condition **All tasks**
Figure 11.3
3-way ANOVA F-Test
p <10^-2 (corrected)
cluster size >67.5 mm^3 (20 voxels)

	Hemisphere	cluster size (mm3)	pFWE-corr	Fmax	x (mm)	y (mm)	z (mm)
Cluster 1		3770					
Region							
Lobule IV/V	ipsilateral			117.62	0	-66	-17
Lobule V/VI	ipsilateral			112.00	13	-56	-13
Lobule V	ipsilateral			107.34	17	-50	-18
Lobule V	ipsilateral			104.51	6	-60	-12
Lobule V	ipsilateral			101.16	14	-49	-13

Group **Test**
Condition **Right hand**
Figure 11.8
3-way ANOVA T-Test
p <5x10^-2 (corrected)
cluster size >67.5 mm^3 (20 voxels)

	Hemisphere	cluster size (mm3)	pFWE-corr	Tmax	x (mm)	y (mm)	z (mm)
Cluster 1		354	<10^-4				
Region							
Lobule V/VI	ipsilateral			9.21	8	-64	-17
Lobule V/VI	ipsilateral			8.62	5	-66	-14
Cluster 2		685	<10^-4				
Region							
Lobule V	ipsilateral			8.93	13	-55	-13
Lobule V	ipsilateral			8.4	14	-52	-17
Cluster 3		81	<10^-4				
Region							
Lobule V/VI	interhemispheric			8.42	0	-65	-18
Lobule VIII	ipsilateral			6.38	3	-64	-21

Tables for cerebellum functional results

Group	**Test**
Condition	**Left hand**
Figure	11.8
3-way ANOVA	T-Test
p	<5x10^-2 (corrected)
cluster size	>67.5 mm^3 (20 voxels)

	Hemisphere	cluster size (mm3)	pFWE-corr	Tmax	x (mm)	y (mm)	z (mm)
Cluster 1		773	<10^-4				
Region							
Lobule V	ipsilateral			9.39	16	-53	-18
Lobule V/VI	ipsilateral			8.71	15	-57	-13
Lobule V	ipsilateral			8.53	6	-60	-12
Lobule V	ipsilateral			7.52	11	-59	-11
Cluster 2		108	<10^-4				
Region							
Lobule V	interhemispheric			8.65	0	-66	-17
Cluster 3		68	<10^-4				
Region							
Lobule V	ipsilateral			7.99	6	-64	-12
Cluster 4		115	<10^-4				
Region							
Lobule VI	ipsilateral			7.38	23	-62	-17

Tables for cerebellum functional results

Group **Test**
Condition **Left and right hand conj.**
Figure 11.9
3-way ANOVA T-Test
p <5x10^-2 (corrected)
cluster size >67.5 mm^3 (20 voxels)

	Hemisphere	cluster size (mm3)	pFWE-corr	Tmax	x (mm)	y (mm)	z (mm)
Cluster 1		1296	<10^-4				
Region							
Lobule V	ipsilateral			7.22	14	-55	-16
Lobule VI	ipsilateral			5.45	23	-61	-17
Cluster 2		496	<10^-4				
Region							
Lobule V/VI	interhemispheric			7.12	0	-65	-17
Lobule V	ipsilateral			6.91	5	-65	-12
Lobule VI	ipsilateral			5.55	1	-69	-11

Group **Test**
Condition **Extension**
Figure 11.14
3-way ANOVA T-Test
p <5x10^-2 (corrected)
cluster size >67.5 mm^3 (20 voxels)

	Hemisphere	cluster size (mm3)	pFWE-corr	Tmax	x (mm)	y (mm)	z (mm)
Cluster 1		466	<10^-4				
Region							
Lobule V	ipsilateral			8.82	17	-50	-18
Lobule V	ipsilateral			8.03	14	-55	-17
Lobule V/VI	ipsilateral			7.12	18	-57	-15
Lobule V	ipsilateral			6.86	7	-60	-13
Cluster 2		95	<10^-4				
Region							
Lobule V	interhemispheric			7.64	0	-65	-19
Lobule V	ipsilateral			6.66	1	-66	-14
Cluster 3		118	<10^-4				
Region							
Lobule V	ipsilateral			7.3	6	-64	-19
Lobule V	ipsilateral			7.25	8	-63	-17

Tables for cerebellum functional results

Group **Test**
Condition **Flexion**
Figure 11.14
3-way ANOVA T-Test
p <5x10^-2 (corrected)
cluster size >67.5 mm^3 (20 voxels)

	Hemisphere	cluster size (mm3)	pFWE-corr	Tmax	x (mm)	y (mm)	z (mm)
Cluster 1		574	<10^-4				
Region							
Lobule V	ipsilateral			9.11	13	-56	-13
Lobule V	ipsilateral			8.45	9	-54	-16
Lobule IV/V	ipsilateral			8.24	13	-53	-17
Cluster 2		172	<10^-4				
Region							
Lobule V	interhemispheric			8.97	0	-65	-17
Lobule V	ipsilateral			7.9	7	-64	-19
Cluster 3		74	<10^-4				
Region							
Lobule V	ipsilateral			8.06	5	-65	-12
Cluster 4		74	<10^-4				
Region							
Lobule VI	ipsilateral			7.23	19	-57	-16
Lobule VI	ipsilateral			6.88	18	-61	-16

Group **Test**
Condition **Extension and Flexion conj.**
Figure 11.15
3-way ANOVA T-Test
p <5x10^-2 (corrected)
cluster size >67.5 mm^3 (20 voxels)

	Hemisphere	cluster size (mm3)	pFWE-corr	Tmax	x (mm)	y (mm)	z (mm)
Cluster 1		628	<10^-4				
Region							
Lobule V	interhemispheric			7.29	0	-65	-18
Lobule V	ipsilateral			6.78	6	-64	-12
Lobule V	ipsilateral			5.99	8	-63	-18
Cluster 2		1569	<10^-4				
Region							
Lobule V	ipsilateral			6.83	6	-60	-12
Lobule IV/V	ipsilateral			6.75	14	-49	-14
Lobule V	ipsilateral			6.68	13	-55	-14

Tables for cerebellum functional results

Group	**Test**
Condition	**Thumb**
Figure	11.22
3-way ANOVA	T-Test
p	<10^-4 (uncorrected)
cluster size	>67.5 mm^3 (20 voxels)

	Hemisphere	cluster size (mm3)	pFWE-corr	Tmax	x (mm)	y (mm)	z (mm)
Cluster 1		5927	<10^-4				
Region							
Lobule V/VI	ipsilateral			5.83	13	-53	-17
Lobule V	ipsilateral			5.76	6	-60	-12
Lobule V/VI	interhemispheric			5.71	0	-65	-18
Lobule VI	ipsilateral			5.42	21	-60	-16
Lobule V	ipsilateral			5.28	14	-49	-14
Cluster 2		95	<10^-4				
Region							
Lobule V/VI	contralateral			4.76	-14	-61	-15

Tables for cerebellum functional results

Group **Test**
Condition **Fingers**
Figure 11.22
3-way ANOVA T-Test
p <10^-4 (uncorrected)
cluster size >67.5 mm^3 (20 voxels)

	Hemisphere	cluster size (mm3)	pFWE-corr	Tmax	x (mm)	y (mm)	z (mm)
Cluster 1		1073	<10^-4				
Region							
Lobule V	ipsilateral			6.82	17	-50	-18
Lobule V/VI	ipsilateral			6.69	14	-55	-17
Lobule V/VI	ipsilateral			5.99	17	-58	-16
Lobules VI	ipsilateral			5.91	22	-62	-17
Cluster 2		142	<10^-4				
Region							
Lobule V/VI	interhemispheric			6.22	0	-66	-17
Lobule V	ipsilateral			4.73	5	-64	-17

Group **Test**
Condition **Wrist**
Figure 11.22
3-way ANOVA T-Test
p <10^-4 (uncorrected)
cluster size >67.5 mm^3 (20 voxels)

	Hemisphere	cluster size (mm3)	pFWE-corr	Tmax	x (mm)	y (mm)	z (mm)
Cluster 1		1998	<10^-4				
Region							
Lobule V	interhemispheric			8.34	0	-66	-16
Lobule V/VI	ipsilateral			6.92	17	-50	-18
Lobule V	ipsilateral			6.67	14	-49	-13
Cluster 2		81	<10^-4				
Region							
Lobule V	ipsilateral			6.48	7	-61	-6
Cluster 3		88	<10^-4				
Region							
Lobule V	ipsilateral			6.06	14	-61	-14

B.2 Clinical results

Tables for clinical functional results

Patient
Condition **Right hand (operated) extension**
Figure 12.1
3-way ANOVA T-Test
p <10^-3 (non-corrected)
cluster size >67.5 mm^3 (20 voxels)

	Hemisphere	cluster size (mm3)	pFWE-corr	Tmax	x (mm)	y (mm)	z (mm)
Cluster 1		878	<10^-4				
Region							
M1	ipsilateral			9.29	41	-13	49
M1	ipsilateral			6.06	38	-19	42
Cluster 2		1691	<10^-4				
Region							
SMA	contralateral			7.64	-3	-12	42
SMA	contralateral			6.70	-5	-8	40
Cluster 3		371	<0.006				
Region							
SMA	ipsilateral			6.30	2	-13	56
SMA	ipsilateral			5.97	4	-10	54
Cluster 4		1094	<0.006				
Region							
S1	contralateral			6.11	-40	-23	45

Patient
Condition **Left hand (non-operated) extension**
Figure 12.1
3-way ANOVA T-Test
p <10^-3 (corrected)
cluster size >67.5 mm^3 (20 voxels)

	Hemisphere	cluster size (mm3)	pFWE-corr	Tmax	x (mm)	y (mm)	z (mm)
Cluster 1		1441	<10^-4				
Region							
SMA	ipsilateral			5.57	2	-19	53
Cluster 2		172	<0.150				
Region							
M1	contralateral			4.33	-19	-29	54
M1	contralateral			4.26	-23	-28	54

Tables for clinical functional results

Patient
Condition **non-operated hand extension > operated hand extension**
Figure 12.2
3-way ANOVA T-Test
p <10^-3 (corrected)
cluster size >67.5 mm^3 (20 voxels)

	Hemisphere	cluster size (mm3)	pFWE-corr	Tmax	x (mm)	y (mm)	z (mm)
Cluster 1		695	<10^-4				
Region							
SMA	contralateral			6.31	-7	-21	45
SMA	contralateral			5.77	-14	-22	47

Patient
Condition **operated hand extension > non-operated hand extension**
Figure 12.3
3-way ANOVA T-Test
p <10^-3 (corrected)
cluster size >67.5 mm^3 (20 voxels)

	Hemisphere	cluster size (mm3)	pFWE-corr	Tmax	x (mm)	y (mm)	z (mm)
Cluster 1		135	<0.288				
Region							
M1	ipsilateral			6.32	41	-14	49
M1	ipsilateral			3.55	36	-15	47

Tables for clinical functional results

Patient
Condition **Righ hand extension (operated hand) at M0**
Figure 12.4
3-way ANOVA T-Test
p <10^-3 (corrected)
cluster size >67.5 mm^3 (20 voxels)

	Hemisphere	cluster size (mm3)	pFWE-corr	Tmax	x (mm)	y (mm)	z (mm)
Cluster 1		3345	<10^-4				
Region							
SMA	ipsilateral			10.71	2	-13	56
SMA	ipsilateral			9.53	2	-19	49
Cluster 2		2909	<10^-4				
Region							
SMA	contralateral			8.63	-12	-13	42
SMA	contralateral			6.99	-3	-19	44
Cluster 3		685	<10^-4				
Region							
M1	ipsilateral			6.53	33	-25	50
M1	ipsilateral			5.84	36	-21	55

Patient
Condition **Righ hand extension (operated hand) at M1**
Figure 12.5
3-way ANOVA T-Test
p <10^-3 (corrected)
cluster size >67.5 mm^3 (20 voxels)

	Hemisphere	cluster size (mm3)	pFWE-corr	Tmax	x (mm)	y (mm)	z (mm)
Cluster 1		216	<0.070				
Region							
SMA	contralateral			9.13	-4	-11	41
Cluster 2		493	<10^-4				
Region							
Pre-central sulcus	ipsilateral			7.20	33	-12	40
Pre-central sulcus	ipsilateral			6.53	30	-6	52

Tables for clinical functional results

Patient
Condition **Righ hand extension (operated hand) at M3**
Figure 12.6
3-way ANOVA T-Test
p <10^-3 (corrected)
cluster size >67.5 mm^3 (20 voxels)

	Hemisphere	cluster size (mm3)	pFWE-corr	Tmax	x (mm)	y (mm)	z (mm)
Cluster 1		111	<0.432				
Region							
M1	ipsilateral			4.26	35	-25	53

Patient
Condition **Righ hand extension (operated hand) at M6**
Figure 12.7
3-way ANOVA T-Test
p <10^-3 (corrected)
cluster size >67.5 mm^3 (20 voxels)

	Hemisphere	cluster size (mm3)	pFWE-corr	Tmax	x (mm)	y (mm)	z (mm)
Cluster 1		3254	<10^-4				
Region							
S1	contralateral			7.41	-40	-22	43
S1	contralateral			4.14	-34	-27	48
Post_central sulcus	contralateral			8.22	-48	-26	43
Cluster 2		203	<0.088				
Region							
Post-central sulcus	contralateral			8.22	-48	-26	43

Patient
Condition **Righ hand extension (operated hand) at M12**
Figure 12.8
3-way ANOVA T-Test
p <10^-3 (corrected)
cluster size >67.5 mm^3 (20 voxels)

	Hemisphere	cluster size (mm3)	pFWE-corr	Tmax	x (mm)	y (mm)	z (mm)
Cluster 1		1016	<10^-4				
Region							
M1	ipsilateral			14.38	43	-16	39
M1	ipsilateral			11.53	38	-19	42
Cluster 2		560	<10^-4				
Region							
Post-central sulcus	ipsilateral			12.20	43	-34	44
Cluster 2		257	<0.035				
Region							
S1	ipsilateral			13.56	38	-21	42

References

[Ardekani 2005] B. A. Ardekani, S. Guckemus, A. Bachman, M. J. Hoptman, M. Wojtaszek and J. Nierenberg. *Quantitative comparison of algorithms for inter-subject registration of 3D volumetric brain MRI scans*. J Neurosci Methods, vol. 142, no. 1, pages 67–76, Mar 2005. (Cited on page 60.)

[Ashburner 1999] J. Ashburner and K. J. Friston. *Nonlinear spatial normalization using basis functions*. Hum Brain Mapp, vol. 7, no. 4, pages 254–66, Jan 1999. (Cited on page 61.)

[Ashburner 2000] J. Ashburner and K. J. Friston. *Voxel-based morphometry–the methods*. NeuroImage, vol. 11, no. 6 Pt 1, pages 805–21, Jun 2000. (Cited on page 6.)

[Ashburner 2005] J. Ashburner and K. J. Friston. *Unified segmentation*. NeuroImage, vol. 26, no. 3, pages 839–51, Jul 2005. (Cited on pages 18, 60, 61, 88, 89, 90 and 91.)

[Ashburner 2007] J. Ashburner. *A fast diffeomorphic image registration algorithm*. NeuroImage, vol. 38, no. 1, pages 95–113, Oct 2007. (Cited on pages 18, 60, 61, 62 and 93.)

[Auzias 2009] G. Auzias, J. Glaunès, O. Colliot, M. Perrot, J.-F. Mangin, A. Trouvé and S. Baillet. *DISCO: a coherent diffeomorphic framework for brain registration under exhaustive sulcal constraints*. Med Image Comput Comput Assist Interv, vol. 12, no. Pt 1, pages 730–8, Jan 2009. (Cited on page 59.)

[Auzias 2011] G. Auzias, O. Colliot, J. Glaunes, M. Perrot, J. Mangin and A. Trouve. *Diffeomorphic Brain Registration Under Exhaustive Sulcal Constraints*. Medical Imaging, IEEE Transactions on, vol. PP, no. 99, page 1, 2011. (Cited on pages 18, 61, 65, 66, 67, 94, 95 and 101.)

[Bajcsy 1983] R. Bajcsy, R. Lieberson and M. Reivic. *A computerized system for the elastic matching of deformed radiographic images to idealized atlas image*. J Computer Assisted Tomograph, vol. 7, no. 4, pages 618–625, 1983. (Cited on page 54.)

[Bandettini 1995] P. A. Bandettini, E. C. Wong, J. R. Binder, S. Rao, A. Jesmanowicz, E. Aron, E. A. Lowry, T. F. Forster, H. V. Hinks and R. S. Hyde. Functional MR imaging using the BOLD

approach: dynamic chararcteristics and data analysis methods. In Diffusion and perfusion magnetic resonance imaging: Applications to Functional MRI. 1995. (Cited on page 85.)

[Beisteiner 2001] R. Beisteiner, C. Windischberger, R. Lanzenberger, V. Edward, R. Cunnington, M. Erdler, A. Gartus, B. Streibl, E. Moser and L. Deecke. *Finger somatotopy in human motor cortex*. NeuroImage, vol. 13, no. 6 Pt 1, pages 1016–26, Jun 2001. (Cited on pages 11, 12, 27, 173, 174 and 175.)

[Berlucchi 2002] G. Berlucchi. *The origin of the term plasticity in the neurosciences: Ernesto Lugaro and chemical synaptic transmission*. J Hist Neurosci, vol. 11, 2002. (Cited on page 4.)

[Bohm 1983] C. Bohm, T. Greitz, B. M. Berggren and L. Olsso. *Adjustable computerized stereotaxic brain atlas for transmission and emission tomograph*. Am J Neuroradiolog, vol. 4, pages 731–733, 1983. (Cited on page 54.)

[Brant-Zawadzki 1992] M. Brant-Zawadzki, G. D. Gillan and W. R. Nitz. *MP RAGE: a three-dimensional, T1-weighted, gradient-echo sequence–initial experience in the brain*. Radiology, vol. 182, no. 3, pages 769–75, Mar 1992. (Cited on page 78.)

[Brett 2002] M. Brett, I. S. Johnsrude and A. M. Owen. *The problem of functional localization in the human brain*. Nat Rev Neurosci, vol. 3, no. 3, pages 243–9, Mar 2002. (Cited on page 16.)

[Broca 1888] P. Broca. *Mémoire d'anthroplogie*. Paris: Reinwald, 1888. (Cited on page 22.)

[Buckner 2011] R. L. Buckner, F. M. Krienen, A. Castellanos, J. C. Diaz and B. T. Thomas Yeo. *The organization of the human cerebellum estimated by intrinsic functional connectivity*. Journal of Neurophysiology, vol. 106, no. 5, pages 2322–45, Nov 2011. (Cited on pages 30 and 31.)

[Cachier 2003] P. Cachier, E. Bardinet, D. Dormont, X. Pennec and N. Ayache. *Iconic feature based nonrigid registration: the PASHA algorithm*. Comput Vis Image Und, vol. 89, no. 2-3, pages 272–298, Jan 2003. (Cited on pages 55 and 58.)

[Caminiti 1991] R. Caminiti, P. B. Johnson, C. Galli, S. Ferraina and Y. Burnod. *Making arm movements within different parts of space: the premotor and motor cortical representation of a coordinate system for reaching to visual targets*. J Neurosci, vol. 11, no. 5, pages 1182–97, May 1991. (Cited on pages 4 and 29.)

[Caulo 2007] M. Caulo, C. Briganti, P. A. Mattei, B. Perfetti, A. Ferretti, G. L. Romani, A. Tartaro and C. Colosimo. *New morphologic variants of the hand motor cortex as seen with MR imaging in a large study population*. AJNR Am J Neuroradiol, vol. 28, no. 8, pages 1480–5, Sep 2007. (Cited on page 20.)

[Chen 2006] C. J. Chen, H. L. Liu, F. C. Wei and N.-S. Chu. *Functional MR imaging of the human sensorimotor cortex after toe-to-finger transplantation*. AJNR Am J Neuroradiol, vol. 27, no. 8, pages 1617–21, Sep 2006. (Cited on page 5.)

[Coffman 2011] K. A. Coffman, R. P. Dum and P. L. Strick. *Cerebellar vermis is a target of projections from the motor areas in the cerebral cortex*. Proc Natl Acad Sci USA, vol. 108, no. 38, pages 16068–73, Sep 2011. (Cited on page 30.)

[Collins 1994] D. L. Collins. *3D Model-based segmentation of individual brain structures from magnetic resonance imaging data*. Department of Biomedical Engineering McGiII University, Montreal, 1994. (Cited on pages 53 and 54.)

[Coulon 2011] O. Coulon, F. Pizzagalli, G. Operto, G. Auzias, C. Delon-Martin and M. Dojat. *Two new stable anatomical landmarks on the Central Sulcus: definition, automatic detection, and their relationship with primary motor functions of the hand*. Conf Proc IEEE Eng Med Biol Soc, vol. 2011, pages 7795–8, Jan 2011. (Cited on page 176.)

[Crum 2006] W. Crum and O. Camara. . . . *Generalized overlap measures for evaluation and validation in medical image analysis*. Medical Imaging, Jan 2006. (Cited on page 101.)

[Cusack 2003] R. Cusack, M. Brett and K. Osswald. *An evaluation of the use of magnetic field maps to undistort echo-planar images*. NeuroImage, vol. 18, no. 1, pages 127–142, 2003. (Cited on page 40.)

[Cykowski 2008] M. D. Cykowski, O. Coulon, P. V. Kochunov, K. Amunts, J. L. Lancaster, A. R. Laird, D. C. Glahn and P. T. Fox. *The central sulcus: an observer-independent characterization of sulcal landmarks and depth asymmetry*. Cereb Cortex, vol. 18, no. 9, pages 1999–2009, Sep 2008. (Cited on pages 22 and 176.)

[Daskalakis 2004] Z. J. Daskalakis, G. O. Paradiso, B. K. Christensen, P. B. Fitzgerald, C. Gunraj and R. Chen. *Exploring the connectivity between the cerebellum and motor cortex in humans*. J Physiol (Lond), vol. 557, no. Pt 2, pages 689–700, Jun 2004. (Cited on page 30.)

[de Moortele 1997] P. F. Van de Moortele, B. Cerf, E. Lobel, A. L. Paradis, A. Faurion and D. Le Bihan. *Latencies in fMRI time-series: effect of slice acquisition order and perception*. NMR Biomed, vol. 10, no. 4-5, pages 230–6, Jan 1997. (Cited on page 85.)

[Dechent 2003] P. Dechent and J. Frahm. *Functional somatotopy of finger representations in human primary motor cortex*. Hum Brain Mapp, vol. 18, no. 4, pages 272–83, Apr 2003. (Cited on pages 9, 12, 13, 27, 173, 174 and 175.)

[Deichmann 2000] R. Deichmann, C. D. Good, O. Josephs, J. Ashburner and R. Turner. *Optimization of 3-D MP-RAGE sequences for structural brain imaging*. NeuroImage, vol. 12, no. 1, pages 112–27, Jul 2000. (Cited on page 77.)

[Diedrichsen 2006] J. Diedrichsen. *A spatially unbiased atlas template of the human cerebellum*. NeuroImage, vol. 33, no. 1, pages 127–38, Oct 2006. (Cited on page 84.)

[Diedrichsen 2009] J. Diedrichsen, J. H. Balsters, J. Flavell, E. Cussans and N. Ramnani. *A probabilistic MR atlas of the human cerebellum*. NeuroImage, vol. 46, no. 1, pages 39–46, May 2009. (Cited on page 84.)

[Doyon 2005] J. Doyon and H. Benali. *Reorganization and plasticity in the adult brain during learning of motor skills*. Curr Opin Neurobiol, vol. 15, no. 2, pages 161–7, Apr 2005. (Cited on pages 6, 7 and 30.)

[Draganski 2004] B. Draganski, C. Gaser, V. Busch, G. Schuierer, U. Bogdahn and A. May. *Neuroplasticity: changes in grey matter induced by training*. Nature, vol. 427, no. 6972, pages 311–2, Jan 2004. (Cited on pages 6 and 46.)

[Draganski 2006] B. Draganski, T. Moser, N. Lummel, S. Gänssbauer, U. Bogdahn, F. Haas and A. May. *Decrease of thalamic gray matter following limb amputation*. NeuroImage, vol. 31, no. 3, pages 951–7, Jul 2006. (Cited on page 6.)

[Draganski 2008] B. Draganski and A. May. *Training-induced structural changes in the adult human brain*. Behav Brain Res, vol. 192, no. 1, pages 137–42, Sep 2008. (Cited on page 4.)

[Du 2011] J. Du, L. Younes and A. Qiu. *Whole brain diffeomorphic metric mapping via integration of sulcal and gyral curves, cortical surfaces, and images*. NeuroImage, vol. 56, no. 1, pages 162–73, 2011. (Cited on page 171.)

[Dubois 2008] J. Dubois, M. Benders, A. Cachia, F. Lazeyras, R. Ha-Vinh Leuchter, S. V. Sizonenko, C. Borradori-Tolsa, J.-F. Mangin and P. S. Hüppi. *Mapping the early cortical folding process in the preterm newborn brain*. Cereb Cortex, vol. 18, no. 6, pages 1444–54, Jun 2008. (Cited on page 60.)

[Fischl 1999] B Fischl, M I Sereno, R B Tootell and A M Dale. *High-resolution intersubject averaging and a coordinate system for the cortical surface*. Hum Brain Mapp, vol. 8, no. 4, pages 272–84, Jan 1999. (Cited on page 171.)

[Fischl 2008] B. Fischl, N. Rajendran, E. Busa, J. Augustinack, O. Hinds, B. T. Thomas Yeo, H. Mohlberg, K. Amunts and K. Zilles. *Cortical folding patterns and predicting cytoarchitecture*. Cereb Cortex, vol. 18, no. 8, pages 1973–80, Aug 2008. (Cited on page 14.)

[Fortier 1989] P. A. Fortier, J. F. Kalaska and A. M. Smith. *Cerebellar neuronal activity related to whole-arm reaching movements in the monkey*. Journal of Neurophysiology, vol. 62, no. 1, pages 198–211, Jul 1989. (Cited on page 29.)

[Friston 1995] K. J. Friston, J. Ashburner, C. D. Frith, J. B. Poline, J. D. Heather and R. S. J. Frackowiak. *Spatial registration and normalization of images*. Hum Brain Mapp, vol. 3, pages 165–189, 1995. (Cited on pages 46, 54, 59 and 61.)

[Friston 1996] K. J. Friston, S. Williams, R. Howard, R. S. Frackowiak and R. Turner. *Movement-related effects in fMRI time-series*. Magn Reson Med, vol. 35, no. 3, pages 346–55, Mar 1996. (Cited on page 86.)

[Fulton 1935] J. Fulton. *A note on the definition of the "motor" and "premotor" areas*. Brain, Jan 1935. (Cited on page 19.)

[Funk 2008a] M. Funk and P. Brugger. *Mental rotation of congenitally absent hands*. J Int Neuropsychol Soc, vol. 14, no. 1, pages 81–9, Jan 2008. (Cited on page 5.)

[Funk 2008b] M. Funk, K. Lutz, S. Hotz-Boendermaker, M. Roos, P. Summers, P. Brugger, M.-C. Hepp-Reymond and S. S. Kollias. *Sensorimotor tongue representation in individuals with unilateral upper limb amelia*. NeuroImage, vol. 43, no. 1, pages 121–7, Oct 2008. (Cited on page 5.)

[Garraux 2004] G. Garraux, A.Bauer, T. Hanakawa, T. Wu, K. Kansaku and M. Hallett. *Changes in brain anatomy in focal hand dystonia*. Ann Neurol, vol. 55, no. 5, pages 736–9, May 2004. (Cited on page 6.)

[Gati 1997] J. S. Gati, R. S. Menon, K. Ugurbil and B. K. Rutt. *Experimental determination of the BOLD field strength dependence in vessels and tissue*. Magn Reson Med, vol. 38, no. 2, pages 296–302, Aug 1997. (Cited on page 16.)

[Georgopoulos 1982] A. P. Georgopoulos, J. F. Kalaska, R. Caminiti and J. T. Massey. *On the relations between the direction of two-dimensional arm movements and cell discharge in primate motor cortex*. J Neurosci, vol. 2, no. 11, pages 1527–37, Nov 1982. (Cited on pages 4 and 29.)

[Geyer 1996] S. Geyer, A. Ledberg, A. Schleicher, S. Kinomura, T. Schormann, U. Bürgel, T. Klingberg, J. Larsson, K. Zilles and P. E. Roland. *Two different areas within the primary motor cortex of man*. Nature, vol. 382, no. 6594, pages 805–7, Aug 1996. (Cited on pages 12, 19, 20, 25, 169 and 173.)

[Gholipour 2007] A. Gholipour, N. Kehtarnavaz, R. Briggs, M. Devous and K. Gopinath. *Brain functional localization: a survey of image registration techniques*. IEEE Trans Med Imaging, vol. 26, no. 4, pages 427–51, Apr 2007. (Cited on page 101.)

[Giraux 2001] P. Giraux, A. Sirigu, F. Schneider and J. M. Dubernard. *Cortical reorganization in motor cortex after graft of both hands*. Nature neuroscience, vol. 4, no. 7, pages 691–2, Jul 2001. (Cited on page 5.)

[Gorno-Tempini 2002] M. L. Gorno-Tempini, C. Hutton, O. Josephs, R. Deichmann, C. Price and R. Turner. *Echo time dependence of BOLD contrast and susceptibility artifacts*. NeuroImage, vol. 15, no. 1, pages 136–42, Jan 2002. (Cited on page 41.)

[Gould 1986] H. J. Gould, C. G. Cusick, T. P. Pons and J. H. Kaas. *The relationship of corpus callosum connections to electrical stimulation maps of motor, supplementary motor, and the frontal eye fields in owl monkeys*. J Comp Neurol, vol. 247, no. 3, pages 297–325, May 1986. (Cited on page 26.)

[Griswold 2002] M. A. Griswold, P. M. Jakob, R. M. Heidemann, M. Nittka, V. Jellus, J. Wang, B. Kiefer and A. Haase. *Generalized autocalibrating partially parallel acquisitions (GRAPPA)*. Magnet Reson Med, vol. 47, no. 6, pages 1202–1210, Jun 2002. (Cited on page 42.)

[Grodd 2001] W. Grodd, E. Hulsmann, M. Lotze, D. Wildgruber and M. Erb. *Sensorimotor mapping of the human cerebellum: fMRI evidence of somatotopic organization*. Hum Brain Mapp, vol. 13, no. 2, pages 55–73, Jan 2001. (Cited on pages 30, 174 and 175.)

[Haase 2011] A. Haase, J. Frahm, D. Matthaei, W. H.änicke and K-D. Merboldt. *FLASH imaging: rapid NMR imaging using low flip-angle pulses. 1986*. J Magn Reson, vol. 213, no. 2, pages 533–41, Dec 2011. (Cited on page 77.)

[Hajnal 1994] J. V. Hajnal, R. Myers, A. Oatridge, J. E. Schwieso, I. R. Young and G. M. Bydder. *Artifacts due to stimulus correlated motion in functional imaging of the brain*. Magn Reson Med, vol. 31, no. 3, pages 283–91, Mar 1994. (Cited on page 86.)

[Hajnal 2001] J. V. Hajnal, Derek L. G. Hill and D. J. Hawkes. Medical image registration. 2001. (Cited on pages 49 and 55.)

[Hebb 1949] D. O. Hebb. *The Organization of Behaviour*. Wiley, New York, 1949. (Cited on page 4.)

[Hellier 2000] P. Hellier and C. Barillot. *Multimodal non-rigid warping for correction of distortions in functional MRI*. Medical Image Computing and Computer-Assisted, Jan 2000. (Cited on page 46.)

[Hellier 2003] P. Hellier, C. Barillot, I. Corouge, B. Gibaud, G. Le Goualher, D. L. Collins, A. Evans, G. Malandain, N. Ayache, G. E. Christensen and H. J. Johnson. *Retrospective evaluation of intersubject brain registration*. IEEE Trans Med Imaging, vol. 22, no. 9, pages 1120–30, Sep 2003. (Cited on pages 17 and 170.)

[Herrero 2002] M.-T. Herrero, C. Barcia and J. M. Navarro. *Functional anatomy of thalamus and basal ganglia*. Childs Nerv Syst, vol. 18, no. 8, pages 386–404, Aug 2002. (Cited on page 24.)

[Hilbig 2001] H. Hilbig, H. J. Bidmon, U. Blohm and K. Zilles. *Wisteria floribunda agglutinin labeling patterns in the human cortex: a tool for revealing areal borders and subdivisions in parallel with immunocytochemistry*. Anat Embryol, vol. 203, no. 1, pages 45–52, Jan 2001. (Cited on page 22.)

[Hlustík 2001] P. Hlustík, A. Solodkin, R. P. Gullapalli, D. C. Noll and S. L. Small. *Somatotopy in human primary motor and somatosensory hand representations revisited*. Cereb Cortex, vol. 11, no. 4, pages 312–21, Apr 2001. (Cited on pages 9, 174 and 175.)

[Hopkins 2010] W. D. Hopkins, O. Coulon and J.-F. Mangin. *Observer-independent characterization of sulcal landmarks and depth asymmetry in the central sulcus of the chimpanzee brain*. Neuroscience, vol. 171, no. 2, pages 544–51, Dec 2010. (Cited on page 29.)

[Hughlings-Jackson 1873] J. Hughlings-Jackson. *On the anatomical and physiological localization of movements in the brain*. Lancet, vol. 1, pages 84–85, 162–164,232–234, 1873. (Cited on page 9.)

[Humphrey 1986] D. R. Humphrey. *Representation of movements and muscles within the primate precentral motor cortex: historical and current perspectives*. Fed Proc, vol. 45, no. 12, pages 2687–99, Nov 1986. (Cited on page 25.)

[Hyde 2001] J. S. Hyde, B. B. Biswal and A. Jesmanowicz. *High-resolution fMRI using multislice partial k-space GR-EPI with cubic voxels*. Magn Reson Med, vol. 46, no. 1, pages 114–25, Jul 2001. (Cited on pages 12, 35 and 42.)

[Indovina 2001] I. Indovina and J. N. Sanes. *Combined visual attention and finger movement effects on human brain representations*. Exp Brain Res, vol. 140, no. 3, pages 265–79, Oct 2001. (Cited on page 174.)

[Jaillard 2005] A. Jaillard, C. Delon Martin, K. Garambois, J. F. Lebas and M. Hommel. *Vicarious function within the human primary motor cortex? A longitudinal fMRI stroke study*. Brain, vol. 128, no. Pt 5, pages 1122–38, May 2005. (Cited on pages 4 and 46.)

[Jezzard 1995] P. Jezzard and R. S. Balaban. *Correction for geometric distortion in echo planar images from B0 field variations*. Magn Reson Med, vol. 34, no. 1, pages 65–73, Jul 1995. (Cited on page 40.)

[Jezzard 1999] P. Jezzard and S. Clare. *Sources of distortion in functional MRI data*. Hum Brain Mapp, vol. 8, no. 2-3, pages 80–5, Jan 1999. (Cited on page 40.)

[Jezzard 2001] P. Jezzard, P. M. Matthews and S. M. Smith. Functional MRI. 2001. (Cited on page 11.)

[Johansen-Berg 2001] H. Johansen-Berg. *Reorganisation and modulation of the human sensorimotor system: implications for recovery of motor function after stroke*. PhD thesis, University of Oxford, 2001. (Cited on pages 20 and 21.)

[Kakei 1999] S. Kakei, D. S. Hoffman and P.L. Strick. *Muscle and movement representations in the primary motor cortex*. Science, Jan 1999. (Cited on pages 25, 29 and 175.)

[Kakei 2001] S. Kakei, D. Hoffman and P. L. Strick. *Direction of action is represented in the ventral premotor cortex*. Nature neuroscience, Jan 2001. (Cited on pages 29 and 105.)

[Kandel 2000] E. R. Kandel, J. H. Schwartz and T. M. Jessel. Principles of neural science fourth edition. 2000. (Cited on page 11.)

[Kassam 1996] A. Kassam and M. L. Wood. *Fourier registration of three-dimensional brain MR images: exploiting the axis of rotation*. J Magn Reson Imaging, vol. 6, no. 6, pages 894–902, Jan 1996. (Cited on page 55.)

[Kim 1999] B. Kim, J. L. Boes, P. H. Bland, T. L. Chenevert and C. R. Meyer. *Motion correction in fMRI via registration of individual slices into an anatomical volume*. Magn Reson Med, vol. 41, no. 5, pages 964–72, May 1999. (Cited on page 46.)

[Klein 2009] A. Klein, J. Andersson, B. A. Ardekani, J. Ashburner, B. Avants, M.C. Chiang, G. E. Christensen, D. L. Collins, J. Gee, P. Hellier, J. H. Song, M. Jenkinson, C. Lepage, D. Rueckert, P. Thompson, T. Vercauteren, R. P. Woods, J. J. Mann and R. V. Parsey. *Evaluation of 14 nonlinear deformation algorithms applied to human brain MRI registration*. NeuroImage,

vol. 46, no. 3, pages 786–802, Jul 2009. (Cited on pages 17, 58, 60, 62, 63, 64, 65, 101 and 170.)

[Klein 2010] A. Klein, S. S. Ghosh, B. Avants, B. T. T. Yeo, B. Fischl, B. A. Ardekani, J. C. Gee, J. J. Mann and R. V. Parsey. *Evaluation of volume-based and surface-based brain image registration methods*. NeuroImage, vol. 51, no. 1, pages 214–20, May 2010. (Cited on pages 17 and 172.)

[Kleinschmidt 1997] A. Kleinschmidt, M. F. Nitschke and J. Frahm. *Somatotopy in the human motor cortex hand area. A high-resolution functional MRI study*. Eur J Neurosci, vol. 9, no. 10, pages 2178–2186, Jan 1997. (Cited on pages 12, 27, 173 and 175.)

[Krüger 2001] G. Krüger, A. Kastrup and G. H. Glover. *Neuroimaging at 1.5 T and 3.0 T: comparison of oxygenation-sensitive magnetic resonance imaging*. Magn Reson Med, vol. 45, no. 4, pages 595–604, Apr 2001. (Cited on page 16.)

[Leow 2007] A. D. Leow, I. Yanovsky, M.-C. Chiang, A. D. Lee, A. D. Klunder, A. Lu, J. T. Becker, S. W. Davis, A. W. Toga and P. M. Thompson. *Statistical properties of Jacobian maps and the realization of unbiased large-deformation nonlinear image registration*. IEEE Trans Med Imaging, vol. 26, no. 6, pages 822–32, Jun 2007. (Cited on page 103.)

[Li 2008] Y. Li, N. Xu, J. M. Fitzpatrick and B. M. Dawant. *Geometric distortion correction for echo planar images using nonrigid registration with spatially varying scale*. Magnetic Resonance Imaging, vol. 26, no. 10, pages 1388–1397, Dec 2008. (Cited on page 46.)

[Lotze 2000] M. Lotze, M. Erb, H. Flor, E. Huelsmann, B. Godde and W. Grodd. *fMRI evaluation of somatotopic representation in human primary motor cortex*. NeuroImage, vol. 11, no. 5 Pt 1, pages 473–81, May 2000. (Cited on page 12.)

[Lotze 2001] M. Lotze, H. Flor, W. Grodd, W. Larbig and N. Birbaumer. *Phantom movements and pain. An fMRI study in upper limb amputees*. Brain, vol. 124, no. Pt 11, pages 2268–77, Nov 2001. (Cited on page 4.)

[Loubinoux 2001] I. Loubinoux, C. Carel, F. Alary, K. Boulanouar, G. Viallard, C. Manelfe, O. Rascol, P. Celsis and F. Chollet. *Within-session and between-session reproducibility of cerebral*

sensorimotor activation: a test–retest effect evidenced with functional magnetic resonance imaging. J Cereb Blood Flow Metab, vol. 21, no. 5, pages 592–607, May 2001. (Cited on page 154.)

[Lugaro 1906] E. Lugaro. *Treatise of Psychiatry*. 1906. (Cited on page 4.)

[Maes 1997] F. Maes, A. Collignon, D. Vandermeulen, G. Marchal and P. Suetens. *Multimodality image registration by maximization of mutual information*. IEEE Trans Med Imaging, vol. 16, no. 2, pages 187–98, Apr 1997. (Cited on page 56.)

[Maintz 1998] J. B. Maintz and M. A. Viergever. *A survey of medical image registration*. Med Image Anal, vol. 2, no. 1, pages 1–36, Mar 1998. (Cited on pages 59 and 101.)

[Mangin 1995] J. Mangin, V. Frouin, I. Bloch, J. R.égis and J. Lopez-krahe. *From 3D magnetic resonance images to structural representations of the cortex topography using topology preserving deformations*. Journal of Mathematical Imaging and Vision, vol. 5, pages 297–318, Jan 1995. (Cited on page 89.)

[Mangin 2004a] J. F. Mangin, D. Rivière, A. Cachia, E. Duchesnay, Y. Cointepas, D. Papadopoulos-Orfanos, D. L. Collins, A. C. Evans and J. Régis. *Object-based morphometry of the cerebral cortex*. IEEE Trans Med Imaging, vol. 23, no. 8, pages 968–82, Aug 2004. (Cited on pages 29, 58 and 65.)

[Mangin 2004b] J.-F. Mangin, D. Rivière, A. Cachia, E. Duchesnay, Y. Cointepas, D. Papadopoulos-Orfanos, P. Scifo, T. Ochiai, F. Brunelle and J. Régis. *A framework to study the cortical folding patterns.* NeuroImage, vol. 23 Suppl 1, pages S129–38, 2004. (Cited on page 89.)

[Mansfield 1977] P. Mansfield. *Multi-planar image formation using NMR spin echoes*. Journal of Physics C: Solid State Physics, vol. 10, page L55, Feb 1977. (Cited on page 35.)

[Marshall 2000] R. S. Marshall, G. M. Perera, R. M. Lazar, J. W. Krakauer, R. C. Constantine and R. L. DeLaPaz. *Evolution of cortical activation during recovery from corticospinal tract infarction*. Stroke, vol. 31, no. 3, pages 656–61, Mar 2000. (Cited on page 4.)

[Mazziotta 2001] J. Mazziotta, A. Toga, A. Evans, P. Fox, J. Lancaster, K. Zilles, R. Woods, T. Paus, G. Simpson, B. Pike, C. Holmes, L. Collins, P. Thompson, D. MacDonald, M. Iacoboni,

T. Schormann, K. Amunts, N. Palomero-Gallagher, S. Geyer, L. Parsons, K. Narr, N. Kabani, G. Le Goualher, D. Boomsma, T. Cannon, R. Kawashima and B. Mazoyer. *A probabilistic atlas and reference system for the human brain: International Consortium for Brain Mapping (ICBM)*. Philos Trans R Soc Lond B Biol Sci, vol. 356, no. 1412, pages 1293–322, 2001. (Cited on page 172.)

[McGonigle 2002] D. J. McGonigle, R. Hannine, S. Salenius, R. Hari, R. S. J. Frackowiak and C.D. Frith. *Whose arm is it anyway? An fMRI case study of supernumerary phantom limb*. Brain, vol. 125, pages 1265–1274, 2002. (Cited on page 46.)

[Meier 2008] J. D. Meier, T. N. Aflalo, S. Kastner and M. S. Graziano. *Complex organization of human primary motor cortex: a high-resolution fMRI study*. Journal of Neurophysiology, vol. 100, no. 4, pages 1800–12, Oct 2008. (Cited on pages 11, 27, 28, 105 and 174.)

[Metaizeau 2004] J. P. Metaizeau. *Stable elastic intramedullary nailing for fractures of the femur in children*. J Bone Joint Surg Br, vol. 86, no. 7, pages 954–7, Sep 2004. (Cited on page 73.)

[Moore 2012] R. D. Moore, C. Gallea, S. G. Horovitz and M. Hallett. *Individuated finger control in focal hand dystonia: An fMRI study*. NeuroImage, vol. 61, no. 4, pages 823–831, Jul 2012. (Cited on page 6.)

[Mugler 1990] J. P. Mugler and J. R. Brookeman. *Three-dimensional magnetization-prepared rapid gradient-echo imaging (3D MP RAGE)*. Magn Reson Med, vol. 15, no. 1, pages 152–7, Jul 1990. (Cited on page 77.)

[Mussa-Ivaldi 2000] F. Mussa-Ivaldi and E. Bizzi. *Motor learning through the combination of primitives*. Phil. Trans. R. Soc. Lond. B, Jan 2000. (Cited on page 29.)

[Nitz 1999] W. R. Nitz and P. Reimer. *Contrast mechanisms in MR imaging*. European radiology, vol. 9, pages 1032 – 1046, Jan 1999. (Cited on page 37.)

[Nudo 1992] R. J. Nudo, W. M. Jenkins, M. M. Merzenich, T. Prejean and R. Grenda. *Neurophysiological correlates of hand preference in primary motor cortex of adult squirrel monkeys*. J Neurosci, vol. 12, no. 8, pages 2918–47, Aug 1992. (Cited on page 26.)

[Nudo 2001] R. Nudo, E. Plautz and S. B. Frost. *Role of adaptive plasticity in recovery of function after damage to motor cortex*. Muscle & nerve, Jan 2001. (Cited on page 4.)

[Olman 2011] C. A. Olman, K. A. Pickett, M.-P. Schallmo and T. J. Kimberley. *Selective BOLD responses to individual finger movement measured with fMRI at 3T*. Hum Brain Mapp, Jun 2011. (Cited on page 27.)

[Peinfield 1937] W. Peinfield and E. Boldrey. *Somatic motor and sensory representation in the cerebral cortex of man as studied by electrical stimulation*. Brain, vol. 60, pages 389–443, 1937. (Cited on page 10.)

[Penfield 1935] W Penfield. *The principles of physiology involved in the management of increased intracranical pressure*. Ann Surg, vol. 102, no. 4, pages 548–54, Oct 1935. (Cited on page 173.)

[Penfield 1950] W. Penfield and T. Rasmussen. The cerebral cortex of man. 1950. (Cited on pages 9, 22 and 25.)

[Perrot 2011] M. Perrot, D. Rivière and J.-F. Mangin. *Cortical sulci recognition and spatial normalization*. Med Image Anal, vol. 15, no. 4, pages 529–50, Aug 2011. (Cited on page 60.)

[Picard 2001] N. Picard and P. L. Strick. *Imaging the premotor areas*. Curr Opin Neurobiol, vol. 11, no. 6, pages 663–72, Dec 2001. (Cited on pages 4 and 22.)

[Pimentel 2011] M. A. F. Pimentel, P. Vilela, I. Sousa and P. Figueiredo. *Localization of the hand motor area by arterial spin labeling and blood oxygen level-dependent functional magnetic resonance imaging*. Hum Brain Mapp, Nov 2011. (Cited on page 12.)

[Pluim 2003] J. P. W. Pluim, J. B. A. Maintz and M. A. Viergever. *Mutual-information-based registration of medical images: A survey*, Jan 2003. (Cited on pages 56 and 57.)

[Postelnicu 2009] G. Postelnicu, L. Zollei and B. Fischl. *Combined volumetric and surface registration*. IEEE Trans Med Imaging, vol. 28, no. 4, pages 508–22, 2009. (Cited on page 171.)

[Pujol 2000] J. Pujol, J. Roset-Llobet, D. Rosinés-Cubells, J. Deus, B. Narberhaus, J. Valls-Solé, A. Capdevila and A. Pascual-Leone. *Brain cortical activation during guitar-induced hand dystonia studied by functional MRI*. NeuroImage, vol. 12, no. 3, pages 257–67, Sep 2000. (Cited on page 5.)

[Rao 1995] S. M. Rao, J. R. Binder, T. A. Hammeke, P. A. Bandettini, J. A. Bonholz, J. A. Frost, B. M. Myklebust, R. D. Jacobson and J. S. Hyde. *Somatotopi mapping of the human primary motor cortex with functional magnetic resonance imaging*. Neurology, vol. 45, no. 5, pages 919–924, Jan 1995. (Cited on pages 27 and 173.)

[Rathelot 2006a] J.-A. Rathelot and P. L. Strick. *Muscle representation in the macaque motor cortex: an anatomical perspective*. Proc Natl Acad Sci USA, vol. 103, no. 21, pages 8257–62, May 2006. (Cited on page 25.)

[Rathelot 2006b] J. A. Rathelot and P. L. Strick. *Muscle representation in the macaque motor cortex: an anatomical perspective*. Proc Natl Acad Sci U S A, vol. 103, no. 21, pages 8257–62, 2006. (Cited on page 174.)

[Ravizza 2005] S. M. Ravizza, C. A. McCormick, J. E. Schlerf, T. Justus and R. B. Ivry. *Cerebellar damage produces selective deficits in verbal working memory*. Brain, vol. 129, no. 2, pages 306–320, Oct 2005. (Cited on page 30.)

[Régis 2005] J. Régis, J.-F. Mangin, T. Ochiai, V. Frouin, D. Riviére, A. Cachia, M. Tamura and Y. Samson. "*Sulcal root*" *generic model: a hypothesis to overcome the variability of the human cortex folding patterns*. Neurol Med Chir (Tokyo), vol. 45, no. 1, pages 1–17, Jan 2005. (Cited on page 60.)

[Rizzolatti 1998] G. Rizzolatti, G. Luppino and M. Matelli. *The organization of the cortical motor system: new concepts*, Jan 1998. (Cited on page 19.)

[Roberts 1998] D. W. Roberts, A. Hartov, F. E. Kennedy, M. I. Miga and K. D. Paulsen. *Intraoperative brain shift and deformation: a quantitative analysis of cortical displacement in 28 cases*. Neurosurgery, vol. 43, no. 4, pages 749–58; discussion 758–60, Oct 1998. (Cited on page 46.)

[Rohlfing 2010] T. Rohlfing, N. M. Zahr, E. V. Sullivan and A. Pfefferbaum. *The SRI24 multichannel atlas of normal adult human brain structure*. Hum Brain Mapp, vol. 31, no. 5, pages 798–819, May 2010. (Cited on page 46.)

[Roland 1996] P. E. Roland and K. Zilles. *Functions and structures of the motor cortices in humans*. Curr Opin Neurobiol, vol. 6, no. 6, pages 773–81, Dec 1996. (Cited on page 19.)

[Rowe 2011] James B. Rowe and Hartwig R. Siebner. *The motor system*. NeuroImage, Dec 2011. (Cited on page 20.)

[Rowe 2012] J. B. Rowe and H. R. Siebner. *The motor system*. Neuroimages, vol. to appear, 2012. (Cited on page 173.)

[Rueckert 2003] D. Rueckert, A. Frangi and J. Schnabel. *Automatic construction of 3-D statistical deformation models of the brain using nonrigid registration*. Medical Imaging, IEEE Transactions on, vol. 22, no. 8, pages 1014 – 1025, 2003. (Cited on page 46.)

[S. D. Jr Stoney 1968] H. Asanuma S. D. Jr Stoney. *Excitation of pyramidal tract cells by intracortical microstimulation: effective extent of stimulating current*. J Neurophysiol, vol. 31, pages 659–669, 1968. (Cited on page 26.)

[Sanes 1995] J. N. Sanes, J. P. Donoghue, V. Thangaraj, R. R. Edelman and S. Warach. *Shared neural substrates controlling hand movements in human motor cortex*. Science, vol. 268, no. 5218, pages 1775–7, Jun 1995. (Cited on pages 26, 27 and 173.)

[Sanes 2000] J. N. Sanes and J. P. Donoghue. *Plasticity and primary motor cortex*. Annu. Rev. Neurosci., vol. 23, pages 393–415, Jan 2000. (Cited on page 4.)

[Sanes 2001] J. Sanes and M. Schieber. *Orderly somatotopy in primary motor cortex: does it exist?* NeuroImage, vol. 13, pages 968–974, Jan 2001. (Cited on pages 174 and 175.)

[Scheuerecker 2010] J. Scheuerecker, E. M. Meisenzahl, N. Koutsouleris, M. Roesner, V. Schöpf, J. Linn, M. Wiesmann, H. Brückmann, H.-J. Möller and T. Frodl. *Orbitofrontal volume reductions during emotion recognition in patients with major depression*. J Psychiatry Neurosci, vol. 35, no. 5, pages 311–20, Sep 2010. (Cited on page 30.)

[Schieber 1993] M. H. Schieber and L. S. Hibbard. *How somatotopic is the motor cortex hand area?* Science, vol. 261, no. 5120, pages 489–92, Jul 1993. (Cited on page 27.)

[Schieber 1998] M. H. Schieber and A. V. Poliakov. *Partial inactivation of the primary motor cortex hand area: effects on individuated finger movements*. J Neurosci, vol. 18, no. 21, pages 9038–54, Nov 1998. (Cited on page 27.)

[Schieber 2001] M. H. Schieber. *Constraints on somatotopic organization in the primary motor cortex*. Journal of Neurophysiology, vol. 86, no. 5, pages 2125–43, Nov 2001. (Cited on pages 4, 9 and 10.)

[Schmahmann 1998] J. D. Schmahmann and J. C. Sherman. *The cerebellar cognitive affective syndrome.* Brain, vol. 121, pages 561–579, Jan 1998. (Cited on page 30.)

[Schmahmann 1999] J. D. Schmahmann, J. Doyon, D. McDonald, C. Holmes, K. Lavoie, A. S. Hurwitz, N. Kabani, A. Toga, A. Evans and M. Petrides. *Three-dimensional MRI atlas of the human cerebellum in proportional stereotaxic space*. NeuroImage, vol. 10, no. 3 Pt 1, pages 233–60, Sep 1999. (Cited on page 23.)

[Schott 1993] G. Schott. *Penfield's homunculus: a note on cerebral cartography.* Journal of Neurology, Jan 1993. (Cited on pages 25 and 26.)

[Sessle 1982] B. J. Sessle and M. Wiesendanger. *Structural and functional definition of the motor cortex in the monkey (Macaca fascicularis)*. J Physiol (Lond), vol. 323, pages 245–65, Feb 1982. (Cited on page 26.)

[Stoodley 2009] C. J. Stoodley and J. D. Schmahmann. *Functional topography in the human cerebellum: a meta-analysis of neuroimaging studies*. NeuroImage, vol. 44, no. 2, pages 489–501, Jan 2009. (Cited on pages 23, 24 and 31.)

[Sun 2011] Z. Y. Sun, S. Klöppel, D. Rivière, M. Perrot, R. Frackowiak, H. Siebner and J.-F. Mangin. *The effect of handedness on the shape of the central sulcus*. NeuroImage, vol. 60, no. 1, pages 332–339, Dec 2011. (Cited on pages 14, 29, 174 and 178.)

[Szameitat 2012] A. J. Szameitat, S. Shen, A. Conforto and A. Sterr. *Cortical activation during executed, imagined, observed, and passive wrist movements in healthy volunteers and stroke patients*. NeuroImage, vol. 62, no. 1, pages 266–280, Aug 2012. (Cited on page 4.)

[Tahmasebi 2009] A. M. Tahmasebi, P. Abolmaesumi, Z. Z. Zheng, K. G. Munhall and I. S. Johnsrude. *Reducing inter-subject anatomical variation: effect of normalization method on sensitivity of functional magnetic resonance imaging data analysis in auditory cortex and the superior temporal region*. Neuroimage, vol. 47, no. 4, pages 1522–31, 2009. (Cited on page 170.)

[Tahmasebi 2011] A. M. Tahmasebi, M. H. Davis, C. J. Wild, J. M. Rodd, H. Hakyemez, P. Abolmaesumi and I. S. Johnsrude. *Is the Link between Anatomical Structure and Function Equally Strong at All Cognitive Levels of Processing?* Cereb Cortex, 2011. (Cited on page 170.)

[Talairach 1988] J. Talairach and P. Tournoux. Co-planar stereotaxic atlas of the human brain: 3-dimensional proportional system - an approach to cerebral imaging. 1988. (Cited on pages 16, 51, 52 and 53.)

[Thirion 1998] J. P. Thirion. *Image matching as a diffusion process: an analogy with Maxwell's demons*. Med Image Anal, vol. 2, no. 3, pages 243–60, Sep 1998. (Cited on page 64.)

[Thomas 2009] A. Thomas, S. Marrett, Z. Saad, D. Ruff, A. Martin and P.A. Bandettini. *Functional but not structural changes associated with learning: An exploration of longitudinal Voxel-Based Morphometry (VBM)*. NeuroImage, Jan 2009. (Cited on page 178.)

[Toxopeus 2011] C. M. Toxopeus, B. M de Jong, G. Valsan, B. A. Conway, K. L. Leenders and N. M. Maurits. *Direction of movement is encoded in the human primary motor cortex*. PLoS ONE, vol. 6, no. 11, page e27838, Jan 2011. (Cited on pages 29 and 175.)

[Triantafyllou 2005] C. Triantafyllou, R. D. Hoge, G. Krueger, C. J. Wiggins, A. Potthast, G. C. Wiggins and L. L. Wald. *Comparison of physiological noise at 1.5 T, 3 T and 7 T and optimization of fMRI acquisition parameters*. NeuroImage, vol. 26, no. 1, pages 243–50, May 2005. (Cited on pages 16 and 37.)

[Tsuge 1969] K. Tsuge and N. Adachi. *Tendon transfer for extensor palsy of forearm*. Hiroshima J Med Sci, vol. 18, no. 4, pages 219–32, Dec 1969. (Cited on pages 3 and 72.)

[Tsuge 1980] K. Tsuge. *Tendon transfers for radial nerve palsy*. Australian and New Zealand Journal of Surgery, Jan 1980. (Cited on pages 72 and 73.)

[Tucholka 2012] A. Tucholka, V. Fritsch, J. Poline and B. Thirion. *An empirical comparison of surface-based and volume-based group studies in neuroimaging*. NeuroImage, Jan 2012. (Cited on page 172.)

[Ungerleider 2002] L. Ungerleider, J. Doyon and A. Karni. *Imaging brain plasticity during motor skill learning*. Neurobiology of learning and memory, Jan 2002. (Cited on page 4.)

[Vercauteren 2009] T. Vercauteren, X. Pennec, A. Perchant and N. Ayache. *Diffeomorphic demons: efficient non-parametric image registration*. NeuroImage, vol. 45, no. 1 Suppl, pages S61–72, Mar 2009. (Cited on pages 18, 59, 61, 64, 94 and 96.)

[Viceic 2009] D. Viceic and al. *Local landmark-based registration for fMRI group studies of nonprimary auditory cortex*. Neuroimage, vol. 44, no. 1, pages 145–53, 2009. (Cited on pages 169 and 170.)

[Vigouroux 2007] L. Vigouroux, F. Quaine, A. Labarre-Vila, D. Amarantini and F. Moutet. *Using EMG data to constrain optimization procedure improves finger tendon tension estimations during static fingertip force production*. Journal of Biomechanics, Jan 2007. (Cited on page 72.)

[Viswanathan 2006] V. Viswanathan, M. Chmayssani, D. J. Adams and J. Hirsch. *Cortical reorganization following intradigital tendon transfer*. Neuroreport, vol. 17, no. 16, pages 1669–73, Nov 2006. (Cited on page 5.)

[Voogd 2003] J. Voogd. *The human cerebellum*. J Chem Neuroanat, vol. 26, no. 4, pages 243–52, Dec 2003. (Cited on page 30.)

[Vorobiev 1998] V. Vorobiev, P. Govoni, G. Rizzolatti, M. Matelli and G. Luppino. *Parcellation of human mesial area 6: cytoarchitectonic evidence for three separate areas*. Eur J Neurosci, vol. 10, no. 6, pages 2199–203, Jun 1998. (Cited on page 23.)

[Vovk 2007] U. Vovk, F. Pernus and B. Likar. *A review of methods for correction of intensity inhomogeneity in MRI*. IEEE Trans Med Imaging, vol. 26, no. 3, pages 405–21, Mar 2007. (Cited on page 89.)

[Weiss 2000] T. Weiss, W. H. Miltner, R. Huonker, R. Friedel, I. Schmidt and E. Taub. *Rapid functional plasticity of the somatosensory cortex after finger amputation*. Exp Brain Res, vol. 134, no. 2, pages 199–203, Sep 2000. (Cited on page 4.)

[White 1997] L. E. White, T. J. Andrews, C. Hulette, A. Richards, M. Groelle, J. Paydarfar and D. Purves. *Structure of the human sensorimotor system. I: Morphology and cytoarchitecture of the central sulcus*. Cereb Cortex, vol. 7, no. 1, pages 18–30, Jan 1997. (Cited on pages 14 and 15.)

[Woolsey 1952a] C. Woolsey, P. Settlage, D. Meyer, W. Sencer, T. Pinto Hamuy and A. Travis. *Patterns of localisation in precentral and "supplementary" motor areas and their relation to the concept of a premotor are*. ResPubAssocNervMentDis, no. 30, pages 228–264, 1952. (Cited on page 19.)

[Woolsey 1952b] C. N. Woolsey. Patterns of localization in sensory and motor areas of the cerebral cortex. 1952. (Cited on page 25.)

[Yassa 2009] M. A. Yassa and C. E. L. Stark. *A quantitative evaluation of cross-participant registration techniques for MRI studies of the medial temporal lobe*. NeuroImage, vol. 44, no. 2, pages 319–27, Jan 2009. (Cited on pages 17, 60 and 64.)

[Yeo 2009] B. Yeo and et al. *Spherical Demons: Fast Diffeomorphic Landmark-Free Surface Registration*. IEEE Trans Med Imaging, vol. 29, no. 3, pages 650–68, 2009. (Cited on pages 171 and 172.)

[Yousry 1997] T. A. Yousry, U. D. Schmid, H. Alkadhi, D. Schmidt, A. Peraud, A. Buettner and P. Winkler. *Localization of the motor hand area to a knob on the precentral gyrus. A new landmark*. Brain, vol. 120 (Pt 1), pages 141–57, Jan 1997. (Cited on pages 14, 15, 20 and 67.)

[Z'Graggen 2009] W. J. Z'Graggen, A. B. Conforto, R. Wiest, L. Remonda, C. W. Hess and A. Kaelin-Lang. *Mapping of direction and muscle representation in the human primary motor cortex controlling thumb movements*. J Physiol (Lond), vol. 587, no. Pt 9, pages 1977–87, May 2009. (Cited on pages 29, 105 and 175.)

[Zilles 1995] K. Zilles, G. Schlaug, M. Matelli, G. Luppino, A. Schleicher, M. Qü., A. Dabringhaus, R. Seitz and P. E .Roland. *Mapping of human and macaque sensorimotor areas by integrating architectonic, transmitter receptor, MRI and PET data*. J Anat, vol. 187 (Pt 3), pages 515–37, Dec 1995. (Cited on page 22.)

[Zoccoli 1979] E. Zoccoli. Structural and dynamic bases of hand surgery. 1979. (Cited on page 72.)